CYPRUS UNIVERSITY OF TECHNOLOGY
FACULTY OF ENGINEERING AND TECHNOLOGY
DEPARTMENT OF CIVIL ENGINEERING AND GEOMATICS

IMPROVING ATMOSPHERIC CORRECTION METHODS FOR AEROSOL OPTICAL THICKNESS RETRIEVAL SUPPORTED BY IN-SITU OBSERVATIONS AND GIS ANALYSIS

Kyriacos Themistocleous

A Dissertation Submitted
in Partial Fulfillment of the Requirements for the Degree of

Doctor of Philosophy

Limassol, 2011

APPROVAL PAGE

Doctor of Philosophy Dissertation

Improving atmospheric correction methods for aerosol optical thickness retrieval supported by in-situ observations and GIS analysis

Presented by

Kyriacos Themistocleous

Research Supervisor _____
Associate Professor Diofantos G. Hadjimitsis

Committee Member (Chairperson) _____
Associate Professor Dr. Nikolaos Soulakellis

Committee Member (advisor) _____
Senior Researcher Dr. Adrianos Retalis

Committee Member (advisor) _____
Senior Researcher Dr. Nektarios Chrysoulakis

Committee Member _____
Assistant Professor Dr. Evangelos Akylas

Cyprus University of Technology

February, 2012

Abstract

Atmospheric correction is an important pre-processing step required in many satellite remote sensing applications. Although there are several available atmospheric correction algorithms, there is limited literature available that examines their effectiveness using in-situ measurements from spectroradiometers and sun-photometers to retrieve reflectance and atmospheric properties. The aims of this thesis are to improve the Empirical Line Method of atmospheric correction, apply the improved Empirical Line Method and the Darkest Pixel method to retrieve the aerosol optical thickness (AOT), and to conduct an accuracy assessment of the results using in-situ measurements from spectroradiometers and sun-photometers. Five commonly located surface materials (gray asphalt, black asphalt, concrete, black sand and compacted sand) were identified as meeting the criteria for pseudo-invariant targets and their spectral signatures were measured from January 2010 to May 2011, in order to assess that their reflectance values did not change over time. The empirical line method was improved by using several pseudo-invariant targets of varying spectral characteristics. The Darkest Pixel method utilized the actual reflectance values of the darkest pixel in the selected area of interest. Eleven satellite images were atmospherically corrected using the improved empirical line method and the darkest pixel method with the actual reflectance values. The study found a strong agreement between the AOT values derived from the algorithm developed in this thesis and the in-situ AOT measurements from the sun photometers. A GIS analysis was conducted using the algorithm developed in this thesis to produce thematic maps to identify AOT distribution in the greater area of Limassol. The proposed AOT retrieval algorithm is a fully image-based method that explicits global applicability.

The innovation of this thesis is the retrieval of AOT by developing an image-based algorithm based on the radiative transfer equation to derive AOT using the reflectance values from the empirical line and darkest pixel method of atmospheric correction. Novel contributions to this thesis include the employment of pseudo-invariant targets for conducting accuracy assessment of both atmospheric correction methods, the improvement of the empirical line method using five pseudo-invariant targets of varying spectral characteristics and assessing the effects of wet and dry conditions on the pseudo-invariant targets. It is the first time that a GIS analysis has been conducted to automatically retrieve AOT using the radiative transfer equations. The integrated use of field spectroscopy, GIS and remote sensing for atmospheric correction of satellite imagery and AOT retrieval is an innovative contribution to the field of remote sensing.

Acknowledgements

I would like to express my sincere thanks to the three members of the PhD committee, Dr. Diofantos Hadjimitsis (Research Supervisor), Dr. Adrianos Retalis, and Dr. Nektarios Chrysoulakis for their invaluable guidance and assistance in this thesis. I would like to thank for their helpful feedback on this thesis. I would like to thank Dr. Chrystalla Demetriades for her expertise and assistance with the algorithm for the GIS model. I also want to thank Dr. Evangelos Akylas and Dr. Nicolaos Soulakellis for accepting to be part of the exaimnation committee.

I wish to thank the Cyprus University of Technology - Research Committee for providing internal funding for the program "Monitoring air pollution in Cyprus using satellite remote sensing and GIS and micro-sensor technology", which is based on this thesis. As well, I would like to thank all the team at the Remote Sensing Laboratory of the Cyprus University of Technology, Department of Civil Engineering and Geomatics for all their helpful assistance and support.

Table Of Contents

Table of Figures

Table of Tables

Table of Symbols and Acronyms

Symbol/ Acronym	Definition
Å	Ångstrom - A measurement of length (10^{-10} m), which is equivalent to 10 nm.
AOT	Aerosol Optical Thickness
AVHRR	Advanced Very High Resolution Radiometer, on board the NOAA polar orbiting satellites, with a spatial resolution 1.1 x 1.1 km.
d	correction coefficient accounting for variations in the Sun-to-Earth distance
DEM	Digital Elevation Model
DN	measured digital number at the satellite sensor
DP	Darkest Pixel
$E_{0\lambda}$	solar irradiance at the top of the atmosphere
E_G	global irradiance reaching the ground
EMR	Electromagnetic radiation - energy propagated through space or through material media in the form of an advancing interaction between electrical and magnetic fields
ERDAS	Earth Resources Data Analysis System - ERDAS Imagine is an image processing and GIS software package produced by ERDAS Inc.
ETM+	Enhanced Thematic Mapper+, sensor onboard the Landsat 7.
GCP	Ground Control Points - a geographic feature of known location that is

	recognizable on images and can be used to determine geometric correction functions for those images.
GIS	Geographical Information System - a tool for organizing data in a structure that focuses on the spatial relationships of the data.
GLOVIS	Global Visualization Viewer
GMT	Greenwich median time
GPS	Global Position System - a network of 24 radio transmitting satellites (NAVSTAR) developed by the US Department of Defense to provide accurate geographical position fixing
GSFC	NASA's Goddard Space Flight Center
FOV	Field-of-view - the solid angle through which an instrument is sensitive to radiation
θ_0	solar zenith angle - equal to 180 degrees minus the Sun elevation angle.
θ_v	sensor viewing angle
IR	Infra-red - portion of the electromagnetic spectrum lying between the red end of the visible spectrum and microwave radiation (700 nm to 1000 μm).
IFOV	Instantaneous-field-of-view - A measure of the area viewed by a single detector on a scanning system at a given moment in time.
Landsat	Land Satellite
Lidar	Light Detection and Ranging
L_{ts}	at-satellite radiance
L_p	atmospheric path radiance

L_{pa}	atmospheric path radiance due to Mie (aerosol) scattering
L_{pr}	atmospheric path radiance due to Rayleigh scattering
λ_c	central wavelength
MSS	Multispectral Scanner - A scanner system that simultaneously acquires images of the same scene in various wavelength bands
MERIS	Medium Resolution Imaging Spectrometer, on board the ENVISAT satellite
MODIS	Moderate Resolution Imaging Spectroradiometer, on board Terra and Aqua satellites and MERIS
NASA	National Aeronautics and Space Administration (USA)
NDVI	Normalised Difference Vegetation Index - an index of vegetation biomass
P'_a	phase function
P_r	Rayleigh scattering phase function
PITs	pseudo-invariant targets
PM	particle matter
ρ	reflectance
ρ_{tg}	at-ground reflectance
ρ_{ts}	at-satellite reflectance
RSR	Relative spectral response- spectral integration of the received radiance through measurements the intensity of the wavelengths of light

RT	radiative transfer
SD	standard deviation
SPOT	Satellite Pour l'Observation de la Terre - French satellite carrying two pushbroom imaging systems
TM	Thematic Mapper- a Landsat multispectral scanner that gather information about the Earth's surface
$to_3 \uparrow$	transmittance factor due to ozone in the upward direction
$to_3 \downarrow$	transmittance factor due to ozone in the downward direction
$t_a \uparrow$	atmospheric transmittance for aerosol-scattered radiation in the upward direction
$t_a \downarrow$	atmospheric transmittance for aerosol-scattered radiation in the downward direction
τ_r	Rayleigh optical thickness in μm
τ_a	aerosol optical thickness
$t(\mu)\uparrow$	direct (upward) target-sensor atmospheric transmittance
t_g	gaseous transmittance
ω_a	is the aerosol single scattering albedo

Chapter 1 Introduction

Atmospheric correction is an important pre-processing step required in many satellite remote sensing applications (Hadjimitsis, 2009; Hadjimitsis et al., 2004; Mahiny and Turner, 2007; Yuen et al., 2004, Janzen et al, 2006; Liang et al., 2001; Teillet, 1996; Tyagi and Bhosle, 2010). Although there are several available atmospheric correction methods, there is limited literature available that utilizes atmospheric correction methods to retrieve aerosol optical thickness (AOT) (Hadjimitsis et al., 2010).

The objectives of this research are the following:

- Improvement and application of the empirical line atmospheric correction method and application of the Darkest Pixel method for atmospheric correction.
- Aerosol optical thickness (AOT) retrieval based on the application of the atmospheric correction methods.
- Accuracy assessment based on in-situ measurement using spectroradiometers and sun photometers.
- Geographic Information System (GIS) analysis to map AOT distribution.

1.1 What is atmospheric correction?

In order to detect changes and identify trends on the Earth's surface, multi-temporal satellite images are often used. However, since these images are acquired under different atmospheric conditions, solar conditions and angles, effective atmospheric correction is necessary to remove radiometric distortion and make the images comparable in order to retrieve the true reflectance values (Mahmoud et al., 2008). The aim of atmospheric correction is to remove atmospheric effects from the satellite image in order to retrieve the true surface reflectance values.

The premise of atmospheric correction is to quantify the reflectance of the target and the brightness of the atmosphere so the analysis can focus on the true reflectance values (Campbell, 2008). Several operational algorithms for relative and absolute atmospheric correction have been developed as discussed by Hadjimitsis et al. (2004), Chrysoulakis et al. (2010) and Mahmoud et al. (2008); however their effectiveness is still an open question.

1.2 Atmospheric correction methods

Previous studies by Hadjimitsis et al. (2009), Hadjimitsis et al. (2004), Wilson and Milton (2010), Mahiny and Turner (2007), Huang et al. (2002), and Liang et al. (2001) indicate that the Darkest Pixel (DP) and the Empirical Line method using Pseudo Invariant Target (PITs) methods are the most effective methods for atmospheric correction. The Darkest Pixel (DP) method is the most widely applied method of atmospheric correction that provides reasonable correction (Schott, 1997; Cheng and Lei, 2001; Hadjimitsis et al., 2004; Hadjimitsis et al., 2009; Wilson and Milton, 2010; Mahiny and Turner, 2007; Huang et al. 2002; Liang et al., 2001). In this thesis, the improved DP method developed by Hadjimitsis and Clayton (2009) was used for atmospheric correction, which utilizes the true reflectance value acquired from in-situ spectroradiometric measurements for the darkest pixel. As well, the empirical line method, which uses a linear regression to relate the in-situ reflectance of pseudo-invariant targets to the at-satellite reflectance values of the targets, was improved in this study by identifying and using five pseudo-invariant targets of varying spectral characteristics, instead of the three targets used in most empirical line methods of atmospheric correction.

1.3 Aerosol optical thickness retrieval from satellite images

Atmospheric measurement began over 250 years ago and most of the atmospheric processes were well understood by the end of the 19th century (Lillesand et al., 2004). Since the beginning of the 20th century, routine measurements of solar radiation have been taking place, with improvements occurring every decade (Wehrle, 2008). The first visual observations of atmospheric effects were made from spacecrafts in the 1960s and progressed to satellites in the mid 1970s (Lee et al., 2009). The first attempt of aerosol retrieval over land was conducted by Kaufman and Joseph in 1982 (Lee et al., 2009).

Aerosol Optical Thickness (AOT) is the degree to which aerosols prevent the transmission of light by absorption or scattering of light (http://disc.sci.gsfc.nasa.gov/data-holdings/PIP/aerosol_optical_thickness_or_depth.shtml). AOT is considered as the most important unknown parameter in any atmospheric correction algorithm as well as in air pollution studies since it is used to solve the radiative transfer equation and remove atmospheric effects from satellite images (Istomina et al., 2011; Lee and Kim, 2010; Xue et al., 2008; Guanter et al., 2008; Xue et al., 2008; Remer et al., 2005; Seidel et al., 2005; Hadjimitsis et al., 2007; Hadjimitsis and Clayton, 2004; Hadjimitsis et al., 2002;

Hadjimitsis, 1999; Kaufman and Sendra, 1998; Kaufman et al., 1997; Kaufman and Tanré, 1996; Forster, 1984). Several methods are described in the literature where AOT is determined using atmospheric models, in-situ measurements, angular variation, and synergistic methods (North et al., 2009; Anderson et al., 2003; Kaufman et al., 2002; Holben et al., 2001; Forster, 1984). However, the retrieval of AOT values using image based atmospheric correction methods is an important issue in satellite remote sensing. In this thesis, AOT values will be retrieved from satellite images after applying the improved Darkest Pixel and improved empirical line method using pseudo-invariant targets atmospheric correction method and then solving the radiative transfer equation.

1.4 What are the advantages of using remote sensing to retrieve AOT?

The main problem with atmospheric correction is the difficulty in determining the atmospheric optical characteristics related to the presence of aerosols, especially AOT (Werhle, 2008; Hadjimitsis, 2008; Hadjimitsis et al., 2004; Kaufman and Sendra, 1998; Kaufman and Tanré, 1996; Anderson et al., 2003; Kaufman et al., 2002; Holben et al., 2001). Therefore, effective aerosol retrieval information, which includes the atmospheric effects caused by scattering and absorption of atmospheric gases, clouds and aerosols is critical to the atmospheric correction of satellite images (Hadjimitsis, 2008; Hadjimitsis et al., 2004; Kaufman and Sendra, 1998; Kaufman and Tanré, 1996). Due to the temporal variation of aerosols, the activity of aerosols in the atmosphere can be summarized by the aerosol optical thickness (AOT), which is a wavelength dependent measure of the total extinction of sunlight due to scattering and absorption by aerosols (Werhle, 2008).

Due to the variability of aerosols, atmospheric aerosol monitoring is difficult and significant efforts to improve aerosol characterizations have included using in-situ measurements, ground-based remote sensing and satellite observations (Anderson et al., 2003; Kaufman et al., 2002; Holben et al., 2001). This thesis will incorporate the use of spectroradiometers to improve and use the empirical line method in order to retrieve AOT from satellite images. Currently, AOT can be retrieved by use of sun photometers or through on-board radiometers on satellites (Anderson et al., 2003; Kaufman et al., 2002; Holben et al., 2001). Sun photometers, either ground-based or hand-held, are used to obtain optical properties (Anderson et al., 2003; Kaufman et al., 2002; Holben et al., 2001). Satellite sensors, such as MODIS, also provide AOT measurements. However, a significant limitation of the MODIS sensor is its spatial resolution, which does not allow for local scale estimation of AOT levels. This is important, since high values of AOT

suggest high concentration of aerosols (Retalis et al., 2010). The application of the improved Empirical line method and Darkest Pixel method of atmospheric correction can assist the retrieval of AOT values for several satellite image sub-areas. Therefore, AOT values can be used as a way of measuring air quality and determining AOT in large scale pollution areas provides a synoptic, cost-effective means to further assess the air quality in these areas (Hadjimitsis and Clayton, 2006; Tang et al., 2005; Kanaroglou et al., 2002, Kaufman et al., 2002; Hadjimitsis et al. 2002; Sifakis et al., 1998; Leon et al., 1995; Sifakis and Deschamps, 1992).

1.5 What is the goal of this thesis?

In this study, two existing atmospheric correction methods, the Darkest Pixel and the Empirical Line Method using Pseudo-invariant Targets are examined and used to retrieve the AOT through the fast atmospheric correction algorithm developed in this thesis. These AOT values derived from the algorithm were compared with the in-situ AOT values obtained with sun photometers during satellite overpass. It is the first time that radiative transfer equations will be used in an image-based atmospheric correction method to solve for AOT and map AOT distribution.

The Darkest Pixel method of atmospheric correction was applied to Landsat TM/ETM+ satellite images. Traditionally, the darkest pixel method involves identifying the darkest pixel in the area of interest and then adjusting the image so that the darkest pixel has a reflectance value of zero. In this thesis, the improved Darkest Pixel method endorsed by Hadjimitsis and Clayton (2009) was used, where the true ground reflectance values of the darkest pixel were used to correct the satellite image. In this way, the corrected satellite image will yield more accurate reflectance values.

The empirical line atmospheric correction method was improved by using five ground targets and then applied to Landsat TM/ETM+ images acquired over the Limassol region of Cyprus. This method is a relatively simple means of surface reflectance calibration, provided that pseudo-variant reference target measurements are available. Previous research indicates that this method requires one dark and one light target; however, the use of more spectrally diverse targets provide greater confidence and more accurate results can be obtained (Hadjimitsis et al., 2009; Wilson and Milton, 2010; Karpouzli and Malthus, 2003; Ferrier and Wadge, 1996). In this study, five pseudo-invariant targets with varying spectral characteristics were used. The pseudo-invariant targets utilized in this research

were selected because of their suitability in terms of size, uniformity and reflectance characteristics, and because they are common objects that are easily identified in any geographical region. It is the first time that a field campaign was conducted measuring the reflectance values of pseudo-invariant targets for an extended time period throughout the year examining how wet and dry ground conditions affect the reflectance values for atmospheric correction. An accuracy assessment of the two atmospheric correction methods was performed using field spectroradiometric measurements obtained during the satellite overpass.

The thesis follows the following format:

- Chapter 2 presents a summary of remote sensing and atmospheric optics and includes a detailed discussion on the importance of atmospheric correction in pre-processing.

- Chapter 3 presents an overview of the existing atmospheric correction methods.

- Chapter 4 provides a detailed discussion of the resources used in this study, including an emphasis on the instruments utilized in this research.

- Chapter 5 provides a detailed review of field spectroscopy, including the procedure used for operating the spectroradiometer.

- Chapter 6 presents the detailed methodology used in this thesis.

- Chapter 7 provides a detailed explanation of the pseudo-invariant targets used in the research. Detailed discussion on the ground reference targets, including their spectral signatures and the procedure used to measure these targets is also provided.

- Chapter 8 critically examines the atmospheric correction methods used in this thesis, which are the improved empirical line method using pseudo-invariant targets and the darkest pixel method. The methodology for improving the PITs method will be discussed in detail.

- Chapter 9 presents the fast atmospheric correction algorithm developed for AOT retrieval, including the GIS analysis conducted through the simplified image based AOT retrieval based on RT equation for GIS modeling.

- Chapter 10 provides the results of the thesis discussed in detail. This includes the accuracy assessment of the pseudo-invariant targets compared with in-situ measurements, evaluation of the effects of precipitation conditions on pseudo-invariant targets, accuracy assessment of the AOT values derived from the fast atmospheric correction algorithm with in-situ AOT values, and the GIS maps produced from the simplified image based AOT retrieval based on RT equation for GIS modeling, including accuracy assessment with in-situ AOT measurements.

- Chapter 11 presents the conclusions of this thesis and future work.

Chapter 2 Basics of Remote sensing

This chapter provides an overview of the basics of remote sensing, atmospheric correction and aerosol optical thickness.

2.1 Basics of Remote Sensing

Remote sensing refers to "deriving information about the Earth's land and water surfaces using images acquired from an overhead perspective, by employing electromagnetic radiation in one or more regions of the electromagnetic spectrum, reflected or emitted from the Earth's surface" (Campbell, 2008, p.6). This section will provide a brief discussion of electromagnetic radiation, the Earth's atmosphere and the interaction processes between the two, followed by discussion of atmospheric correction and aerosol optical thickness, including an examination of the current research.

2.1.1 Electromagnetic Radiation

The electromagnetic spectrum refers to the range of all possible wavelengths of electromagnetic radiation. In remote sensing, the radiations of certain wavelength in the electromagnetic spectrum can be used to distinguish different objects, since each object reflects energy differently (Mather and Koch, 2011; Campbell, 2008; Richards, 2005). The Earth's Sun emits radiation from 0.5–4.0 micrometers (Mather and Koch, 2011; Richards, 2005). Various features of the Earth's surface reflect, absorb, transmit and emit electromagnetic energy from the Sun. This radiation is filtered by the Earth's atmosphere, as energy is absorbed in a series of wavelengths in the Earth's atmosphere (Campbell, 2008). Because the Earth has a lower temperature than the Sun, this energy is re-emitted at higher wavelengths (Mather and Koch, 2011). When electromagnetic energy reaches the Earth's surface, it is reflected, absorbed, emitted or transmitted, as shown in Figure 2-1.

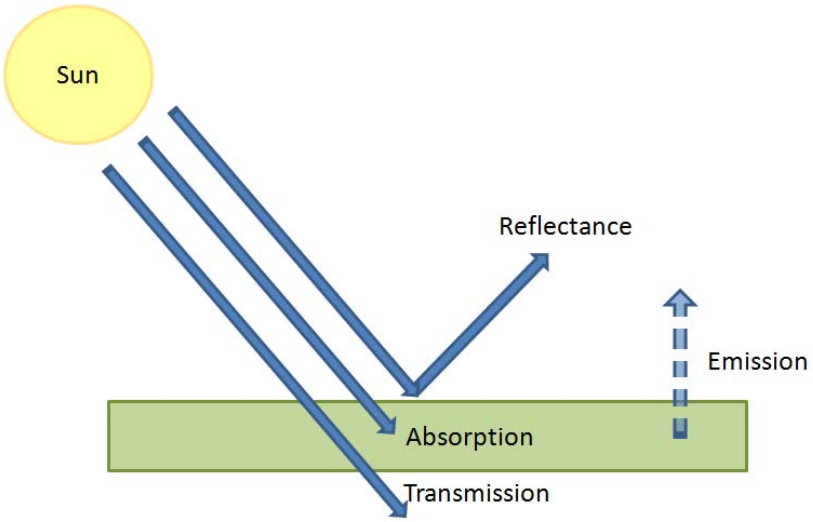

Figure 2-1 Electromagnetic energy interaction (Campbell, 2008)

There are four forms of interaction that can occur when energy strikes the surface of the Earth: transmittance, absorption, reflection and emission. In absorption, the electromagnetic radiation is retained by the substance, while in transmittance, the electromagnetic radiation passes through the surface. In emission, the surface emits a characteristic spectral signature, and in reflectance, the electromagnetic radiation changes direction once it refracts on the surface. Absorption occurs when the atmosphere prevents transmission of electromagnetic radiation or solar energy through the atmosphere. Schott (2007) defined absorption as the process of removing energy (photons) from the beam by converting the electromagnetic energy to another form, usually thermal. The three gases responsible for most absorption of solar radiation are ozone (O_3), carbon dioxide (CO_2) and water vapor (H_2O). These gases absorb radiation in specific areas of the electromagnetic spectrum, known as absorption bands, where absorption is very strong in certain parts of the optical spectrum. As well, there are other regions of the spectrum with low absorption and high transmission that can be used, which are called atmospheric windows (Campbell, 2008).

The electromagnetic energy reaching the Earth's surface that is reflected (or refracted) changes direction and travels again through the atmosphere before reaching the satellite sensor (Chuvieco 2009). Refraction occurs in the atmosphere as light passes through atmospheric layers of varying visibility, humidity and temperature. Such variations affect the density of the atmosphere, resulting in light rays bending as they pass between atmospheric layers. Radiation from the Earth's surface interacts significantly with the atmosphere before it reaches the satellite sensor, especially when the target surface consists

of non-bright landscape features such as water or vegetation (Campbell, 2008). Visible and near infrared radiation is affected by the atmosphere through gaseous absorption of water vapor and ozone as well as scattering by aerosols. Atmospheric effects can significantly alter the radiation by absorbing and attenuating it in various wavelengths and by adding to it as a result of energy that is scattered in the atmosphere and radiated to the satellite sensor (Campbell, 2008). Therefore, atmospheric effects vary along time and space as a result of changes in atmospheric moisture and pollution.

Reflectance, which is the ratio of energy reflected from land, water and other targets, is used to describe energy in the field of remote sensing. The amount of energy that is reflected from these surfaces is expressed as a percentage of the amount of energy striking a surface (Chuvieco, 2009). If a surface, such as a mirror, has 100% reflectance, all the light that bounces off an object is detected by the satellite sensor. If no light is reflected from the surface, reflectance is considered to be 0%. However, in order to get accurate surface reflectance, the Sun, target and sensor geometry, the landscape surface characteristics and atmospheric interaction need to be accounted for (Teillet, 1992; Tanré et al., 1992).

The ratio of energy reflected in each wavelength is indicative of the characteristics of the surface and can be shown as a spectral signature. Spectral signatures are the specific combination of reflected and absorbed electromagnetic radiation at varying wavelengths which can uniquely identify an object. The ratio of reflectance by wavelength can be plotted in order to identify the spectral signature of the surface. In this way, materials can be distinguished from one another by examining which portions of the spectrum they reflect and absorb. In principle, different surfaces can be identified based on their spectral signatures, as these vary depending on their material (Campbell, 2008).

Since reflection occurs when a ray of light is redirected as it strikes a non-transparent surface, the reflection is dependent on the size of the surface irregularities in relation to the wavelength of radiation under consideration. If the surface is rough in relation to the wavelength, it acts as a diffuse or isotropic reflector (Campbell, 2008). Many landscape features behave as diffuse reflectors for visible radiation. A perfectly diffused reflector has equal brightness when observed from any angle and this is called a Lambertian surface. However, the Lambertian model is not applicable to most landscape features. Figure 2-2 shows a diffused Lambertian surface which obeys the cosine law by distributing reflected energy in proportion to the cosine of the reflected angle.

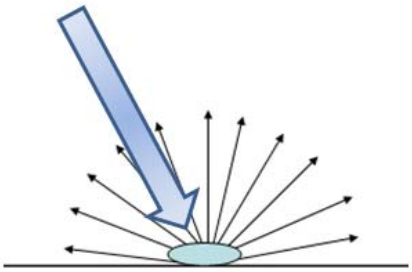

Figure 2-2 Lambertian surface
(http://people.usd.edu/~schieber/trb2000/sld038.htm)

2.1. 2 Atmospheric Constituents

The atmosphere consists of four layers:

1. The troposphere, extending 8-15 km from the Earth's surface, which is composed primarily of nitrogen and oxygen.

2. The stratosphere, extending above the troposphere to a height of 50 km above the Earth's surface. This is where there is intense interaction between radiative and chemical processes. The stratosphere ozone layer absorbs solar ultraviolet energy and is therefore warmer than the upper troposphere.

3. The mesosphere extends 50-80 km above the Earth's surface. In this layer, there is a lower ozone concentration and radiative cooling becomes more important.

4. The thermosphere begins at a height of 80 km above the Earth. This layer is further subdivided into the ionosphere and the exosphere. The ionosphere extends 80-550 km above the Earth. The exosphere extends 550 km to thousands of km into space. It is in the exosphere that satellites orbit the Earth.

Atmospheric gases are composed of 78% nitrogen, 21% oxygen (O_2) and small amounts of water vapour (H_2O). Carbon dioxide (CO_2) and ozone (O_3) account for about 1% of the atmosphere (Chahine, 1983). Atmospheric aerosols are liquid or solid particulates that are suspended in the air. The main sources of atmospheric aerosols are land sources, oceans, human activity and gases in which chemically active gases are transformed into liquid form into the atmosphere. According to the United States Geological Survey (2011), the main sources of airborne particulate matter are soil dust, sea salt, primary sources (such as emissions from road transport, power stations and agricultural activity) and secondary sources (such as those from the chemical oxidation of atmospheric gases). Particulate

matter ranges in size from a few nanometers to tens of micrometers. The majority of particulate matter is smaller than 10μm. Particles with a diameter of less than 2.5 μm are described as fine and those with a diameter between 2.5-10 μm are defined as coarse particles. In order to determine aerosol optical characteristics, routine observations of aerosol optical thickness and precipitable water vapor are often made (Ganesh et al, 2010). The easiest way to define these two parameters is through the use of sun photometers and/or satellite sensors. Aerosol optical thickness will be discussed in section 2.4.1 and sun photometers and spectroradiometers will be discussed in Chapter 4.

2.1. 3 Interaction Processes

The atmosphere varies as a result of molecular scattering and absorption. Scattering refers to the redirection of electromagnetic energy by particles in the atmosphere or by the larger molecules of atmospheric gases. The result of scattering is the redirect of radiation, so that a percentage of the incoming solar energy is directed back to space and also towards the Earth's surface (Campbell, 2008). The amount of scattering depends on several factors, including the size and abundance of such particles, their wavelength, and the depth of the atmosphere through which the energy is travelling. The main effects of atmospheric scattering are atmospheric radiance or path radiance and atmospheric absorption (Slater, 1980). There are three different types of atmospheric scattering: **Rayleigh scattering, Mie scattering and non-selective scattering**.

Rayleigh scattering occurs when atmospheric particles have diameters smaller than the wavelength of the radiation. These particles include small specks of dust and atmospheric gases such as nitrogen (N_2) and oxygen (O_2). Since Rayleigh scattering can occur in the absence of atmospheric impurities, it is also called clear atmosphere scattering (Campbell, 2008; Guanter, 2006). This is the dominant scattering technique in the upper atmosphere, at altitudes up to 10 km. Rayleigh scattering is wavelength dependent, since the amount of scattering changes greatly according to the different regions of the spectrum. (Campbell, 2008; Guanter, 2006).

Mie scattering is caused by large atmospheric particles, including dust, pollen, smoke and water droplets. These particles have diameters that are approximately equivalent to the wavelength of the scattered radiation (Campbell, 2008; Guanter, 2006). Mie scattering tends to be greatest in the lower atmosphere (up to 5 km) where large particles are

abundant. Mie scattering can affect a broad range of wavelengths in and near the visible spectrum (Campbell, 2008; Guanter, 2006).

Non selective scattering results from particles that are much larger than the wavelength of the scatter radiation (Campbell, 2008). For radiation in and near the visible spectrum, this may include particles such as larger water droplets and large particles of airborne dust. This scattering is called non-selective since scattering is not wavelength dependent and all visible wavelengths are scattered equally (Campbell, 2008).

Scattering significantly affects remote sensing in the following ways:

1. Scattering directs energy from outside the sensor's view field to the sensor's aperture, thus decreasing the spatial detail recorded by the sensor.
2. Scattering tends to make dark objects appear brighter and bright objects appear darker, which decreases the contrast recorded by the sensor.
3. Scattering obscures fine detail on the image data.

2.2 Pre-Processing of Remotely Sensed data

Pre-processing refers to the processing of raw data into standard physical units of spatial and radiometric measurement (McCloy, 1995). Therefore, pre-processing of remotely sensed data refers to the operations that occur before image display and analysis (Campbell, 2008; Mather and Koch, 2011). The quality of remotely sensed data is degraded as a result of limitations on the spectral, spatial, temporal and radiometric resolution of the sensors, which affects the accuracy of analysis of the data received (Yuen et al., 2004; Jensen, 1996). Since the remotely sensed data received from the imaging sensors contains flaws and deficits, these must be corrected through pre-processing in order to achieve an accurate interpretation of the remotely sensed data (Tyagi and Bhosle, 2010; Morillo-Contreras et al., 2004; Yuen et al., 2004; Datt et al., 2003; Teillet, 1996). Pre-processing techniques include geometric and radiometric correction (Lillesand et al., 2004; Teillet, 1996). Radiometric corrections are further characterized between those effects that are scene related (such as atmospheric effects, topographic, view angle effects, illumination effects and target characteristics) and those that are sensor related (such as sensor calibration and de-stripping) (Teillet, 1996). It is important to realize that there are no standardized pre-processing steps since each image required individual attention. Figure 2-3 indicates the cycle of remote sensing, including the steps required for pre-processing.

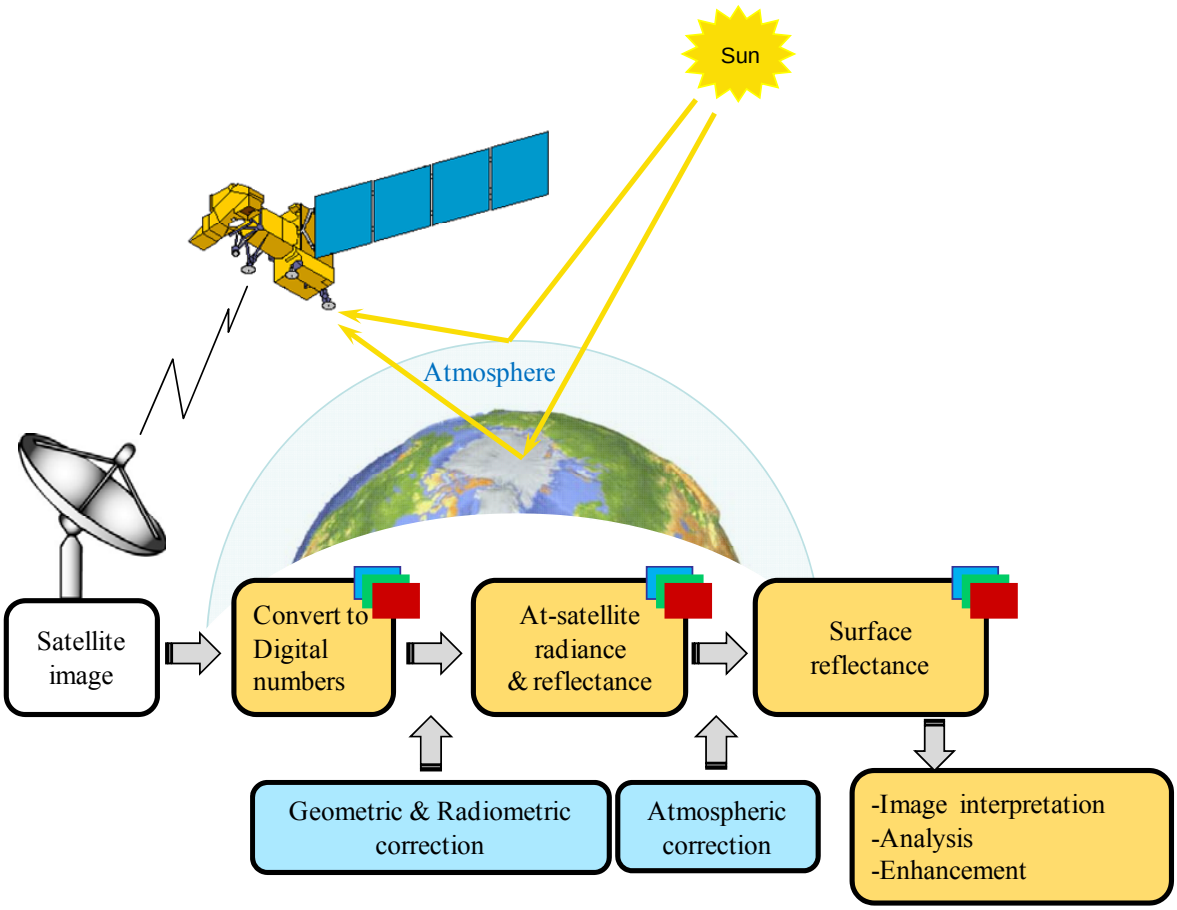

Figure 2-3 Remote Sensing Cycle

2.2.1 Geometric Correction

Geometric correction focuses on factors that create geometric distortions of image data, such as the Earth's curvature, the Earth's rotation during image acquisition, panoramic distortion and platform instability (Lillesand et al., 2004). Geometric correction is a two-step procedure for correction of systematic distortions (which are predictable) and the correction of random distortion (which are unpredictable). The correction for systematic distortions is done through established mathematical modelling. However, random and unknown systematic distortions are corrected by using ground control points (GCPs).

In order to use GCPs, the image first needs to be registered on a mapping grid. A number of GCPs are required, which are located on both the map co-ordinate system as well as the image line/pixel co-ordinate system (Hummel, 2011; Cheng et al., 2008; Schowengerdt, 2007; Lillesand et al., 2004; Novak, 1992; Forster, 1989). These two sets of coordinates are used to determine the relationship between the image and map co-ordinates by use of transformation equations. The transformation equation is dependent on the complexity of the correlation between the image and map projections. For a first order transformation, a

minimum of three GCPs are needed to calculate the transformation coefficients. The GCPs must be well defined, be small in feature size, unchanging over time and with high contrast in all the images of interest (Schowengardt, 2007). GCPs can be environmental features such as road intersections, river features or even the corners of agricultural fields. By using the transformational equation, every pixel in the image can then be transformed to its equivalent map positions. Next, resampling takes place, where the pixel values necessary to fill the output matrix from the original image matrix need to be determined. The simplest resampling method is the near-neighbour method, where the value of the pixel in the input image closest to the computed co-ordinates is assigned to the output pixel (Lillesand et al., 2004; Schowengerdt, 2007).

2.2.2 Radiometric Correction

Radiometric correction refers to operations intended to remove systematic or random noise affecting the amplitude (brightness) of a satellite image with the goal of restoring an image to the condition it would have been if the imaging process were flawless (Mather and Koch, 2011; Schroeder, 2006).

Radiometric errors tend to have two causes, which include problems with the instrument used to record the data (such as individual detectors not working properly or incorrectly calibrated sensors) and/or the presence of the atmosphere contributes significant noise and therefore the signal recorded by the sensor does not represent the signal reflected by the target.

Radiometric correction is used to calibrate pixel values to in-situ reflectance values by taking into account variations in ground surface irradiance, absorption and scattering processes and the influence of sensor parameters. In radiometric correction, the following techniques are used: sensor calibration, de-striping, illumination, view angle effects, and atmospheric correction.

Sensor Calibration: When the user needs to compare images that are acquired at different times and/or from different sensors, or if the remotely sensed data is used to determine reflectance values, digital numbers (DN) need to be converted to radiance or reflectance values (Mather and Koch, 2011; Chander et al., 2010; Chander et al. 2009). This calibration in units of radiance (or reflectance) is a critical processing step before atmospheric correction can be applied and is done by converting the DN to at-satellite radiance values using calibration offset and gain co-efficients for each spectral band. These

calibration co-efficients are updated periodically from ground measurements due to the deterioration of the sensors over time. Following, the at-satellite radiance values are converted into at-satellite reflectance using the solar irradiance at the top of the atmosphere, the Sun-Earth distance correction and the solar zenith angle.

Destriping: The destriping method removes the systematic horizontal banding pattern that occasionally appears on the images produced on electromechanical scanners such as Landsat TM/ETM. The main cause of the banding pattern is the imbalance in the detectors used in the scanning process. It is recommended that destriping be applied prior to any geometric correction while the data array is alight to the scan direction.

Illumination and view angle effects: The magnitude of the signal recorded by the satellite sensor depends upon the solar elevation angle, the angle of view of the sensor and the slope of the ground target relative to the Sun. The angle of view of the sensors is important since it controls the upward path length. The Sun elevation correction takes into account the position of the Sun relative to the Earth as a result of the season. The Sun elevation correction can be determined by dividing each pixel value by the cosine of the Sun's angle from the zenith (Lillesand et al., 2004).

Topographical effects: Although the solar zenith angle is easily calculated on flat terrain, in order to calculate the incidence angle on non-flat terrain, a digital elevation model (DEM) is required, which should be expressed in the same co-ordinate system as the image to be corrected. The slope angle effects from a DEM can be easily calculated with the Lambertian cosine assumption (Mather and Koch, 2011).

2.3 Atmospheric Correction

Atmospheric correction is a critical aspect of data pre-processing since it is impossible to estimate the target reflectance from a remotely sensed image without calculating the effects of incoming and outgoing electromagnetic radiation within the atmosphere (Liang et al., 2001; Yuen and Bishop, 2004; Morillo-Contreras et al., 2004). The atmospheric contribution to the satellite signal occurs when electromagnetic radiation from the Sun passes through the atmosphere, is reflected from the Earth and is detected by the satellite sensor as it passes again through the atmosphere. The interaction processes which occur during this passage are scattering and absorption, which increase or decrease the true ground-leaving radiance. When estimates of atmospheric effects are successful, it is

possible to retrieve the true target radiance. However, significant spatial and temporal variations of atmospheric conditions make atmospheric correction difficult and complex (Chahine, 1983). For an atmospheric correction to be conducted, first the satellite image is geometrically corrected, if needed to be geo-referenced, then the DN needs to be converted to radiance and reflectance, the atmospheric effects need to be removed and finally the true target radiance or reflectance can be retrieved. Atmospheric correction of a satellite image requires a model of the atmosphere at the time of satellite overpass. A good atmospheric correction model is able to simulate the atmospheric phenomena as well as correct the influences caused by scattering and absorption, and remove the perturbations of the satellite signal due to Rayleigh scattering, aerosol scattering and gas absorption in the atmosphere. As well, atmospheric correction eliminates atmospheric haze by rescaling each band.

Image based atmospheric correction consists mainly of parametric estimation of the atmosphere and surface reflectance retrieval. Surface reflectance retrieval is straightforward if all the atmospheric parameters are known and the target surface is determined to be Lambertian. The atmosphere can be parameterized as a function of gaseous transmissions, Rayleigh and aerosol transmission, cloud spherical albedo, atmospheric reflectance and the reflectance at the top of the atmosphere (ToA). In order to proceed with atmospheric correction, the radiative transfer (RT) equation is used (described in more detail in Chapter 2.4.2). The RT equation (or model) requires full descriptions of the atmospheric components at fixed altitudes throughout the atmosphere, since the atmosphere is affected by absorption, scattering and emission. Further discussion of the basics of the RT equation can be found in Forster (1984) and Turner and Spencer (1972).

The goal of atmospheric correction is to retrieve the surface reflectance and target radiance from remotely sensed images by removing the atmospheric effects including atmospheric noise and attenuation. In order to choose the appropriate atmospheric correction method for the specific application, it is necessary to consider the nature of the application, the type and characteristics of the remotely sensed system being used to collect data and the amount of in-situ atmospheric data available. However, effective application of atmospheric correction is problematic for the following reasons:

1. The data necessary for full accommodation are usually not available.
2. The atmospheric composition is highly variable both temporally and spatially.

3. Available information about the atmosphere at the time of satellite overpass is usually limited.

Since it is difficult to obtain atmospheric data for all available images, atmospheric parameters are usually estimated (Schowengerdt, 2007). Sophisticated methods of atmospheric correction use information about the atmosphere from either standardized databases, by in-situ measurements taken simultaneously or by inerative techniques (Turner and Spencer, 1972; Kneizys et al., 1988; Richter, 1996; Vermote et al., 1997).

2.3.1 Factors Affecting the Choice of Atmospheric Correction

The choice of an atmospheric correction method depends on the type of target, its application and the satellite characteristic. Research by Gill et al. (2012), Hsu et al. (2004), Hadjimitsis (1999) and Kaufman (1989) has found that the target characteristics are critical to selection and development of an atmospheric correction method. For example, dark targets are affected by atmospheric back scattering of direct sunlight to the sensor and dark areas surrounded by bright objects are affected by the high up-welling radiance of the surrounding land which affects the satellite signal of a dark object (Fraser and Kaufman, 1985). Factors such as the range of values of the surface reflectance, the special variability of the target and the type of target also need to be considered.

Atmospheric correction is dependent on the application of the remotely sensed data. For applications where ground reflectance do not change significantly over time (such as deserts or glaciers), pseudo-invariant targets can be used (Huang et al., 2008; Heo and Fitzhugh, 2000; Escadafel et al., 1997; Caselles and Garcia, 1989; Schott et al., 1988). For low-reflectance surfaces, such as water bodies (Hall et al., 1991) specific atmospheric corrections methods have been developed, as described in chapter 3. For applications where vegetation indices are used, the differences between the atmospheric effects in the two wavelengths are used (Caprioli et al., 2008; Schroeder et al., 2006; Berger, 2001).

2.4 Atmospheric Optics

In this section, critical parameters of atmospheric optics are described, including optical thickness, extinction coefficients and scattering phase function. Atmospheric optics are essential parameters when detailed modelling is performed, especially aerosol optical thickness, as it describes the optical state of the atmosphere. The fundamental parameter in the atmospheric optics is the optical thickness based on the Lambert-Bouger law of

transmission, which states that when a beam of radiant energy propagates from a source at x_1 to receiver at x_2, there is loss of energy due to the effects of scattering and absorption (Slater, 1980; Chahine, 1983). It is important to realize that if there was no atmosphere, the transmission of solar radiation would be 100%. Due to the interaction processes of scattering and absorption, not all incident solar radiation passes through the atmosphere and reaches the Earth's surface. Transmittance refers to the amount of solar radiation that does pass, relative to that for no atmosphere. The fraction of the energy transmitted along a homogeneous path for a particular wavelength (λ) is given by the Lambert-Bouger law (see equation 2-1 below):

$$T(\lambda, x_2 - x_1) = \exp\left[-K_e(\lambda)(x_2 - x_1)\right] \tag{2-1}$$

where

T is the transmittance (fraction of energy transmitted)

K_e is the volume-extinction coefficient

The volume extinction coefficient, K_e (km^{-1}) refers to the energy loss from the direct beam as a result of atmospheric constituents. The exponent product index in equation 2-1 is defined as the optical thickness, τ (Slater, 1980, Kaufman, 1989). Since the volume extinction coefficient, K_e, is not constant along the path, the optical thickness can be calculated by from the integral, as indicated in equation 2-2 below :

$$\tau(\lambda, x_2 - x_1) = \int_{x_1}^{x_2} K_e(\lambda)(dx) \tag{2-2}$$

The atmospheric optical thickness in the vertical direction from the Earth's surface (z_1) to the top of the atmosphere (z_2) is defined by Turner and Spencer, (1972) and indicated in equation 2-3 below:

$$\tau(\lambda, z) = \int_{z1}^{z2} K_e(\lambda)(dx) \tag{2-3}$$

where

z is the height variable

$z_1=0$ is at the Earth's surface

$z_2=\infty$ is at the top of the atmosphere

The angular distribution of the scattered light is described by the scattering phase function, $P'a(\theta)$ where θ is the scattering angle (Hadjimitsis and Clayton, 2009; Chandrasekhar,

1960). The scattering phase function specifies the fraction of the radiation scattered in the forward and backward direction. Generally, $P'a(\theta)$ defines the magnitude or amount of scattering (Schott, 2007). The combination of the molecular scattering with an increasing amount of aerosol makes the phase function asymmetric (Kaufman, 1989). As most atmospheric correction method model all the atmospheric mechanisms in relation with the at-satellite received radiance or reflectance and use the radiative transfer calculations to solve this problem, it is crucial to formulate a radiative transfer equation that describes all the interaction transactions (Chandrasekhar, 1960; Cracknell and Hayes, 1993).

Since atmospheric effects are caused by scattering and absorption of atmospheric gases, clouds and aerosols, the modelling of these characteristics of the atmosphere is an important component of atmospheric correction. The optical characteristics can be established from various sources, including the general climatology of the area under investigation, the image itself and ground measurements (Kneizys et al., 1988; Fraser et al., 1984; Gordon et al., 1983; Kaufman and Fraser, 1983). Molecular scattering and absorption do not vary temporally or spatially (Kaufman, 1989). However, aerosol scattering and absorption do vary both temporally and spatially and are the main variables in the atmospheric effect on remotely sensed data (Kaufman, 1989; Wilson, 1989). According to Kaufman (1989), there are four parameters of atmospheric optical characteristics:

1. aerosol optical thickness.
2. phase function.
3. the single scattering albedo.
4. the gaseous absorption.

Due to their spatial and temporal variability, atmospheric aerosol monitoring is difficult and significant efforts to improve aerosol characterizations have included using in-situ measurements, ground based remote sensing, and satellite observations (Anderson et al., 2003; Holben et al., 2001; Kaufman et al., 2002). The optical activity of aerosols in the atmosphere can be summarized by the aerosol optical depth, which is a wavelength dependent measure of the total extinction of sunlight due to scattering and absorption by aerosols (Werhli, 2008). The American Meteorological Society has defined aerosol optical thickness as the dimensionless line integral of the extinction coefficient along any path in an optical medium, while optical depth indicates the optical thickness measured vertically above a given attitude. However, in aerosol literature, optical thickness is often used as a synonym of optical depth (Werhli, 2008).

2.4.1 Aerosol Optical Thickness

The aerosol optical thickness (τ_a) is defined as the integrated extinction coefficient over a vertical column of unit cross section or, alternately, the degree to which aerosols prevent the transmission of light (NASA, 2011). Aerosol optical thickness (AOT) has been described as an optical property as a function of light scattering from the aerosol particle (Gupta and Christopher, 2008) and as a measure of aerosol loading in the atmosphere (Retalis et al., 2010). Higher AOT values indicate a higher column of aerosol loading and, therefore, lower visibility (Wang and Christopher, 2003). AOT is the most important unknown parameter in every atmospheric correction algorithm since it is used to solve the radiative transfer equation and remove atmospheric effects from satellite images (Istomina et al., 2011; Lee and Kim, 2010; Xue et al., 2008; Guanter et al., 2008; Xue et al., 2008; Remer et al., 2005; Seidel et al., 2005; Hadjimitsis et al., 2007; Hadjimitsis and Clayton, 2004; Hadjimitsis et al., 2002; Hadjimitsis, 1999; Kaufman and Sendra, 1998; Kaufman et al., 1997; Kaufman and Tanré, 1996; Forster, 1984).

Effective aerosol retrieval information is critical to the atmospheric correction of satellite images (Kaufman and Tanré, 1996; Kaufman and Sendra, 1998; Hadjimitsis et al., 2004; Hadjimitsis, 2008). Current approaches of aerosol retrieval include angular variation, synergistic methods, measuring aerosols and four imaged based processing techniques, which include the “ocean method”, “brightness method”, “contrast reduction method” and the “dark vegetation method" (North et al., 2009; Teillet and Fedosejevs, 1995; Tulloch and Li, 2004; Hadjimitsis and Clayton, 2006). These techniques are usually found in atmospheric correction algorithms, where AOT needs to be determined.

Another way that AOT can be determined is by using the visual range rather than direct measurement (Forster, 1984). Turner and Spencer (1972) graphed AOT as a function of visual range for a number of wavelengths. The AOT measured from satellite and sun photometers is the AOT along a vertical or any given path, or the quantity corresponding to the integral of the aerosol extinction on co-efficient along the atmospheric columns. Visibility data related to the atmospheric extinction coefficient is along a horizontal path (Vermote et al., 2002). Kaufman (1990) developed an algorithm for determining AOT based on the difference in the upward radiance recorded by a satellite between a clear and hazy day, based on the assumption that the surface reflectance between the clear day image and the hazy day image does not change. Kaufman et al. (1990) recommended choosing images that are a short temporal distance apart, so that the solar zenith angles and

observation angles be as close as possible to avoid any effects of non-Lambertian surfaces, as this may result in different reflectance values.

Several researchers used dark targets to retrieve AOT values, including Kaufman et al. (1997a, 1997b), Kaufman and Tanre, (1998), Liu et al. (1996), Seidel et al. (2005) and Gaunter et al. (2008). Kaufman (Kaufman et al., 1997a; 1997b; Kaufman and Tanre, 1998) developed the dark target approach to AOT retrieval where a dark target over dense vegetation was used as it reduces atmospheric influence from the surface. This approach states that as a dark target dense vegetation has low reflectance in the blue and red wavelengths, and the surface reflectance at wavelengths in the visible are proportional to those in the mid-infrared, AOT can be retrieved over dark targets (Hansen et al., 1990). According to Seidel et al. (2005), aerosols increase the apparent reflectance over dark targets due to scattering but may reduce the at-sensor radiance over a white target. Liu et al. (1996) recommended AOT retrieval over dark pixels, such as water or vegetation. According to Gilabert et al. (1994), Landsat TM channel 1 (blue) and TM channel 3 (red) bands are sufficient to estimate the main characteristics of aerosols.

AOT retrieval over land is difficult for several reasons, including the complexity of the surface reflectance, the complexity of the aerosol compositions and the low reflectance of aerosol layers at longer wavelengths (Istomina et al., 2011; Seidel et al., 2005; Lee and Kim, 2010; Xue et al., 2008). Surface reflectance and aerosols vary both temporally and spatially (Lee and Kim, 2010; Wen et al., 1999; Guanter et al., 2008; Xue et al., 2008). However, it is difficult to separate the surface and atmospheric scattering contributions (Kaufman et al., 1997; Remer et al., 2005). Over land, so far there have been limited attempts to retrieve aerosol on a global scale. This is because the measured signal is a composite of reflection of sunlight by the variable surface cover and backscattering by the semi-transparent aerosol layer, which makes remote sensing of aerosol difficult (Kaufman and Sendra, 1988). Wang et al. (2007) and Hess et al. (1998) found an increase in AOT values in summer time due to increase in the amount of particle matter under high humid conditions. Further, summer weather, especially in urban areas, is affected by very hazy skies and hot humid weather which can make it difficult to distinguish cloud boundaries (Gupta and Christopher, 2008). As a result, these weather conditions can produce relatively large values of aerosol optical thickness (greater than 0.3-0.5) that may not represent the actual state of the atmosphere (Gupta and Christopher 2008).

Lee and Kim (2010) recommended satellite observation as a major tool for aerosol studies due to their global and continuous coverage. AOT can be retrieved by use of sun photometers or through on-board radiometers on satellites. Several satellite sensors provide AOT measurements, including MODIS (Moderate Resolution Imaging Spectroradiometer) on board Terra and Aqua satellites and MERIS (Medium Resolution Imaging Spectrometer) on board ENVISAT satellite. MODIS is considered the industry standard for retrieving AOT. MODIS satellites have been monitoring daily AOT measures globally (Lee and Kim, 2010; Lee et al., 2009; Kaufman et al., 2003). MODIS provides daily satellite images over Cyprus. As well, research indicates that through ground-based measurements used to obtain atmospheric optical properties, target reflectance can be successfully retrieved from remotely sensed data (Slater et al., 1987; Maracci et al., 1996). The Guang et al. (2008) study combined satellite observations with in-situ measurements to retrieve AOT over dry land and found consistent AOT retrieval using ASTER (Advanced Spaceborne Thermal Emission and Reflection Radiometer), AERONET and MODIS aerosol measurements (Nisantzi et al., 2010; Hadjimitsis et al., 2010; Lee and Kim, 2010; Lee et al., 2009; Guang et al., 2008; Schaap et al., 2008). However, AOT derived from satellite images often requires further validation (Retalis et al., 2010). The accuracy of satellite derived AOT is frequently assessed by comparing satellite based AOT with AERONET or field based sun photometers (Hadjimitsis, 2008; Huang et al., 2008; Hadjimitsis et al., 2010).

The Aerosol Robotic Network (AERONET) is a global network of automatic sun photometers and data archive, which provides spectral aerosol optical thickness and aerosol microphysical properties (Holben et al., 1998; Tang et al., 2005) and is considered the industry standard in ground based sun photometer measurements. Several researchers used the AOT values retrieved from AERONET in order to validate the AOT measurements they had derived from satellite AOT measurements. Wen et al. (1999) used path radiance to retrieve AOT values from Landsat data in Bands 1, 2 and 4, which were then verified with AERONET AOT values. Seidel et al. (2005) used the high spatial resolution Apex spectrometer that was compared with AERONET AOT measurements. Guanter et al. (2008) compared AOT values retrieved from the MERIS radiometer with the AOT values retrieved from AERONET; however, the main weakness of the study was the $30\times30km^2$ pixel cells of the radiometer, since variations between pixels could not be identified, especially in topologically complex areas. Schaap et al. (2008), Xue et al. (2008), and Lee and Kim (2010) all used MODIS AOT measurements, which were

compared to the ground measurements received from AERONET. Kahn et al. (2009) derived AOT values by using the MISC spectroradiometer and comparing the results to the ground measurements received from AERONET. Cervino et al. (2011) compared AOT values derived from the GOME (Global Ozone Monitoring Experiment) radiometer with ground measurements received from AERONET. Istomina et al. (2011) compared AOT values derived over snow and which were compared to the ground measurements received from AERONET.

2.4.2 Simulation of atmospheric effects

Kaufman (1989) defined atmospheric effect as the interactions between direct solar radiation and the radiation reflected from the target with the atmospheric constituents. Atmospheric effects include molecular and aerosol scattering, and absorption by gases (including water vapour, ozone, oxygen and aerosols), which scatter and absorb solar radiation by changing its spectral and spatial distribution as recorded by the satellite sensor. Although molecular scattering and absorption by ozone and oxygen tend to be temporally and spatially stable, atmospheric scattering and absorption are highly wavelength dependent and atmospheric transmittances are not equal across spectral wavelengths (Gaut, 1975). The most difficult component of atmospheric correction to eliminate is the effect of aerosol, which is further complicated by the fact that aerosols tend to be distributed heterogeneously (Liang, 2001). Figure 2-4 indicates the atmospheric components examined in this thesis.

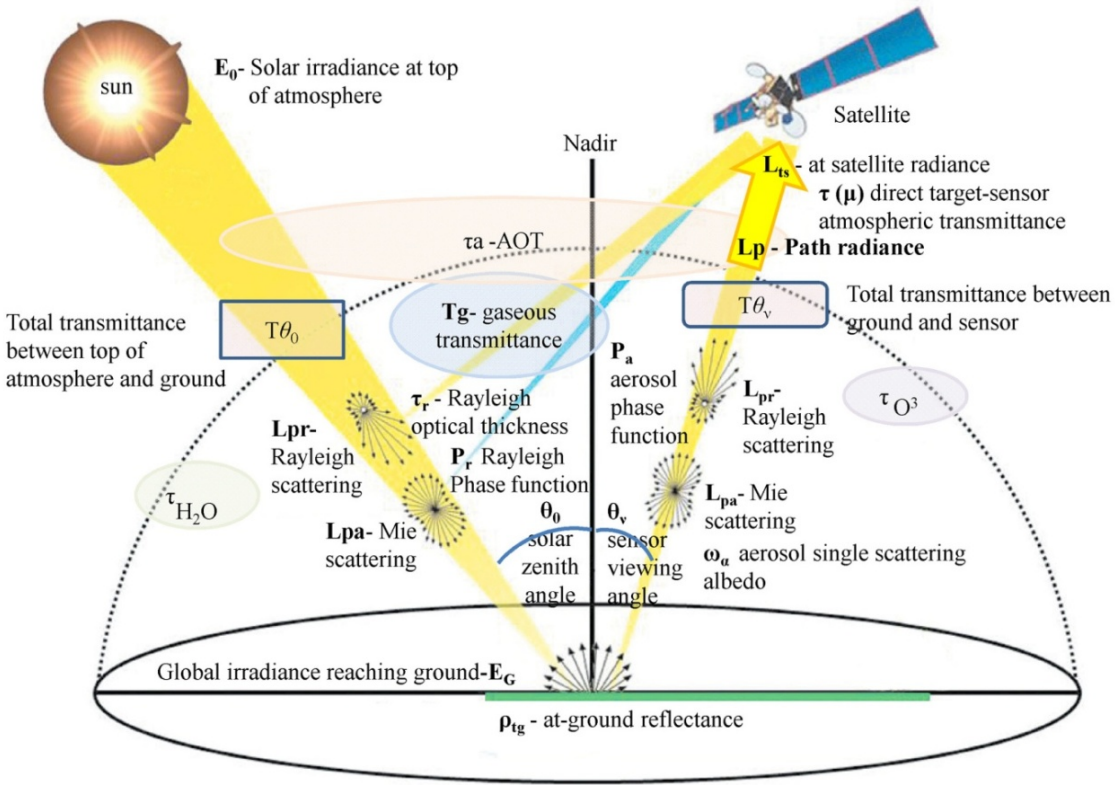

Figure 2-4 Atmospheric components examined in the thesis

To estimate the effects of the atmosphere, a model of all the atmospheric mechanisms in relation with the at-satellite received signal is needed. The radiative transfer (RT) equation provides a model that quantitatively describes the parameters involved in the attenuation of the electromagnetic radiation which leaves the target and reaches the satellite sensor (Matzler, 2006; Thomas and Stames, 1999; Marchuk et al., 1986; Sabins, 1987; Apresyen and Kravtsov, 1996; Chandrasekhar, 1960). Therefore, the RT equation must be formulated in a way which will adequately describe all the interaction processes that occur (Chandrasekhar, 1960; Cracknell and Hayes, 1993).

Turner et al. (1971), Turner and Spencer (1972), Turner (1975) and Hill and Sturm (1991) considered the state of the atmosphere to be described by equation 2-4 (Hill and Sturm, 1991). In order to calculate path radiance in the algorithm (as described in Chapter 9), the below formula was used.

$$\rho = \frac{\pi \left(L - L_p\right)}{t\left(\mu\right) E_G} \tag{2-4}$$

where

ρ is the target reflectance factor
L is the at-satellite radiance

L_p is the atmospheric path radiance
$t(\mu)$ is the upward direct or beam transmittance
E_G is the global irradiance at ground

Although the atmospheric path radiance is one of most difficult parameter to be determined, due to the complexity of the multiple scattering process, it has been resolved in a variety of ways by different researchers. Turner and Spencer (1972) derived a correction algorithm for determining atmospheric path radiance by considering the effects of background reflectance and atmospheric scattering. Hill and Strum (2001) separated the background reflectance from the atmospheric path radiance and calculated the background reflectance by using a moving average filter for the target under investigation. Hadjimitsis and Clayton (2008) found that using the radiative transfer and atmospheric modelling in conjunction with field measurements of aerosol optical thickness can yield more accurate atmospheric corrections instead of using simple image based techniques.

AOT is directly related to the atmospheric aerosol load, which is the main variable describing the effects of aerosols on radiative transfer in the Earth's atmosphere. According to Guanter et al. (2008), modeling atmospheric constituents and surface reflectance involves modeling the radiative transfer across the atmosphere. The radiative transfer equation was used by several researchers in order to calculate AOT (Istomina et al., 2011; Seidel et al., 2005; Lee and Kim, 2010). According to Kokhanovsky et al. (2007, 2009a, 2009b) and Mishchenko et al. (2007), there are uncertainties and discrepancies in any of the AOT retrieval methods. Several researchers indicated the importance of exact values in deriving accurate AOT values. Kaufman et al. (1997b) and Soufflet et al. (1997) found that an inaccurate surface reflectance estimation of 0.01 can result in an uncertainly of 10% in AOT estimation.

According to Gilabert et al. (1994) and Kaufman and Sendra (1988), phase function and single scattering albedo are a major source of uncertainty in the radiative transfer equation. The aerosol single scattering albedo (ω_a) is defined by Forster (1984) as the amount of scattering that takes places and equals unity if no absorption attenuation occurs. It refers to the ratio between the aerosol scattering coefficient and the total extinction coefficient, or the ratio between scattering and absorption (Kaufman, 1989). It can also be considered as the ratio of scattering to scattering + absorption (Penner et al., 2010). Single scattering albedo determines the sign (heating or cooling) of aerosol radiative forcing (Penner et al.,

2010). The single-scattering albedo can be estimated from the collection of particles on filters, preferably by aircraft sampling of the entire atmospheric boundary layer and from the measurements of their absorption (Radke et al., 1991), or alternatively determined from accurate measurements of the downward flux or radiance (King, 1999; Wang and Gordon, 1993). According to Hsu et al. (2004), deriving the aerosol properties for a specific scattering angle will also result in a better precision, because of elimination of part of the variability in the uncertainty in the aerosol scattering phase function.

Phase function refers to the fraction of radiation scattered from its initial forward direction to another direction, as indicated in Figure 2-10 (b). It consists of the combined effect of scattering caused by aerosol particles and Rayleigh scattering. Phase function refers to the angular dependence of light scattering and determines the magnitude of aerosol forcing (Hansen et al., 1997). Phase function (P'_a) is difficult to be estimated due to the variability of aerosol particles. The aerosol phase function is determined by the Rayleigh phase function and the aerosol phase function (Forster, 1084; Gilabert et al., 1984). Many aerosols are characterised by a large amount of back scattering as well as a strong forward scattering. Hadjimitsis and Clayton (2009) recommended the Two-term Henyey Greenstein phase function (TTHG), due to its strong agreement with Mie scattering calculations. According to Gilabert et al. (1994), the TTHG equation, as shown in equation 2-5, is often used to solve for the aerosol scattering phase function (P'_a):

$$P'a = \alpha \left(1 - g_1^2\right)/\left(1 + g_1^2 - 2g_1\mu\right)^{3/2} + (1 - \alpha) \left(1 - g_2^2\right)/(1 + g_2^2 - 2g_2\mu)^{3/2} \quad (2\text{-}5)$$

For equation 2-5, the following values are used for continental conditions, where a=0.978, g_1=0.884 and g_2=0.749 and for maritime conditions, the values of a=0.935, g_1=0.795 and g_2=0.568 are used. Forster (1984) recommended the continental phase function scattering chart by Deirmendjian (1964) for calculating phase functioning, as indicated in Figure 2-5 (a).

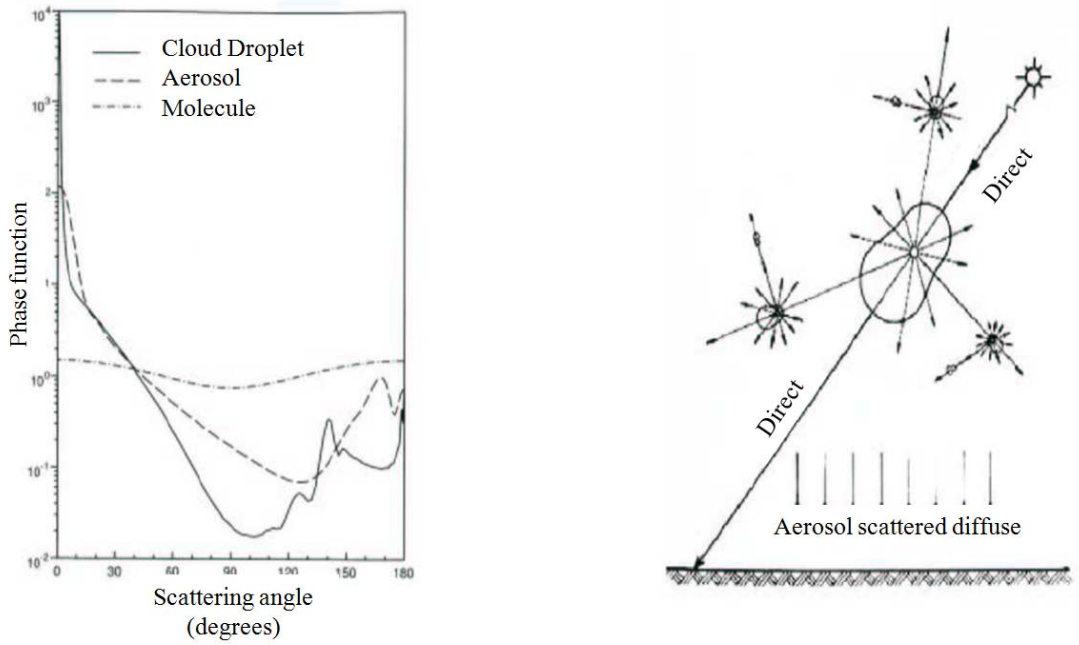

Figure 2-5 Spatial distribution of particle scattering. Left (a), phase functions for cloud droplets, aerosols and molecules, computed from the Lorenz-Mie theory; Right (b): analog scheme for aerosol scattering (Guanter, 2008)

Cervino et al. (2011) stated that inaccuracies in AOT retrieval are often due to an incorrect scattering angle and inaccuracies in the phase function. As well, knowledge of the surface bidirectional reflectance distribution function is necessary, since inaccuracies of 0.01 of the surface reflectance can result in AOT variations of 0.1 (Hauser et al., 2004; Xue et al., 2008; Istomina et al., 2011). It is also critical to take into consideration the location where measurements are taken. For example, DeLeeuw et al. (2000) and Penner et al (2010) found that high concentrations of sea spray aerosols affect AOT values while suspended sediments in shallow water may also result in high AOT values (Robles Gonzalaz et al., 2000; Chu et al., 2002). Guanter et al. (2008) state that most of the algorithms for optical remote sensing use surface reflectance and the conversion of top of atmosphere radiance to surface reflectance (atmospheric correction) is used to correct the distortion caused by interaction between solar radiation and atmospheric components. Seidel et al. (2005) states that the single scattering albedo is an important source of uncertainty in the retrieval of AOT. Guanter et al. (2008) found that AOT influence is highest in the shorter wavelengths due to scattering. According to Istomina et al. (2011) single scattering albedo is also variable. According to Dubovik et al. (2000), errors in the AERONET derived single scattering albedo were estimated to be around 0.03 and 0.05-0.07. Errors of the single scattering albedo can turn to higher-error on retrieved AOT because of increased/decreased radiance, when ω_a is increasing or decreasing; for example, an uncertainly of 0.05 in the

single scattering albedo can cause uncertainty in the retrieved AOT by as much as 0.08 (Dubovik et al., 2000).

2.4.3 Atmospheric Pollution and AOT

Every air pollution problem is due mainly to the presence of aerosol particles (Lyons and Scott, 1990). Aerosols are an indicator of air pollution due to their suspension and transport potential and their relationship with SO_2 and NO_2 (Hadjimitsis, 2009). Atmospheric pollution has received considerable attention by local and global communities (Wald et al., 1999). The study of aerosols and other atmospheric pollutants relies on spatial and temporal data series received from air quality monitoring networks (Al-Saadi et al., 2005). Although air quality monitoring stations have been established in major cities and provide means for alert, these measuring stations are scarcely distributed and they do not provide sufficient tools for mapping atmospheric pollution since air quality is highly variable (Wald et al., 1999).

The key parameter for assessing atmospheric pollution is the aerosol optical thickness, which is also the most important unknown of every atmospheric correction algorithm for solving the radiative transfer equation and removing atmospheric effects from satellite remotely sensed images (Hadjimitsis et al., 2007; Hadjimitsis and Clayton, 2004; Hadjimitsis et al., 2002; Hadjimitsis, 1999; Forster, 1984). The aerosol optical thickness has been used as a tool of assessing atmospheric pollution using satellite remotely sensed imagery (Kanaroglou et al., 2002; Kaufman et al., 1990). Therefore, the determination of the atmospheric pollution through the derivation of the aerosol optical thickness from the satellite images can be used to assess the levels of pollution.

Satellite remote sensing is a valuable tool for assessing and mapping air pollution as satellites are able to provide synoptic views of large areas in one image on a systematic basis due to the temporal resolution of the satellite sensors (Kaufman et al., 1990; Paronis and Sifakis, 2003; Tulloch and Li, 2004). Research indicates that the determined aerosol optical thickness (AOT) from satellite image data can be used as a tool to assess air pollution (Sifakis and Deschamps, 1992; Sifakis et al., 1998; Retalis et al., 1999; Hadjimitsis and Clayton 2006; Leon et al., 1995; Hadjimitsis, 2002; Tang et al., 2005; Kanaroglou et al. 2002; Kaufman et al. 2002). Satellite observations make it possible to derive aerosol source regions (Prospero et al., 2002). AOT derived from the atmospheric

path radiance can be used to assess and monitor atmospheric pollution and air quality (Hadjimitsis et al., 2009).

According to the European Directive 2008/50/EC for the quality of air in Europe, the threshold for PM10 should not exceed 50Mgr/m^3 more than 35 times within a 12 month period (http://www.airquality.dli.mlsi.gov.cy). Several researchers have also studied air pollution by examining AOT and $PM_{2.5}$ and PM_{10} values. Retalis et al. (2003) used AVHRR (Advanced Very High Resolution Radiometer) images and the differential textural analysis algorithm to calculate AOT and then compared the AOT values with PM_{10} measurements. According to Retalis et al. (2003), one of the limitations of the study was the low resolution of AVHRR; the study indicated that Landsat is considered the most appropriate for AOT retrieval in order to study pollution. Lim et al. (2004) and Tan et al. (2011) examined pollution levels by correlating retrieved AOT with PM_{10} measurements, which found a linear relationship between the two variables. Gupta and Christopher (2009) have examined how air-quality monitoring can be aided by using satellite aerosol products, which was done by comparing MODIS AOT data and $PM_{2.5}$ data and using this data to make accurate PM estimations from satellite images through the use of an artificial neural network framework. Determining AOT in large scale pollution areas provides a synoptic, cost effective means to further assess the air pollution in these areas

2.5 Geographical Information System (GIS)

Geographic Information System (GIS) has also been used as a means to study atmospheric properties. GIS is a computer based tool that uses heterogeneous data, which can be used to digitally analyze geographical trends. It has been a useful tool for studying AOT values. Combining satellite remote sensing and GIS provides a quick and cost effective way to provide an improved qualitative assessment of pollution. The development of spatial data management in GIS allows for environmental modeling, monitoring and assessment, including air quality modes on both global and local spatial scales. GIS can be integrated with remote sensing data to analyze and display air pollution measures, which are indicated by high AOT values.

Geographic Information System (GIS) is a computer based tool that uses heterogeneous data, which can be used to digitally analyze geographical trends. According to Schott (2007), a GIS consists of many types of information that describe spatially distributed variables, where all the attributes of the spatial variables can be accessed and any attribute

can be mapped or displayed as an image. GIS is often used to perform spatial analysis and data models, as it can be used to depict two dimensional and three dimensional characteristics of the Earth's surface, subsurface, and atmosphere from points or areas where data has been collected. The way in which maps and other data have been stored or filed as layers of information in a GIS makes it possible to perform complex analyses (Schott, 2007). According to Schott (2007), the formatting and processing of GIS data is based on the ability to transfer spatial data into a common coordinate system (geo-reference), and then to re-sample the data so it can be easily accessed and processed from the same spatial location simultaneously. Once the spatial data are assembled and associated to a common geodetic coordinate system, GIS analysis can be applied to the data.

According to Raju (2003), data models convert geographical variations into computer representations of these features. In order to produce a data model, the first step is to create a layer stack of data sets that are relevant for the model being used. From this layer stack, a comprehensive list of elements that are used in the model are created (Wilmelmi et al., 2005). The most commonly used structure data types used in GIS include points, lines, polygons and raster data. Attribute data describe spatial features, which can be entered or imported into the GIS database. Database queries can be conducted according to the characteristics of spatial, geographical, geometrical or attribute data. Attributes and entity types can be displayed by color, line patterns or point symbols, graphs, interpolation, etc. There are several components of a GIS, including raster and vector data, text data, layers and thematic maps.

Raster data is a type of digital image, such as a satellite image, while the data itself is depicted as rows and columns of cells with each cell having a single value. Rasters can be represented in the database and therefore are included in the data model as a single object (Wilmelmi et al., 2005). The raster images describe a continuous data surface on which each pixel in the image can be treated as a sample point and changes between sample points are assumed to be continuous (Zhou, 1995). The vector geospatial data format is the most common way data is shown in GIS. Vectors are often stored as shapefiles and indicate geometries such as points, lines, and polygons. Each of these geometries may have attributes that describe each item (such as name or AOT value). Text can be stored as attributes or parameters or can be stored in external or internal databases that combine information or data that can be linked to vector or raster data. Simple tabulated databases

are often utilized, such as Excel, Access and Oracle. Text data can also be used to define attributes, and to digitize and convert a raster to vector data in order to make analysis and data processing easier, as data incompatibility is a common problem in GIS. The characteristic of each layer within a layer-based GIS is that all locations within each layer are considered to belong to a single cell, although it is possible for each region to have multiple attributes (Raju, 2003). A thematic map is a map that emphasizes a particular theme or special topic. Thematic maps provide specific information about particular locations, spatial patterns and can be used to compare patterns on two or more maps. GIS can be used with tools such as ERDAS Imagine and ESRI ArcGIS, which have the ability to manipulate satellite images. In this thesis, GIS was used to create thematic maps in order to track temporal AOT changes.

Several researchers studying pollution and atmospheric modeling have produced GIS maps created for retrieved AOT values, including Lim et al. (2004), Soulakellis et al. (2004), Xue et al. (2008) and Tan et al. (2011). However, Schaap et al. (2008) stated that application of mapping procedures are limited to areas with similar retrieval approaches due to differences of retrieval models or sudden changes in surface properties across the coastline. Lim et al. (2004) and Tan et al. (2011) suggested that AOT studies can be generated by using the Kriging interpolation method. Soulakellis et al. (2004) created AOT maps based on retrieved AOT value derived from DTA software.

Research by Soulakellis (Soulakellis et al. 2002; Soulakellis and Sifakis, 1997) focused on using GIS to map air pollution levels. Soulakellis et al. (2004) utilized three different software codes based on high spatial resolution sensors in order to retrieve AOT. In the Differential Textural Analysis (DTA) developed by Sifakis and Deschamps (1992), AOT is retrieved by performing a radiometric comparison on a geometrically corrected two-image set: a reference image acquired under clear conditions and a “polluted” image by use of the “blurring effect” or “contrast reduction principle”, as described by Tanre et al. (1988). The Satellite Mapping of Aerosol (SMA) code was developed for use only with Landsat images and utilized the blurring effect and the opacity effect, as described by Sifakis et al. (1998). Last, the Satellite Image Processing for Haze and Aerosol (SIPHA) mapping code provides estimates and maps of AOT through use of Landsat images and consideration of the surface features.

Merging satellite remote sensing and GIS tools provides a quick and cost effective way to provide an improved qualitative assessment of pollution. GIS is a tool that can be used for assessing and displaying air pollution through the use of AOT values retrieved directly from satellite imagery or in-situ sun-photometers distribution of measurement. Based on the determined AOT over an area of interest, and through interpolation, thematic maps can be generated using colour themes showing the levels of the AOT and/or pollution. Such information can be used as a tool for decision-makers to address air quality and environmental issues more effectively.

2.6 Summary

In this section, the role of atmospheric correction and aerosol optical thickness retrieval in satellite image processing was examined in detail. As discussed, pre-processing techniques are most important in multi-temporal studies where geometric corrected images in radiance or reflectance are required. Although geometric, destriping, illumination and topographic corrections are well-defined, the correction for atmospheric effects is not well–defined and this is problematic as the removal of atmospheric effects is a necessary step in the pre-processing of remotely sensed data. The next section provides an overview of the available atmospheric correction algorithms and provides a critical assessment of these methods.

Chapter 3 Literature Review On Atmospheric Correction Methods

This chapter gives an overview of the available atmospheric correction algorithms and also includes a critical assessment of these methods. In this chapter, the empirical line method using pseudo-invariant targets and the Darkest Pixel are briefly explained as they will be examined in more detail in Chapters 8.

3.1 Atmospheric Correction Methods

The problem of atmospheric intervention has received considerable attention from many researchers who have developed a range of methods, either simple or sophisticated (Hadjimitsis and Clayton, 2009; Hadjimitsis et al., 2004). The sophisticated methods require auxiliary information about the state of the atmosphere which is obtained either from standard databases or from simultaneous in-situ field measurements, and also require meteorological data. Atmospheric correction methods can be classified as absolute corrections and relative atmospheric correction algorithms (Mahiny and Turner, 2007; Liang et al., 2001; Hadjimitsis et al., 2004; Lu et al., 2002). However, classification of atmospheric correction methods is difficult due to the overlapping nature and inter-dependence of some of the methods (Mahiny and Turner, 2007; Liang et al., 2001; De Haan et al., 1991). Several atmospheric correction methods have been developed to retrieve the surface reflectance or target radiance from remotely sensed images by removing the atmospheric effects including atmospheric noise and attenuation. Most atmospheric correction methods have been developed to resolve specific issues for specific targets.

3.1.1 Absolute correction methods

Absolute corrections are atmospheric correction methods that lead to surface reflectance by removing atmospheric effects. Absolute corrections consists the following atmospheric correction algorithms, which are described in brief below:

- Low-Resolution Transmittance (LowTran7) (Richter, 1990; Kneizys et al., 1988)
- Moderate Resolution Atmospheric Radiance and Transmittance Model (MODTRAN) (Kneizys et al., 1988)
- 6S Model (Vermote, 1996; Tanré et al., 1990)

- Simplified Method of Atmospheric Correction (SMAC) (Rahmen and Dedieu, 1994; Quaife and Barnsley, 1999)
- Darkest pixel (DP) (Crane, 1971; Chavez, 1975; Moran et al., 1992)
- Covariance Matrix Method (CMM) (Switzer et al., 1981; Mather, 1987)
- Regression Intersection Method (RIM) (Crippen, 1987)
- Spherical Harmonic Discrete Ordinate Method (SHDOM) (Evans and Wiscombe, 2003)
- Atmospheric and Topographic Correction (ATCOR) (Richter, 1996; 2009)
- Advanced Modeling of the Atmospheric Radiative Transfer for Inhomogeneous Surfaces (AMARTIS) (Miesch et al. 1999; 2002; 2004; Thomas et al, 2011).

Low-Resolution Transmittance - LOWTRAN 7: In 1985, Richter developed the LOWTRAN 7 computer program based on radiative transfer codes (Richter, 1990). The LOWTRAN 7 atmospheric transmittance and radiance computer program (Kneizys, 1988) provide optical thickness, atmospheric temperature and altitude distribution of aerosol content. The calculation for correction of thermal infrared band data requires accurate calculation of the Earth surface temperature. Since there were several limitations with this computer code, it was modified by Berk et al. (1989) and renames as MODTRAN (Toril et al., 1995).

MODTRAN: MODTRAN, the Moderate Resolution Atmospheric Radiance and Transmittance Model, includes all the capabilities of LOWTRAN 7, but incorporates a much more sensitive molecular band model with 2 cm-l resolution (Berk et al., 1989; Toril et al., 1995). MODTRAN has been adopted by some researchers in the AVIRIS program as a radiative transfer code to derive surface reflectance from AVIRIS measurements (Lu et al., 2002; Rahmen and Dedieu, 1994). In 2000, the MODTRAN 4 was released, which included the implementation of the correlated-k algorithm which provided accurate calculations of multiple scattering and sets of bi-directional radiance distribution functions (BRDFs) that allowed for surface scattering to be other than Lambertian. These two features improved scattering accuracy, as had the implementation of azimuthal asymmetries (U.S. Air Force, 2011). The MODTRAN5, released in 2005, included several improved features, such as finer spectral resolution through the spectrally enhanced resolution MODTRAN (SERTRAN) molecular band mode to improve model accuracy in the mid and long wave infra-red atmospheric widths, a fully coupled treatment of auxiliary molecular species to allow the addition of the suite of HITRAN molecular line species and

a rapid, high fidelity multiple scattering option that permits the calculation of vis-NIR databases that include high fidelity scattering radiances.

6S model: In 1990, Tanré et al. developed the 5S model, which stands for Simulation of the Satellite Signal in the Solar Spectrum (Tanré et al., 1990). Due to the limitations of this radiative transfer code, it was revised by Vermote in 1997 to enlarge the application field of 5S, in order to include new possibilities such as non-Lambertian surface conditions, target elevation, near-nadir plane observations and new absorbing species. The 6S model stands for Second Simulation of the Satellite Signal in the Solar Spectrum (Vermote et al., 1997), which is an advanced radiative transfer code designed to simulate the reflection of solar radiation by a coupled atmosphere-surface system for a wide range of atmospheric, spectral and geometrical conditions. The code operates on the basis of an SOS (successive orders of scattering) method and accounts for the polarization of radiation in the atmosphere. The 6S code enables accurate simulations of satellite and plane observation, accounting for elevated targets, use of anisotropic and Lambertian surfaces and calculation of gaseous absorption (Nunes and Marcal, 2004). The code is based on the method of successive orders of scatterings approximations and its first vector version (6SV1) was capable of accounting for radiation polarization. It was publicly released in May, 2005.

Simplified method for atmospheric correction (SMAC): In 1994, Rahmen and Dedieu develop the simplified method of atmospheric correction (SMAC), which is further developed by Quaife and Barnsley (1999), which is based on the 6S model. SMAC is based on a set of equations with coefficients which depend on the spectral band of the sensor. Semi-empirical formulas are used to describe the different interactions of solar radiation with atmospheric constituents during its traverse through the atmosphere. Once the coefficients for a specific spectral band are determined, the inputs of the model are vertically integrated gaseous contents, aerosol optical depth at 550 nm, geometric conditions and reflectance at the top of the atmosphere (TOA).

Darkest pixel method (DP): In 1971, Crane developed darkest pixel method of atmospheric correction, which is further developed by Chavez (1975) and Moran et al. (1992). The DP (darkest pixel method) or darkest object subtraction (DOS) approach (Campbell 1993) is one of the simplest atmospheric correction methods. The Dark Object Subtraction (DOS) model is based on the assumption that dark objects exist within an

image and have zero reflectance (Gilabert et al., 1994; Moran et al., 1992). This approach assumes that the pixel with the lowest digital number (DN) in each band should, in reality, be zero, and therefore, its radiometric DN value represents the atmospheric additive effect (Crane, 1971; Crippen, 1987; Fraser et al., 1992; Hadjimitsis et al., 2003; Campbell, 2008). The DP may correspond to a large water body or another dark object or feature within the scene. Teillet and Fedosejevs (1995) modified the DP method and included radiative transfer calculations to retrieve AOT measurements. Hadjimitsis et al. (2003) modified the DP method to assume a known surface reflectance for the dark target instead of using a zero reflectance value for the dark target.

Covariance matrix method - CMM: In 1981, Switzer developed the covariance matrix method (CMM), which enables estimation of atmospheric path radiance. This method was further developed by Mather (Mather and Koch, 2011). The CMM (Covariance Matrix Method) uses the statistical relationship between all the selected bands of a satellite sensor simultaneously (rather than one at a time as in the regression method), and examines the set of variances and covariance between all band pairs in the image data (Mather and Koch, 2011; Switzer et al., 1981). The CMM provides an average pixel correction for a specified part of a satellite image. In this method, it is necessary to know beforehand the value for the atmospheric path radiance on one spectral band and, from this, CMM enables the estimation of the atmospheric path radiances in all the other bands (Hadjimitsis, 1999).

Regression intersection method - RIM: The regression intersection method (RIM) was developed by Crippen (1987) and refined by Mather (1987). The RIM is based on contrasts between the spectral properties of various homogeneous areas in rugged terrain. Bi-spectral regression (first principal component) lines are determined for each area and are projected, in pairs, to intersection points. The median result from several site-pair and band-pair comparisons are used in order to statistically mitigate noise and minor variations due to natural variability. Therefore the regression method uses the application of the regression model by “band by band” correlation.

Spherical Harmonic Discrete Ordinate Method - SHDOM: The Spherical Harmonic Discrete Ordinate Method (SHDOM) for Atmospheric Radiative Transfer (Evans and Wiscombe, 2003; Pincus and Evans, 2009) computes unpolarized monochromatic or spectral band radiative transfer in a one, two, or three-dimensional medium for collimated solar and/or thermal emission sources of radiation. The SHDOM uses an iterative process

to compute the source function (including the scattering integral) on a grid of points in space. The angular part of the source function is represented with a spherical harmonic expansion. A discrete ordinate representation is used in the solution process since the streaming of radiation is more physically (and correctly) computed in this way. In this method, it is recommended to use an adaptive grid as the source function is usually rapidly varying in some regions and slowly varying in others.

Atmospheric and Topographic Correction – ATCOR: The Atmospheric and Topographic Correction for wide FOV airborne optical scanner data (ATCOR 4) calculates correction for flat areas by applying constant or varying atmospheric accounting for adjacency effects (Ritcher, 1996; Ritcher et al., 2009). The ATCOR provides a self-contained determination of aerosol map and spatial water vapor map as well as haze and cirrus cloud removal. ATCOR 3 includes all the capabilities of the ATCOR and ATCOR 2 software, and can be integrated with a DEM for atmospheric correction of images depicting rugged terrain. ATCOR 3 is restricted to high spatial resolution satellite sensors such as GeoEye-1, WorldView-1, WorldView-2, QuickBird, IKONOS, ASTER, SPOT-5 and LANDSAT TM. The software is licensed to ReSe Applications Schläpfer for commercial marketing and currently is being further developed by Dr. R. Richter in collaboration with ReSe. ReSe Applications Schläpfer specializes in remote sensing data processing, specifically imagery spectroscopy (www.rese.ch). The software has been integrated into ERDAS IMAGINE software.

Advanced Modeling of the Atmospheric Radiative Transfer for Inhomogeneous Surfaces (AMARTIS) The Advanced Modeling of the Atmospheric Radiative Transfer for Inhomogeneous Surfaces (AMARTIS) radiative transfer code was developed for use in urban areas (Miesch et al. 1999; 2002; 2004). Limitations of AMARTIS included describing the landscape as 2-dimensional and considering urban surfaces, such as walls, roofs, etc to be uniform with unique optical properties. These limitations were resolved in AMARTIS v2, where the actual 3D description of the landscape was considered and each scene element is defined by its spectral bidirectional reflectance (Thomas et al., 2011). The AMARTIS v2 allows for simulation of airborne and space borne multi-angular observations of 3D scenes in the 0.4μm to 2.5μm domain with the ground's geometry, with the urban materials optical properties, atmospheric modeling and sensor characteristics being entirely defined by the user (Thomas et al., 2011).

3.1.2 Relative atmospheric correction methods

Relative atmospheric correction models are used to remove or normalize the variation within a scene and normalize the intensities between images of same study area collected on different dates. Relative atmospheric corrections consists the following atmospheric correction algorithms, which are described in brief below:

- Chromaticity method (Afoldi and Munday, 1978; Munday, 1983; Lindell et al., 1986).
- Multi-temporal Normalization Method (MTN) (Schott et al., 1988)
- Empirical line method using standard calibration targets (Hadjimitsis et al., 2004).
- Adaptive empirical line method (AELM) (Bartlett and Schott, 2007).

Chromaticity method: In 1978, Afoldi and Munday developed the chromaticity method of atmospheric correction, which was further developed by Munday (1983) and Lindell (1986). This method can be used to generate quantitative maps of suspended sediment concentration levels. The colour saturation on the chromaticity plane is used for adjusting the atmospheric condition of one image date to coincide with the conditions of another date and then the suspended sediment concentration calibration established for one date can be applied to the other.

Multi-Temporal Normalization method (MTN): The MTN (Multi-Temporal Normalization method) assumes the normalization of the spectral data of all the images to a standard image which is defined as the reference scene (Schott et al., 1988; Berger, 1989; Caselles and Garcia, 1989; Hadjimitsis et al., 1998; Du et al., 2001; Du et al., 2002; Song and Woodcock, 2003; Canty et al., 2004; Schroeder et al., 2006). This reference scene usually possesses the lowest contribution of atmospheric effect, meaning that it is cloud free with high contrast. This normalization is applied using known pseudo-invariant targets within the scene. Pseudo–invariant targets (PITs) utilize man-made features in the environment that do not change spectrally from image to image and are used when atmospheric conditions are unknown in order to normalize multi-temporal data sets to a single reference scene (Schott et al., 1988; Berger, 1989; Caselles and Garcia, 1989; Hall et al., 1991).

Empirical line method: In 1998, Emery et al. developed the empirical line method, which was further developed by Schroeder et al. (2006) and Hadjimitsis et al. (2009) with the use of pseudo-invariant targets and by Lach and Kerekes (2008) with 3D scene geometry from Lidar imagery. The empirical line method two or more targets within a scene with different

reflectance characteristics covering a range of reflectance values in the spectral bands recorded by the satellite sensor (Emery et al., 1998). The reflectance values for each of the calibration targets are then measured in-situ with field spectroradiometers for the required wavelengths and also extracted from the satellite images. Subsequently, a linear relationship between the satellite reflectance and the in-situ reflectance (surface reflectance) is established to define the atmospheric path radiance which is the intercept on the graph. Separate relationships are developed for each waveband to produce images in units of reflectance. The method has been recently extended and revised by Hadjimitsis et al. (2009) by using pseudo-invariant targets (PITs) and using assuming reflectance values in place of the calibration targets in the empirical line method which are obtained from ground measurements and are considered to be suitable for specific type of PITs. Following, the average ground reflectance measurements of the selected non-variant targets are established as the 'true values' for all the time-series images and ground reflectance values are regressed against the at-satellite reflectance for each image.

Adaptive empirical line method (AELM): Bartlett and Schott (2007) used ground measurements to modify the empirical line method approach on a per-pixel approach. What is notable about this method is that it includes the presence of clouds in atmospheric correction. A physics-based model of the atmosphere is used to generate a spatial correction for the empirical line method through use of the MODTRAN radiative transfer code. The model is then used to achieve a per-pixel correction by adjusting the ELM slope spatially. The adaptive empirical line method (AELM) is a unique method of atmospheric correction, as it combines both absolute and relative atmospheric correction methods and includes the presence of clouds in the calculations.

3.2 Critical assessment of the existing atmospheric correction methods

Mahiny and Turner (2007) indicate that each atmospheric correction method has its advantages and disadvantages. There are several limitations in the atmospheric correction methods discussed. In this chapter, the main limitation with the models which are based on the radiative transfer equation is that they are complex and require many input parameters from the in-situ field atmosphere (Lu et al., 2002). In radiative transfer equations, it is often impossible to collect the in-situ atmospheric parameters for many applications, especially when using historical remotely sensed data (Lu et al., 2002). Therefore, many of these atmospheric parameters require approximations, which can negatively affect the results. For example, knowledge of the bi-directional reflectance distribution function

(BRDF), which refers to the angular reflectance properties of light on an opaque surface. is essential, as inaccuracies of even 0.01 of the surface reflectance can lead to AOT variations of 0.1) (Istomina et al., 2011; Xue et al., 2008; Hauser et al., 2004). As well, errors of the single scattering albedo can lead to a higher error on retrieved AOT because of increased/decreased radiance, with an uncertainty of 0.05 leading to a discrepancy in AOT retrieval as much as 0.08 (Dubrovik et al., 2000). According to Gilabert et al. (1994), most of the atmospheric correction methods are not easily applicable in real cases and the most sophisticated models require inputs which are not commonly available.

As well, although the SHDOM is considered to be one of the most capable explicit representation 3D atmospheric radiative transfer model developed, it has limitations in handling many modeling situations. The major disadvantages of the SHDOM method include its limited memory (which limits the size to 32-64 pixels), it include pre-computed sets of output angles which require interpolation and, since there is no embedded MIE-code, the method needs to be used in combination with a MIE-code to simulate aerosols (Kotchenova and Vermote, 2007).

Image based atmospheric correction methods, such as the DP method, avoid many of the problems of physically based atmospheric correction methods since they avoid collecting in-situ atmospheric information and depend instead on the image information, such as gain, offset, solar zenith angle, radiance and atmospheric transmittance (Lu et al., 2002). However, the main disadvantages of relative calibration methods is that they cannot remove atmospheric impacts because these impacts vary across wavelengths and relative calibrated data are not suitable for quantitative analysis such as image ratio (Lu et al., 2002). One of the criticisms of the DP method is that it merely removes scattering and haze, but does not yield real reflectance data (Gilabert et al., 1994). This issue was addressed by Hadjimitsis et al. (2009) by using calibration targets with known reflectance values to perform the DP method. Mahiny and Turner (2007) found that for the PITs method to produce acceptable results, a large sample of pixels should be selected across the image.

According to Hadjimitsis et al. (2004), in comparing the PITs method with other relative correction methods, the PITs method is endorsed due to the unreliable results from the other atmospheric correction methods in the study. Hadjimitsis et al. (2004) found that the MTN method was ineffective as the reference image retained a significant amount of

atmospheric effect after atmospheric correction. Hadjimitsis et al. (2004) found that the main limitation of the regression method is that the mean corrected values were congruent with the ground targets, but the standard deviation was very large, which indicates high variability. As well, the two main limitation of the chromaticity method are that it is unreliable since it requires a clear image against which other images can be normalized and a special processing system is required to display all DN in the form of a chromaticity chart (Hadjimitsis et al., 2004). Hadjimitsis et al. (2004) found that the CMM did not correctly account for atmospheric addition and attenuation since the correction between corrected at-satellite and the estimated ground reflectance produced scattered results that were variable across multi-temporal images. Also, Hadjimitsis et al. (2004) found that the RIM method produced high estimates of path radiance and poor performance in removing atmospheric effects.

It has been shown by several researchers such as Wilson and Milton (2010), Hadjimitsis et al. (2009), Mahiny and Turner (2007), Wu et al. (2005), Ben-dor et al. (2004), Huang et al. (2002), Clark et al. (2002), Cheng and Lei (2001), and Liang et al. (2001) that the two most accurate atmospheric correction methods are the DP (absolute correction method) and empirical line method using pseudo-invariant targets (relative correction method). The Darkest Pixel (DP) method is the most widely applied method of atmospheric correction that provides reasonable correction, especially in cloud-free skies (Schott, 1997; Cheng and Lei, 2001; Hadjimitsis et al., 2004). Several studies have used the linear regression technique to normalise image data to field spectral data to remove atmospheric effects and target calibration has been successfully employed in the correction of satellite data for atmospheric effects (Chrysoulakis et al., 2010; Karpouzli and Malthus, 2003; Brest and Goward, 1987; Kruse et al., 1990; Stow et al., 1996). Mahiny and Turner's (2007) study of atmospheric correction method found the PITs method to be the most accurate compared with other atmospheric correction methods. Although the empirical line method can be used with two targets (one light and one dark), there is a current trend to using more reference targets, since it allows the parameters of the relationship between at-sensor radiance and at-surface reflectance to be estimated with greater confidence (Baugh and Groeneveld, 2008; Price et al., 1995; Smith and Milton 1999; Karpouzli and Malthus, 2003).

3.3 Summary

This chapter presented a critical assessment of the existing atmospheric correction methods. Research indicates that the Darkest Pixel (DP) and empirical line method using pseudo-invariant targets are the most accurate in comparison to other atmospheric correction methods. The empirical line and DP method are further examined in Chapter 8.

Chapter 4 Study Area, and Materials

In this chapter an outline of the study area and materials used for this PhD thesis are presented. The study area and the resources used in the thesis are explained in detail.

4.1 The study area

The study area is near Limassol, Cyprus, and the Akrotiri Bay (Lady's Mile Beach), as indicated in Figure 4-1. The Limassol port and Akrotiri Bay are located south of Limassol and are on the southern coast of the island. Every spring, dust from the Sahara desert significantly affects visibility in the city. Rainfall is approximately 410 mm annually (Cyprus Meteorological Service, 2010). The pseudo-invariant targets used in this thesis are two asphalt targets and one concrete target located in the Limassol port and two sand targets located in the Akrotiri Bay next to the British bases.

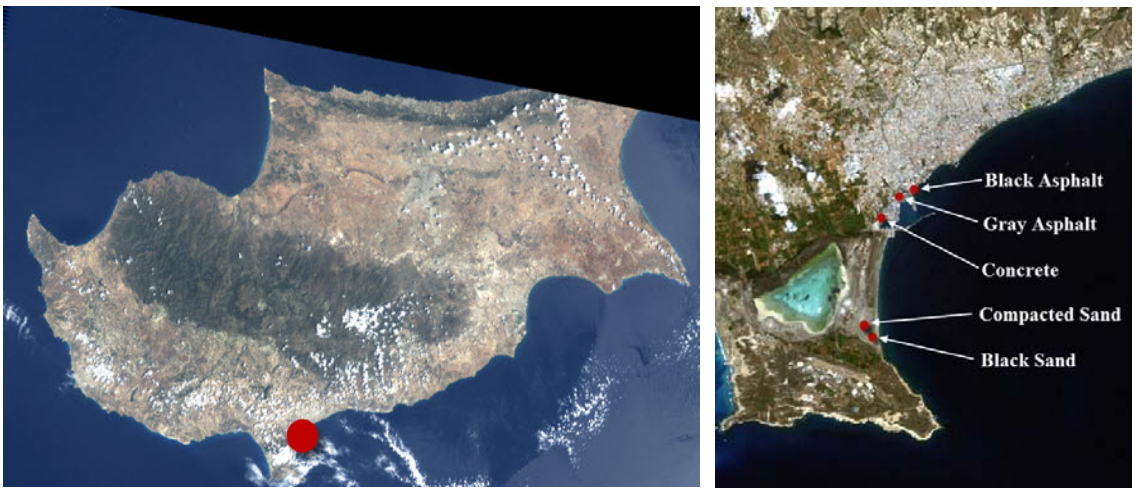

Figure 4-1: Landsat 5 TM satellite image of Cyprus and Limassol (24/6/2010) showing the location of the in-situ targets used

The Limassol port is a major transportation hub and, as a result, generates much pollution. The two asphalt targets are asphalt based surfaces, clear from any debris or markings and are used as parking for bonded cars. As the bonded cars are not parked for an extended period of time, the two asphalt targets are an ideal target as cars are seldom located on the site. The concrete target consists of interlock concrete blocks and is a large empty area next the port. The sand targets are at Akrotiri beach, near the British bases, approximately 3 kilometers from the Limassol port. One of the sand targets consists of volcanic (black) sand while the other sand target is compacted sand that is leveled and often used on

weekends by hobbyists as a launch pad for remote-controlled model airplanes. Both sand targets are affected by seasonal changes, due to their proximity to the salt lake and sea. The reason the sand targets were chosen is that similar targets can be found in many coastal locations in large areas. Also, the targets are large enough to be suitable to use with the Landsat pixel size. The reference targets are further examined in Chapter 7.

4.2 Resources

This section briefly describes the resources used in the study. The following resources were used to carry out this research study: (a) ERDAS Imagine v. 2011 software (b) ArcGIS software (c) MATLAB software (d) Landsat 5 TM, and Landsat 7 EMT+ satellite images (e) SVC HR1024 spectroradiometers, and (f) Microtops II and Cimel Sun photometers. Detailed information regarding these resources are found below.

4.2.1 Digital image processing system

The digital image processing system refers to the image processing software used to analyse digital image data. The ERDAS IMAGINE (v.2011 Professional) by Leica Geosystems was used to pre-process and post-process all the available multi-series imagery. ERDAS Imagine is a remote sensing application with raster graphics editor capabilities designed by ERDAS, Inc for geospatial applications and the latest version is 2011, version 11. ERDAS IMAGINE is aimed primarily at geospatial raster data processing and allows the user to prepare, display and enhance digital images for mapping use in GIS or in CAD software. Therefore, by manipulating imagery data values and positions, it is possible to see features on the satellite image that would not normally be visible and to locate geo-positions of features that would otherwise be graphical. ERDAS IMAGINE v.2011 professional is produced by the Engineering Department of ERDAS, Inc., Atlanta, Georgia, USA (http://www.erdas.com).

4.2.2 Geographical Information System

ArcGIS is a group of geographic information system (GIS) software products produced by ESRI. ArcGIS is built around the geo-database, which uses an object-relational database approach for storing spatial data. ArcGIS allows the user to author data, maps, globes, and models. ArcGIS, in parallel with the ERDAS Imagine, was used for the GIS analysis, as described in Chapter 9.

4.2.3 Mathematical Processing

MATLAB (**mat**rix **lab**oratory) is a high-performance language for technical computing that integrates computation, visualization, and programming. The software was developed by MathWorks and is often used in conducting image processing. The program was used in order to perform the equations required for the AOT retrieval algorithm that is described in Chapter 9. The equations were entered into the MATLAB program in order to solve for AOT.

4.2.4 Satellite images

Landsat-5 TM, and Landsat-7 ETM+ images are used in this research study. The Landsat Thematic Mapper (TM/ ETM+) is an advanced, multi-spectral scanning Earth resources sensor designed to achieve higher spatial resolution, sharper spectral separation, improved geometric fidelity, and greater radiometric accuracy and resolution than the previous Multispectral Scanner (MSS) sensor (Guanter, 2006). Benefits of the Landsat TM/ ETM+ include exceptional temporal coverage, moderate spatial resolution (30 m) reliable geometric integrity, validated radiometric quality and multispectral range (reflective wavelengths covering the visible, near-infrared and short wave infrared) which provide the ideal data set for studies of natural resources (Moran et al., 2001).

The first Landsat satellite was launched in 1972 and, to date, 7 satellites have been launched. Landsat 1, Landsat 2, and Landsat 3 carried two sensors: the Return Beam Vidicon (RBV) camera and the Multispectral Scanner (MSS). The second generation of Landsat satellites started in July 1983 when Landsat 4 was launched with a slightly modified version of MSS and a new sensor, the Thematic Mapper (TM). Landsat TM sensors have been orbiting the Earth since 1982, providing near continuous coverage every 16 days. An identical satellite, Landsat 5 was launched on 1 March 1984 and is still in operation. In 1993, Landsat 6 was lost immediately after launch. Landsat 7 was launched in April 1999 and is equipped with an enhanced Thematic Mapper (ETM+), which is a new high resolution scanner.

The Landsat TM/ ETM+ is a multi-spectral imaging system that records energy in the visible, reflective-infrared, middle-infrared and thermal-infrared regions of the spectrum. The sensor collects radiometric data at 256 radiance levels in seven spectral bands with a higher spatial, spectral, temporal and radiometric resolution than the Landsat MSS. Band 6 scans thermal (heat) infrared radiation while the other bands scan in the visible and

infrared. The ground resolution of TM is 30m × 30m in the six reflective bands, and 120m × 120m in the thermal infrared band for Landsat 5 TM and 60m × 60m for the Landsat 7 ETM+. The satellite operates with a FOV of ±7.2 (swath width of 185 km) and is a nadir viewing instrument. TM data are scanned simultaneously in 7 spectral bands. A Landsat 5 TM scene has an IFOV of 30 m^2 in bands 1 through 5 and band 7; band 6 has an IFOV of 120 m^2 on the ground. The image size (or scene) is 185 × 172 km, or 5760 lines × 6928 pixels. One of the limitations of the Landsat 5 TM is that it is an old sensor with comprised radiometric accuracy. The Landsat 7 ETM+ has several acquisition problems, notably due to the failure of the Landsat ETM+ Scan Line Corrector (SLC) and several lines of each swath are replaced by simulated values (Hadjimitsis and Clayton, 2009). The problem with the failure of the Landsat ETM+ Scan Line Corrector (SLC) does not affect the area of the satellite images used in this study, as the study area was located in the middle of the Landsat ETM+ image within the 22 kilometers region which is unaffected by the data loss; therefore; the satellite image data is of the same quality as data collected prior to the SLC failure (UGSG, 2010).

The satellite views the entire Earth every 16 days. The satellite operates in a repetitive, circular, near-polar orbit at a nominal altitude of 705.3 km. It is sun-synchronous, which means that it orbits about the Earth at the same angular rate at which the Earth moves about the Sun, which allows the satellite to cross a line of latitude at the same local solar time every day. Completing each orbit in about 99 minutes, the satellites achieve over 14 orbits per day, providing complete coverage of the Earth every 16 days. There is a temporal offset of 8 days between the satellites. Cyprus is on orbit path 178. Ground receiving stations record the incoming data on high-density digital tapes (HDDT) which are later processed and the remotely sensed data for each 185×185 km^2 area is extracted to form a single multi-spectral scene, which are distributed in various raw formats (ERDAS, 2010). Landsat 5 TM and Landsat 7 ETM+ characteristics are shown in Table 4-1 and Table 4-2.

Band	Band edges (μm)	Spatial resolution
Blue-Green, TM 1	0.452-0.518	30 m
Green, TM 2	0.528-0.609	30 m
Red, TM 3	0.626-0.693	30 m
Near-IR, TM 4	0.776-0.904	30 m
Mid-IR, TM 5	1.567-1.784	30 m
Thermal-IR, TM 6	10.40-12.50	120 m
Mid-IR, TM 7	2.097-2.349	30 m
Swath width: 185 km **Radiometric resolution**: 8 bits (256 grey levels) for all bands **Orbit characteristics:** Sun-Synchronous **Inclination:** 98.2°		

Table 4-1 Landsat -5 TM characteristics

Band	Band edges (μm)	Spatial resolution
Panchromatic	0.515-0.896	15m
Blue-Green, TM 1	0.452-0.514	30 m
Green, TM 2	0.519-0.601	30 m
Red, TM 3	0.631-0.692	30 m
Near-IR, TM 4	0.772-0.898	30 m
Mid-IR, TM 5	1.547-1.748	30 m
Thermal-IR, TM 6	10.31-12.36	60 m
Mid-IR, TM 7	2.065-2.346	30 m
Swath width: 185 km **Radiometric resolution**: 8 bits (256 grey levels) for all bands **Orbit characteristics:** Sun-Synchronous **Inclination:** 98.2°		

Table 4-2 Landsat -7 ETM+ characteristics

Typical snapshots from the Landsat TM and ETM+ for the Cyprus region are shown in Figure 4-7 and Figure 4-8. Partial scenes for the Limassol area of interest are shown in Figure 4-9.

Figure 4-2 Figure Landsat 5 TM image of Cyprus

Figure 4-3 Landsat 7 ETM+ image of Cyprus

Figure 4-4 Partial scene: Landsat 7 ETM+ image of Limassol (13/4/2010)

There is availability of Landsat images, as NASA catalogues existing and archived Landsat images and makes these images freely available to non commercial users upon request. Landsat 5 TM consists of seven channels and only one channel is designated for the thermal infrared zone (10.4 μm – 12.5 μm), while the Landsat 7 ETM+ four channels are designated for the visual range and two channels are designated for the infrared range

(Toril et al., 1995). In infrared TM bands, the main effects of atmosphere are from air molecules and aerosol particle scattering, although this does not occur in the thermal infrared bands. Landsat 7 ETM+ provides observations at higher spatial resolutions and with greater measurement precision than previous TM (Goward and Williams, 1997; Liang et al., 2002). The effect of water vapor is significant for the Landsat 7 ETM+ near infrared (IR) channels (Liang et al., 2001). Landsat 7 ETM+ 7 band (around 2.1 μm) can be used for dense vegetation as their reflectance have strong correlations with band 1 (blue) and 3 (green) reflectance, while Landsat 7 ETM+ bands 4, 5, and 7 are less contaminated by aerosols (Liang et al., 2001). Hadjimitsis et al. (2004) found that the DP method performed well in Landsat 5 TM bands 1, 2, and 3.

Satellite Images Used

In this thesis, Landsat 5 TM and Landsat 7 ETM+ satellite images corresponding to the date of field measurement were acquired. Landsat images were used due to their high resolution and their availability. Even though the Landsat satellite passes over Cyprus every 16 days, there was still difficulty in collecting images, as not all Landsat images were available. Eleven Landsat images were chosen for this thesis, even though there were over 30 field measurements, due to the unavailability of the Landsat images. The Landsat 5 TM images were acquired for 24 June 2010, 10 July 2010, 27 August 2010, and 28 September 2010 and the Landsat 7 ETM+ images were acquired for 13 April 2010, 29 April 2010, 31 May 2010, 16 June 2010, 7 November 2010, 9 December 2010 and 2 May 2011. Visual examination identified all the satellite images with low cloud cover using black and white quick look views provided from GLOVIS (http://glovis.usgs.gov.). All the images are presented in Appendix 4, on the attached CD.

Satellite images with cloud cover over the reference targets were not used. The availability of cloud free images for this research project was critical as clouds can affect the quality of the satellite image (Gaunter et al., 2008; Seidel et al., 2005). In conducting atmospheric correction, cloud-free images are recommended. Cirrus clouds (which are the highest clouds in the atmosphere) permanently cover more than 20% of the Earth, interact with aerosols and solar radiation and affect the Earth's radiation budget (Liu, 1986; Chepfer et al., 2001; D'Almeida et al., 1987). Cirrus clouds pose a potential problem for in-situ measurements, even though they are often thin and may not appear to block a significant amount of sunlight. However, cirrus clouds reduce the transmission of sunlight even when they are almost invisible. Further, clouds can have a significant impact on AOT by

changing humidity, which affects aerosol through the aerosol swelling effect. Cloud cover depends greatly on geographical position and the prevailing weather conditions for the area of interest. Cyprus tends to have good weather conditions, which increases the availability of cloud-free images and is beneficial in studies using satellite remote sensing in multi-temporal studies of those areas (Hadjimitsis et al, 2010; Hadjimitsis, 2009; Hadjimitsis, 2008; Hadjimitsis and Clayton, 2008; Hadjimitsis, 1999).

4.2.5 Spectroradiometers

Ground spectroradiometric reflectance data were acquired using the SVC HR-1024 spectroradiometer (see Figure 4-5) provided by the Remote Sensing and Geomatics Laboratory of the Cyprus University of Technology. The SVC HR-1024 was used to obtain in-situ spectral reflectance data from the five pseudo-invariant targets. The SVC HR-1024 spectroradiometer is manufactured by the Spectra Vista Corp. in Poughkeepsie, NY, USA (http://www.spectravista.com). The instrument has been designed to produce high resolution data between 450 nm and 2500 nm quickly and efficiently. Its light size and weight makes it useful for in-situ measurements. It provides the highest level of spectral resolution in the full VIS-NIR-SWIR region. The use of 100% linear array detectors ensure wavelength stability, while its thermoelectrically cooled InGaAs and extended InGaAs detectors provide radiometric stability. The fixed foreoptics and hard-mounted internal spectroradiometer elements provide a robust optical path to insure reliable data delivery in the field. The spectroradiometer can take a full day of spectral measurements without the need for an external computer.

Figure 4-5 SVC HR-1024 spectroradiometer and reference panel

In order to ensure accurate spectral measurements, a stable control surface (reference panel) with known characteristics is required. A reference panel made of Spectralon material was used in order to take reference panel measurements. Spectralon is a hard and durable white surface with a reflectance averaging about 99% varying with wavelength from 95.0 to 99.4 % and is spectrally flat over the UV-VIS-NIR spectrum (McCloy, 2005). Reference panels of Spectralon material are recommended for in-situ reference measurements, as they are durable, washable, impervious to harsh weather conditions and chemically inactive (McCloy, 2005; http://www.spectravista.com). The technical specifications of the SVC HR 1024 are listed in Table 4-3, while the physical specifications of the SVC HR-1024 are listed in Table 4-4. Information on the Spectralon panel is provided in Table 4-5.

SVC HR-1024 Spectroradiometer Technical Specifications	
Spectral Range	450-2500nm
Internal Memory	500 scans
Channels	1024
Linear Array	(1) 512 Si, 450-1000 nm (1) 256 InGaAs, 1000-1890 nm (1) 256 Extended InGaAs, 1890-2500 nm
Spectral Resolution (FWHM)	< 4.5 nm, 700 nm < 9.5 nm, 1000-1890 nm < 6.5 nm, 1890-2500 nm
Bandwith (nominal)	≤1.5 nm, 450-1000 nm ≤4.8 nm, 1000-1890 nm ≤2.5 nm, 1890-2500 nm
Minimal Integration	1 millisecond
FOV	4° standard, 8° or 14° optional 25° optional armored fiber optic
Stray light	<0.1% @ 500 nm
Noise Equivalent Radiance (1.0 sec scan)	$\leq 8.0 \times 10^{-10}$ W/cm^2/nm/sr @ 700 nm, $\leq 1.5 \times 10^{-9}$ W/cm^2/nm/sr @ 1500 nm $\leq 4.0 \times 10^{-9}$ W/cm^2/nm/sr @ 2000 nm
NER 1.0 sec integration time, W cm^{-2}nm^{-1}sr^{-1}	$< 1.2 \times 10^{-9}$ @ 700 nm $< 4.5 \times 10^{-9}$ @ 1500 nm $< 4.0 \times 10^{-9}$ @ 2000 nm
Radiometric Calibration Accuracy (NIST Traceable)	±5% @ 400 nm ±4% @ 700 nm ±7% @ 2200 nm
Maximum Radiance	1.4×10^{-4} W/cm^2/nm/sr @ 700 nm
Wavelength Repeatability	0.1 nm
Wavelength accuracy	1 nm visible and near infrared (VNIR) 4 nm shortwave infrared (SWIR)
Digitization	16 bit
Dark Current Correction Spectrum Averaging	Automatic/selectable Selectable
Operating Environment Humidity Temperature Sighting	 to 90% RH, non-condensing -10° to +40°C diode laser

Table 4-3 SVC HR-1024 Spectroradiometer Specifications

SVC HR-1024 Spectroradiometer Physical Specifications	
Power	7.4 V, 18 W
Size	8.5” x 11.5” x 4.25” 22 cm x 29 cm x 8cm
Weight	7.4 lbs, 4.4 kg
Battery Type	7.4 V Lithium ion
Battery Life	4 hours
Host Communications Interface	USB, Bluetooth
Sealing	Sealed against dirt and dust
Tripod mounting	Standard ¼ “ – 20 mounting
Watertight case	17” x 20” x 9” 44cm x 51 cm x 24 cm
Weight (including HR 1024, PDA, Batteries, chargers and watertight case)	15 kg

Table 4-4 Physical specification of the SVC HR-1024 spectroradiometer

White panel Manufacturer's designation	
Manufacturer	Spectralon
Reflectance value	99%
Reflective Area (cm)	10 x 10
Size mounted (cm)	10 x 10
Material	Spectralon
Colour	White

Table 4-5 SVC HR-1024 Spectralon panel

4.2.6 Sun photometers

Two Solar Light Microtops II hand-held sun photometers and one CIMEL sun photometer in association with the AERONET project were used to measure AOT.

Figure 4-6 Solar Light Microtops II hand-held sun photometer

The Microtops II (Solar Light Company, USA) hand-held sun photometer (see Figure 4-6) provides AOT and columnar water vapour from instantaneous measurements, at five channels (440, 500, 670, 936, and 1,020 nm), as indicated in Table 4-6.

Optical Channels
440 ± 1.5 nm, 10 nm FWHM
500 ± 1.5 nm, 10 nm FWHM
675 ± 1.5 nm, 10 nm FWHM
870 ± 1.5 nm, 10 nm FWHM
936 ± 1.5 nm, 10 nm FWHM

Table 4-6 Bands of the Microtops sun-photometer

The Microtops II sun photometers take measurements of the direct solar irradiance to derive the AOT. The handheld sun-photometer measures the attenuation of direct sunlight as it passes through the atmosphere. Since the aperture of the instrument is small, the light intensity measured by the sun-photometer is not influenced by atmospheric scattering for moderate AOT values. The collimators and band pass filters captured incoming radiation and radiated it onto photodiodes. The radiation was amplified and converted into a digital signal. AOT calculation assumes Bouguer-Lambert-Beer Law (BLB) which refers to the empirical relationship relating the absorption of light to the properties of the material the light is travelling through. There is an exponential dependence between the transmission of light through a substance and the concentration of the substance, and between the transmission and the length of material that the light travels through. Microtops uses equation 4-1 to calculate AOT:

$$AOT_\lambda = \frac{In(V_{0\lambda}) - In(V_\lambda \times SDCORR)}{M} - \tau_{R\lambda}\frac{P}{P_0} \qquad (4\text{-}1)$$

where

$\ln(V_{0\lambda})$	is the AOT calibration constant
V_λ	is the signal intensity in millibar
SDCORR	is the Earth-Sun distance correction
M	is the optical airmass in millibar
$\tau_{R\lambda}$	is the Rayleigh optical thickness
P	is the station pressure in millibar
P_0	is the standard SLP (1012.25 mb)

Figure 4-7 Microtops sun photometer mounted on a tripod

The Microtops sun-photometer was mounded on a tripod in a fixed location each time to ensure best results (see Figure 4-7). In order to get valid results, collection periods could only occur during cloud-free daylight hours and for AOT comparison, during periods coinciding with polar orbiting satellites overpasses. A Garmin Etrex GPS was connected to the Sun-photometer for location and time input (see Figure 4-8).

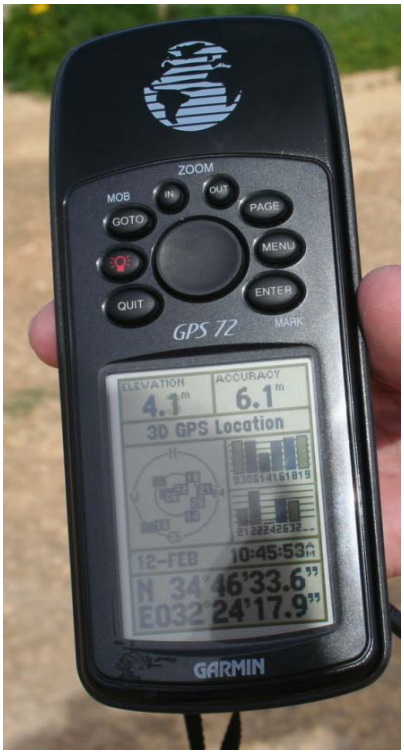

Figure 4-8 Garmin GPS

As the Microtops sun-photometers are manually operated, the operator can select cloud-free periods to perform the measurements and therefore avoid cloud contamination. GPS measurements were also taken at the same time. To take an AOT measurement, the user opened the black cover on the front of the Sun photometer and pointed the unit at the Sun. On the unit there was a window labelled “Sun target”; when a small bright white dot (actually the solar disc) passed through the center of the sun target window, this meant that the Sun photometer was aligned with the Sun. Once this dot appeared as close to the center of the target as possible, the user ensures that the instrument is stable and pressed “scan”. The instrument beeped once and a message appeared on the display saying “Scan X. Point at the Sun” (where X is the scan ID number). Once the instrument finished collecting the measurement, it emitted 2 beeps. For each measurement, one to two measurements were taken using the Microtops II sun photometer. The user noted the date, time, scan number and weather conditions. The measurements were downloaded into a personal computer through use of the Microtops II organizer software and were available in Excel format. The main errors in the Microtops sun photometers, apart from errors due to cloud contamination, include inaccurate pointing to the Sun, and neglecting to clean the front quartz window (www.solarlight.com). These issues were taken into consideration during data measurements.

Figure 4-9 Cimel CE 318 Sun photometer

The Cimel CE 318 sun photometer (see Figure 4-9) is an automatic Sun tracking photometer which measures Sun and sky radiance in order to derive total column water vapour, and aerosols properties by using a combination of spectral filters at 440, 670, 870, 936, and 1020 nm. The purpose of the instrument is to acquire sky radiance observations through a large range of scattering angles from the Sun through a constant aerosol profile to retrieve size distribution, phase function and aerosol optical thickness. The instrument belongs to the Cyprus University of Technology and is located on the roof of the Department of Civil Engineering and Geomatics Remote Sensing Laboratory of the Cyprus University of Technology. The site coordinates are 34.67481º North and 33.04275º East, with an elevation of 22.0 meters. The instrument conducts a direct Sun measurement in eight spectral bands and a sequence of three solar measures can be made, thus creating a triplet observation per wavelength. In this study, the retrieved AOT was compared to the AOT measured by the Cimel sun photometer at the same time as the satellite overpass. This is important, as sun photometers have been found to be supportive tools for validating the derived AOT from the satellite images. The Cimel sun photometer is the sun photometer that is recommended for the NASA AERONET program (discussed below in detail), of which the Cyprus University of Technology is a member. The purpose of the AERONET project is to receive AOT measurements from all over the world. The sun photometer data is sent daily to NASA. The collaboration with AERONET provides globally distributed observations of spectral aerosol optical depth (AOD), inversion products, and precipitable water in diverse aerosol regimes. Aerosol optical depth data are computed for three data quality levels: Level 1.0 (unscreened), Level 1.5 (cloud-screened), and Level 2.0 (cloud-screened and quality-assured). In this study, Level 2.0 data was used and, when unavailable, level 1.5 data was used.

AERONET is a federated ground-based remote sensing network of well-calibrated sun-photometers and radiometers that measure aerosols and their characteristics located at over 200 sites worldwide (http://aeronet.gsfc.nasa.gov). AERONET imposes standardization of the instruments, calibration and processing to all participants of the network (Holben et al., 1998; 2001; Guang et al., 2008). Uniformly acquired and processed data are available from all stations as a result of consistent calibration, cloud-screening and retrieval methods and have been widely used for aerosol process studies and for validation of satellite remote sensing applications (Chin et al., 2002; Yu et al., 2003; Yu et al., 2006; Remer et al., 2005; Kahn et al., 2005a). AERONET measurements are often calibrated by other ground based networks and with Lidar networks (Chin, 2009).

AERONET stations provide direct, calibrated measurement of spectral AOT at wavelengths of 440, 670, 870, and 1020 nm with an accuracy of ±0.015 (Eck et al., 1999). AERONET provides AOT observations at mid-visible wavelengths with an accuracy of 0.01 – 0.02 which is 3-5 times more accurate than satellite retrievals (Chin, 2009; Eck et al., 1999). AERONET has developed inversion-based retrievals of various effective column-mean properties, including aerosol single-scattering albedo, size distributions, fine-mode fractions, degree of non-sphericity, phase function and asymmetry factor (Dubovik et al., 2000; Dubovik and King, 2000; Dubovik et al., 2002; O'Neill et al., 2004). However, the single scattering albedo can be retrieved with an accuracy of ±0.03 but only for AOT greater than 0.4 (Dubovik et al., 2002) which precludes most of the planet. These retrieved parameters have been validated by comparison with in-situ measurements (Haywood et al., 2003; Magi et al., 2005; Leahy et al., 2007). Recent developments associated with AERONET's data products include simultaneous retrieval of aerosol and surface properties using combined AERONET measurements, satellite measurements, and surface reflectance, which significantly improves AERONET single scattering albedo retrieval accuracy (Eck et al., 2008; Sinyuk et al., 2007).

4.3 Summary

In this chapter, an outline of the study area description and materials used were discussed. An overview of the main resources used in this research study such as image processing software, field spectroradiometers and sun-photometers was provided.

Chapter 5 Field Spectroscopy

Field spectroscopy in remote sensing is used to obtain the spectral signatures of the ground targets. The field data in this thesis from spectroradiometers are utilized to establish the spectral properties of the five reference targets in order to establish the ground truth of these targets. Following, atmospherically corrected reflectance values are compared directly with the ground truth.

5.1 Field spectroscopy

Field spectroscopy is the measurement of radiant energy interactions with in-situ surfaces in the environment, which are considered the spectral characteristics of the in-situ objects (McCloy, 2005; Milton et al., 1995). This technique refers to the quantitative measurement of radiance, irradiance and reflectance (Meroni and Columbo, 2009). Direct solar radiation and scattered radiation form a hemisphere of incident radiation striking the surface of the Earth. This incident solar energy is labelled irradiance and the reflected energy is called radiance. The reflectance of a particular point of a target can be expressed as a ratio of the radiance to the irradiance (McCloy 2005). Reflectance (ρ) is a ratio of the target radiance to the reference panel radiance, which can also be written as

$$\rho = \frac{radiance\ of\ target}{radiance\ of\ reference\ panel} k \tag{5-1}$$

where

ρ	is the reflectance
radiance of target	is the radiance leaving the target
radiance of the reference panel	is the radiance leaving the reference panel
k	panel correction factor

The constant k, which is the reference panel correction factor, is a ratio of solar irradiance to panel radiance and should ideally be near 1. It is assumed that the reference panel is a Lambertian reflector and that it would have the same correction constant regardless of variations in zenith or azimuth angles of the incident radiation (Jackson et al., 1992).

Field spectroradiometers are used to make direct material identifications in the field. Since the 1980s, there has been an increase in field-portable spectroradiometers due to improvements in instrument and detector design (Milton et al., 2006). Due to the high cost

of field spectroradiometers, most measurements are ‘single-beam’, where the same instrument is used to measure the spectral radiance of the target and the reference panel (Milton et al., 2006). However, the main limitation of single-beam measurements is that, due to the time lag between scans, illumination conditions are not the same for both the reference panel and the target surface. ‘Dual-beam’ methodologies overcome this limitation, since they use two well-matched sensors to measure the target and the panel simultaneously (Milton et al., 2006). Rollin et al. (1998) recommends the dual beam method as the most efficient means of collecting reflectance data, since it allows simultaneous sampling of both the target and the reference panel, thus eliminating errors due to irradiance temporal variations. However, the high cost of spectroradiometers makes this option difficult.

In order to minimize the amount of scattered light, measurements with field spectroradiometers are often handheld, usually with the sensor head mounted on a pole or yoke to keep it away from the operator's body (Kimes et al., 1983). As well, field spectroradiometers require a wide spectral range to meet the extremes of peak solar radiation reflected from very bright surfaces such as white reference panels and the very low values of radiance typical of dark surfaces such as water, or organic soils in regions of the spectrum where the atmosphere absorbs most of the incident radiation (Milton et al., 2006).

Field spectroscopy is used in remote sensing in the areas of calibration, prediction, modelling and measurement:

Calibration: field spectroscopy can be used to quantify the spectral behaviour of ground targets and monitor their suitability as targets over time. For calibration to be optimal, it is recommended that inter-calibration of data from different platforms or the calibration of data from the same sensor at different times be used (Milton, 1987; McCloy, 2005).

Prediction: field spectroscopy can be used to identify the optimum bands to be used and the ideal time of year for a particular task (Milton, 1987; McCloy, 2005). Field spectroscopy is useful for understanding the reflectance values and interaction mechanisms of surface features and assists in the development of suitable remote sensing sensors for specific application (McCloy, 2005).

Modelling: field spectroscopy is useful in the development and assessment of models for determining the spectral characteristics of surface features (Milton, 1987; McCloy, 1995; Milton et al., 1995).

Measurement: spectroradiometers are used to measure the spectral values of surface targets. These instruments are often used for studies that require collection of field data of surface targets that require precise image analysis and investigation. According to Milton et al. (1995), the development of modern, portable spectroradiometers allows the efficient use of field spectroscopy in remote sensing research, due to their highly developed data acquisition speed, spectral resolution and processing, as well as data storage.

5.2 Field Spectroradiometric measurements

As discussed in Chapter 4, section 4.2.5, the SVC HR-1024 spectroradiometer manufactured by Spectra Vista Corporation (http://www.spectravista.com) was used to take measurements.

Figure 5-1 Field spectroradiometric measurement using a white spectral panel at the Compacted Sand target

5.2.1 Field measurement of reflectance

There are two methods that can be used to determine reflectance in the field, the direct and the reference method. The direct method calculates both incident and reflected radiation are calculated directly from a pair of observations. In the reflectance method, the reflectance factor of the target is defined by the measurement of the target and a reference panel (Milton, 1987; McCloy, 1995). In this thesis, the reference panel method was used (see Figure 5.1). The SVC HR 1024 spectroradiometer was used to acquire measurements on the target and on the control panel. The reflectance of the target was obtained by applying the ratio of the reflected radiance from the target to the reflected radiance from the Spectralon panel and by taking into account the control panel correction.

Milton (1987) and McCloy (2005) provided general guidelines for measuring reflectance spectra in order to minimize error through consistent procedures for each measurement. The guidelines that were used in this study are briefly described below:

1) Field work took place during periods of high Sun, approximately two hours before and after solar noon, since variations in incident radiation occur as sunlight passes through longer stretches of atmosphere with increasing path lengths through dust and haze.

2) The spectroradiometer was approximately 1.2 meter above the upper surface of the target (see Figure 5-1 and Figure 5-3).

3) The sensor was consistently oriented and the researcher and all equipment were in the same position relative to the Sun. This is significant, as Daughtry et al. (1982) found that the height above the target may make a difference in the reflectance recorded by the spectroradiometer.

4) A consistent viewing geometry relative to the solar azimuth angle was maintained to assure that spectral samples were taken from the same portion of the target radiance hemisphere with each measurement. This was done by having the researcher stands toward the Sun at every measurement site while measuring both the reference panel and the target, so that his shadow was not cast on the reference panel or on the target (see Figure 5-1). Consistency in distance of the sensor from the target was maintained as part of the viewing geometry.

5) The field equipment and the people involved were positioned in such a way as to avoid shadows over the target area since reflections from nearby objects are additional sources of incident radiation (see Figure 5-1).

6) The standard panel was larger than the field of view of the spectroradiometer. Any shading of the panel from the instrument was avoided. This condition was required to establish an appropriate distance from the sensor to either the panel or the target (see Figure 5-1 and Figure 5-3).

7) Multiple measurements were taken to ensure reliable reflectance spectra and the average value of the measurements were used.

8) Since the reflectance values of the standard panel at various wavelengths are known and do not change during the course of measurements, the reflectance panel was cleaned and changed periodically so that panel reflectance values did not change due to dirt or moisture during measurement.

9) Measurements were made at a time when direct solar flux was the incident radiation, in a perfectly clear sky with no haze, because direct solar irradiance is the main source of energy incident on the target. This assumption can never be fully met because skylight is always present and as atmospheric haze increases, the proportion of scattered skylight increases.

10) Irradiance is constant while measuring both the reference panel and the target. This was done to minimize small differences in solar irradiance that can occur as a result of thin cirrus clouds that are not visible to the eye or as a result of dust movement through the atmosphere. The time required for the instrument to take a measurement was very short and the researcher redirected the spectroradiometer quickly from reference panel to target.

Although Cyprus has excellent weather conditions, a perfectly clear sky is not always present, so compromises were sometimes made. When there are many small cumulus clouds moving across the sky, the magnitude and frequency of variations in incident radiation is greatest, which increases the potential for a difference in illumination between measurements of the reference panel and the target; therefore, time between measurements was minimized. An overcast sky offers different challenges, as there are great variations in the thickness of the clouds and variations in brightness. As well, the incident light under an overcast sky is entirely scattered light, which has a different spectral characteristic than

direct sunlight. Therefore, measurements taken in overcast conditions have high variability and may not compare with measurements taken at any other time. Measurements were avoided if the sky was overcast.

Single beam measurements were taken, where the spectroradiometer was used to take measurements of the surface targets and the reference panel. The time delay between the target and panel measurements was kept as short as possible, since large temporal variations can occur due to the complexity and variability of the irradiation environment (McCloy, 2005; Milton et al., 1995).

As many variables affect spectral responses, notes and photos were taken for reference. The spectroradiometer was programmed to time-stamp each measurement for reference and identification. A log-sheet (see Appendix 3) was completed every time measurements were taken which include the following:

- name of project and site location.
- date and time.
- type of target measured.
- name of researcher and others in the field.
- environmental information regarding terrain, sky, wind, and any other features that may affect irradiance.
- cloud cover.
- reference scan used (new scan or previous scan).
- details of geometry including solar zenith angle, solar azimuth angle, instrument azimuth, zenith and distance and size of field of view.

5.2.2 Location information

Location data provides useful information about the geographical characteristics of the sampling area and enables field measurements to be matched with the satellite imagery of the same data. Global positioning system (GPS) technology provides a convenient and inexpensive way to find location information. The GPS (see Figure 4-13) was used to establish latitude, longitude and altitude of the pseudo-invariant targets.

5.2.3 Reporting the data

A log-sheet was used to report the sequence and any information regarding the acquisition of ground measurements, including information about the site, data, operator, what type of optic is used, reference panel, time of acquisition, reference and target numbering columns, filename, sky conditions and filename after processing. As previously mentioned, an example of the log-sheet used during the study is presented in Appendix 3.

5.3 Steps for spectroradiometric measurements

Specific steps were followed when taking in-situ measurements using the HR 1024 spectroradiometer. When initially turned on, the instrument disables its membrane switches and displays the instrument's model number on the top LCD row. During this initial power-on period, which is less than a minute, the spectroradiometer is waiting for the thermal-electric coolers to reach operating temperature before data collection can begin. When complete, the LCD message "REF x.xx" is displayed. The spectroradiometer was turned on approximately 15 minutes prior to first use in the same environment where scanning took place, since this allowed the detector temperatures and other electronics to stabilize before taking spectral measurements and reduces errors caused by differential warming.

The spectroradiometer was set up with its black external heat sink fins oriented vertically and the heat sink was oriented away from the Sun to maximize internal heat dissipation. To align the instrument to the target being measures, a sighting laser was used. The spectroradiometer was positioned in such a way so the target completely fills the field of view of the spectroradiometer (Figure 5-2). The sighting laser was activated by pressing the laser scan switch on the top of the instrument.

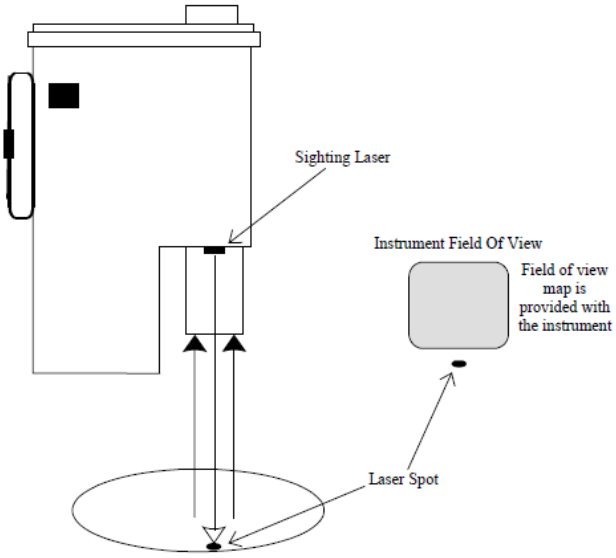

Figure 5-2 HR-1024 IFOV alignment

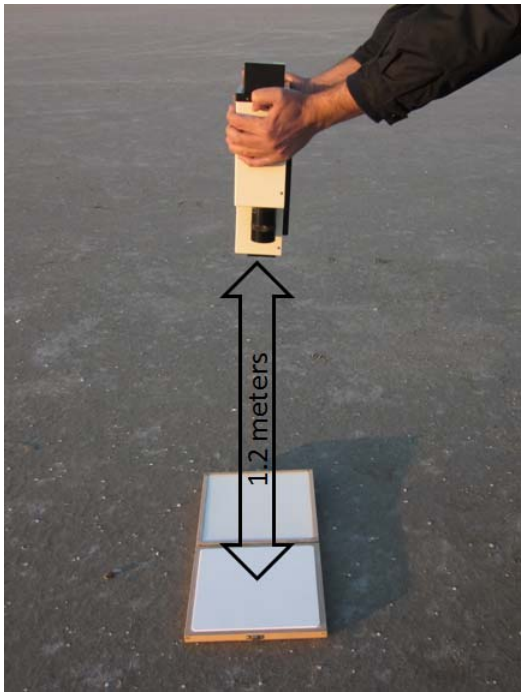

Figure 5-3 IFOV alignment and distance

A dark measurement was automatically taken by the spectroradiometer (through Autodark Mode) prior to taking reference or target measurements. The AutoDark Mode ensured that the latest dark values were subtracted on every scan and the dark measurement was subtracted from the Reference and Target measurements. A reflectance measurement takes the scan of a reference panel and calculates the ratio of the target scan to that reference. A new reference measurement was always taken at the beginning of a new set of scans, when

lighting conditions have changed, and if the spectroradiometer had been idle for an extended period or has been turned off.

Figure 5-4 illustrates the spectroradiometer panel. In taking reference measurements with a Spectralon panel, the following steps were taken:

1. Check that the power was enabled through the illuminated LED Power Indicator.
2. Press the Menu membrane switch until the LSCN menu item appeared; then the Edit membrane switch is pressed so that ON appeared.

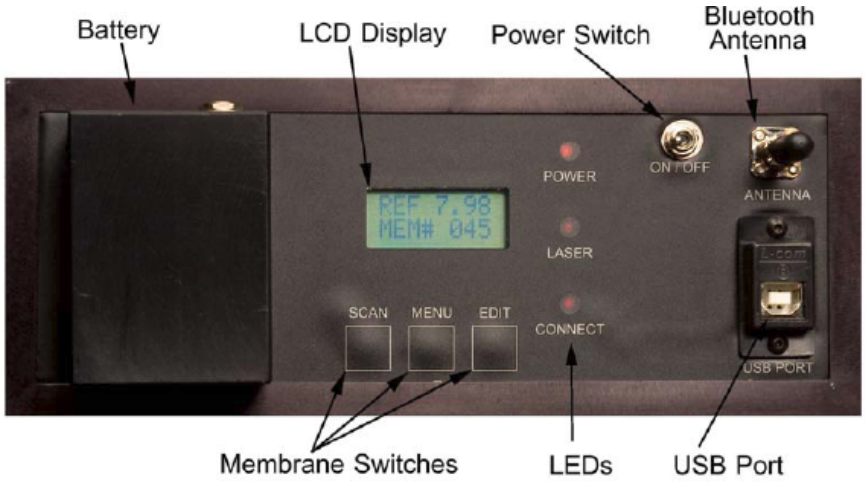

Figure 5-4 Spectroradiometer panel

3. The user pressed the Scan membrane switch until the REF x.xx scan message illuminates on the LCD (x.xx indicates battery voltage). The user checked to see if battery were adequately charged.
4. The Spectralon reference panel was used at the point of measurement and the user ensured that the panel completely filled the field of view of the spectroradiometer. This reference measurement was associated with all succeeding measurements until a new reference measurement was established.
5. The user then would press and hold the Laser Scan button to activate the sighting laser and verify the placement of the reference plate relative to the laser spot as required to fill the field of view.
6. The user would release the Laser Scan button to record the measurement and the LCD counter increments to display the next available memory location.

In order to take a target measurement, the following steps were followed:

1. Check that the LED Power Indicator was illuminated indicating that the power was enabled.

2. Press the Menu membrane switch until the LSCN menu item appeared and then press the Edit membrane switch so that ON appeared.
3. Press the Scan membrane switch until the TAR xxx scan message appeared on the LCD (x.xx indicates battery voltage). At this point, the user would check to see if the battery was properly charged.
4. Place the spectroradiometer over the target, making sure to completely fill the field-of-view of the instrument.
5. Press and hold the Laser Scan button to activate the sighting laser and verify the placement of the target to be measured relative to the laser spot as required to fill the field of view.
6. Release the Laser Scan button to record the measurement and the LCD counter increments to display the next available memory location. Additional target measurements are made by pressing and releasing the Laser Scan switch.

Upon returning to the laboratory, the spectroradiometer data were downloaded through the SVC software. To view and analyze the data acquired by the HR-1024 spectroradiometer, the data was downloaded from the memory of the instrument to the memory of a computer running the Windows PC operating system. The PC Data Acquisition program developed by Spectra Vista Corporation was used to download all data. Upon launching the SVC software for the HR 1024 spectroradiometer, the researcher opened a new directory for the measurements taken. In setting up the file, the optic file was set to Unity function, to save data as raw digital numbers (DN). As well, the averaging function was selected, as increasing the averaging of measurements increased the signal to noise ratio. Data was provided in the SIG file spectral data format and all measurements were provided as four columns of data; Column 1 refers to wavelengths measured in nanometers, Column 2 refers to Reference Values, Column 3 refers to Target Values and Column 4 refers to Reflectance measured in percentage. It is important to note that reference and target values' units depended on which calibration table or fore-optic was in use (either Radiance $W/cm^2/nm/sr \times 10^{-10}$, Irradiance $W/cm^2/nm \times 10^{-10}$ or RAW DN counts)

The Spectralon panel reference measurement was presented in a two-column text file known as the White Place Reflectance Data File. The first column contained wavelength values, in nanometers. This file included all wavelengths in the instrument's spectral range. The second column contained reflectance values that corresponded to the white plate's true reflectance at each wavelength.

5.4 Summary

This chapter provided a detailed explanation of field spectroscopy and the use of the spectroradiometer, including how spectroscopy was conducted in this thesis. The following chapter will provide detailed information regarding the methodology utilized in the thesis.

Chapter 6 Overall Methodology

This chapter presents an outline of the research methodology used for this thesis. Research indicates that, among all other atmospheric correction methods, the Darkest Pixel (DP) and the Empirical Line method using Pseudo Invariant Target (PITs) methods focused on in this thesis are considered to be the two most effective methods for image-based atmospheric correction (Wilson and Milton, 2010; Hadjimitsis et al., 2009; Mahiny and Turner, 2007; Wu et al., 2005; Ben-dor et al., 2004; Huang et al., 2002; Clark et al., 2002; Cheng and Lei, 2001; Liang et al., 2001).

The overall methodology that has been used in this thesis is based on the following components:

- First, to improve the existing Empirical line atmospheric correction method using five pseudo-invariant targets (PITs) with varying spectral characteristics.
- Second, to apply the Darkest Pixel (DP) and the improved PITs atmospheric correction methods to eleven Landsat 5 TM and Landsat 7 ETM+ satellite images and apply the fast atmospheric correction algorithm developed in this thesis in order to retrieve AOT values from the satellite images and map the AOT distribution on GIS using GIS analysis methods.
- Finally, an accuracy assessment was performed for both atmospheric correction methods using field spectroradiometers and sun photometer measurements to validate the results.

6.1 Overall Methodology

The thesis methodology was carried out in the following steps:

1. Selection of five types of commonly located surfaces to be used as the pseudo-invariant targets based on the following criteria: a) suitable size, b) uniformity, c) colour, d) proximity distance and e) spectral characteristics.

2. Field campaign using spectroradiometer to measure the reflectance of five targets from October 2009 to May 2011. Sun photometer measurements were taken with the Microtops II hand-held sun photometer during satellite overpass in order to retrieve AOT values.

3. The targets were evaluated to determine that they were non-variant. The changes in the reflectance values of the targets as a function of wet and dry conditions was also examined.

4. Preprocessing of the satellite images that corresponded to the field campaign was conducted. To allow comparisons of at-satellite and in-situ measurements, the in-situ reflectance values of the pseudo-invariant targets were filtered by relative spectral response factors of the satellite sensors. Geometric and radiometric correction was conducted, followed by atmospheric correction

5. The DP and PITs atmospheric correction methods, considered to be the two most effective atmospheric correction methods, were applied to eleven Landsat 5 TM and Landsat 7 ETM+ satellite images. The spectroradiometric measurements were used to develop the improved empirical line method using pseudo-invariant targets atmospheric correction method (further discussed in Chapter 8).

6. The fast AOT retrieval algorithm developed in this thesis was used to retrieve the AOT levels from the satellite images by using the radiance and reflectance values from the corrected satellite image (further discussed in Chapter 9). GIS analysis was performed using the RT equation in order to map AOT levels based on the application of the PITs and DP method of atmospheric correction (further discussed in Chapter 9).

7. An accuracy assessment was performed for the two atmospheric correction methods (DP and PITs method) based on the acquired field spectroradiometer and sun-photometer (AOT) measurements (further discussed in Chapter 10).

The overall methodology is presented in Figure 6.1.

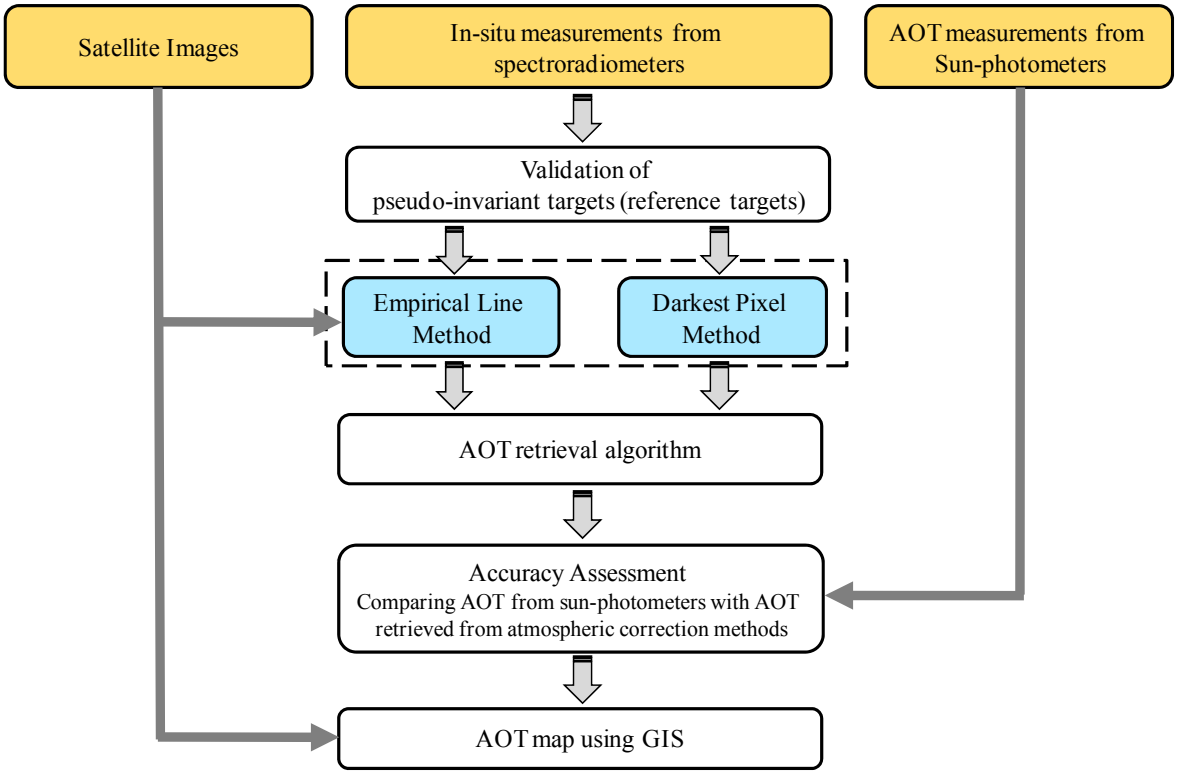

Figure 6-1 Detailed Overall Methodology

6.2 Field measurements

The field campaign began in October 2009 and lasted until May 2011. During the field campaign, the Spectravista SVC HR 1024 field spectroradiometer with a single sensor head equipped with a 4° lens was used to measure the reflectance values of the five targets. Measurements were collected between 11:00 and 13:00 local time under conditions of clear skies or scattered cumulus clouds. The measurement campaigns were carried out at the Limassol Port and Akrotiri Bay. The measurements were taken with the SVC HR-1024 spectroradiometer and the white Spectralon reference panel by using the operator-assisted technique to take measurements. The spectroradiometer was held 1.2 meters above the target and the reference panel. The sampling area of each reference target was larger than 100 × 100 m. The area was divided into a grid and enough measurements were randomly taken approximately every 5 to 10 meters within the grid in order to get a representative sample of the grid area, as indicated in Figure 6-2 and Figure 6-3.

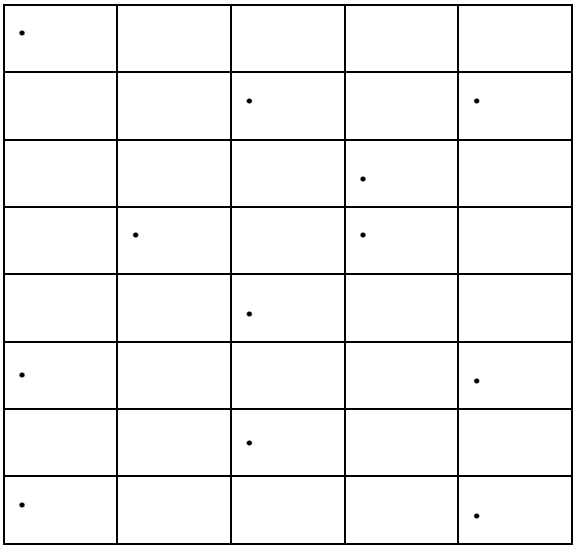

Figure 6-2 Sample grid patterns used in in-situ measurements

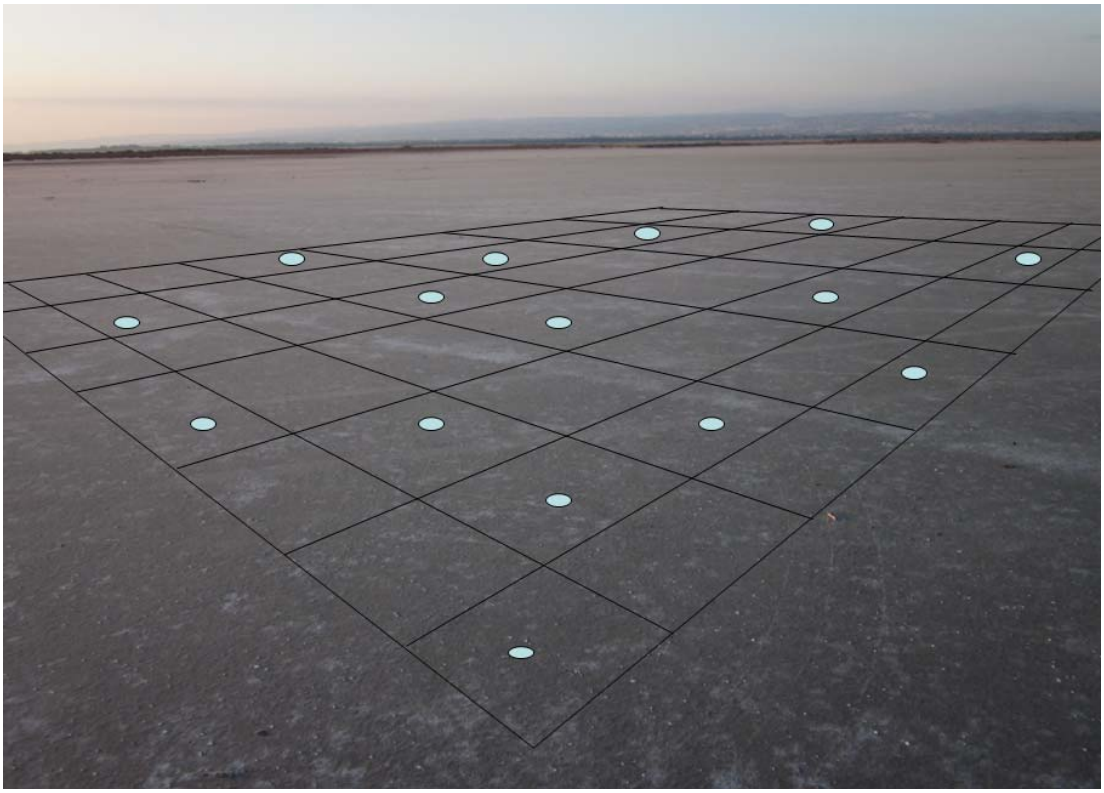

Figure 6-3 Target area with grid pattern overlay

6.2.1 Identification and spectral characteristics of pseudo-invariant targets

In order to select the appropriate targets that were used as non-variant, several possible reference targets were chosen. The targets were chosen as they met the criteria for reference targets, which include suitable size (at least 100 × 100 m), surface uniformity, surface colour, proximity distance, and spectral characteristics, as described in Chapter 4.

Through visual examination of the satellite image, several potential targets were chosen that were suitable surfaces near the area of interest (Limassol port and Akrotiri Bay). Of these potential targets, several measurements were taken with a spectroradiometer and five spectrally diverse targets were selected whose reflectance values did not change significantly during the evaluation period. Over 2,000 measurements were taken on 46 different measurement dates between October 2009 to May 2011 in order to evaluate their non-variability. For each target, measurements were first taken of the reference panel and then 4-10 measurements were taken across the target surface. To determine non-variance, precipitation conditions of the target surface were also noted to determine if there was any effect on the reflectance value. In the laboratory, these measurements were downloaded onto the computer. The SVC software stored the measurements into signature files (sig. files), which included measurement information, date, time, number of measurements, wavelength, radiance, irradiance, and reflectance.

The average reflectance values found from each measurement campaign for each target were calculated by band. To determine that the reflectance values of the reference target did not change significantly over time, the spectral signatures of all the measurements were displayed in a graph form, as indicated in Figure 6-4, which shows the spectral signature of the Black asphalt material from January 2010 to May 2011.

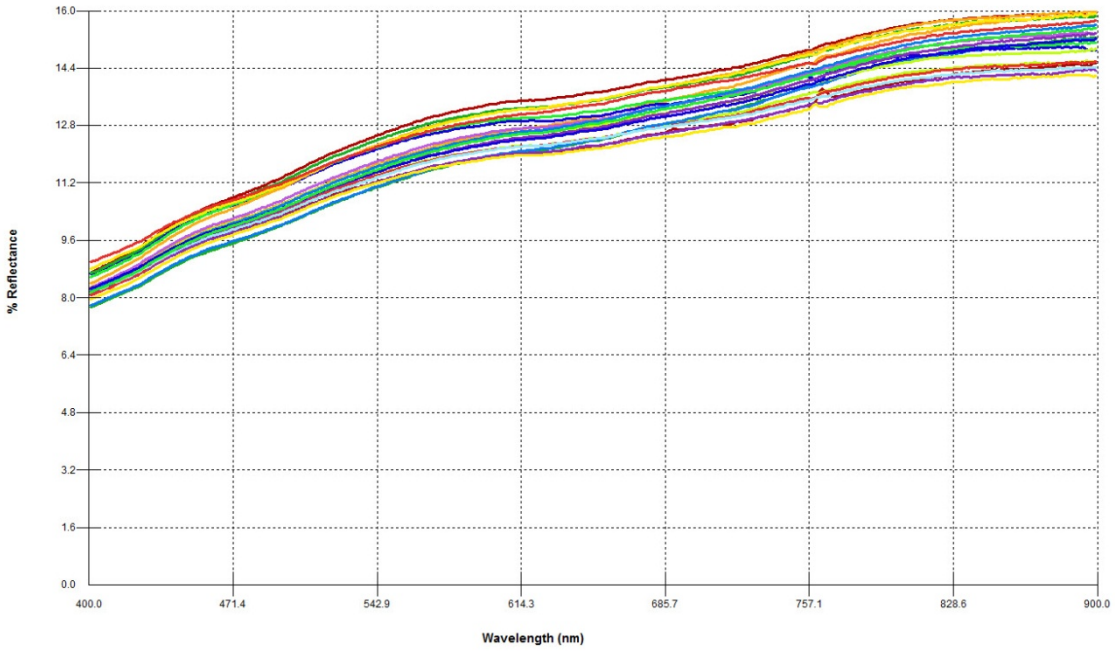

Figure 6-4 Black Asphalt Spectral Signatures from 46 measurements taken from January to May 2011, all measurements, including wet and dry conditions

In Appendix 1, the field campaign measurements are presented for each pseudo-invariant target. The spectral signatures of the five pseudo-invariant targets are examined in detail in Chapter 7.

6.2.2 AOT measurements

AOT measurements were taken at the target sites during satellite overpass using the Microtops II hand-held sun photometer. AOT measurements were also collected from the Cimel stationary sun photometer, located at the Cyprus University of Technology, which is in close proximity to the reference targets, as described in Chapter 4. The Microtops II sun photometer measurements were downloaded using the Solar Light software. The Cimel sun photometer readings were downloaded from the AERONET website (http://aeronet.gsfc.nasa.gov). However, there are no Cimel sun photometer readings prior to April 13, 2010, as the sun photometer was not yet operational at the university. The sun photometer measurements for the Cimel and Microtops sun photometer are presented in Appendix 2.

6.3 Satellite imagery

Eleven Landsat images were used in this thesis, which were the available satellite images that corresponded to the field campaign. Four of the satellite images were Landsat 5 TM images and seven of the satellite images were Landsat 7 ETM+. Geometric correction was applied to the available satellite images by using ground control points and geo-referencing as explained in section 6.3.1. Following, radiometric correction was applied to the available satellite images. All raw digital numbers (DN) were converted to units of radiance and reflectance using standard calibration equations so as to be comparable with the ground measurements. The methodology for the satellite images consisted of downloaded the compacted file containing the satellite image of all bands and the header file from the Landsat website at http://landsat.usgs.gov. The images for bands 1, 2, 3 and 4 were combined using the layer stack command in order to get one image with four layer bands. Following, the image digital numbers (DN) (pixel values) were converted to radiance and the radiance pixel value was converted to reflectance, creating two separate images. The satellite image with the reflectance values was used for both the darkest pixel and empirical line atmosphere correction methods. In the empirical line method, a linear regression of the in-situ reflectance values and the reflectance values retrieved from the satellite image are used to correct the satellite image for each band, as explained in Chapter

8. In the darkest pixel method, the average reflectance value of the black asphalt target was used as the darkest pixel in the image in order to adjust the image, as explained in Chapter 8. Figure 6-5 indicates the procedure followed with the satellite imagery used in this thesis.

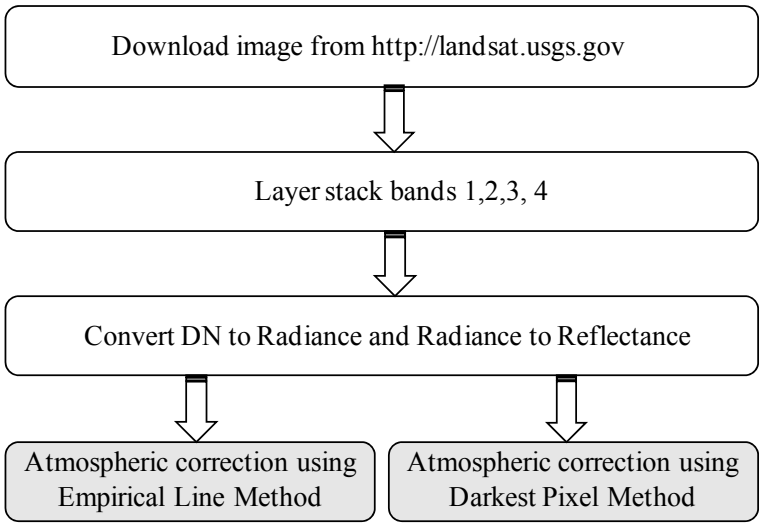

Figure 6-5 Procedure for satellite imagery

6.3.1 RSR

In order to compare in-situ ground reflectance values with satellite image reflectance values, the relative spectral response (RSR) of the sensor is required, which is also called "filtering" (Hadjimitsis et al., 2009, Tassan, 1992; Wilson, 1988). The spectral resolution of the Landsat 5 TM and Landsat 7 ETM+ is indicated by the RSR of the spectral bands. RSR describes the spectral integration of the received radiance through measurements the intensity of the wavelengths of light (Schott, 1997; Schowengerdt, 1997; USGS, 2011). The overall RS for a TM/ETM+ band is defined by the spectral components that contribute to the spectral response, which are the filter detectors and optical surfaces (Markham and Barker, 1985). In order to match a spectral measurement with a Landsat TM band, it is necessary to use the Landsat TM/ETM+ RSR functions and average within the limits of every TM/ETM+ band to obtain the equivalent in-band reflectance values. The surface reflectance values were calculated to be equivalent to the Landsat TM/ETM+ bands 1, 2, 3 and 4. To filter the data through the relative spectral response (RSR) values of Landsat TM/ETM+, the HR1024 reflectance values were interpolated to obtain the reflectance values at the incremental wavelength of the RSR (at 450, 451,451 nm etc.). This was done since the HR1024 reflectance values were given at a different incremental wavelength scale (e.g. 449.81, 451.48, 453.15 nm). Then, the HR1024 experimental data were filtered through the RSR functions and averaged within the limits of the first four TM/ETM+ bands, to yield the in-band reflectance values. The HR 1024 data was filtered by

multiplying the interpolated real spectrum reflectance values by the RSR filter function. The filter was calculated by multiplying the RSR filter function by 100. After using the relative response filters, the HR1024 real spectrum was converted to satellite in-band reflectance to make the reflectance values comparable to the reflectance values of satellite images. This was done for all the dates of acquisition of reflectance, using the HR1024 and compared with the respective satellite images of Landsat TM/ETM+. An example of the procedure can be found in Appendix 1.

By overlaying the spectral curves from different spectra (features), it can be determined which bands of the selected sensor(s) will work for the application and then the RSR according to every nm is determined (USGS, 2011). Following, the ground reflectance percentage is multiplied by the RSR (as shown in Figure 6-6) and the average measurement of in-band reflectance is determined. The Spectral Characteristics Viewer, which can be accessed at http://landsat.usgs.gov/tools_spectralViewer.php, is an interactive tool that allows the user to visualize how the bands, or channels, of different satellite sensors measure the intensity of the many wavelengths (colors) of light and also indicates how changes in irradiative energy reflected by surface materials can be used to identify features of interest.

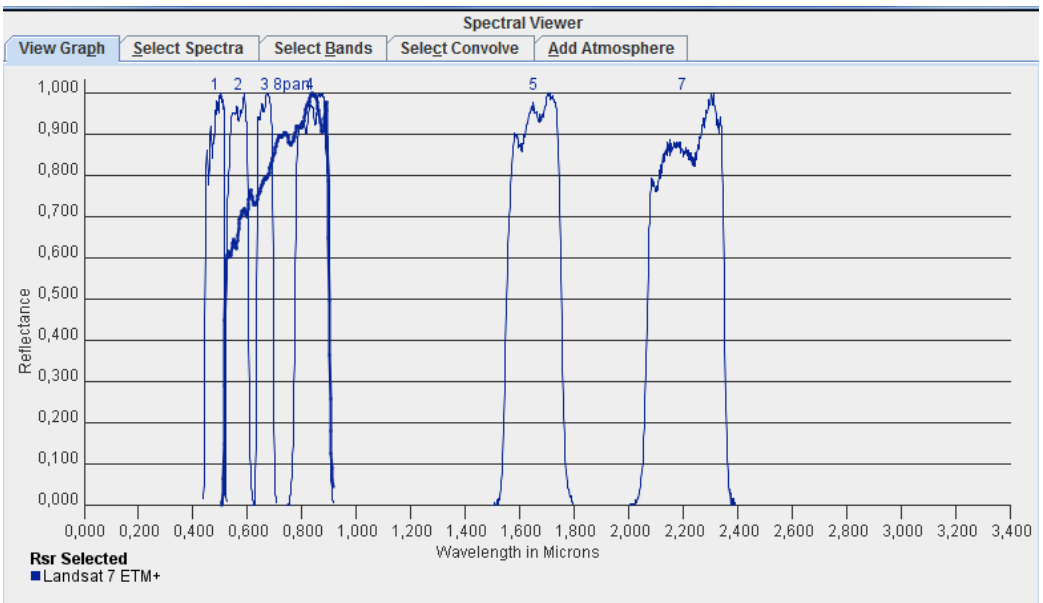

Figure 6-6 Spectral Characteristics Viewer for Landsat 7 ETM+

6.3.2 Geo-referencing and registration

To correspond with the GIS data, geo-referencing is necessary. Geo-referencing and registration of an image to a ground co-ordinate system is an essential step in the pre-

processing of raw data, since the researcher can make comparisons of the characteristics at the same position at every image (Lillesand et al., 2004; Schowengardt, 2007). In this study, geometric registration was carried out using standard techniques with ground control points (GCP's) and a first order polynomial equation (ERDAS, 2011). Well-defined features such as road intersections and geographical features in the area were chosen as GCP's. Following, an output file was created. If the grid of pixels in the source image did not match the reference image, the pixels were re-sampled using the nearest neighbor resampling method so that new data file values for the output file were calculated. A WGS84 coordinate system was used to geo-reference all the satellite images in order to geo-reference all the GIS data used in GIS analysis.

6.3.3 Sensor calibration and radiometric calibration

A satellite image consists of a series of spectral bands, with each pixel having a digital number (DN). The pixel DN is a linearly transformed representation of at-sensor radiance for a specific area of the Earth's surface. Digital numbers (*DN*) were converted to at-satellite radiance (L_{ts}) in order to transform the data from each band to the same physical units for the available Landsat TM/ETM+ images. This allows comparisons to be made since multi-temporal images were used in this study. Satellite sensors measure the total radiance reflected from a particular ground target and store this information as a digital number (DN) (Hill and Sturm, 1991). These DNs need to be converted to reflectance values, which is a two step process. First, the DNs need to be converted to radiance values using the bias and gain values that are specific to the individual scenes (Figure 6-7). Following, the radiance values need to be converted to top of atmosphere (ToA) reflectance.

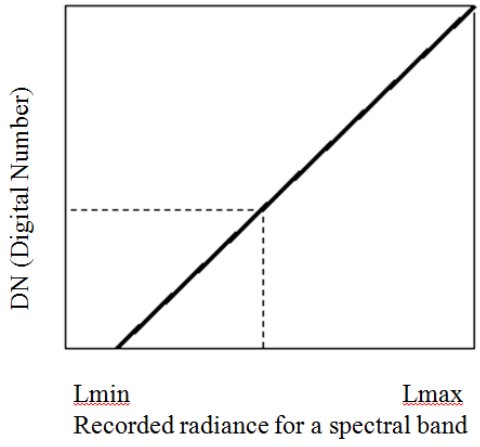

Figure 6-7 Conversion of DN to radiance

There are two formulas that can be used to convert DN to radiance, which are presented in equations 6-1 and 6-2. The method used depends on the scene calibration data available on the header file. For the four bands of Landsat 5 TM and Landsat 7 ETM+ used in this thesis, at-satellite radiances (L_{ts}) can be calculated using equation 6-1 (Schowengerdt, 2007; Chander et al., 2007; Chander et al., 2009; Chander et al., 2010; Roder et al., 2005; Hill and Aifadopoulou, 1990; Maracci and Aifadopoulou, 1990). To estimate the total within-band radiance, the values obtained from equation 6-1 must be multiplied by the width of the spectral band under consideration. To solve for the at-satellite radiance (L_{ts}) for Landsat satellite images that contain Gain and Bias values in the header file, equation 6-1 can be used, as described in the Landsat 7 Handbook (2011):

$$L_{ts} = gain * DN + offset \tag{6-1}$$

where

L_{ts}	is the at-satellite radiance in W/(m^2 μm sr)
offset	is calibration offset in W/(m^2 μm sr)
gain	is the calibration gain in W/(m^2 μm sr)
DN	is the measured digital number at the satellite sensor

The retrieval of these radiances involved the use of calibration gain and offset coefficients. For each spectral band, the gain and offset of the Landsat TM/ETM+ satellite sensor were obtained from the header file of the image.

The Landsat 7 handbook also includes a second formula that is used to convert DN to radiance, which is the spectral radiance scaling method for each band at digital numbers 0, as calculated in equation 6-2, which was the equation used in this thesis. The radiance values for the satellite images used can be found in appendix 1.

$$L_\lambda = \frac{LMAX_\lambda - LMIN_\lambda}{QCALMAX - QCALMIN}(QCAL - QCALMIN) + LMIN_\lambda \tag{6-2}$$

where

L_λ	is the cell value as radiance
QCAL	is the digital number
$LMIN_\lambda$	is the spectral radiance scales to QCALMIN
$LMAX_\lambda$	is the spectral radiance scales to QCALMAX
QCALMIN	is the minimum quantized calibrated pixel value
QCALMAX	is the maximum quantized calibrated pixel value, typically 255

After converting digital numbers (DN) to units of radiance, the next step is to convert radiance to at-satellite reflectance using equation 6-3 (Hill and Sturm, 1991; Turner and

Spencer, 1972; Landsat 7 Handbook). The at-reflectance values for the satellite images used can be found in Appendix 1.

$$\rho_{ts} = \frac{\pi L_{ts} d^2}{E_0 \cos(\theta_0)} \quad (6\text{-}3)$$

where

ρ_{ts} is the reflectance at the top of the atmosphere, sometimes termed the "at-satellite" or "apparent" reflectance
L_{ts} is the target radiance as measured at the sensor ("at-satellite" radiance)
E_0 is the solar irradiance at the top of the atmosphere,
θ_0 is the solar zenith angle
d is the correction coefficient accounting for variation in the Sun-to-Earth distance.

Each satellite image contains a calibration file, which provides the exact values of the solar irradiance at the top of the atmosphere. As well, the calibration file can be found at the following website: http://landsat.usgs.gov/science_L5_cpf.php. The correction coefficient accounting for the variation in the Sun-to-Earth distance can be found in Appendix 3. The most recent solar irradiance calculated from the last satellite calibration can be found in table 6-1 for Landsat 5 and table 6-2 for Landsat 7.

Band	Band edges	Band-width	Central Wave-length, λ_C (µm)	Solar irradiance (W/(m^{2}µm) for Landsat5 TM ($E0_\lambda$)	Solar irradiance (W/(m^2) for Landsat5 TM ($E0$)
1	0.452-0.518	0.066	0.485	1983	130.88
2	0.528-0.609	0.081	0.569	1796	145.48
3	0.626-0.693	0.067	0.660	1536	102.91
4	0.776-0.904	0.128	0.840	1031	131.97
5	1.567-1.784	0.217	1.676	220.0	47.74
7	2.097-2.349	0.252	2.223	83.44	21.03

Table 6-1 Landsat -5 TM spectral characteristics and solar irradiance at the top of the atmosphere (Chander et al., 2009)

Band	Band edges	Band-width	Central Wave-length, λ_C (µm)	Solar irradiance (W/(m^{2}µm) For Landsat7 ETM+ ($E0_\lambda$)	Solar irradiance (W/(m^2) for Landsat7 ETM+ ($E0$)
1	0.452-0.514	0.062	0.483	1997	123.81
2	0.519-0.601	0.082	0.560	1812	148.58
3	0.631-0.692	0.061	0.662	1533	93.51
4	0.772-0.898	0.126	0.835	1039	130.91
5	1.547-1.748	0.201	1.648	230.8	46.39
7	2.065-2.346	0.281	2.206	84.90	23.86

Table 6-2 Landsat -7 TM spectral characteristics and solar irradiance at the top of the atmosphere (Chander et al., 2009)

To convert at-satellite radiance into reflectance, a number of simplifying assumptions about the target, sensor and solar irradiance characteristics are made, which are listed below:

1) Firstly, Lambert's reflectance law was assumed to be valid for any point on the surface, that the reflecting surfaces were assumed to be perfectly diffuse, appearing equally bright from all viewing directions and incident energy is scattered more or less equally in all directions (Teillet, 1986; Campbell, 1996).

2) The target surface was assumed to be illuminated by the Sun with solar irradiance at the top of the atmosphere and the values found in the literature by several experiments were used (Neckel and Labs, 1984).

3) Nadir viewing (i.e. vertical observation) was assumed for Landsat 5 TM (considering the relatively small field of view of the Landsat 5 TM ± 7.5°).

An algorithm was created in the Model Maker program of the ERDAS Imagine 2011 software, which converted DN to radiance and then converted the radiance to reflectance (Figure 6-8).

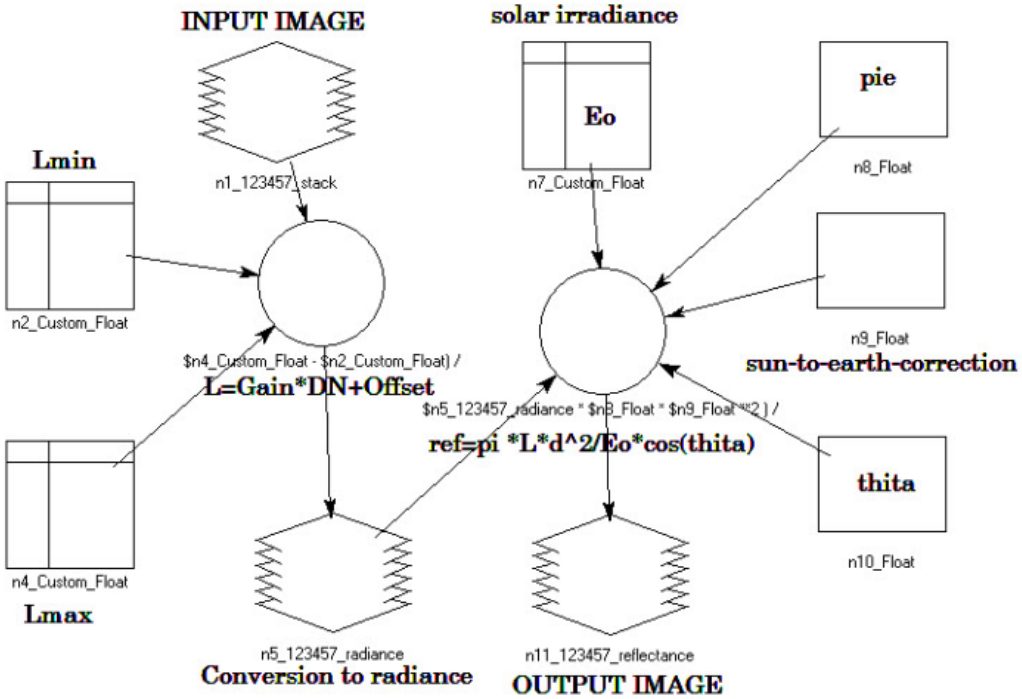

Figure 6-8 "DN to radiance to reflectance" model using ERDAS Imagine modeller

In the model, the user enters in the relevant variables, as applicable. The unknown variables include the solar irradiance, which can be found in Table 6-1 and 6-2, the Sun-to-Earth correction, which can be found in Appendix 3, and the Lmax, Lmin, and Sun elevation angle, all of which can be found in the metadata header file for each image (included with the satellite images downloaded from the Landsat website). The variables

indicated in Table 6-3 were entered into the modeller program:

Date	Landsat	SZA	Band	Lmax	Lmin	d	E_0
13/4/2010	L7	33.3382	Band 1	293.7	-6.2	0.99133	1997
			Band 2	300.9	-6.4		1812
			Band 3	234.4	-5.0		1513
			Band 4	241.1	-5.1		1039
29/4/2010	L7	28.6134	Band 1	191.6	-6.2	0.99556	1997
			Band 2	196.5	-6.4		1812
			Band 3	152.9	-5.0		1513
			Band 4	241.1	-5.1		1039
31/5/2010	L7	23.5249	Band 1	293.7	-6.2	1.01387	1997
			Band 2	300.9	-6.4		1812
			Band 3	234.4	-5.0		1513
			Band 4	241.1	-5.1		1039
16/6/2010	L7	23.2414	Band 1	191.6	-6.2	1.01586	1997
			Band 2	196.5	-6.4		1812
			Band 3	152.9	-5.0		1513
			Band 4	241.1	-5.1		1039
24/6/2010	L5	23.8451	Band 1	193	-1.52	1.01642	1983
			Band 2	365	-2.84		1796
			Band 3	264	-1.17		1536
			Band 4	221	-1.51		1031
10/7/2010	L5	25.0885	Band 1	193	-1.52	1.01664	1983
			Band 2	365	-2.84		1796
			Band 3	264	-1.17		1536
			Band 4	221	-1.51		1031
27/8/2010	L5	32.9704	Band 1	193	-1.52	1.01037	1983
			Band 2	365	-2.84		1796
			Band 3	264	-1.17		1536
			Band 4	221	-1.51		1031
28/9/2010	L5	41.8109	Band 1	193	-1.52	1.00205	1983
			Band 2	365	-2.84		1796
			Band 3	264	-1.17		1536
			Band 4	221	-1.51		1031
7/11/2010	L7	53.9897	Band 1	293.7	-6.2	0.99102	1997
			Band 2	300.9	-6.4		1812
			Band 3	234.4	-5.0		1513
			Band 4	157.4	-5.1		1039
9/12/2010	L7	60.799	Band 1	293.7	-6.2	0.98493	1997
			Band 2	300.9	-6.4		1812
			Band 3	234.4	-5.0		1513
			Band 4	157.4	-5.1		1039
2/5/2011	L7	27.6832	Band 1	293.7	-6.2	1.00781	1997
			Band 2	300.9	-6.4		1812
			Band 3	234.4	-5.0		1513
			Band 4	241.1	-5.1		1039

Table 6-3 Variables used for radiance and reflectance conversion

A model is used to convert the image to radiance and reflectance in order to produce two images, one with radiance values and one with reflectance values. The radiance values and reflectance values from the satellite image are both required in the AOT algorithm discussed in Chapter 9. An area of interest (AOI) of Limassol was created so that a consistent subset of Limassol was utilized. To minimize errors, the user used the ground control points and co-ordinates to identify the five targets. The minimum, maximum and average radiance and at-satellite reflectance values and reflectance values of each reference target were identified. These satellite reflectance values were used in the DP and the PITs method of atmospheric correction, as explained in Chapters 8.

6.4 Atmospheric correction methods

Atmospheric correction was conducted on eleven Landsat satellite images by using the improved empirical line (PITs) method and the darkest pixel method. For the empirical line method, the methodology indicated in Figure 6-9 and described in Chapter 8 was followed. The in-situ spectroradiometric measurements were taken of the five pseudo-invariant targets during satellite overpass. Following, Landsat 5 TM and Landsat 7 ETM+ satellite images were acquired from NASA at http://landsat.usgs.gov. A linear regression of in-situ reflectance to at-satellite reflectance values was conducted for each target and each band. The intercept value (c) was used to calculate the at-satellite reflectance value in order to atmospherically correct the satellite image. The reflectance values following atmospheric correction were then compared with the in-situ reflectance values.

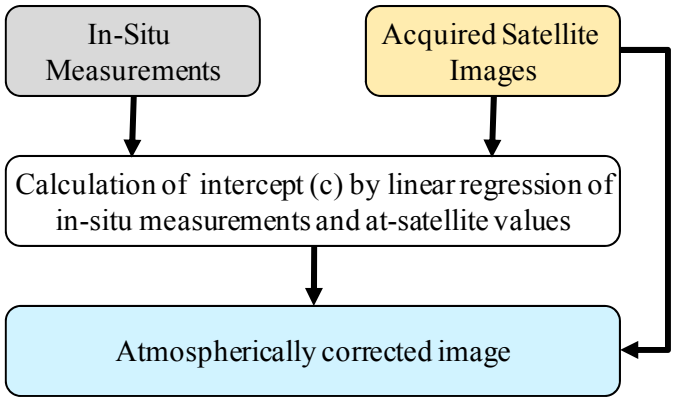

Figure 6-9 Methodology used in the empirical line method

For the darkest pixel method, the methodology described in Figure 6-10 and described in Chapter 8 was followed. Geometric correction was applied and the digital number of the image was converted to radiance and then to reflectance. The in-situ reflectance value for

the Black Asphalt target was used for the darkest pixel value and the satellite image was then corrected as described in Chapter 8. Following the atmospheric correction, the reflectance values derived from the PITs and darkest pixel method were compared with the in-situ ground reflectance measurements in the accuracy assessment, as described in Chapter 10.

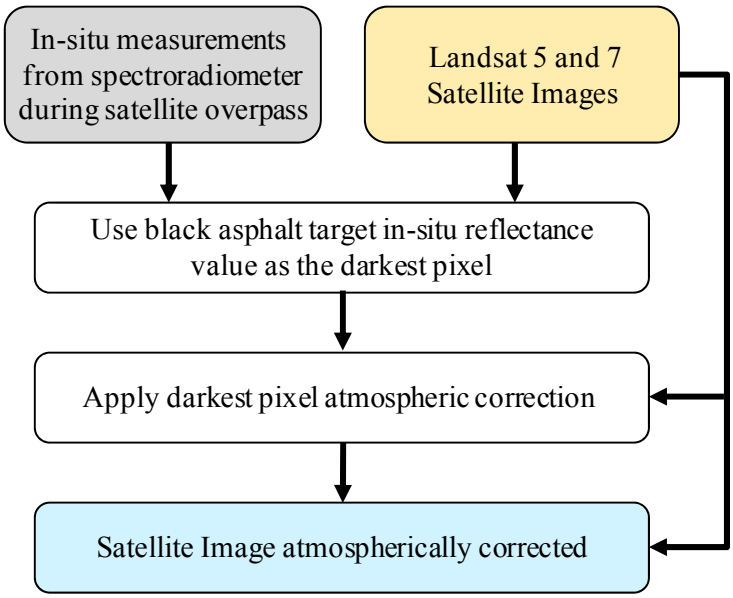

Figure 6-10 Darkest Pixel methodology

6.5 AOT Retrieval

The corrected satellite images and their corresponding at-satellite reflectance values were used for the AOT retrieval algorithm, which is discussed in detail in Chapter 9. The methodology is indicated in Figure 6-11. Specific parameters from the spectroradiometric measurements, sun photometer measurements satellite images and the reflectance values from the atmospherically corrected images were used to develop the fast atmospheric correction algorithm. Further, the AOT values retrieved using the algorithm presented in this thesis were compared with the in-situ sun-photometer measurements from the Microtops and Cimel Sun photometers, as indicated in Chapter 10. Following, GIS analysis and GIS maps were developed to assess AOT levels over Limassol, by using the AOT values derived directly from the Landsat 5 TM and Landsat 7 ETM+ satellite imagery, as described in Chapter 9.

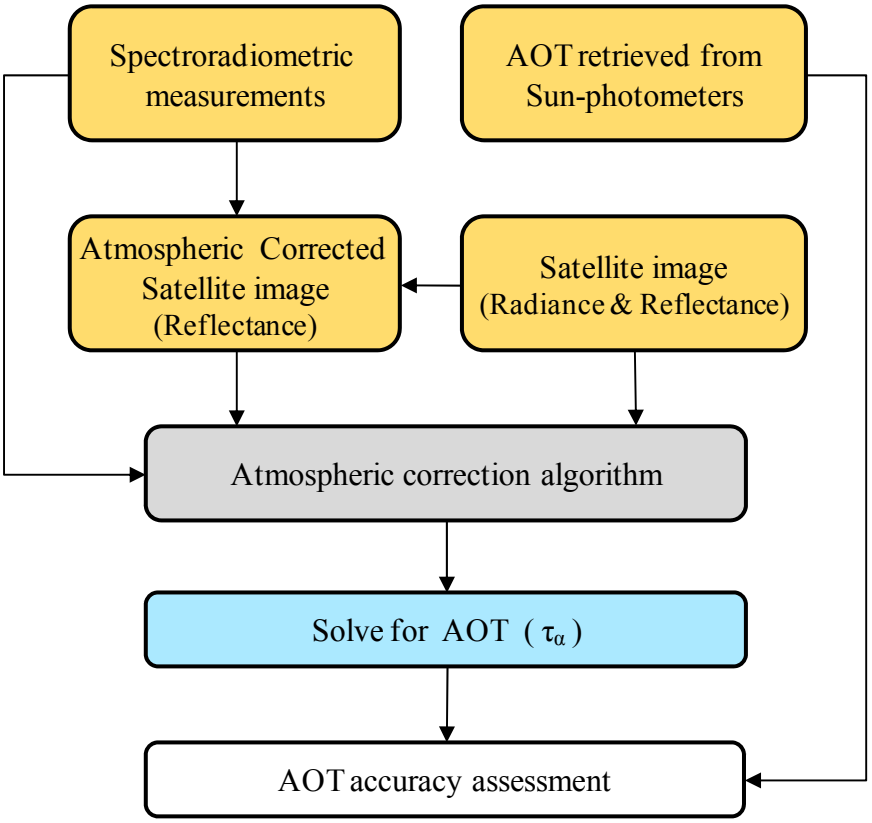

Figure 6-11 Methodology for AOT retrieval and accuracy assessment

6.6 GIS Analysis

The GIS analysis was conducted and GIS maps were developed to show the distribution of AOT over Limassol, by using the AOT values produced by the algorithm using the Landsat 5 TM and Landsat 7 ETM+ satellite imagery, as described in Chapter 9. The methodology used for the GIS analysis is described in Figure 6-12. MATLAB and ERDAS Image software was used in order to run the simplified algorithm model to calculate AOT values for every pixel in the satellite image. Since the algorithm is applicable only for dark pixels with near-Lambertian surfaces, the high reflectance values were subtracted from the image prior to running the model. The AOT values produced from the model were exported into ASCII format so that the values could be imported into ArcGIS to conduct the analysis. The image pixels were converted into points with AOT values in order to create an AOT dataset. Only AOT values between 0-4 were used for the final image to show the AOT distribution since AOT values cannot be negative or higher than 4 (Penner et al, 2010). Kriging interpolation was used to estimate the values for the "no data" cells to produce thematic maps which indicated the distribution of AOT over Limassol. The maps were overlaid with vector data from the Land and Surveys Department, which included information such as roads and municipal boundaries. In this

way the end-user was able to visualize the AOT distribution over Limassol or create queries using the GIS database.

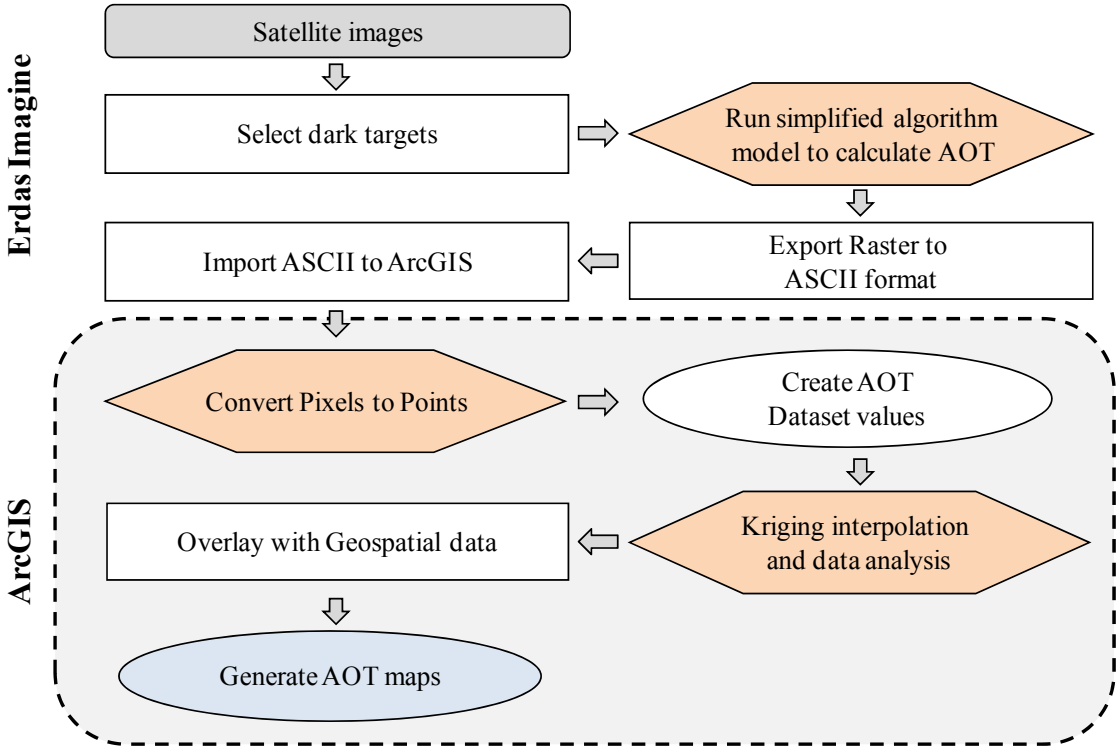

Figure 6-12 Methodology for GIS analysis

6.7 Accuracy Assessment

An accuracy assessment was also conducted to examine the effects of precipitation on the pseudo-invariant targets. The methodology used is featured in Figure 6-13 and discussed in detail in Chapter 7. The results of the accuracy assessment are presented in Chapter 10.

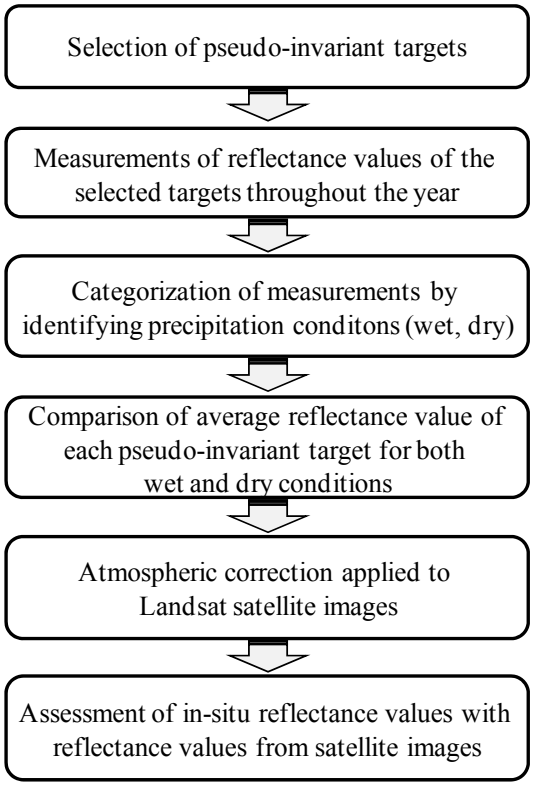

Figure 6-13 Methodology for assessment of precipitation effects

An accuracy assessment was conducted that assessed the accuracy of the AOT values calculated using the Empirical line an Darkest Pixel atmospheric correction method with the in-situ values. The methodology is presented in Figure 6-14 and the results of the assessment are presented in Chapter 10.

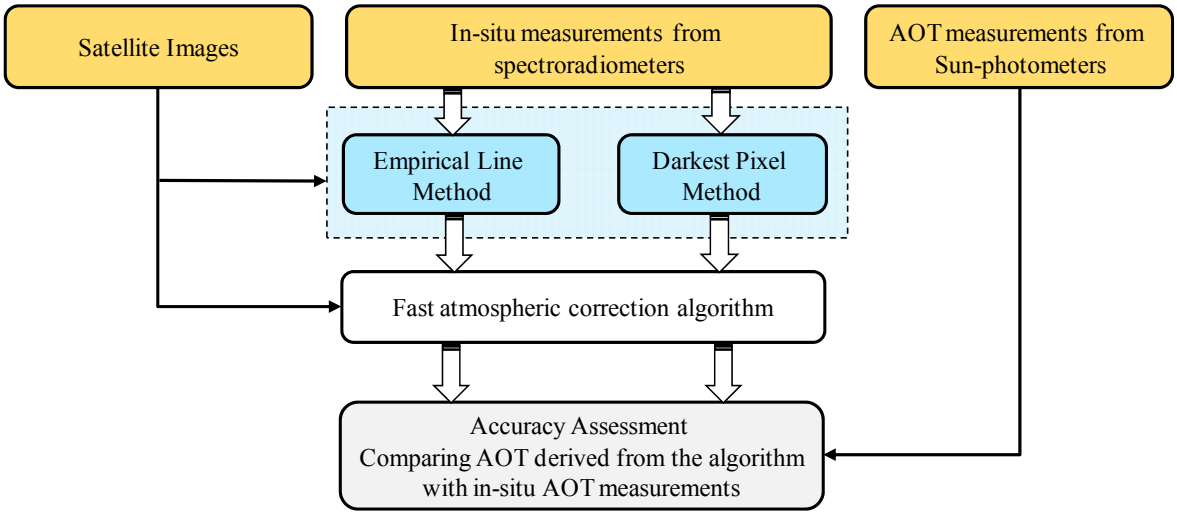

Figure 6-14 Accuracy assessment of AOT values

The final accuracy assessment compared the AOT values featured in the GIS maps, as calculated from the fast atmospheric correction algorithm with in-situ AOT values. The

methodology is presented in Figure 6-15, and the detailed methodology is presented in Chapter 9. The accuracy assessment and GIS maps can be found in Chapter 10.

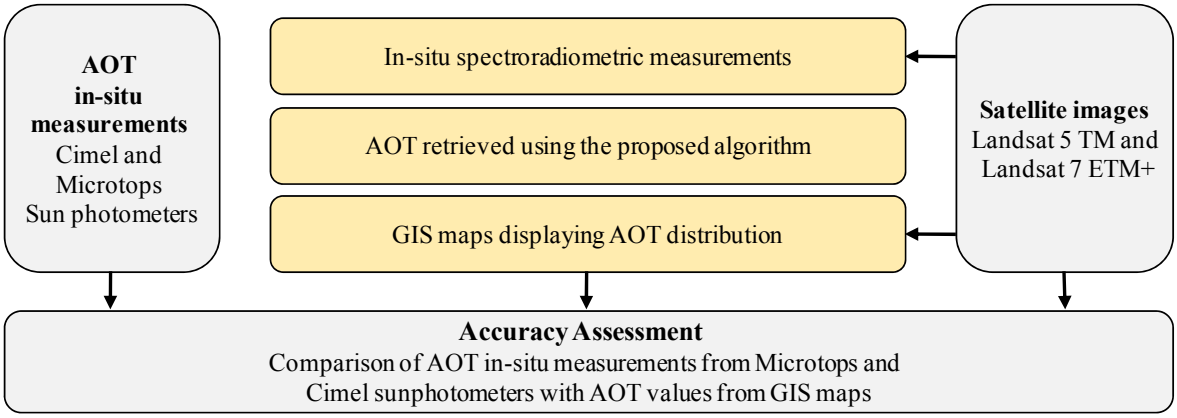

Figure 6-15 Accuracy assessment of in-situ AOT with AOT from GIS maps

6.8 Summary

In this chapter, an outline of the overall research methodology was described. Each specific section of the methodology will be further explained in the following chapters. The following chapter explains the pseudo-invariant targets used to improve the empirical line method of atmospheric correction in this thesis.

Chapter 7 Pseudo-Invariant Targets

This chapter will evaluate the use of five selected pseudo-invariant targets in this thesis in order to apply the 'empirical line' atmospheric correction method. This thesis used five pseudo-invariant targets of varying spectral properties for use with the empirical line and darkest pixel atmospheric correction methods.

7.1 Pseudo-invariant targets

There has been extensive research and literature available on pseudo-invariant targets. Using pseudo-invariant targets assumes that the spectral properties of the pseudo-invariant targets do not change significantly over time and, therefore, their spectral values are used to normalize scenes to a base image using regression techniques (Schott et al., 1988; Heo and Fitzhugh, 2000; Huang et al., 2008). Ground features recognized as having low temporal variability are used as pseudo-invariant targets (Schott et al., 1988; Caselles and Garcia, 1989; Escadafel et al., 1997). If ground measurements cannot be made concurrent with the imagery acquisition, the proposed targets should, if possible, be checked for spectral stability over time to determine if their reflectance values are to be taken from other studies as constant values.

According to Eckhardt et al. (1990), there are five acceptable criteria for pseudo-invariant targets:

1. The targets should be approximately the same elevation so the thickness of the atmosphere over each target is approximately the same.
2. The targets should contain only minimum amounts of vegetation, since the spectral reflectance of vegetation changes over time.
3. The targets must be in relatively flat areas so that changes in sun angle between images will produce the same values.
4. The spatial pattern of the normalization target should not change over time.
5. A set of targets must have a wide range of brightness for the regression model to be reliable.

However, several researchers state that pseudo-invariant targets with constant reflectance do not exist, especially in remote areas (Du et al., 2001; 2002; Janzen et al., 2006; Yuan and Elvidge, 1996). According to Janzen et al. (2006), the presence of suitable pseudo-invariant targets can be confounded by a combination of factors, including variable cloud

cover, variable climate leading up to the date of the image capture, high topographic complexity in the imagery and lack of urban development. As well, the longer the time intervals between satellite images, the higher the probability that a given pseudo-invariant target will have changed (Janzen et al., 2006).

In this thesis, five targets were examined to be used as pseudo-invariant targets for atmospheric correction. It is the first time that a field campaign was conducted measuring the reflectance values of pseudo-invariant targets for an extended time period throughout the year examining how wet and dry ground conditions affect the reflectance values for atmospheric correction. Table 7-1 indicated the size and location of these five targets, including their distinguishing characteristics.

Target#	Target	Color	Area	Location (Latitude, Longitude)
1	**Gray Asphalt**	Gray	Limassol Port	34.656, 33.015
2	**Black Asphalt**	Black	Limassol Port	34.658, 33.02
3	**Concrete**	Gray	Limassol Port	34.648, 33.007
4	**Black Sand**	Beige	Akrotiri	34.607, 32.999
5	**Compacted Sand**	Beige	Akrotiri	34.603, 33.005

Table 7-1 Target sites

The reason these particular targets were chosen are as follows:

- Close proximity to the Cyprus University of Technology where the Cimel sun photometer (used in the AERONET project) is located.
- The large size of the targets make them easily identifiable on a satellite image due to the pixel size of the Landsat TM/ETM+ images that are 30 m × 30 m. The targets are larger than 3 × 3 pixels (90 m × 90 m), so they are easy to be identified and selected.
- The targets are flat, uniform, are not easily affected by any drastic surface changes and can be considered as a near-Lambertian surface. The near-Lambertian assumption is considered to be reasonable, as shown by Hadjimitsis et al. (2009).
- The spectral signatures of the targets remained consistent throughout the year, with a standard deviation between 1-3%.
- The targets are commonly found in any area in the world, so the targets can be easily located in any geographical area.

The five reference targets are located in the vicinity of the Limassol Port and Akrotiri Bay. Figures 7-1 to 7-5 indicate each target, with a close-up of the surface material.

Figure 7-1 Target 1 (Gray Asphalt)

Figure 7-2 Target 2 (Black Asphalt)

Figure 7-3 Target 3 (Concrete)

Figure 7-4 Target 4 (Black Sand)

Figure 7-5 Target 5 (Compacted Sand)

Below is the table of field measurements, including the reference target that was measured on the particular date.

Date	Gray Asphalt	Black Asphalt	Concrete	Black Sand	Compacted Sand
29/10/09	x		x		
05/11/09	x		x		
06/11/09	x		x		
08/11/09	x		x	x	

10/11/09		x	x	x	
12/11/09		x	x	x	
13/11/09		x	x		
14/11/09		x	x	x	
18/11/09		x	x	x	x
16/02/10	x		x	x	x
24/02/10	x	x	x	x	x
26/02/10	x	x	x		
02/03/10	x	x	x		x
03/03/10	x	x	x	x	x
04/03/10	x	x	x	x	x
09/03/10	x	x	x	x	x
10/03/10	x	x	x	x	x
12/03/10	x	x	x	x	x
15/03/10	x	x	x	x	x
17/03/10	x	x	x	x	x
18/03/10	x	x	x		x
19/03/10	x	x	x	x	x
20/03/10	x		x	x	x
22/03/10	x	x	x	x	x
23/03/10	x	x	x	x	x
24/03/10	x	x	x		x
04/04/10	x	x	x	x	x
13/04/10	x	x	x	x	x
19/04/10	x	x	x	x	x
20/04/10	x	x	x	x	x
21/04/10	x	x	x	x	x
22/04/10	x	x	x	x	x
23/04/10	x	x	x	x	x
26/04/10	x	x	x	x	x
27/04/10	x	x	x	x	x
28/04/10	x	x	x	x	x
29/04/10	x	x	x	x	x
30/04/10	x	x	x	x	x
07/05/10	x	x	x	x	x
10/05/10	x	x	x	x	x
31/05/10	x	x	x	x	x
07/06/10	x	x	x	x	x
15/06/10	x	x	x	x	x
16/06/10	x	x	x	x	x
24/06/10	x	x	x	x	x
02/07/10	x	x	x	x	x
10/07/10	x	x	x	x	x
18/07/10	x	x	x	x	x
03/08/10		x	x	x	x
27/08/10	x	x	x	x	x
04/09/10			x	x	x
28/09/10	x	x	x	x	x
06/10/10	x		x	x	x
7/11/10	x	x	x	x	x
9/12/2010	x	x	x	x	x
2/5/2011	x	x	x	x	x

Table 7-2 Dates of in-situ measurements of pseudo-invariant targets

A preliminary study was conducted to identify possible targets by identifying homogenous areas on existing satellite imagery of the target area. As mentioned in Chapter 6, several possible targets were selected for the preliminary study based on the criteria of suitable size (at least 30×30 m), surface uniformity, surface colour, and proximity distance. The accessibility of the target area was an important consideration, as calibration sites often have limited accessibility (Baugh and Groeneveld, 2008). Approximately twenty potential targets that met the above criteria in the Limassol District were visually identified from the satellite imagery, including parking lots, schools, playgrounds and roads. The potential targets were then assessed to verify that they met the criteria for pseudo-invariant targets in terms of size, surface homogeneity, near-Lambertian surface, lack of markings and debris and non-variant reflectance values (Wilson and Milton, 2010; Karpouzli and Malthus, 2003; Eckhardt et al., 1990). Several spectroradiometric measurements of each possible target were made and the spectral signatures of the targets were assessed. Multi-temporal analysis of the spectral signatures identified five surfaces that were large areas suitable for this study whose spectral signatures were non-variant. These five surfaces were gray and black asphalt, concrete, black sand and compacted sand, which are discussed in detail in the next section.

7.2 Assessment of Pseudo-invariant targets

In order to assess whether the specific targets are non-variant, the maximum, minimum, and average values of reflectance values were determined for each of the five targets by date and by band. Field measurements of the five reference materials were taken on 46 different dates, and over 2,000 measurements were taken. For each non-variant target, the average reflectance value and standard deviation was determined plotted in graph form in Figures 7-8 to 7-11, Figures 7-12 to 7-15, Figures 7-16 to 7-19, Figure 7-20 to 7-23 and Figure 7-24 to 7-27, respectively. The averaged reflectance values for each target indicated a good range of reflectance across all bands. The standard deviation was also calculated, in order to determine the percentage of variance between maximum and minimum measurements. The standard deviation for the asphalt and sand targets ranged from 1-3%, with concrete showing the greatest heterogeneity of 3%. The in-situ measurements were divided into wet and dry measurements, in order to assess if weather conditions affect the variability of the targets. Weather data was collected from the nearly weather station at the British Bases, which are located at Akrotiri Bay. There were several instances where the minimum and average reflectance value of the target was low, which corresponded with rainfall in the past few days. It is notable that the higher the amount of rainfall, the lower

the reflectance value of the target, which was especially notable with the compacted sand target. Figure 7-6 indicates the spectral signature of the five pseudo-invariant targets by average reflectance value according to wet and dry conditions. It is notable that although precipitation affects the reflectance value for each target, it does not change the spectral signature between wet and dry conditions (Philpot, 2010). The sand targets presented the greatest sensitivity to changes in atmospheric conditions due to moisture penetrating below the surface of the sand (Omerci and Ekercin, 2008; Philpot, 2010).

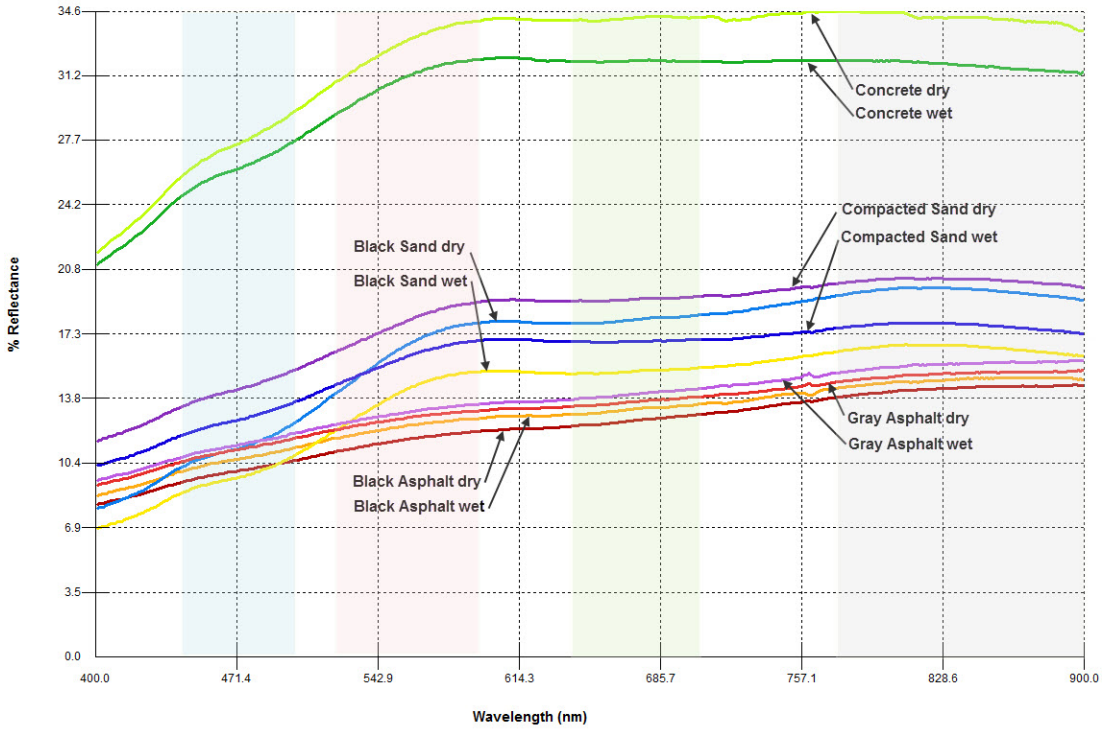

Figure 7-6 Average spectral signatures of the five pseudo-invariant targets, including wet and dry conditions

Field campaign measurements were assessed from October 2009 to May 2011 to determine the invariability of the targets. Appendix 1 provides the field campaign measurements for each reference target. The reflectance values were measured using the SVC HR 1024 spectroradiometer and were plotted in graph form to indicate minimum, maximum and average reflectance values, and standard deviation, as shown in Figures 7-7 to 7-23 and Figures 7-25 to 7-28. The standard deviation for the five targets in both wet and dry conditions ranged from 1% to 2.5%, respectively, with wet compacted sand showing the greatest heterogeneity. The average reflectance value for wet surface conditions (shown as a dotted red line in the graph) and dry surface conditions (shown as a dashed green line in the graph) was also calculated. Surface reflectance is affected by precipitation for all targets in varying amounts. Dates where the surface was wet due to rain in previous days

are indicated by a red circle in the graph. There were elevated temperatures ranging from 30° to 35° Celsius from May to September, which are indicated by a blue box in the graph. Detailed explanations of each surface are explained below.

7.2.1 Asphalt

Gray and Black Asphalt showed nearly identical average measurements and standard deviations for both wet and dry conditions in all wavelengths. The reflectance value for the wet conditions is slightly higher than the reflectance values for the dry conditions, which is expected, as the presence of water on a surface, such as asphalt, causes the surface to become specular (Jensen et al., 1999). Asphalt appears to be unaffected by temperature in all wavelengths. Black Asphalt was the darkest of all the pseudo-invariant targets validated. As this target had the lowest reflectance value across all bands, it was used as the darkest pixel in-situ reflectance value for the darkest pixel method.

Figures 7-7 to 7-10 indicates the in-situ values for Gray Asphalt in Bands 1-4 in graph form, including the wet and dry averages and precipitation conditions. Table 7-3 indicates the average reflectance values for Gray Asphalt for wet and dry conditions in Landsat TM/ETM+ bands 1-4, including the difference between wet and dry conditions Figures 7-11 to 7-14 indicates the in-situ values for Gray Asphalt in Bands 1-4 in graph form, including the wet and dry averages and precipitation conditions. Table 7-4 indicates the average reflectance values for Black Asphalt for wet and dry conditions in Landsat TM/ETM+ bands 1-4, including the difference between wet and dry conditions.

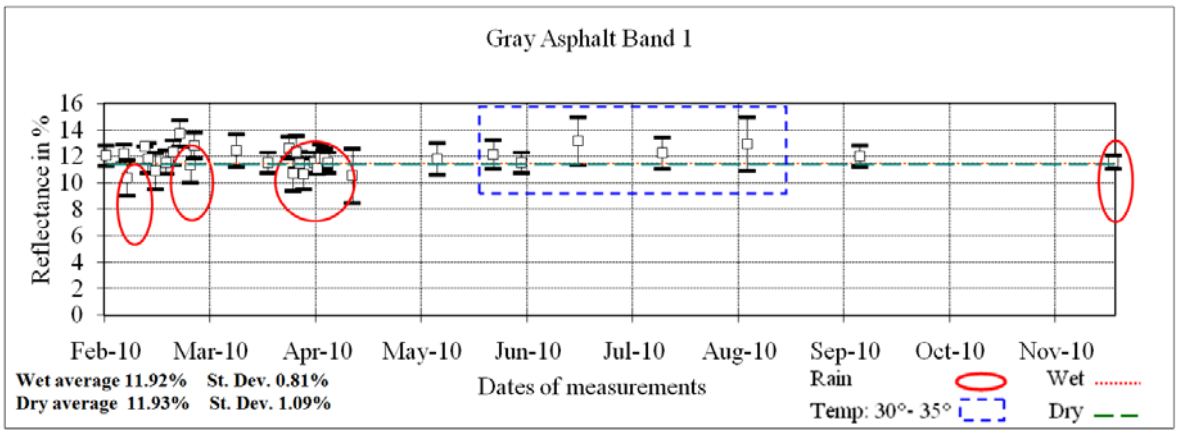

Figure 7-7 Graph of in-situ reflectance values from February to December 2010 for Gray Asphalt, Band 1

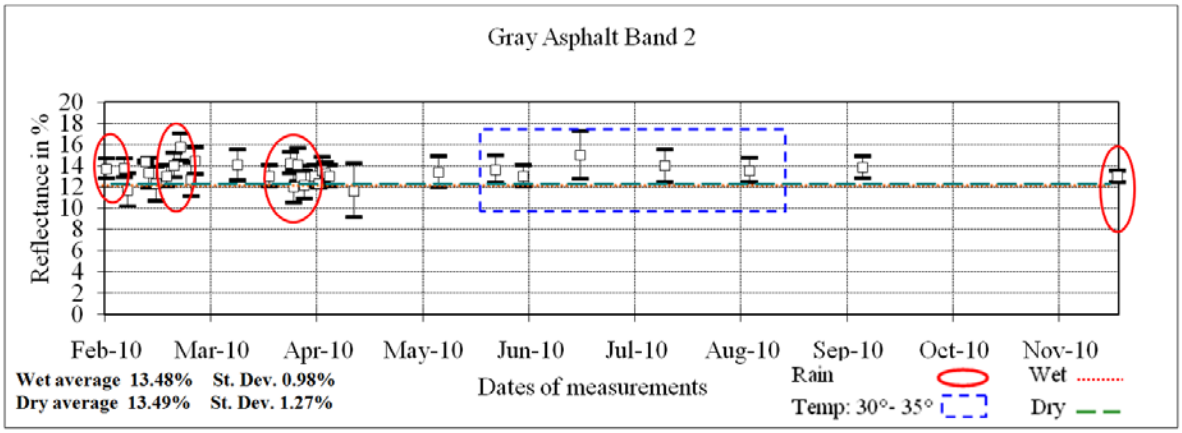

Figure 7-8 Graph of in-situ reflectance values from February to December 2010 for Gray Asphalt, Band 2

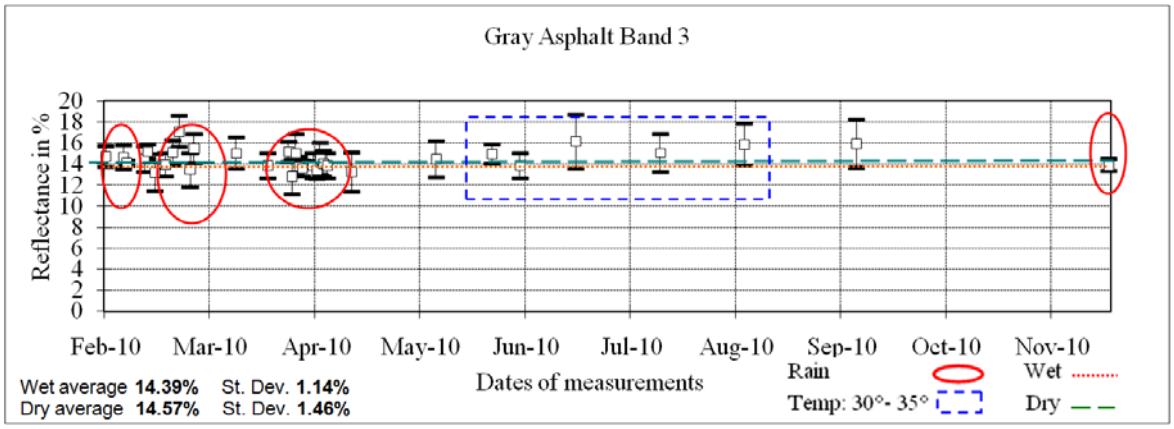

Figure 7-9 Graph of in-situ reflectance values from February to December 2010 for Gray Asphalt, Band 3

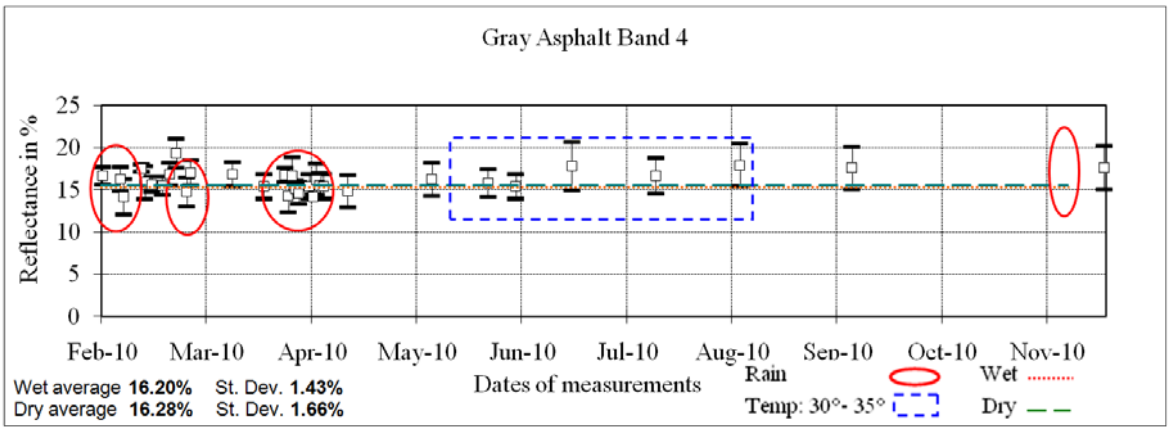

Figure 7-10 Graph of in-situ reflectance values from February to December 2010 for Gray Asphalt, Band 4

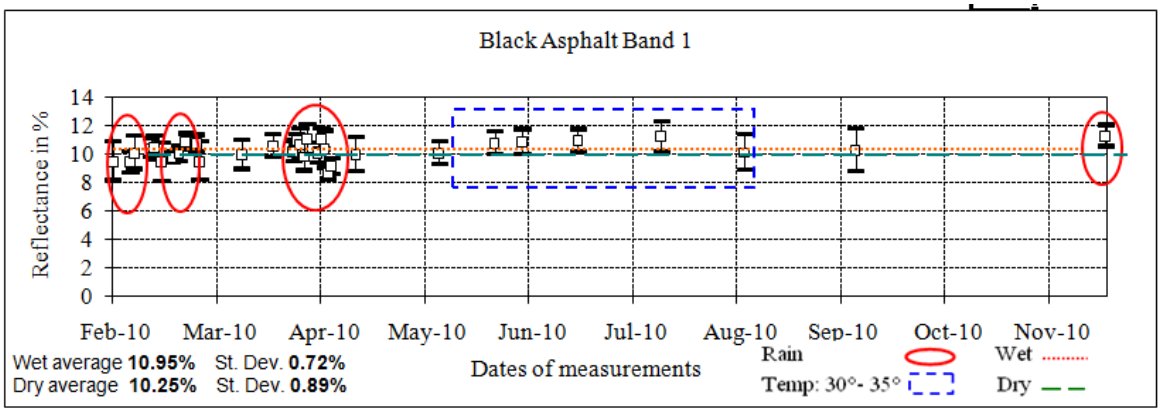

Figure 7-11 Graph of in-situ reflectance values from February to December 2010 for Black Asphalt, Band 1

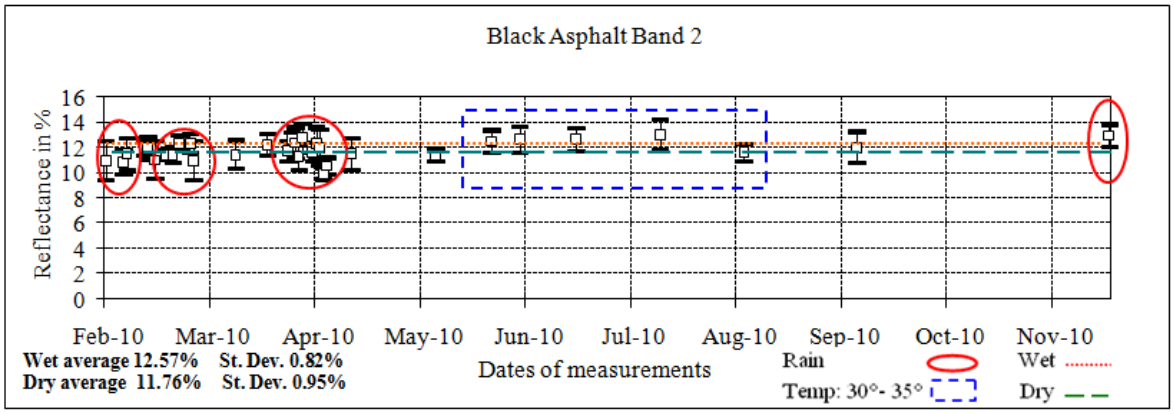

Figure 7-12 Graph of in-situ reflectance values from February to December 2010 for Black Asphalt, Band 2

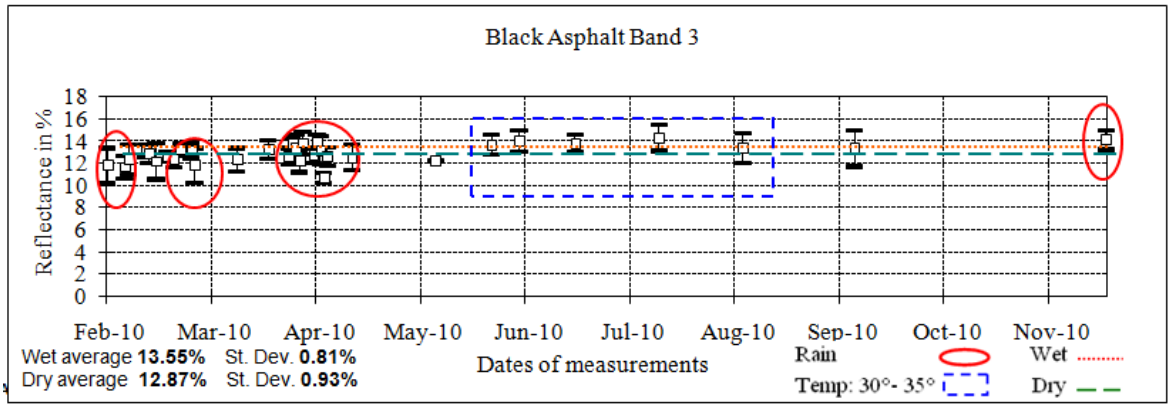

Figure 7-13 Graph of in-situ reflectance values from February to December 2010 for Black Asphalt, Band 3

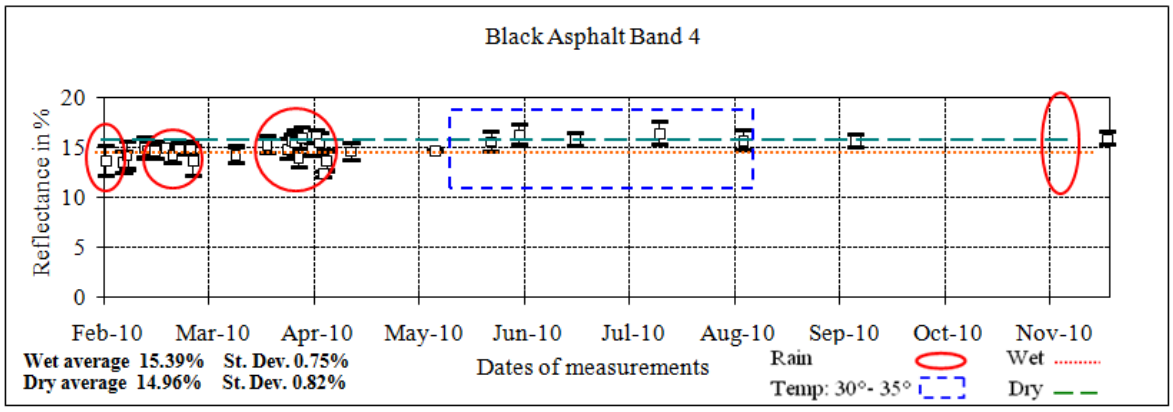

Figure 7-14 Graph of in-situ reflectance values from February to December 2010 for Black Asphalt, Band 4

7.2.2 Concrete

Concrete showed nearly identical average measurements and standard deviations for both wet and dry conditions in all bands. The reflectance value for the dry conditions is slightly higher than the reflectance values for the dry conditions, which is expected, as wet conditions lead to a darkening of the color, thus slightly reducing the reflectance value (Jenness and Singer, 2007). Table 7-5 shows the average reflectance values, including standard deviation, for both wet and dry conditions for Landsat bands 1, 2, 3 and 4, including the difference between reflectance values as a function of wet and dry conditions. Figures 7-15 to 77-18 indicate the in-situ values for Concrete in Bands 1-4 in graph form, including the wet and dry averages and precipitation conditions.

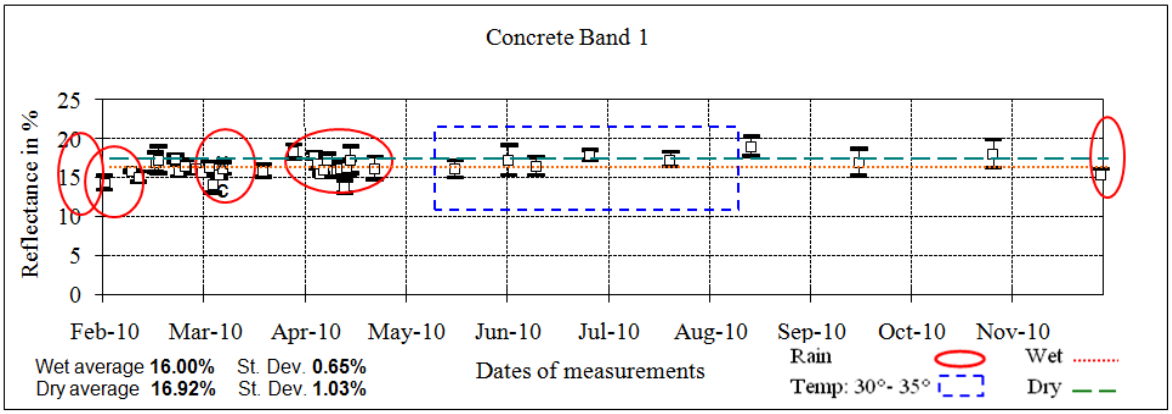

Figure 7-15 Graph of in-situ reflectance values from February to December 2010 for Concrete, Band 1

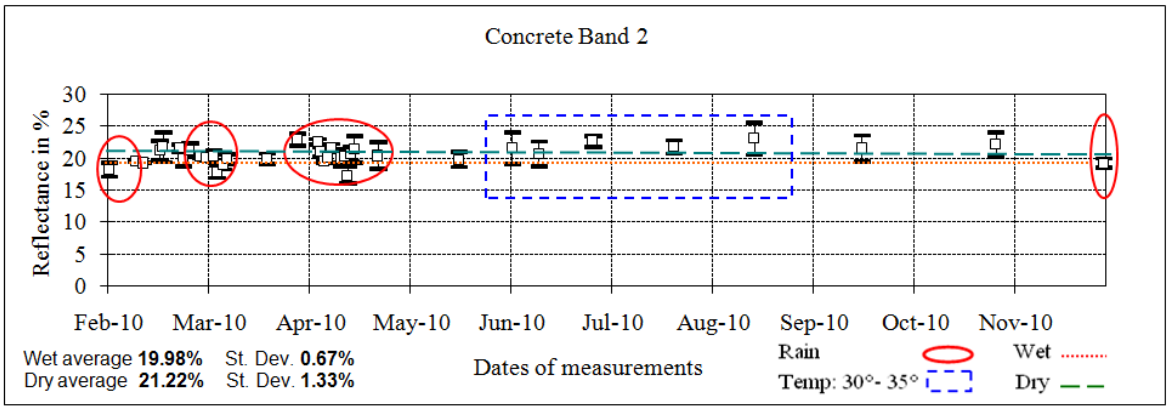

Figure 7-16 Graph of in-situ reflectance values from February to December 2010 for Concrete, Band 2

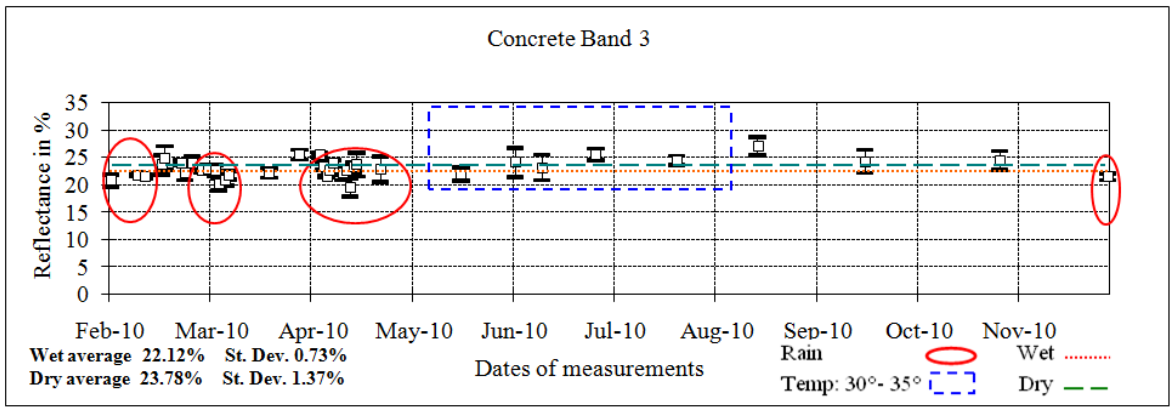

Figure 7-17 Graph of in-situ reflectance values from February to December 2010 for Concrete, Band 3

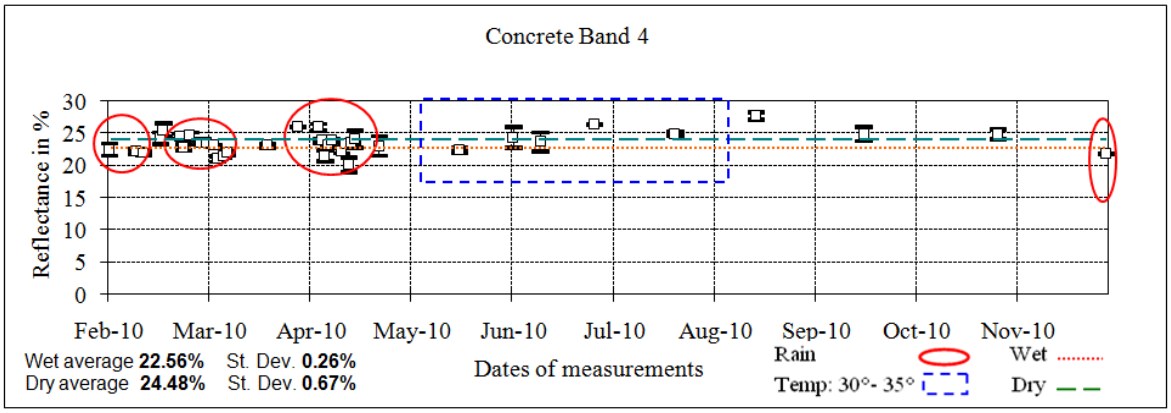

Figure 7-18 Graph of in-situ value Graph of in-situ reflectance values from February to December 2010 for Concrete, Band 4

7.3.3 Sand

Black Sand and Compacted Sand exhibited varying reflectance values which were dependent on rainfall. Research (Schuman and Rea, 1981; Dobos, 2003; Adam et al., 2006;

Garcia-Rodriguez, 2011) indicates that high levels of moisture affect sand by making it darker and reducing its reflectance. There is a notable decrease in reflectance when there is increased moisture in sand; however, the rate of decrease in relative reflectance becomes more moderate with increasing moisture, since at very high sand moisture contents, the sand is already quite dark and further moisture added to the sand has less of an effect on the reflectance (Bowers and Hanks, 1965; Baumgardner et al., 1985; Twomey et al., 1986; Ishida et al., 1991; Whiting et al., 2000; Kaleita et al., 2005; Bogrekci and Lee, 2005; Lesaignoux et al., 2007). For both sand targets, the lowest reflectance value corresponds to heavy rainfall the previous day, indicating that sand targets are affected by rain. Conversely, the highest reflectance values were in the months of July and August, which were over five months after the last rainstorm, indicating that the target was fully dry. Clusters of white spots were observed on the surface of the compacted sand target during the field measurements (see Figure 7-19). These white spots are actually salt deposits that emerged as a result of an evaporation of moisture below the surface of the sand due to the high temperatures present from May to September 2010. According to Omerci and Ekercin (2008), the upward flow of water into the soil, combined with evaporation, leaves a high concentration of salt on or near the surface of the sand, resulting in a higher reflectance value.

Figure 7-19 Salinization of Compacted Sand

Figures 7-20 to 7-23 indicate the in-situ values for Black Sand in Bands 1-4 in graph form, including the wet and dry averages and precipitation conditions. Figures 7-24 to 7-27 indicate the in-situ values for Compacted Sand in Bands 1-4 in graph form, including the wet and dry averages and precipitation conditions. Tables 7-6 and 7-7 indicate the average reflectance values, including standard deviation, for Black Sand and Compacted Sand, respectively, for both wet and dry conditions for Landsat bands 1, 2, 3 and 4. It is

important to note that wet conditions exhibited a decrease of 4% to 7% in reflectance value, for both black and compacted sand.

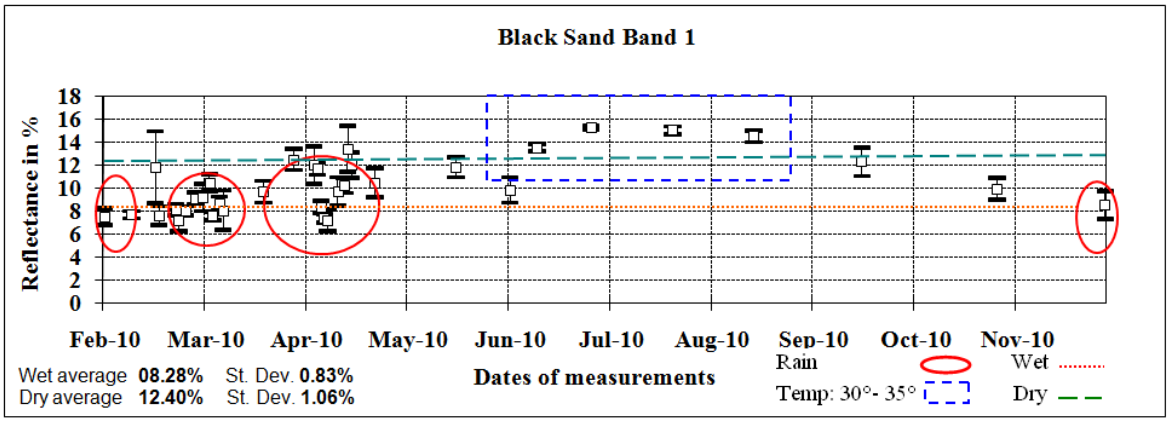

Figure 7-20 Graph of in-situ reflectance values from February to December 2010 for Black Sand, Band 1

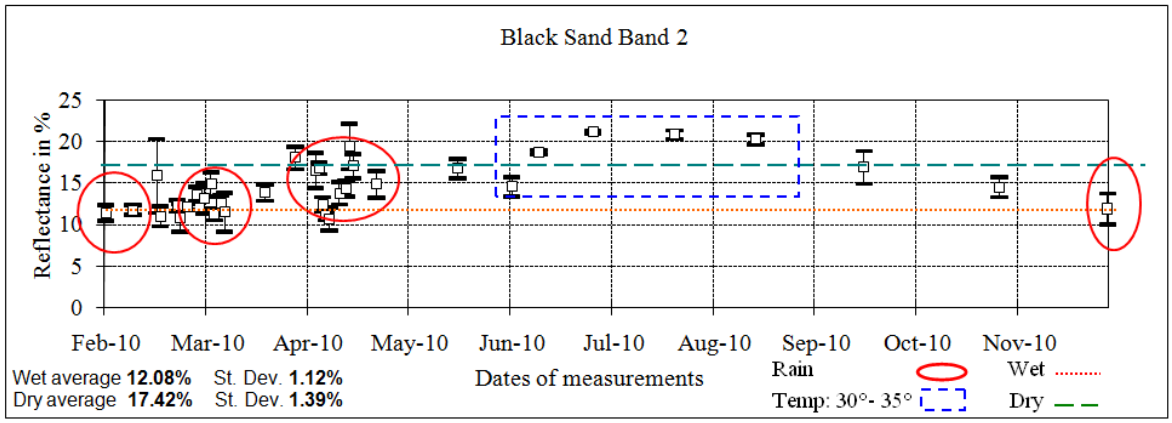

Figure 7-21 Graph of in-situ reflectance values from February to December 2010 for Black Sand, Band 2

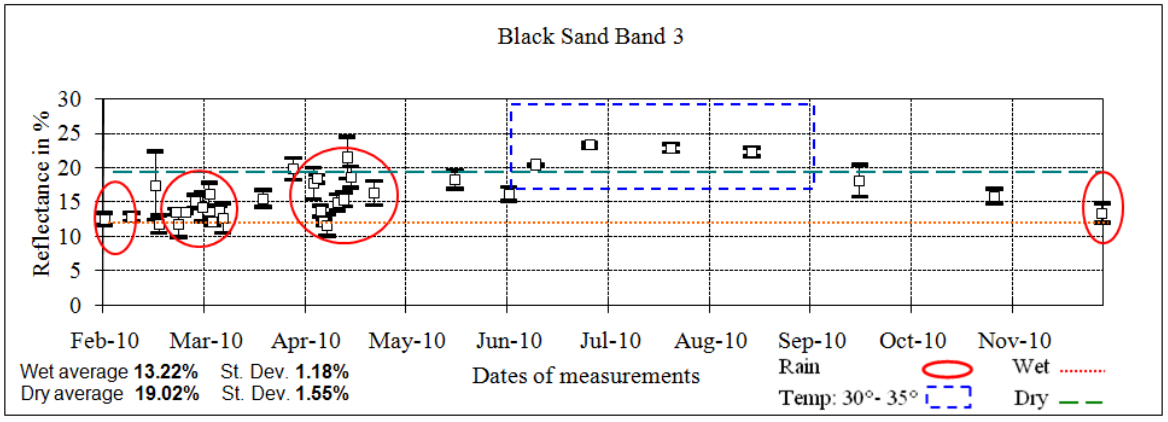

Figure 7-22 Graph of in-situ reflectance values from February to December 2010 for Black Sand, Band 3

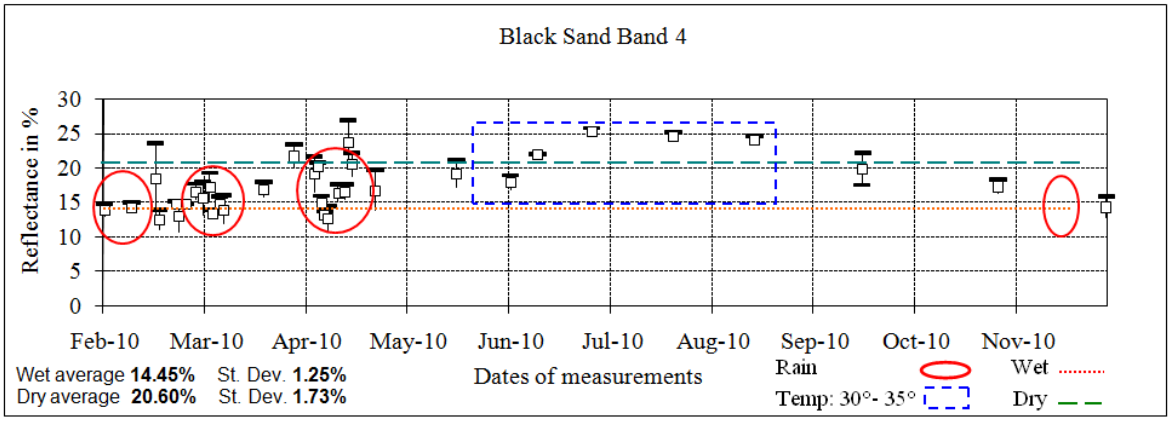

Figure 7-23 Graph of in-situ reflectance values from February to December 2010 for Black Sand, Band 4

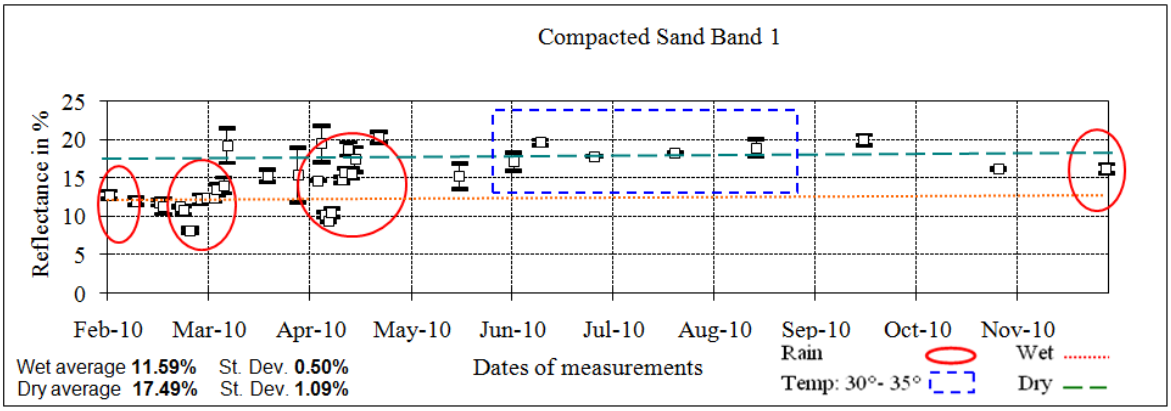

Figure 7-24 Graph of in-situ reflectance values from February to December 2010 for Compacted Sand, Band 1

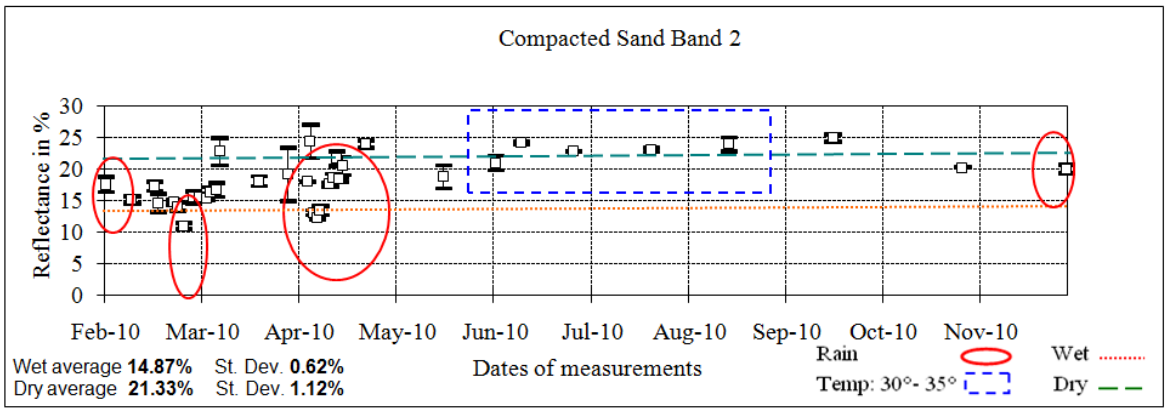

Figure 7-25 Graph of in-situ reflectance values from February to December 2010 for Compacted Sand, Band 2

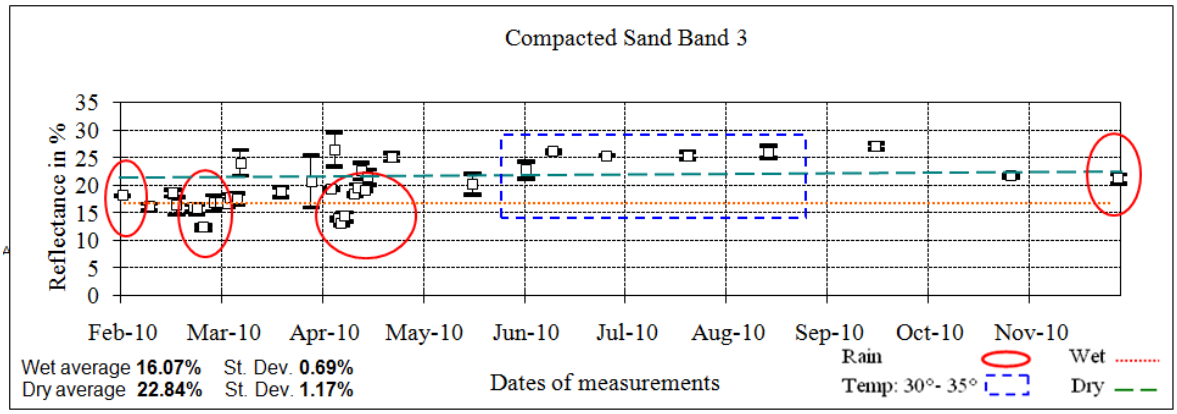

Figure 7-26 Graph of in-situ reflectance values from February to December 2010 for Compacted Sand, Band 3

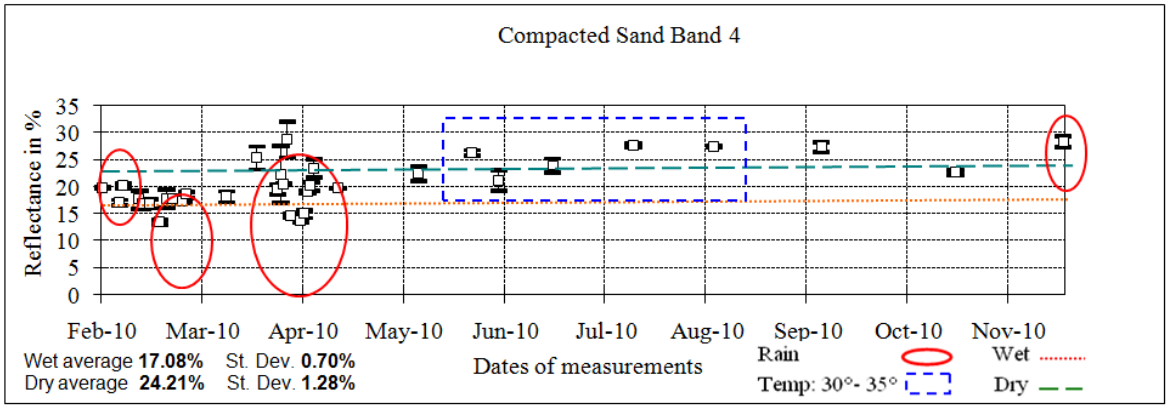

Figure 7-27 Graph of in-situ reflectance values from February to December 2010 for Compacted Sand, Band 4

The average, minimum, maximum measurements of the pseudo-invariant targets and the standard deviation, by band and by are indicated in Table 7-3. As is evident, the standard deviation is low, indicating the non-variance of the reference targets.

Band 1		ρ Min	ρ Max	ρ Average	St. Dev.
Grey Asphalt	all measurements	10.84	13.02	11.93	1.09
Grey Asphalt	wet conditions	11.01	12.83	11.92	0.81
Grey Asphalt	dry conditions	10.84	13.02	11.93	1.09
Black Asphalt	all measurements	9.36	11.67	10.52	1.16
Black Asphalt	wet conditions	10.23	11.67	10.95	0.72
Black Asphalt	dry conditions	9.36	11.14	10.25	0.89
Concrete	all measurements	15.35	17.95	16.65	1.30
Concrete	wet conditions	15.35	16.65	16.00	0.65
Concrete	dry conditions	15.89	17.95	16.92	1.03
Black Sand	all measurements	7.45	13.46	10.46	3.01
Black Sand	wet conditions	7.45	9.11	8.28	0.83
Black Sand	dry conditions	11.34	13.46	12.40	1.06
Compacted Sand	all measurements	7.78	21.88	14.83	7.05
Compacted Sand	wet conditions	7.78	15.06	11.59	3.64
Compacted Sand	dry conditions	14.29	21.88	17.49	3.80

Band 2		ρ Min	ρ Max	ρ Average	St. Dev.
Grey Asphalt	all measurements	12.22	14.76	13.49	1.27
Grey Asphalt	wet conditions	12.50	14.46	13.48	0.98
Grey Asphalt	dry conditions	12.22	14.76	13.49	1.27
Black Asphalt	all measurements	10.83	13.44	12.14	1.31
Black Asphalt	wet conditions	11.75	13.44	12.57	0.82
Black Asphalt	dry conditions	10.83	12.73	11.78	0.95
Concrete	all measurements	19.32	22.55	20.94	1.62
Concrete	wet conditions	19.32	20.65	19.98	0.67
Concrete	dry conditions	19.89	22.55	21.22	1.33
Black Sand	all measurements	10.96	18.81	14.89	3.93
Black Sand	wet conditions	10.96	13.20	12.08	1.12
Black Sand	dry conditions	16.03	18.81	17.42	1.39
Compacted Sand	all measurements	14.25	22.45	18.35	4.10
Compacted Sand	wet conditions	14.25	15.49	14.87	0.62
Compacted Sand	dry conditions	20.21	22.45	21.33	1.12

Band 3		ρ Min	ρ Max	ρ Average	St. Dev.
Grey Asphalt	all measurements	13.11	16.03	14.57	1.46
Grey Asphalt	wet conditions	13.25	15.53	14.39	1.14
Grey Asphalt	dry conditions	13.11	16.03	14.57	1.46
Black Asphalt	all measurements	11.94	14.36	13.15	1.21
Black Asphalt	wet conditions	12.74	14.36	13.55	0.81
Black Asphalt	dry conditions	11.94	13.80	12.87	0.93
Concrete	all measurements	21.39	25.15	23.27	1.88
Concrete	wet conditions	21.39	22.85	22.12	0.73
Concrete	dry conditions	22.51	25.15	23.78	1.37
Black Sand	all measurements	12.04	20.57	16.31	4.27
Black Sand	wet conditions	12.04	14.40	13.22	1.18
Black Sand	dry conditions	17.47	20.57	19.02	1.55
Compacted Sand	all measurements	15.38	24.01	19.70	4.32
Compacted Sand	wet conditions	15.38	16.76	16.07	0.69
Compacted Sand	dry conditions	21.67	24.01	22.84	1.17

Band 4		ρ Min	ρ Max	ρ Average	St. Dev.
Grey Asphalt	all measurements	14.62	17.94	16.28	1.66
Grey Asphalt	wet conditions	14.77	17.63	16.20	1.43
Grey Asphalt	dry conditions	14.62	17.94	16.28	1.66
Black Asphalt	all measurements	14.14	16.14	15.14	1.00
Black Asphalt	wet conditions	14.64	16.14	15.39	0.75
Black Asphalt	dry conditions	14.14	15.76	14.96	0.82
Concrete	all measurements	22.30	25.15	23.73	1.43
Concrete	wet conditions	22.30	22.82	22.56	0.26
Concrete	dry conditions	23.81	25.15	24.48	0.67
Black Sand	all measurements	13.20	22.33	17.77	4.57
Black Sand	wet conditions	13.20	15.70	14.45	1.25
Black Sand	dry conditions	18.87	22.33	20.60	1.73
Compacted Sand	all measurements	16.38	25.49	20.94	4.56
Compacted Sand	wet conditions	16.38	17.78	17.08	0.70
Compacted Sand	dry conditions	22.93	25.49	24.21	1.28

Table 7-3 Reflectance values for all targets in Bands 1-4, including all measurements and reflectance values for wet and dry conditions

7.4 Spectral signatures

The spectral signatures for the five targets were calculated through use of the SVC HR-1024 software, as described in Chapter 6 and compiled according to the date of satellite overpass. The spectral signatures are indicated below in a graph form in Figures 7-28 to 7-37.

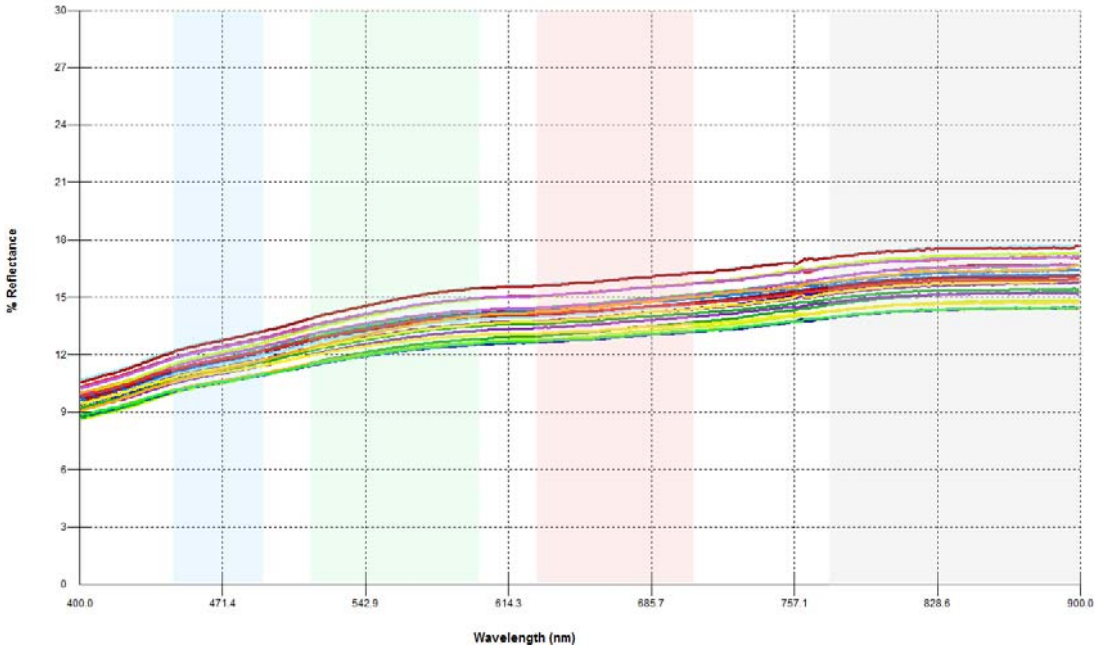

Figure 7-28 Spectral Signature of the Gray Asphalt target, dry

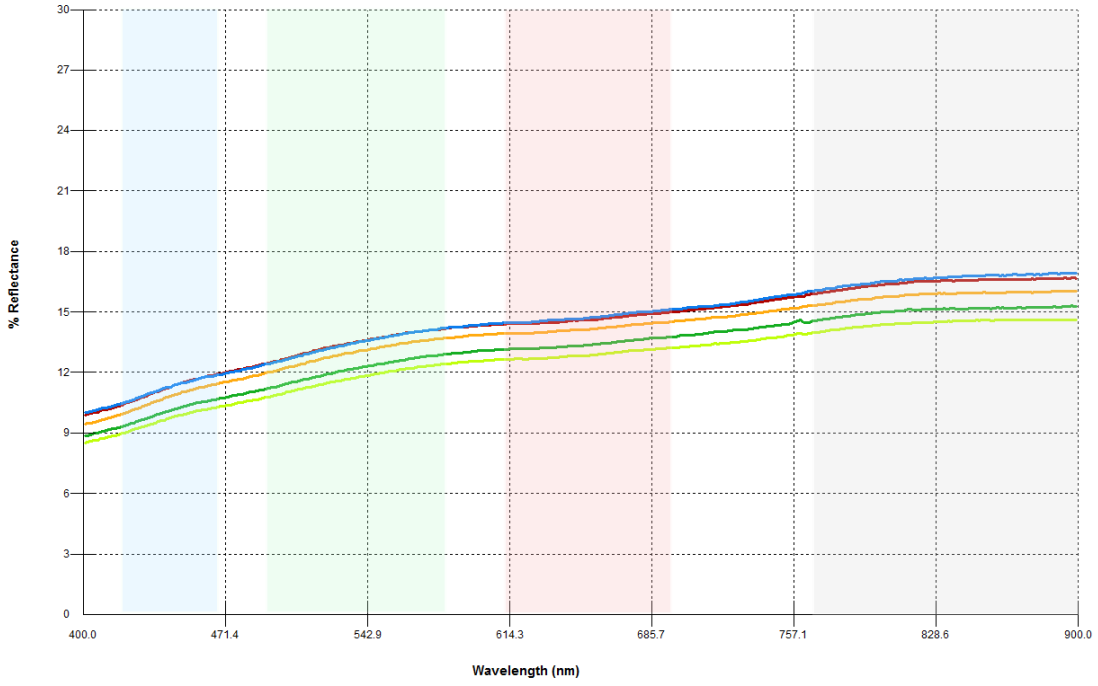

Figure 7-29 Spectral Signature of the Gray Asphalt target, wet

The Gray Asphalt target indicated consistent reflectance values, with an average reflectance value of 11.93 in dry conditions with a standard deviation of 1.09, and an

average reflectance value of 11.92 in wet conditions, with a standard deviation of 0.81. The spectral characteristics of the target were straight across all bands. The spectral characteristics of the target did not change as a result of wet and dry conditions.

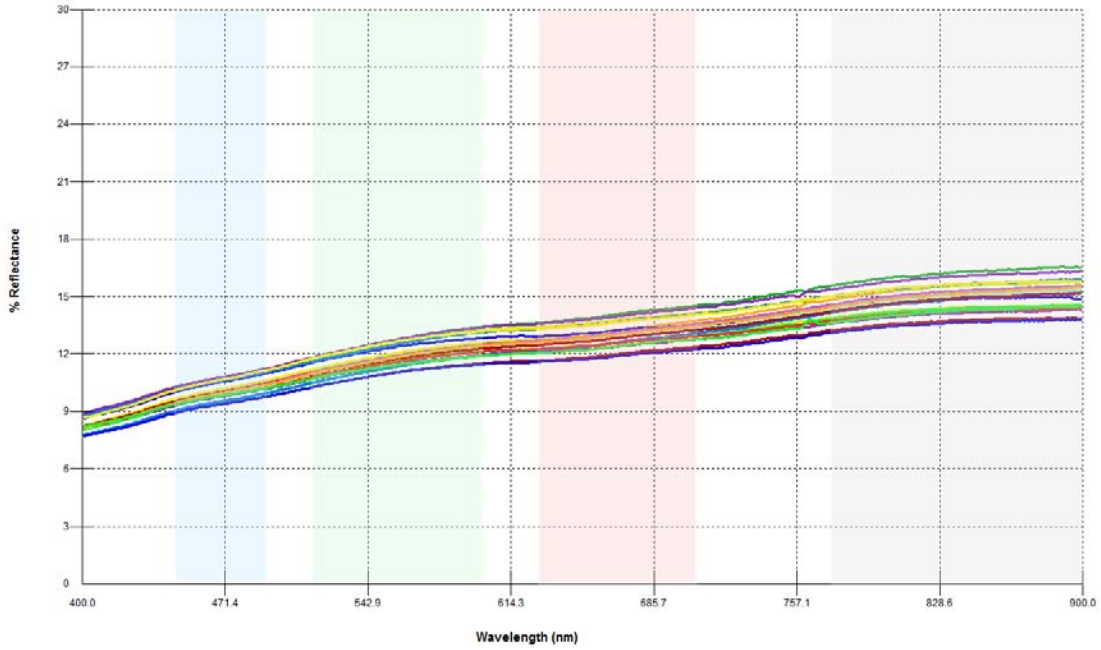

Figure 7-30 Spectral Signature of the Black Asphalt target, dry

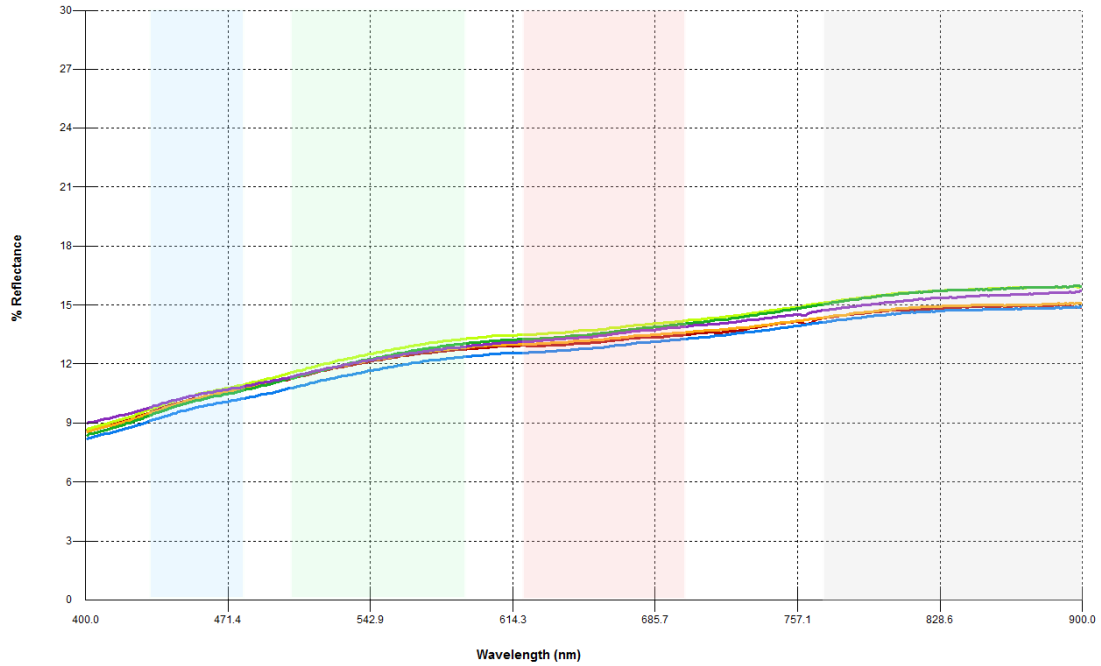

Figure 7-31 Spectral Signature of the Black Asphalt target, wet

The Black Asphalt target indicated consistent reflectance values, with an average reflectance value of 10.25 in dry conditions with a standard deviation of 0.89, and an average reflectance value of 10.95 in wet conditions, with a standard deviation of 0.72. The spectral characteristics of the target were straight across all bands. The spectral characteristics of the target did not change as a result of wet and dry conditions.

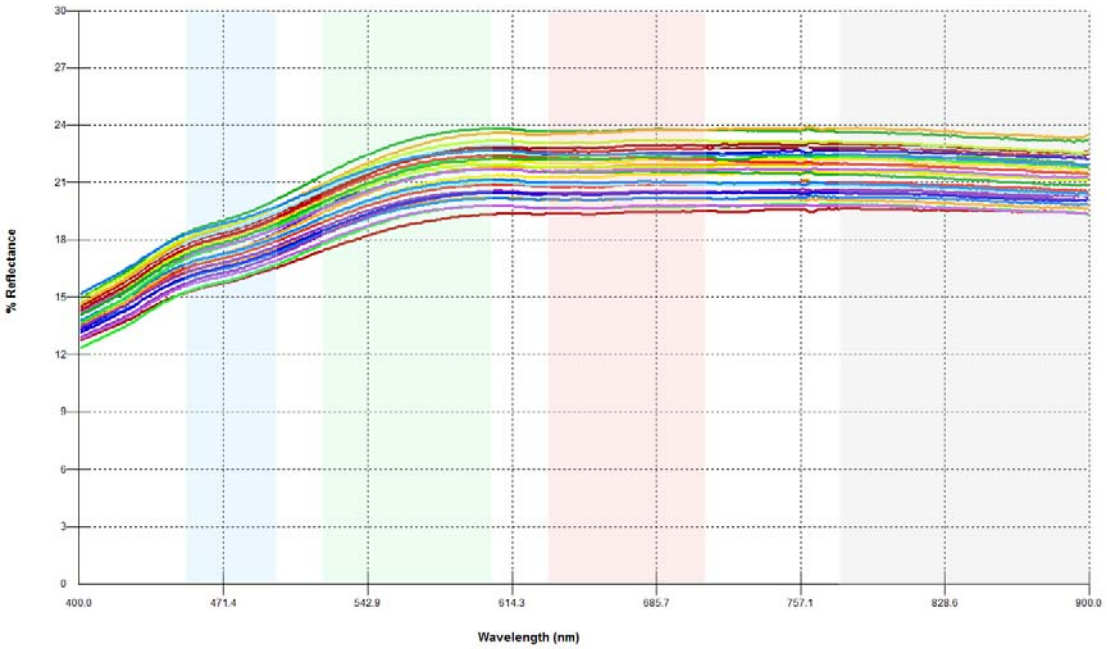

Figure 7-32 Spectral Signature of the Concrete target, dry

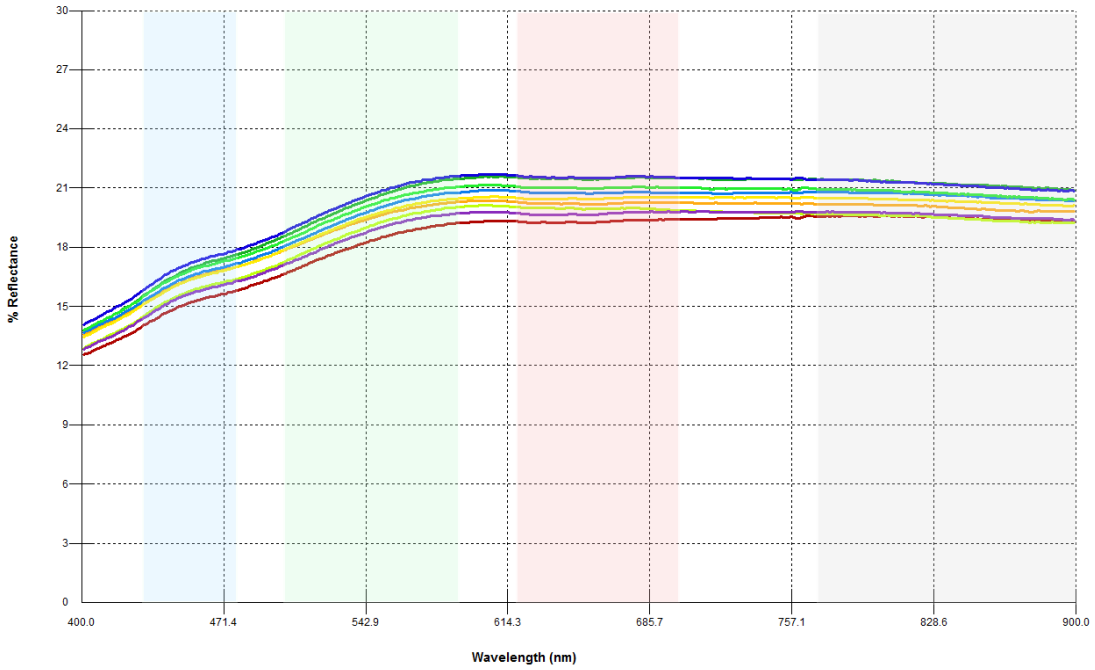

Figure 7-33 Spectral Signature of the Concrete target, wet

The Concrete target indicated consistent reflectance values, with an average reflectance value of 16.92 in dry conditions with a standard deviation of 1.03, and an average reflectance value of 16.00 in wet conditions, with a standard deviation of 0.65. The spectral characteristics of the target peaked in band 2, and then was straight across bands 3 and 4. The spectral characteristics of the target did not change as a result of wet and dry conditions.

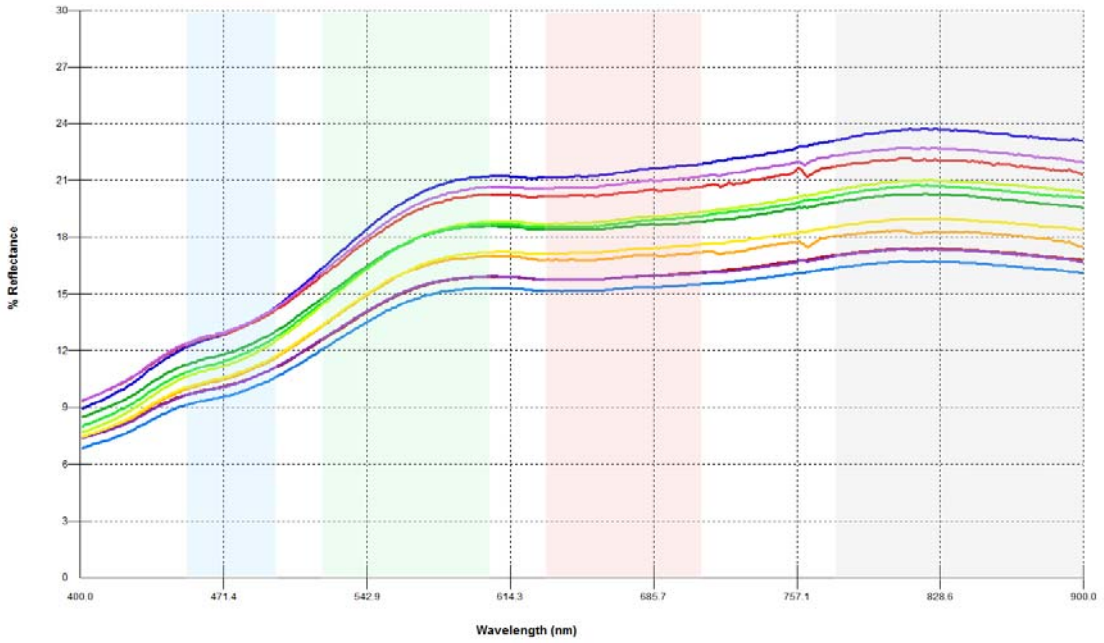

Figure 7-34 Spectral Signature of Black Sand target, dry

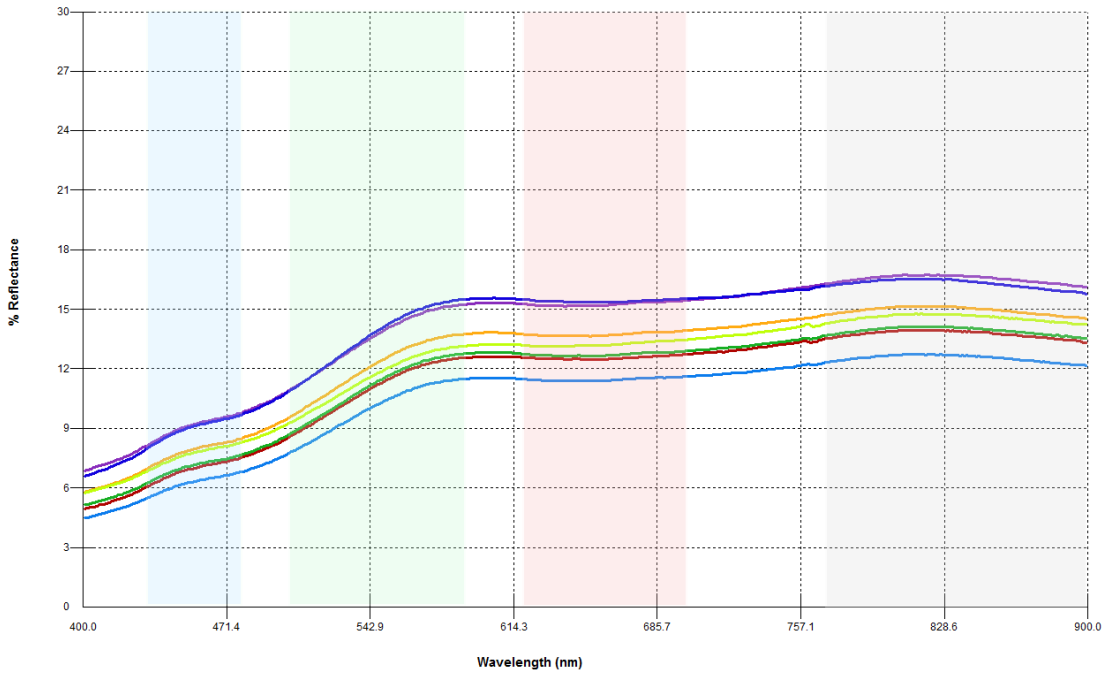

Figure 7-35 Spectral Signature of Black Sand target, wet

The Black Sand target was affected by precipitation values, with an average reflectance value of 12.40 in dry conditions with a standard deviation of 1.06, and an average reflectance value of 8.28 in wet conditions, with a standard deviation of 0.83. The spectral characteristics of the target peaked slightly in bands 2 and 4. The spectral characteristics of the target did not change as a result of wet and dry conditions.

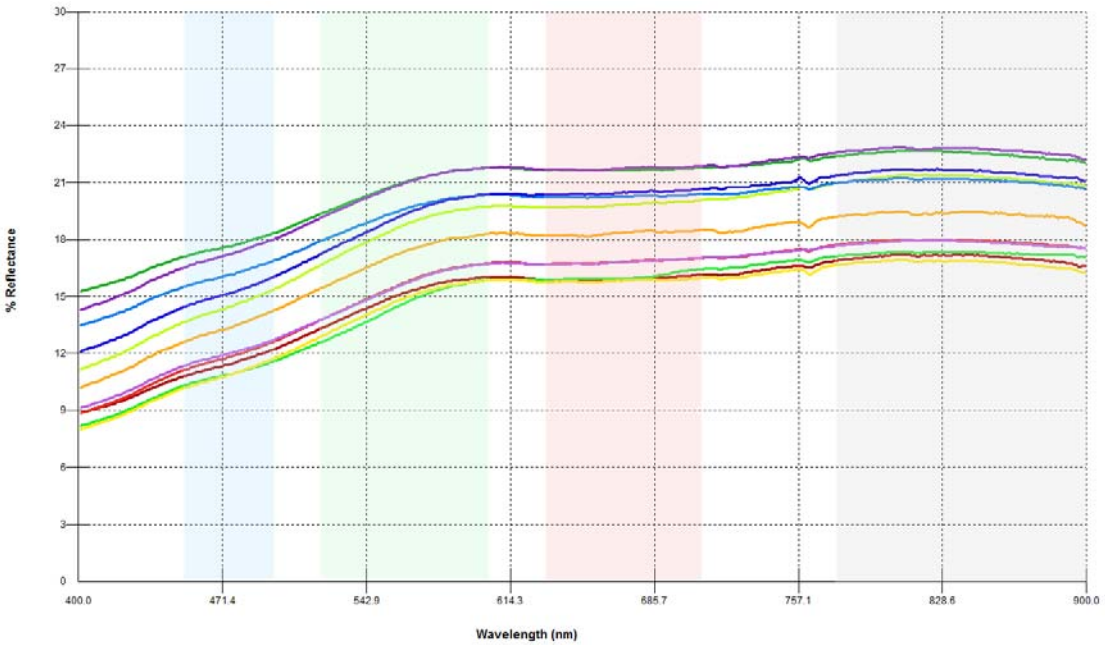

Figure 7-36 Spectral Signature of Compacted Sand target, dry

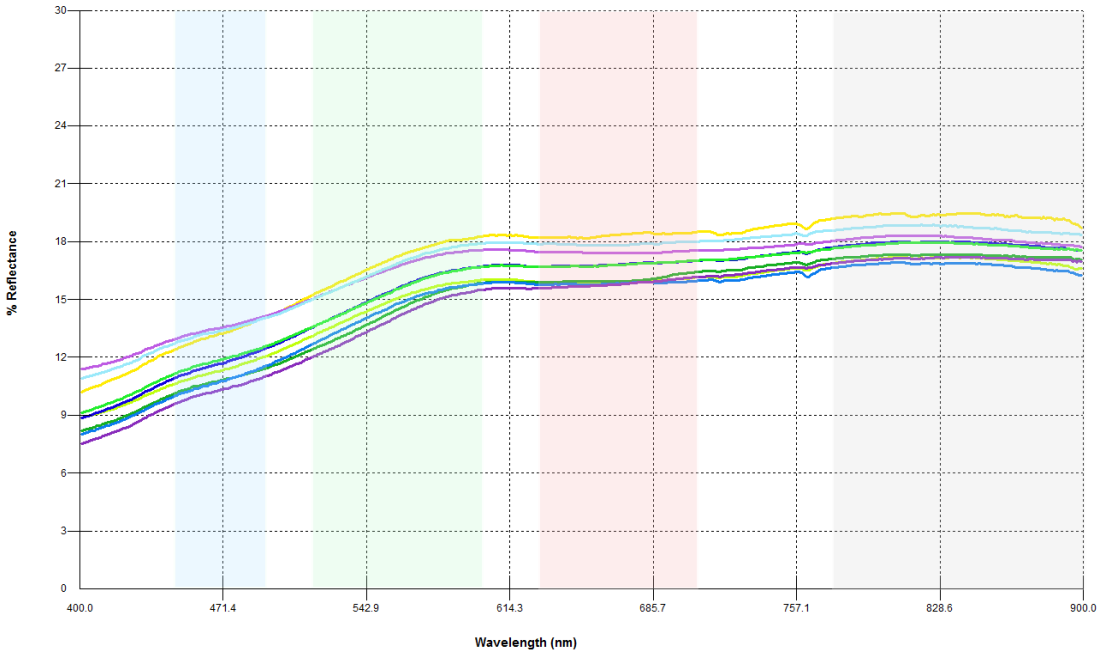

Figure 7-37 Spectral Signature of Compacted Sand target, wet

The Compacted Sand target was affected by precipitation values, with an average reflectance value of 11.59 in dry conditions with a standard deviation of 1.09, and an average reflectance value of 12.49 in wet conditions, with a standard deviation of 0.50. The spectral characteristics of the target peaked slightly in bands 2 and 4. The spectral characteristics of the target did not change as a result of wet and dry conditions.

7.4 Summary

Field measurements over the course of a year, in both wet and dry conditions established that the reflectance values of the targets did not vary significantly, making them suitable for the empirical line method. One of the significant findings of the study is that sand has a lower reflectance value when wet. Therefore, it is recommended that the reflectance value of wet sand and the reflectance value of dry sand be used separately.

Chapter 8 Atmospheric Correction Methods

Two atmospheric correction methods were used in this thesis, the empirical line method and the darkest pixel method. The empirical line method is based on the use of at least two targets, with minimum one dark and one bright target and uses the linear regression method to regress the ground reflectance values to at-satellite reflectance values. This method is improved by using five pseudo-invariant targets of varying spectral characteristics ranging from light to dark. This chapter also examined the darkest pixel (DP) atmospheric correction method used in this thesis where the actual reflectance values of the asphalt surface is used as the darkest pixel. The results of the atmospheric correction methods are presented, following their application to the eleven Landsat TM/ETM+ images.

8.1 Empirical line method

The empirical line method using pseudo-invariant targets (PITs method) is based on the assumption that, without atmospheric effects, the radiance reaching the satellite from a pseudo-invariant target would be unchanged on different image dates and that ground data can be used to apply the atmospheric correction. The atmospheric correction involves a linear regression to relate the in-situ reflectance values of the PITs to the "at-satellite" reflectance of pseudo-invariant targets in each band. In the PITs method, the slope and intercept of the regression equation represent the correction coefficients required to correct the whole image. A separated regression equation is fitted for each wavelength. The empirical line method assumes that across the image, the effects of the atmosphere are uniform and there are no differences in illumination.

8.1.1 Background

Volchok and Schott (1986) were the first to outline the use of pseudo-invariant targets. Several researchers utilized two pseudo invariant targets for calibration with at least one light and one dark target (Schott et al., 1988; Caselles and Garcia, 1989; Kruse et al., 1990; Ben-dor et al., 1994; Van Der Meer, 1994). Ferrier and Wadge (1996) attempted to use four pseudo-invariant calibration targets while Escadafal et al. (1997) used two pseudo-invariant targets to perform a radiometric correction based on a simple linear stretch and offset. Smith and Milton (1999) also attempted to use four pseudo-invariant calibration targets. Berger (2001) utilized vegetation and biophysical variables as pseudo-invariant

targets, while Hall et al. (2002) used water bodies, especially glaciers as pseudo-invariant targets. Du et al. (2001; 2002) developed the pseudo invariant feature regression that used the major axis of scatter plots from image pairs to determine the pseudo-invariant targets and adjusts each image based on the mean and standard of the pseudo-invariant targets. Du et al. (2002) developed the Principal Component Analysis (PCA) to aid in the selection of invariant targets. Huang et al. (2002) also used pseudo-invariant targets to develop a normalization algorithm. As well, Karpouzli and Malthus (2003) used the empirical line method and established reflectance measurements using four pseudo invariant targets. Canty et al. (2004) developed the multivariate alteration detection (MAD) method based on pseudo-invariant targets, which was validated for forest environments by Schroeder et al. (2006). Caprioli et al. (2008) used the MAD method on Landsat images of a mountainous region and found this normalization algorithm to be effective. According to Baugh and Groeneveld (2008) there is a currently a trend in the research in using more pseudo-invariant targets.

Hadjimitsis et al. (2009) proposed a new and relatively simple atmospheric correction method that used three pseudo-invariant targets of varying spectral characteristics in conjunction with the empirical line method. This method selects a number of suitable pseudo invariant targets on the basis that they are large, distinctive in shape and occur in many geographic areas. It uses a linear regression model by regressing ground reflectance values obtained from previous ground measurements against at satellite reflectance for the selected pseudo-invariant targets. In this thesis, five pseudo-targets with different spectral characteristics were used to conduct the linear regression, as indicated in Figure 8-1.

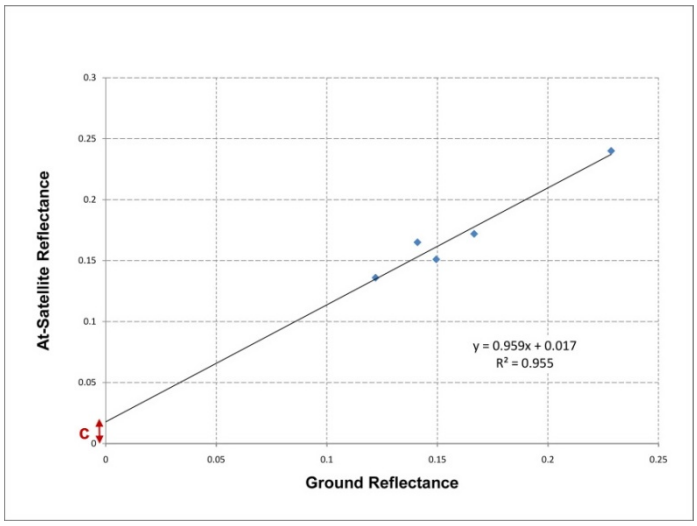

Figure 8-1 Application of the empirical line atmospheric correction method. The intercept on the x-axis represents the atmospheric path component

8.1.2 Reference Targets

Research by Brest and Goward (1987) and Smith and Milton (1999) found that the selection of suitable reference targets must be taken into account since validation of a linear relationship between image DN, radiance, or reflectance with field data is assumed. It is recommended that a wide range of reflectance are measured and preliminary spectral measurements are made before the final selection of the targets in order to reduce extrapolation beyond the reference data (Karpouzli and Malthus 2003). Research by Emery et al. (1998) indicated that the empirical line calibration is more effective when bright and dark targets with sufficient size to enable accurate selection of image pixels are used. The most commonly used reference targets are large bright concrete and asphalt surfaces (bright asphalt), and dark asphalt and water targets (dark objects).

In order to use pseudo-invariant targets in the empirical line method, the following assumptions are made:

- The reflectance of the pseudo invariant targets do not vary between the images.
- The reflectance at ground level can be obtained from ground measurements or from standard values.
- The five targets have varying spectral characteristics from light to dark.
- The effects of multiple scattering are neglected.
- The images are acquired over a short time interval.
- Relative humidity does not have a significant effect on aerosols in band 1 (Hadjimitsis et al., 2002).

8.2 Methodology

In this thesis, the author revised the existing empirical line method by using five pseudo-invariant targets of varying spectral characteristics (PITs method) and by providing standard ground spectroradiometric measurements for both wet and dry conditions. The methodology used for the empirical line method is presented in Figure 6-8.

As discussed in Chapter 7, a preliminary study was conducted to determine possible targets by identifying homogenous areas on existing satellite imagery of the target area and five different surfaces were identified as non-variant. Hadjimitsis et al. (2009) used the atmospheric model for a homogeneous Lambertian surface (Deschamps et al., 1983a and b; Lach and Kerekes, 2008; Bartlett and Schott, 2009; Caselles and Garcia, 1989; Kaufman,

1989; Markham and Barker, 1985) to develop the empirical line method using pseudo-invariant targets equation. Hadjimitsis et al. (2009), recommended equation 8-1 for the empirical line method, which is present below:

$$\rho_{ts} = (c + m)\rho_{tg} \tag{8-1}$$

where

ρ_{ts} is the at-satellite reflectance,
ρ_{tg} is the at-ground reflectance,
c is the intercept
m is the slope

Equation 8-1 indicates the linear relationship between the in-situ target reflectance and the at-satellite reflectance; therefore high and low radiance targets can then be used to determine the constants for the assumed reflectance of the PITs for each band. The intercepts (c) represent the additive effect due to atmospheric path radiance and the slopes (m) represent the correction for atmospheric attenuation. The intercept and slope coefficients are then used for the whole image to extract the corrected reflectance at ground level for any target in the scene, as indicated in Equation 8-2.

$$\rho_{tg} = \frac{\rho_{ts}}{m} - \frac{c}{m} \tag{8-2}$$

8.2.1 Application of the PITs method

The PITs method was conducted through a linear regression using equation 8-2 done with Excel software program. For each separate field campaign date, a linear regression was conducted for the in-situ spectroradiometric reflectance values and the at-satellite reflectance values of each band of the five targets. The average reflectance value of each target from the satellite image was used in the linear regression, as was the average reflectance value of the Gray Asphalt, Black Asphalt, and Concrete target. However, the minimum reflectance value of the Black Sand and Compacted Sand targets was used in the linear regression. This is because the surface of both sand targets was affected by several factors, such as the mineralogy and grain of the sand, dried salt, and wet areas. Therefore,

the lowest in-situ reflectance value of the Black Sand and Compacted Sand was used. A chart was created that used x-y scatterplots in order to conduct a linear regression for each date by band. Through the linear regression, the atmospheric path radiance component (*c*), slope *(m)* and the correlation coefficient for each band was calculated. The value derived from equation 8-2 is subtracted from the image in each band in order to produce the atmospherically corrected image. The atmospheric path radiance component was then used in the radiative transfer equation to determine the AOT derived from the satellite image.

The PITs method was applied to the Landsat-5 TM and Landsat 7 ETM+ images by using five pseudo-invariant targets described in Chapter 7. Figures 8-3 to 8-13 that indicate the graphs for the satellite image by band indicating the correlation coefficient are presented below. Following, Table 7-2 presents the slope *(m)* and intercept *(c)* as derived from the improved PITs method. Table 7-3 indicates the reflectance values in percentage in each band before and after the atmospheric correction.

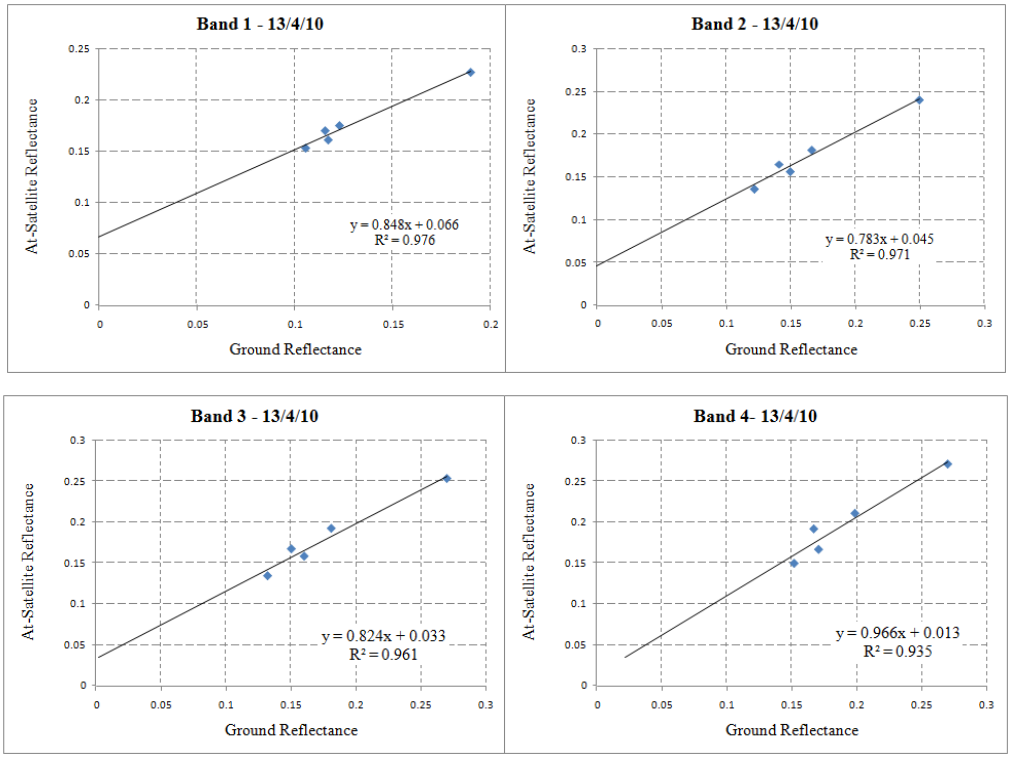

Figure 8-2 Empirical line method for 13/4/10, bands 1, 2, 3 and 4

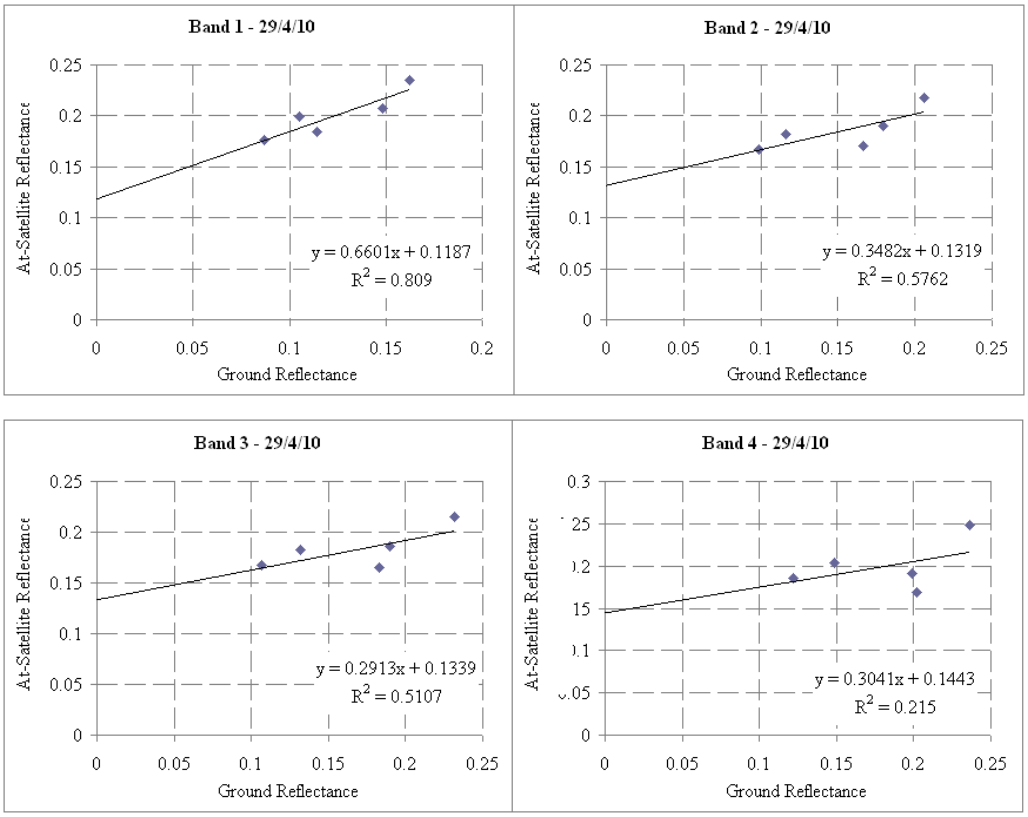

Figure 8-3 Empirical line method for 29/4/10, bands 1, 2, 3 and 4

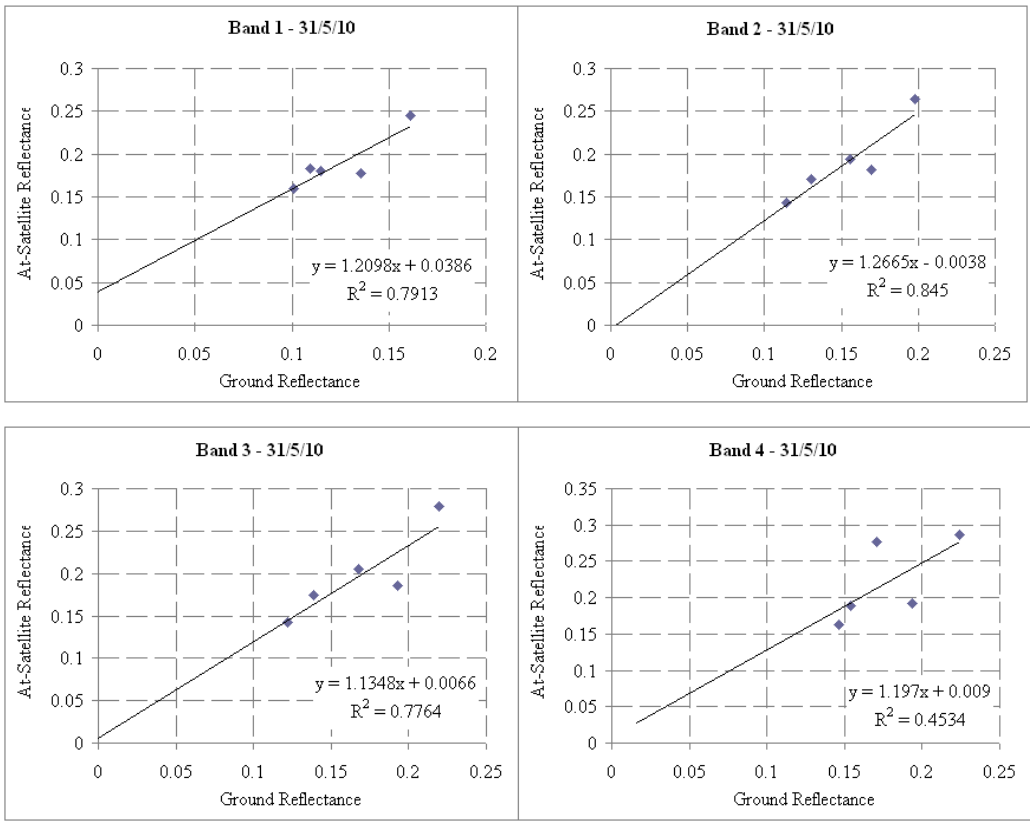

Figure 8-4 Empirical line method for 31/5/10, bands 1, 2, 3 and 4

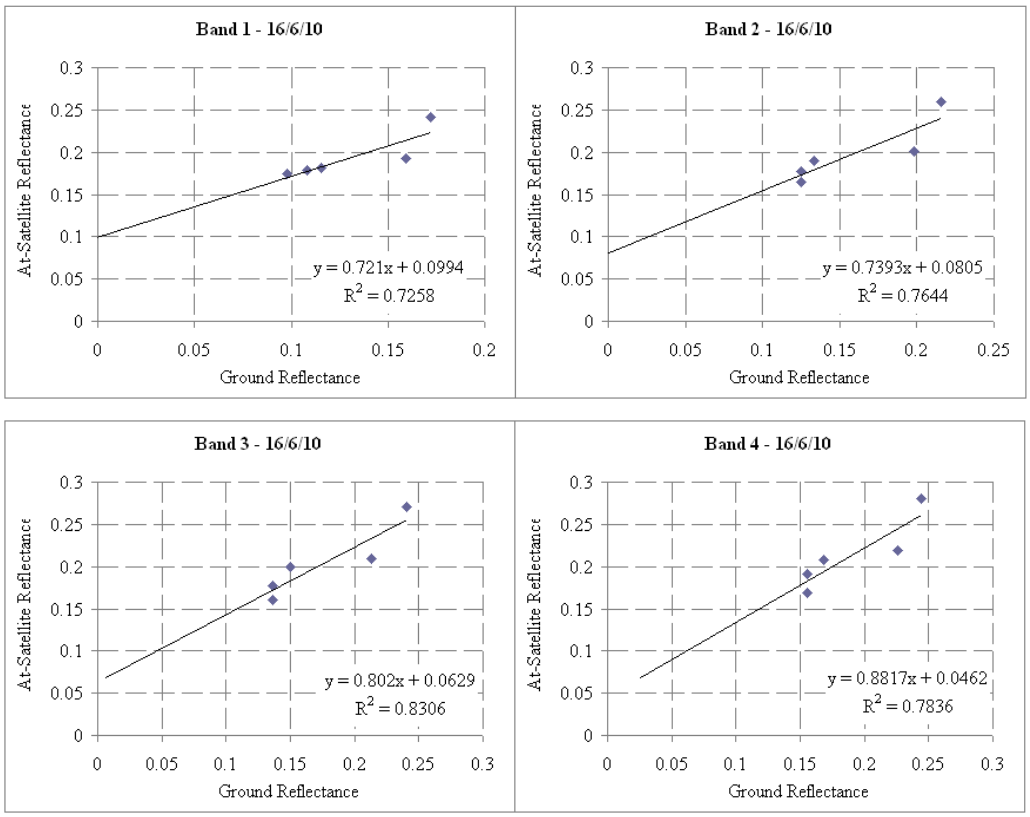

Figure 8-5 Empirical line method for 16/6/10, bands 1, 2, 3 and 4

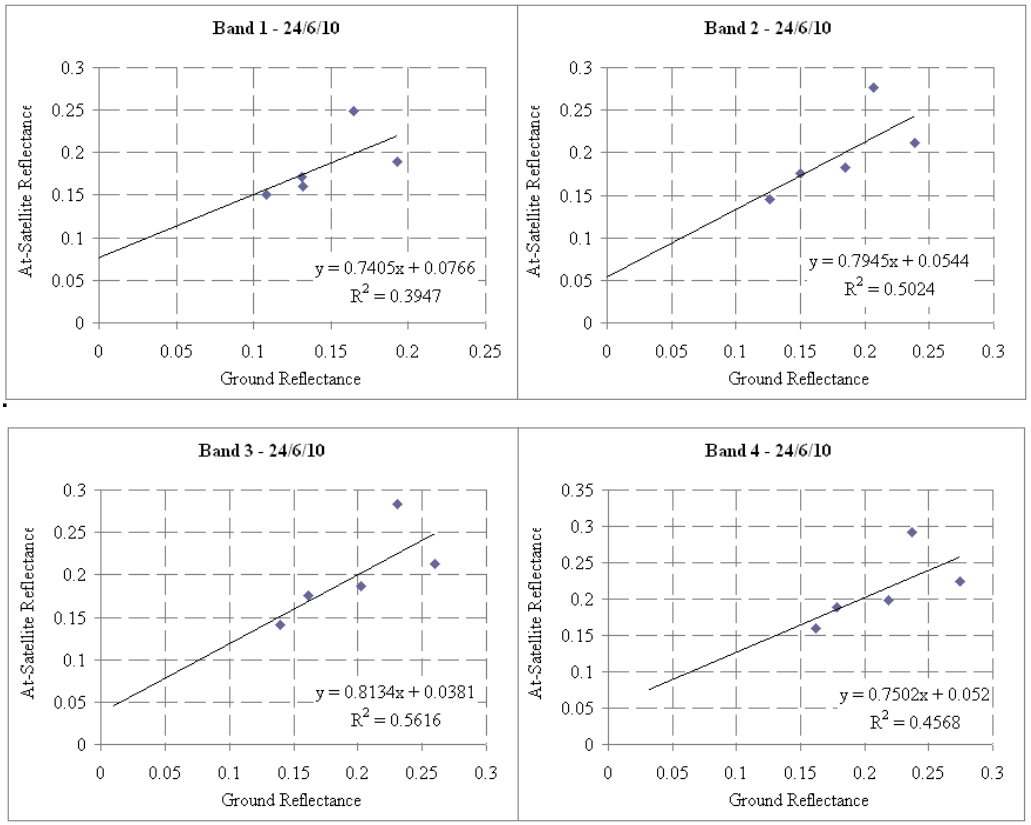

Figure 8-6 Empirical line method for 24/6/10, bands 1, 2, 3 and 4

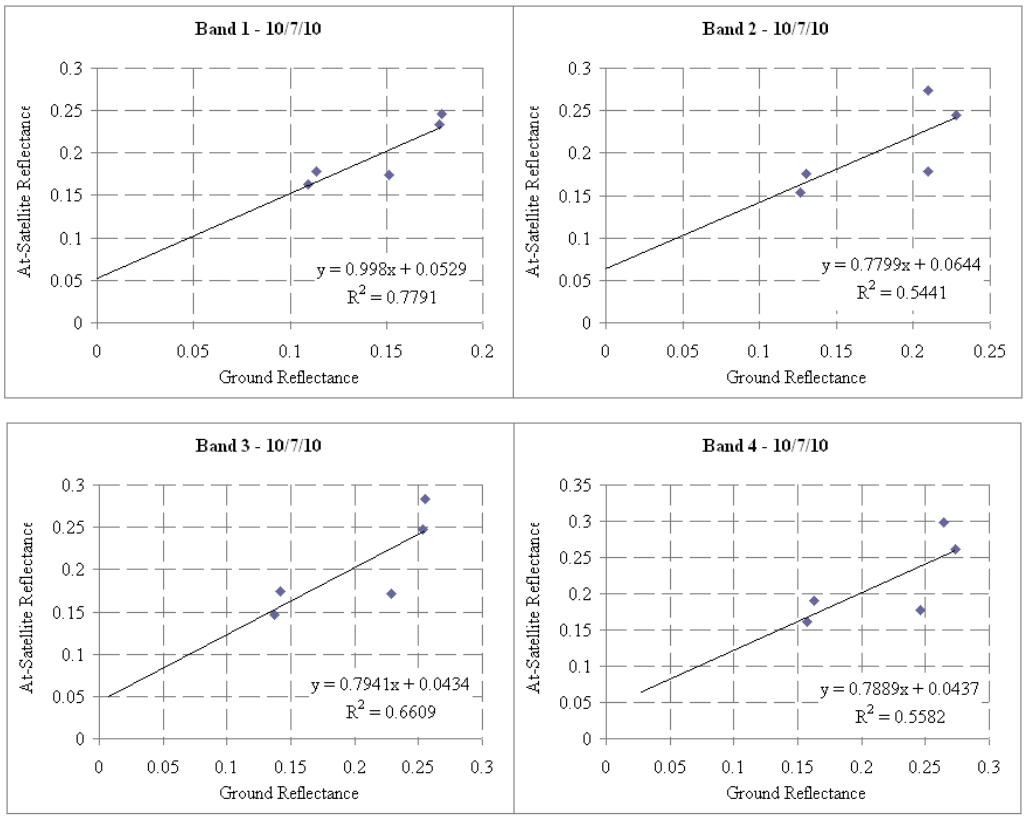

Figure 8-7 Empirical line method for 10/7/10, bands 1, 2, 3 and 4

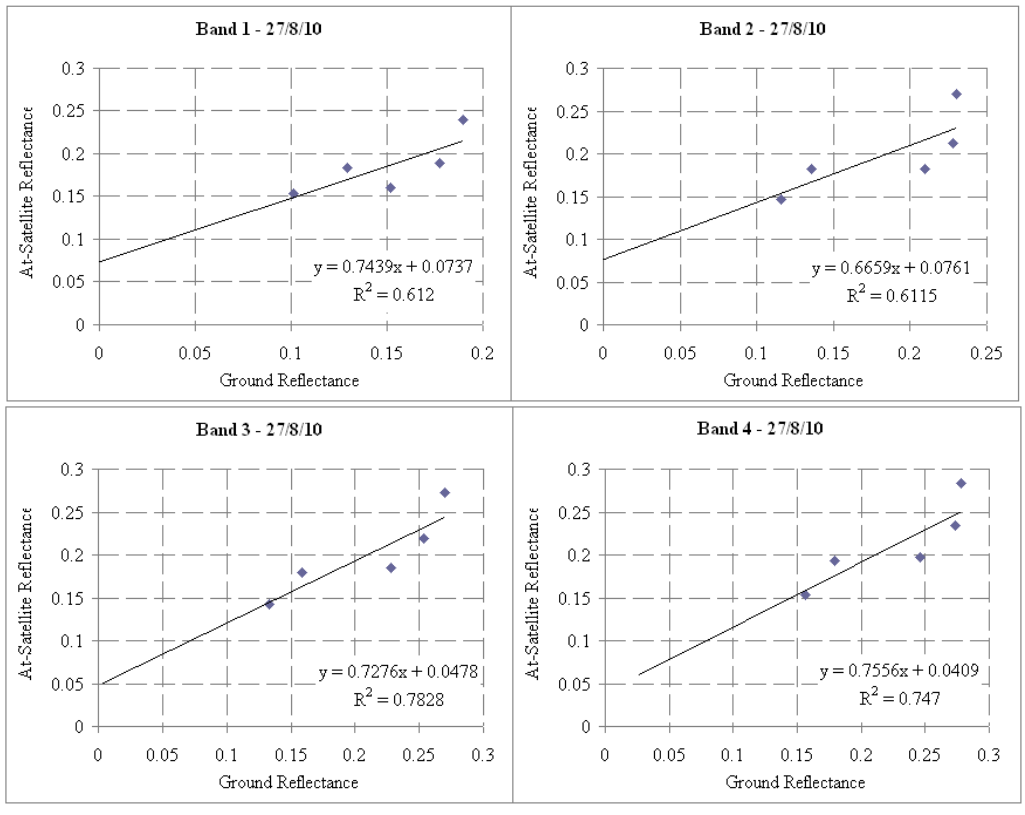

Figure 8-8 Empirical line method for 27/8/10, bands 1, 2, 3 and 4

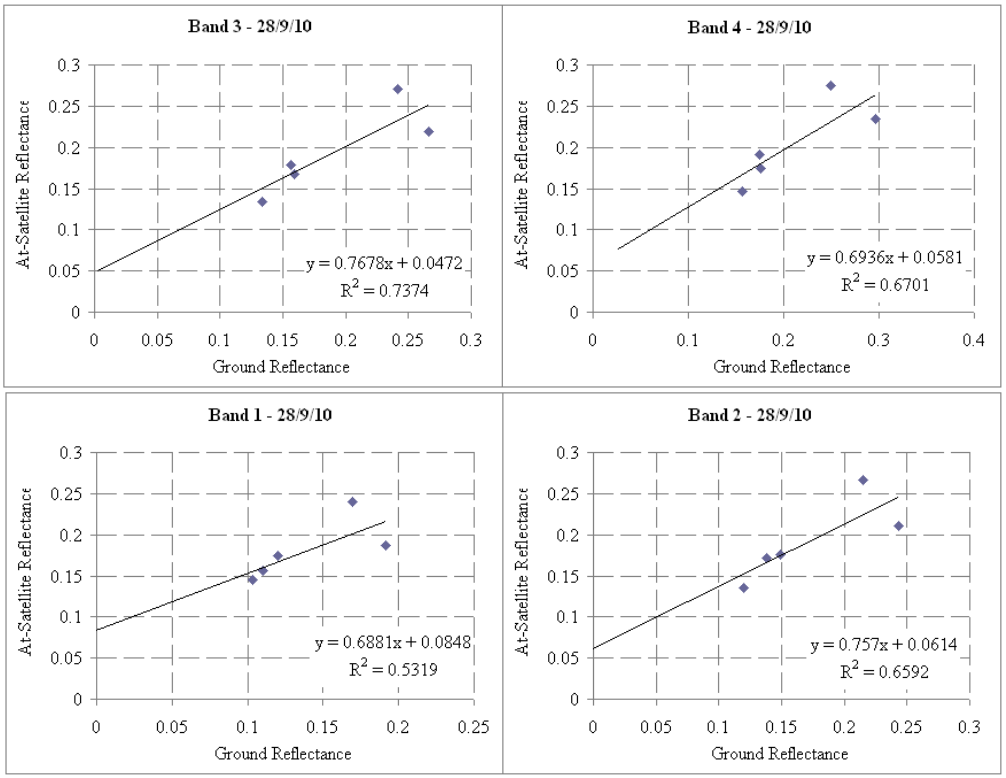

Figure 8-9 Empirical line method for 28/9/10, bands 1, 2, 3 and 4

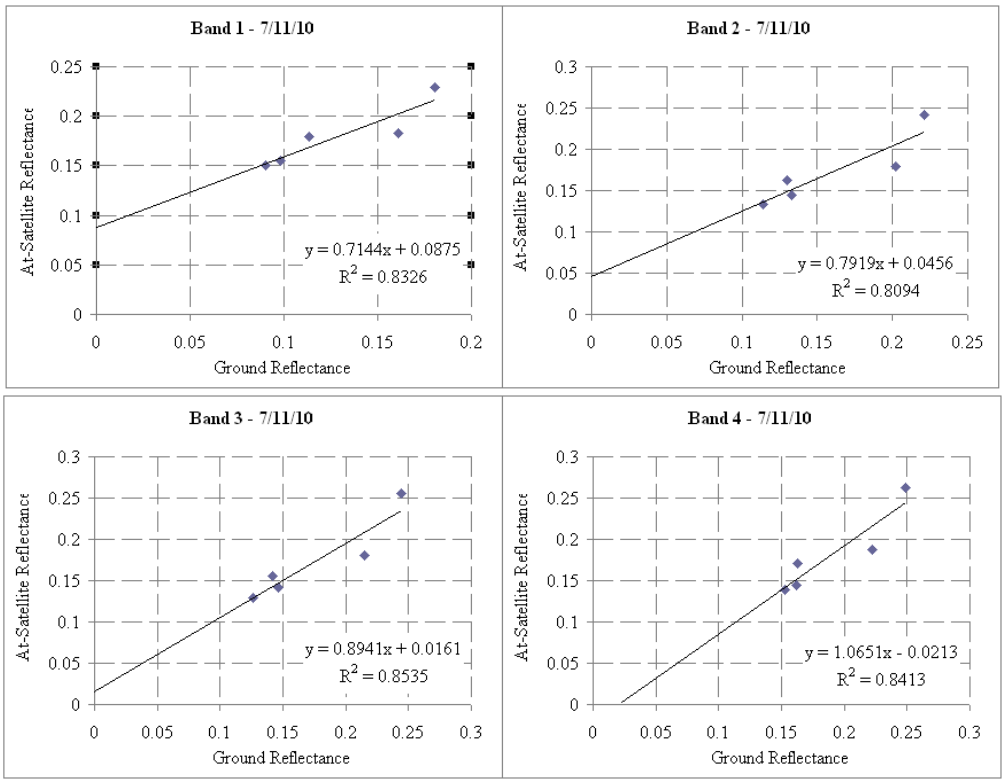

Figure 8-10 Empirical line method for 7/11/10, bands 1, 2, 3 and 4

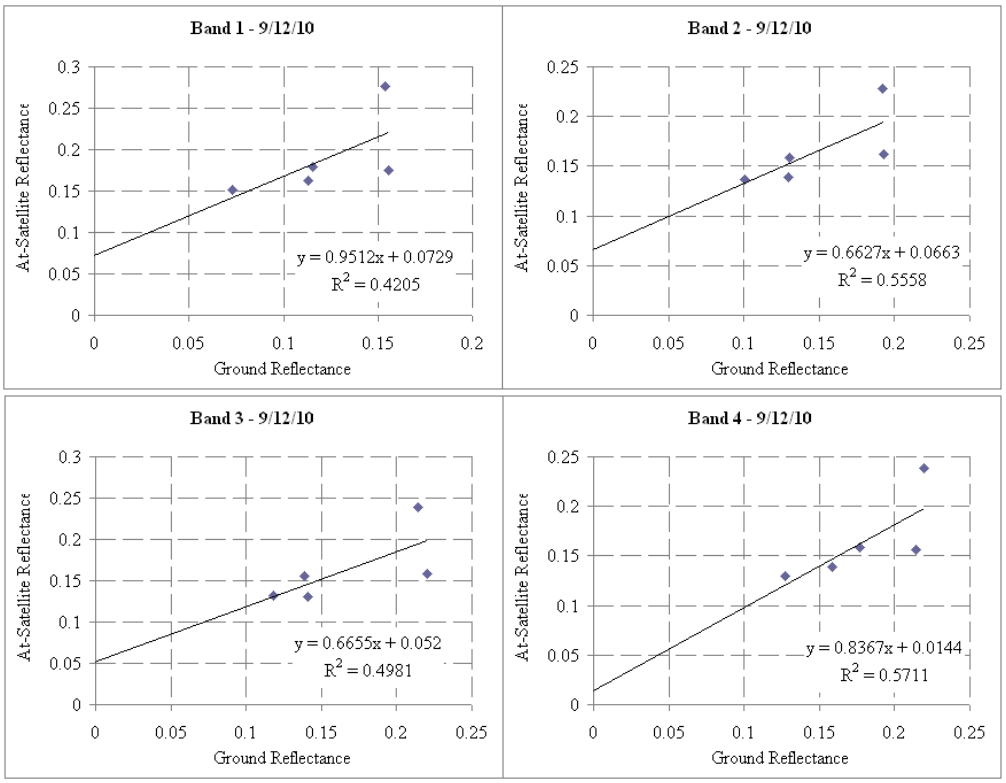

Figure 8-11 Empirical line method for 9/12/10, bands 1, 2, 3 and 4

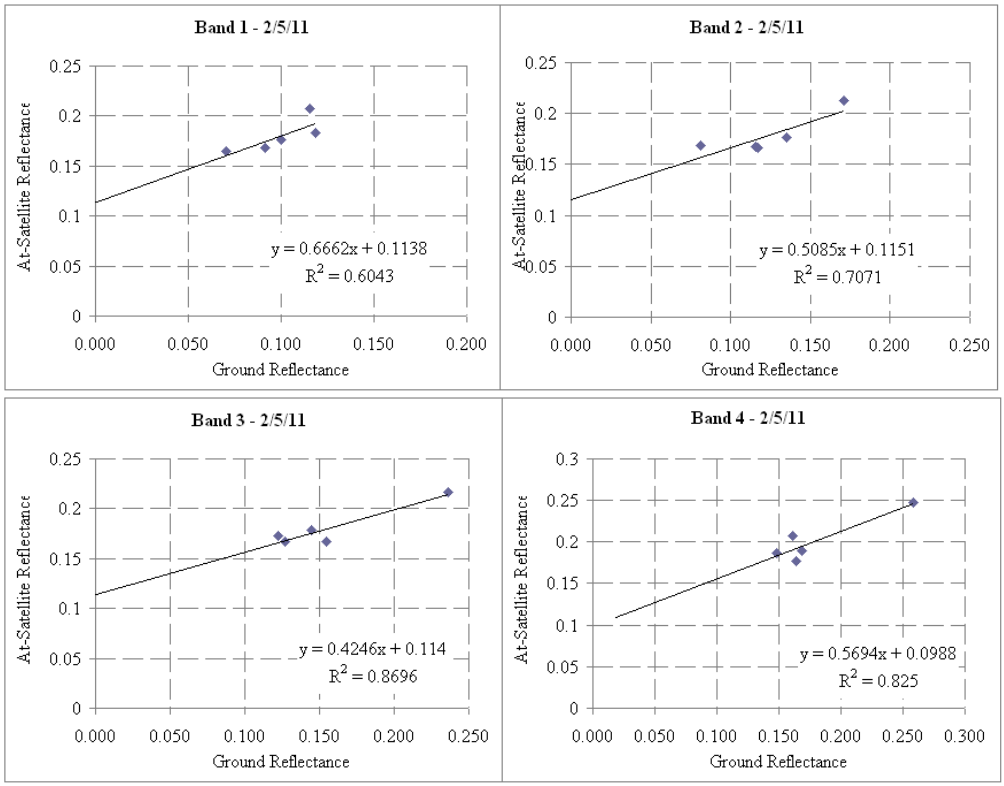

Figure 8-12 Empirical line method for 2/5/10, bands 1, 2, 3 and 4

Below are the regression coefficients calculated by using the empirical line method.

Image date	TM bands	Slope *(m)*	Intercept *(c)*
13/4/10	1	0.97	0.05
	2	0.94	0.01
	3	0.92	0.01
	4	1.01	-0.08
29/4/10	1	0.66	0.12
	2	0.35	0.13
	3	0.29	0.13
	4	0.30	0.14
31/5/10	1	1.21	0.04
	2	1.27	0.04
	3	1.13	0.01
	4	1.20	0.01
16/6/10	1	0.72	0.99
	2	0.74	0.08
	3	0.80	0.06
	4	0.88	0.05
24/6/10	1	0.74	0.08
	2	0.79	0.05
	3	0.81	0.04
	4	0.75	0.05
10/7/10	1	1.00	0.05
	2	0.78	0.06
	3	0.79	0.04
	4	0.79	0.04
27/8/10	1	0.74	0.07
	2	0.67	0.08
	3	0.73	0.05
	4	0.76	0.04
28/9/10	1	0.69	0.08
	2	0.76	0.06
	3	0.77	0.05
	4	0.69	0.06
7/11/10	1	0.71	0.09
	2	0.79	0.05
	3	0.89	0.02
	4	1.07	-0.02
9/12/10	1	0.95	0.07
	2	0.66	0.06
	3	0.67	0.05
	4	0.84	0.01
2/5/11	1	0.67	0.11
	2	0.51	0.12
	3	0.42	0.11
	4	0.57	0.04

Table 8-1 Regression coefficients calculated using the empirical line method

Below are the reflectance values that were calculated using the new PIT method for Bands 1,2,3 and 4.

Date	Target	BAND 1 (in-situ)	Band 1 (satellite)	Ground Reflectance after correction
13/4/2010	Gray Asphalt	0.12	0.18	0.13
	Black Asphalt	0.11	0.15	0.11
	Concrete	0.18	0.23	0.19
	Black Sand	0.12	0.16	0.12
	Compacted Sand	0.12	0.16	0.11
29/4/2010	Gray Asphalt	0.11	0.20	0.12
	Black Asphalt	0.09	0.18	0.09
	Concrete	0.16	0.24	0.18
	Black Sand	0.11	0.18	0.10
	Compacted Sand	0.15	0.21	0.13
31/5/2010	Gray Asphalt	0.11	0.18	0.12
	Black Asphalt	0.10	0.16	0.10
	Concrete	0.16	0.25	0.17
	Black Sand	0.11	0.18	0.12
	Compacted Sand	0.14	0.18	0.12
16/6/2010	Gray Asphalt	0.12	0.18	0.11
	Black Asphalt	0.11	0.18	0.11
	Concrete	0.17	0.24	0.20
	Black Sand	0.10	0.17	0.10
	Compacted Sand	0.16	0.19	0.13
24/6/2010	Gray Asphalt	0.13	0.17	0.13
	Black Asphalt	0.11	0.15	0.10
	Concrete	0.16	0.25	0.17
	Black Sand	0.13	0.16	0.11
	Compacted Sand	0.19	0.19	0.18
10/7/2010	Gray Asphalt	0.11	0.18	0.13
	Black Asphalt	0.11	0.16	0.11
	Concrete	0.18	0.25	0.19
	Black Sand	0.15	0.17	0.14
	Compacted Sand	0.18	0.23	0.18
27/8/2010	Gray Asphalt	0.13	0.18	0.15
	Black Asphalt	0.10	0.15	0.11
	Concrete	0.19	0.24	0.22
	Black Sand	0.15	0.16	0.14
	Compacted Sand	0.18	0.19	0.16
28/9/2010	Gray Asphalt	0.12	0.17	0.13
	Black Asphalt	0.10	0.15	0.09
	Concrete	0.17	0.24	0.18
	Black Sand	0.11	0.16	0.10
	Compacted Sand	0.19	0.19	0.20
7/11/2010	Gray Asphalt	0.11	0.18	0.13
	Black Asphalt	0.10	0.16	0.10
	Concrete	0.18	0.23	0.20
	Black Sand	0.09	0.15	0.09
	Compacted Sand	0.16	0.18	0.13
9/12/2010	Gray Asphalt	0.12	0.18	0.11

	Black Asphalt	0.11	0.16	0.09
	Concrete	0.15	0.28	0.17
	Black Sand	0.07	0.15	0.08
	Compacted Sand	0.16	0.18	0.14
2/5/2011	Gray Asphalt	0.12	0.18	0.10
	Black Asphalt	0.10	0.18	0.09
	Concrete	0.12	0.21	0.14
	Black Sand	0.07	0.17	0.08
	Compacted Sand	0.09	0.17	0.08

Table 8-2 Reflectance values for all five targets after empirical line atmospheric correction method, band 1

Date	Target	BAND 2 (in-situ)	Band 2 (satellite)	Ground Reflectance after correction
13/4/2010	Gray Asphalt	0.14	0.17	0.16
	Black Asphalt	0.12	0.14	0.13
	Concrete	0.23	0.24	0.23
	Black Sand	0.17	0.17	0.16
	Compacted Sand	0.15	0.15	0.14
29/4/2010	Gray Asphalt	0.12	0.18	0.14
	Black Asphalt	0.10	0.17	0.11
	Concrete	0.21	0.22	0.25
	Black Sand	0.17	0.17	0.11
	Compacted Sand	0.18	0.19	0.17
31/5/2010	Gray Asphalt	0.13	0.17	0.10
	Black Asphalt	0.11	0.14	0.08
	Concrete	0.20	0.26	0.17
	Black Sand	0.16	0.19	0.18
	Compacted Sand	0.17	0.18	0.11
16/6/2010	Gray Asphalt	0.12	0.18	0.13
	Black Asphalt	0.12	0.16	0.11
	Concrete	0.22	0.26	0.24
	Black Sand	0.13	0.19	0.15
	Compacted Sand	0.20	0.20	0.16
24/6/2010	Gray Asphalt	0.15	0.18	0.16
	Black Asphalt	0.13	0.15	0.12
	Concrete	0.21	0.28	0.29
	Black Sand	0.18	0.18	0.16
	Compacted Sand	0.24	0.21	0.20
10/7/2010	Gray Asphalt	0.13	0.18	0.15
	Black Asphalt	0.13	0.15	0.11
	Concrete	0.21	0.27	0.26
	Black Sand	0.21	0.18	0.15
	Compacted Sand	0.23	0.25	0.24
27/8/2010	Gray Asphalt	0.14	0.18	0.16
	Black Asphalt	0.12	0.15	0.11
	Concrete	0.23	0.27	0.29
	Black Sand	0.21	0.18	0.16
	Compacted Sand	0.23	0.21	0.20
28/9/2010	Gray Asphalt	0.14	0.17	0.14

	Black Asphalt	0.12	0.14	0.10
	Concrete	0.21	0.27	0.27
	Black Sand	0.15	0.18	0.16
	Compacted Sand	0.24	0.21	0.20
7/11/2010	Gray Asphalt	0.13	0.16	0.14
	Black Asphalt	0.11	0.13	0.11
	Concrete	0.22	0.24	0.25
	Black Sand	0.13	0.15	0.13
	Compacted Sand	0.20	0.18	0.17
9/12/2010	Gray Asphalt	0.13	0.16	0.14
	Black Asphalt	0.13	0.14	0.11
	Concrete	0.19	0.23	0.25
	Black Sand	0.10	0.14	0.11
	Compacted Sand	0.19	0.16	0.14
2/5/2011	Gray Asphalt	0.14	0.18	0.13
	Black Asphalt	0.12	0.17	0.11
	Concrete	0.17	0.21	0.19
	Black Sand	0.08	0.17	0.11
	Compacted Sand	0.12	0.17	0.11

Table 8-3 Reflectance values for all five targets after empirical line atmospheric correction method, band 2

Date	Target	BAND 3 (in-situ)	Band 3 (satellite)	Ground Reflectance after correction
13/4/2010	Gray Asphalt	0.15	0.17	0.16
	Black Asphalt	0.13	0.13	0.12
	Concrete	0.25	0.25	0.24
	Black Sand	0.18	0.18	0.17
	Compacted Sand	0.16	0.15	0.14
29/4/2010	Gray Asphalt	0.13	0.18	0.16
	Black Asphalt	0.11	0.17	0.12
	Concrete	0.23	0.22	0.30
	Black Sand	0.18	0.17	0.12
	Compacted Sand	0.19	0.19	0.19
31/5/2010	Gray Asphalt	0.14	0.17	0.14
	Black Asphalt	0.12	0.14	0.12
	Concrete	0.22	0.28	0.24
	Black Sand	0.17	0.21	0.18
	Compacted Sand	0.19	0.19	0.16
16/6/2010	Gray Asphalt	0.14	0.18	0.15
	Black Asphalt	0.14	0.16	0.12
	Concrete	0.24	0.27	0.26
	Black Sand	0.15	0.20	0.17
	Compacted Sand	0.21	0.21	0.18
24/6/2010	Gray Asphalt	0.16	0.18	0.18
	Black Asphalt	0.14	0.14	0.13
	Concrete	0.23	0.28	0.30
	Black Sand	0.20	0.19	0.19
	Compacted Sand	0.26	0.21	0.21
10/7/2010	Gray Asphalt	0.14	0.17	0.16

Date	Target	BAND 3 (in-situ)	Band 3 (satellite)	Ground Reflectance after correction
	Black Asphalt	0.14	0.15	0.13
	Concrete	0.26	0.28	0.30
	Black Sand	0.23	0.17	0.16
	Compacted Sand	0.25	0.25	0.26
27/8/2010	Gray Asphalt	0.16	0.18	0.18
	Black Asphalt	0.13	0.14	0.13
	Concrete	0.27	0.27	0.30
	Black Sand	0.23	0.19	0.19
	Compacted Sand	0.25	0.22	0.24
28/9/2010	Gray Asphalt	0.16	0.17	0.16
	Black Asphalt	0.13	0.13	0.11
	Concrete	0.24	0.27	0.29
	Black Sand	0.16	0.18	0.17
	Compacted Sand	0.27	0.22	0.22
7/11/2010	Gray Asphalt	0.14	0.16	0.16
	Black Asphalt	0.13	0.13	0.13
	Concrete	0.24	0.26	0.27
	Black Sand	0.15	0.14	0.14
	Compacted Sand	0.22	0.18	0.18
9/12/2010	Gray Asphalt	0.14	0.16	0.16
	Black Asphalt	0.14	0.13	0.12
	Concrete	0.21	0.24	0.28
	Black Sand	0.12	0.13	0.12
	Compacted Sand	0.22	0.16	0.16
2/5/2011	Gray Asphalt	0.14	0.18	0.16
	Black Asphalt	0.13	0.17	0.13
	Concrete	0.24	0.22	0.25
	Black Sand	0.12	0.17	0.13
	Compacted Sand	0.15	0.17	0.13

Table 8-4 Reflectance values for all five targets after empirical line atmospheric correction method, band 3

Date	Target	BAND 4 (in-situ)	Band 4 (satellite)	Ground Reflectance after correction
13/4/2010	Gray Asphalt	0.17	0.19	0.27
	Black Asphalt	0.15	0.15	0.23
	Concrete	0.26	0.27	0.35
	Black Sand	0.20	0.20	0.28
	Compacted Sand	0.17	0.16	0.24
29/4/2010	Gray Asphalt	0.15	0.20	0.19
	Black Asphalt	0.12	0.19	0.15
	Concrete	0.24	0.25	0.35
	Black Sand	0.20	0.17	0.09
	Compacted Sand	0.20	0.19	0.15
31/5/2010	Gray Asphalt	0.15	0.19	0.16
	Black Asphalt	0.15	0.16	0.13

Date	Target	BAND 4 (in-situ)	Band 4 (satellite)	Ground Reflectance after correction
	Concrete	0.22	0.29	0.24
	Black Sand	0.17	0.28	0.23
	Compacted Sand	0.19	0.19	0.16
16/6/2010	Gray Asphalt	0.16	0.19	0.16
	Black Asphalt	0.16	0.17	0.14
	Concrete	0.24	0.28	0.27
	Black Sand	0.17	0.21	0.19
	Compacted Sand	0.23	0.22	0.20
24/6/2010	Gray Asphalt	0.18	0.19	0.18
	Black Asphalt	0.16	0.16	0.14
	Concrete	0.24	0.29	0.32
	Black Sand	0.22	0.20	0.20
	Compacted Sand	0.27	0.23	0.24
10/7/2010	Gray Asphalt	0.16	0.19	0.19
	Black Asphalt	0.16	0.16	0.15
	Concrete	0.26	0.30	0.32
	Black Sand	0.25	0.18	0.17
	Compacted Sand	0.27	0.26	0.27
27/8/2010	Gray Asphalt	0.18	0.19	0.20
	Black Asphalt	0.16	0.15	0.14
	Concrete	0.28	0.28	0.31
	Black Sand	0.25	0.20	0.21
	Compacted Sand	0.27	0.23	0.25
28/9/2010	Gray Asphalt	0.18	0.18	0.18
	Black Asphalt	0.16	0.15	0.13
	Concrete	0.25	0.28	0.32
	Black Sand	0.18	0.19	0.19
	Compacted Sand	0.30	0.23	0.25
7/11/2010	Gray Asphalt	0.16	0.17	0.18
	Black Asphalt	0.15	0.14	0.15
	Concrete	0.25	0.26	0.26
	Black Sand	0.16	0.14	0.15
	Compacted Sand	0.22	0.19	0.20
9/12/2010	Gray Asphalt	0.18	0.16	0.17
	Black Asphalt	0.16	0.14	0.15
	Concrete	0.22	0.24	0.27
	Black Sand	0.13	0.13	0.14
	Compacted Sand	0.21	0.16	0.17
2/5/2011	Gray Asphalt	0.16	0.21	0.30
	Black Asphalt	0.15	0.19	0.27
	Concrete	0.26	0.25	0.37
	Black Sand	0.17	0.19	0.27
	Compacted Sand	0.16	0.18	0.25

Table 8-5 Reflectance values for all five targets after empirical line atmospheric correction method, band 4

8.3 Darkest Pixel Method

The Darkest Pixel (DP) method is the most widely applied method of atmospheric correction that provides reasonable correction, especially in cloud-free skies (Schott, 1997; Cheng and Lei, 2001; Hadjimitsis et al., 2004). This simple and widely used method of atmospheric correction is also called the histogram minimum method (Campbell, 2008; Schott, 1997), the darkest object subtraction method (Crane, 1971; Chavez, 1988; Chavez, 1989; Moran et al., 1992), the dark target approach (Teillet and Fedosejevs, 1995) and the single-image normalisation method using histogram adjustment (Jensen, 1996). The darkest pixel (DP) method is based on the assumption that the pixel with the lowest digital number (DN) in each band should in reality be zero and therefore its radiometric DN value represents the atmospheric additive effect (Crane, 1971; Crippen, 1987; Campbell, 1996).

According to the DP method, most of the signal reaching a satellite sensor from a dark object is affected by the atmosphere at visible wavelengths. Therefore, the amount of upwelling path radiance in each band can be measured from the pixels from dark targets on the satellite image. Since the atmospheric path radiance affects the surface radiance of the dark target, the radiance resulting from corresponding pixels is considered proportional to the atmospheric path radiance and can used to account for the additive effect of atmospheric scattering (Wu et al., 2005). Therefore, the selection of an appropriate dark target is crucial (Gilabert et al., 1994). The DP method incorporates histogram adjustment, which is based on the premise that visible bands, especially the blue band, have a higher brightness value. Therefore, band histograms are adjusted by subtracting the bias for each histogram, so that each histogram starts at zero. This method assumes that the darkest pixels should have zero reflectance. However, according to Gilabert et al. (1994), one of the limitations of the traditional dark object subtraction method of atmospheric correction is that it only removes haze but does not provide actual reflectance values.

Hadjimitsis (2004; 2009) found that the DP method is more efficient for wavelength regions of 0.45-0.70 μm. Chrysoulakis et al. (2010) compared several atmospheric correction methods for the area of Crete and found that the DP method provided satisfactory results for visible, near infrared and short-wave infrared spectral areas. Hadjimitsis and Clayton (2009) developed the improved DP method that differs from the traditional DP method in that it incorporates the true reflectance value acquired from in-situ spectroradiometric measurements of selected pseudo-invariant dark targets and combines both the darkest pixel method and the radiative transfer equation. In this thesis,

the DP method is used to calculate the atmospheric path radiance component and then retrieve the AOT values using the radiative transfer equations. The methodology used for the darkest pixel method is indicated in Figure 6-9.

8.4 Darkest pixel method using radiance and reflectance

The DP algorithm is discussed below using the physical units of radiance and a simple mathematical simulation, since digital numbers are given a physical meaning in terms of water and land surface characteristics in most research. Firstly, the conversion of DNs to radiance is made, followed by the conversion of radiance to reflectance, as discussed in Chapter 6. Following, the satellite image is opened, and the closest darkest pixel is determined. In this thesis, the improved darkest pixel method was used on the Black Asphalt target, as it had the lowest reflectance value of all the five targets, and finding the darkest pixel within the area of interest. This was done by identifying the area of interest (AOI) and finding the average, minimum and maximum reflectance values for each band within the AOI area. A model was created in order to subtract the lowest reflectance values from the darkest pixel. The lowest reflectance value of the darkest pixel in each band was subtracted from the entire image. Therefore, the entire image was atmospherically corrected to reflect the in-situ spectral measurements. An accuracy assessment was conducted to compare the in-situ measurements with the atmospherically corrected satellite reflectance values, as presented in Chapter 10.

8.4.1 Application of the Darkest Pixel method to Landsat TM/ETM+ images

The DP atmospheric correction method was been applied to a series of Landsat 5 TM and Landsat 7 ETM+ satellite images. In Tables 8-6 to Tables 8-9, the average reflectance value before and after the DP method of atmospheric correction are presented, as well as the minimum, maximum and average reflectance values of the in-situ measurements taken with the SVC HR 1024 spectroradiometer by date and band for the Black Asphalt. Figures 8-15 to 8-36 indicate the satellite images before and after the atmospheric correction by date.

Image date	ρ% before DP	ρ% after DP	SVC HR 1024 Min in %	SVC HR 1024 Max in %	SVC HR 1024 Average in %
13/4/10	15.3	10.6	9.83	11.36	10.59
29/4/10	17.6	8.91	8.27	9.10	8.69
31/5/10	15.9	10.1	9.35	10.85	10.10
16/6/10	17.8	10.8	10.05	11.56	10.81
24/6/10	15.1	10.9	9.99	11.72	10.86
10/7/10	16.3	10.9	10.18	11.72	10.95
27/8/10	15.4	10.1	8.90	11.40	10.15
28/9/10	14.5	10.3	8.86	11.75	10.31
7/11/10	15.5	9.9	8.83	10.86	9.85
9/12/10	16.3	11.3	10.58	12.01	11.30
2/5/11	17.6	10.0	6.62	8.43	9.98

Table 8-6 Reflectance values for Black Asphalt, Band 1 before and after DP method of atmospheric correction

Image date	ρ% before DP	ρ% after DP	SVC HR 1024 Min in %	SVC HR 1024 Max in %	SVC HR 1024 Average in %
13/4/10	13.6	12.2	11.39	13.03	12.21
29/4/10	16.7	9.92	9.43	10.40	9.91
31/5/10	14.3	11.5	10.90	11.97	11.44
16/6/10	16.4	12.5	11.64	13.348	12.49
24/6/10	14.5	12.7	11.66	13.63	12.64
10/7/10	15.4	12.7	11.77	13.47	12.62
27/8/10	14.7	12.7	10.89	12.29	11.59
28/9/10	13.6	12.1	10.78	13.22	12.00
7/11/10	13.3	11.3	10.21	12.54	11.37
9/12/10	13.9	12.9	12.08	13.78	12.93
2/5/11	16.7	11.6	13.20	15.08	11.56

Table 8-7 Reflectance values for Black Asphalt, Band 2 before and after DP method of atmospheric correction

Image date	ρ% before DP	ρ% after DP	SVC HR 1024 Min in %	SVC HR 1024 Max in %	SVC HR 1024 Average in %
13/4/10	13.4	13.2	12.40	14.02	13.21
29/4/10	16.7	10.70	10.28	11.13	10.71
31/5/10	14.3	12.2	12.13	12.27	12.20
16/6/10	16.0	13.7	12.75	14.52	13.63
24/6/10	14.1	14.0	13.00	14.96	13.98
10/7/10	14.7	13.8	12.97	14.54	13.75
27/8/10	14.2	13.3	11.97	14.67	13.32
28/9/10	13.4	13.3	11.68	14.94	13.31
7/11/10	12.9	12.6	11.39	13.79	12.59
9/12/10	13.0	14.0	13.20	14.95	14.07
2/5/11	16.7	12.7	16.70	19.27	12.69

Table 8-8 Reflectance values for Black Asphalt, Band 3 before and after DP method of atmospheric correction

Image date	ρ% before DP	ρ% after DP	SVC HR 1024 Min in %	SVC HR 1024 Max in %	SVC HR 1024 Average in %
13/4/10	15.0	15.2	14.37	16.01	15.19
29/4/10	18.6	12.2	11.91	12.55	12.23
31/5/10	16.3	14.6	14.50	14.69	14.60
16/6/10	16.9	15.5	14.556	16.48	15.52
24/6/10	16.0	16.1	15.18	17.22	16.20
10/7/10	16.1	15.7	15.11	16.34	15.72
27/8/10	15.4	15.6	14.64	16.59	15.62
28/9/10	14.6	15.6	15.00	16.21	15.61
7/11/10	13.9	15.3	14.13	16.49	15.31
9/12/10	13.9	15.8	15.20	16.44	15.82
2/5/11	18.6	14.9	18.65	21.94	14.84

Table 8-9 Reflectance values for Black Asphalt, Band 4 before and after DP method of atmospheric correction

Satellite image 13/4/2010, by band, before atmospheric correction

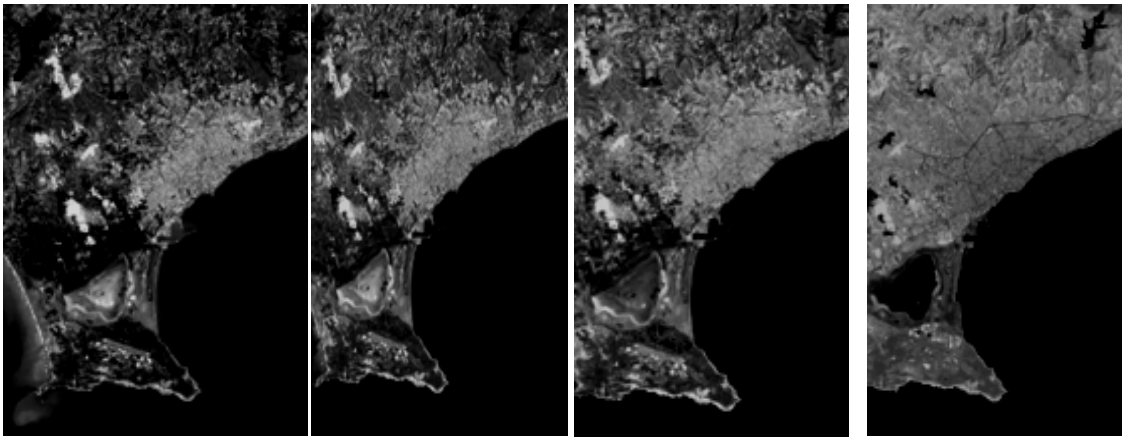

Band 1 Band 2 Band 3 Band 4

Satellite image 13/4/2010, by band, after atmospheric correction

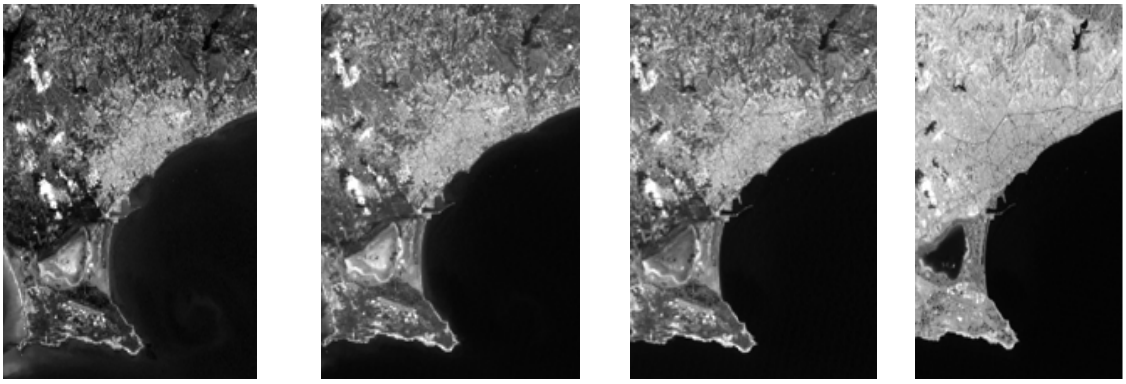

Band 1 Band 2 Band 3 Band 4

Figure 8-13 Satellite image (13/4/2010) before and after atmospheric correction by band

Figure 8-14 Satellite image acquired on 13/4/2010 before (left) and after (right) atmospheric correction using DP method

Satellite image 29/4/2010, by band, before atmospheric correction

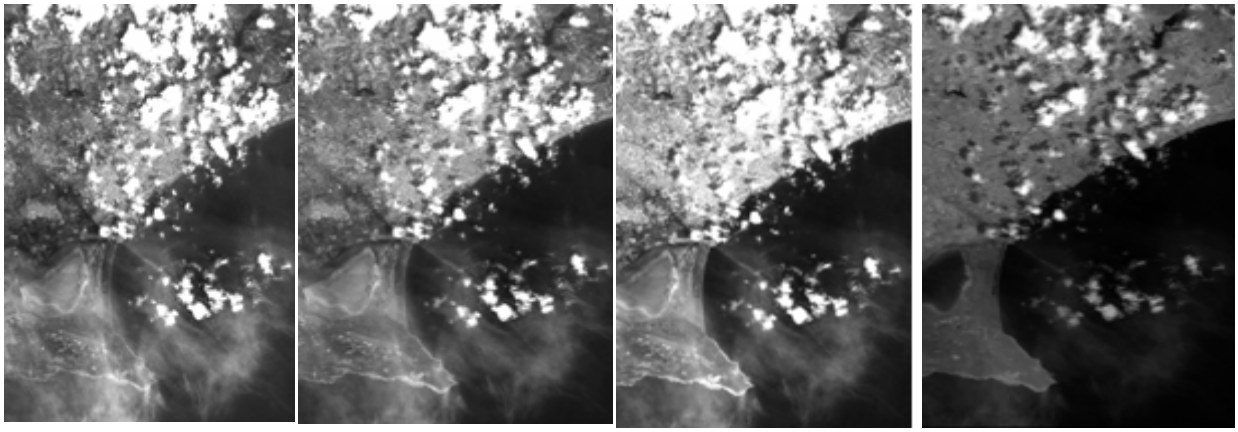

Band 1 Band 2 Band 3 Band 4

Satellite image 29/4/2010, by band, after atmospheric correction

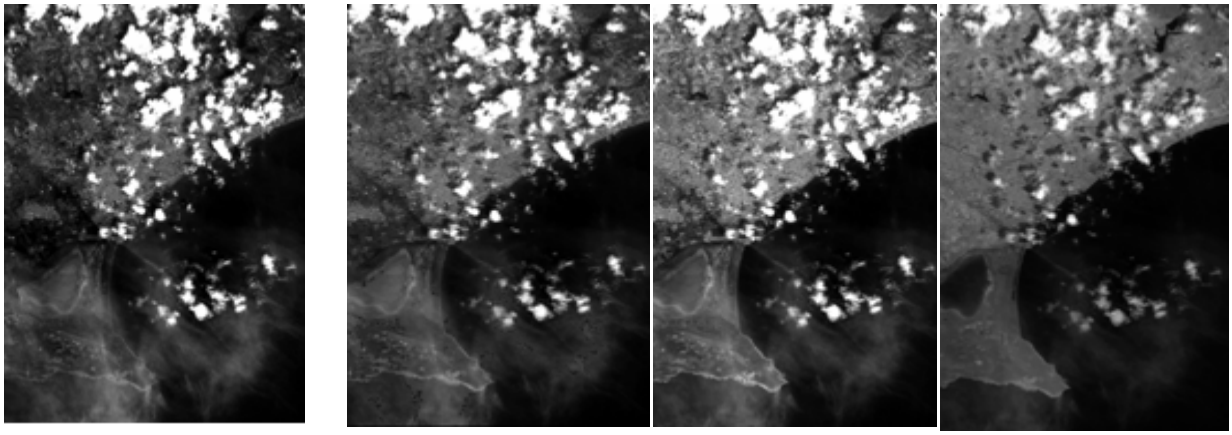

Band 1 Band 2 Band 3 Band 4

Figure 8-15 Satellite image (29/4/2010) before and after atmospheric correction by band

Figure 8-16 Satellite images acquired 29/4/2010 before (left) and after (right) atmospheric correction using DP method

Satellite image 31/5/2010, by band, before atmospheric correction

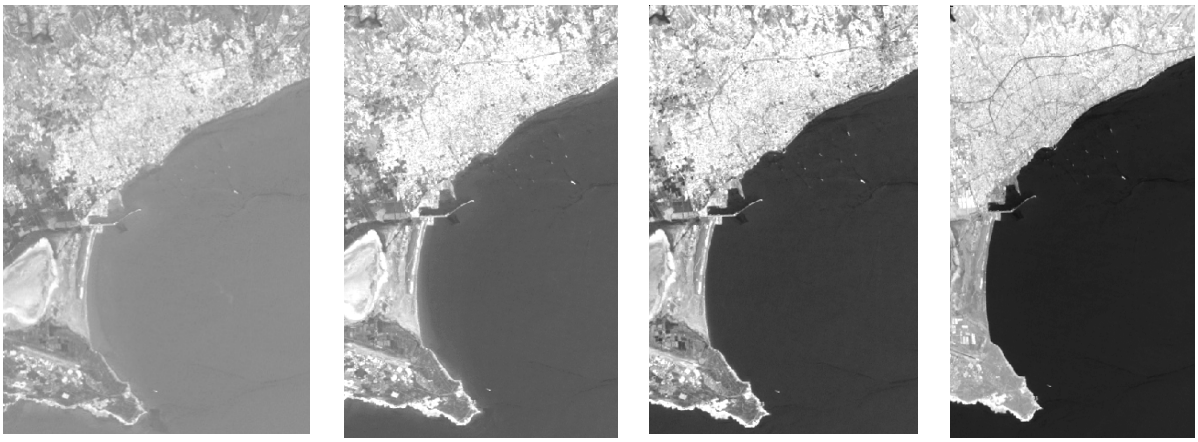

Band 1 Band 2 Band 3 Band 4

Satellite image 31/5/2010, by band, after atmospheric correction

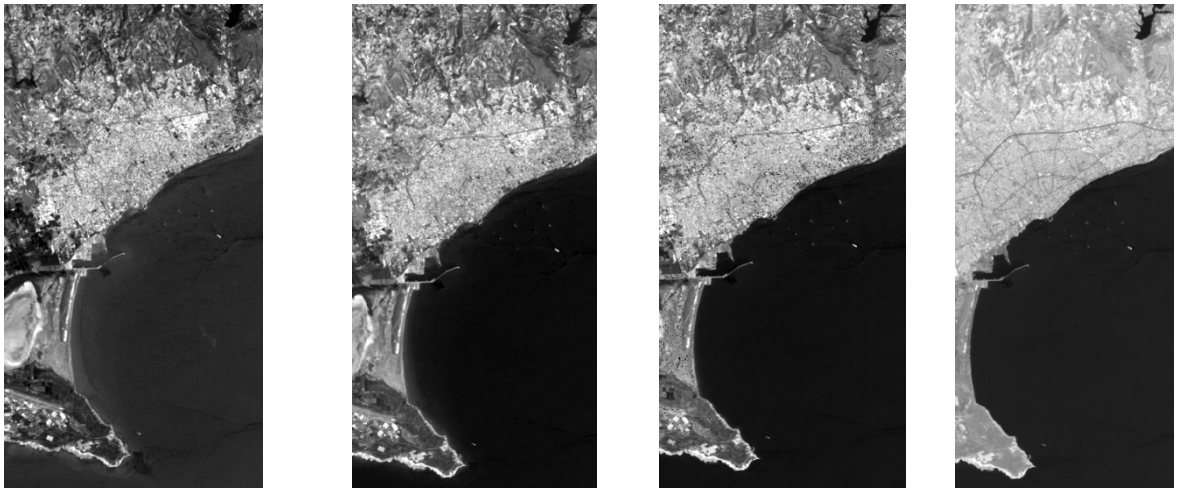

Band 1 Band 2 Band 3 Band 4

Figure 8-17 Satellite images (31/5/2010) before and after atmospheric correction by band

Figure 8-18 Satellite images acquired 31/5/2010 before (left) and after (right) atmospheric correction using DP method

Satellite image 16/6/2010, by band, before atmospheric correction

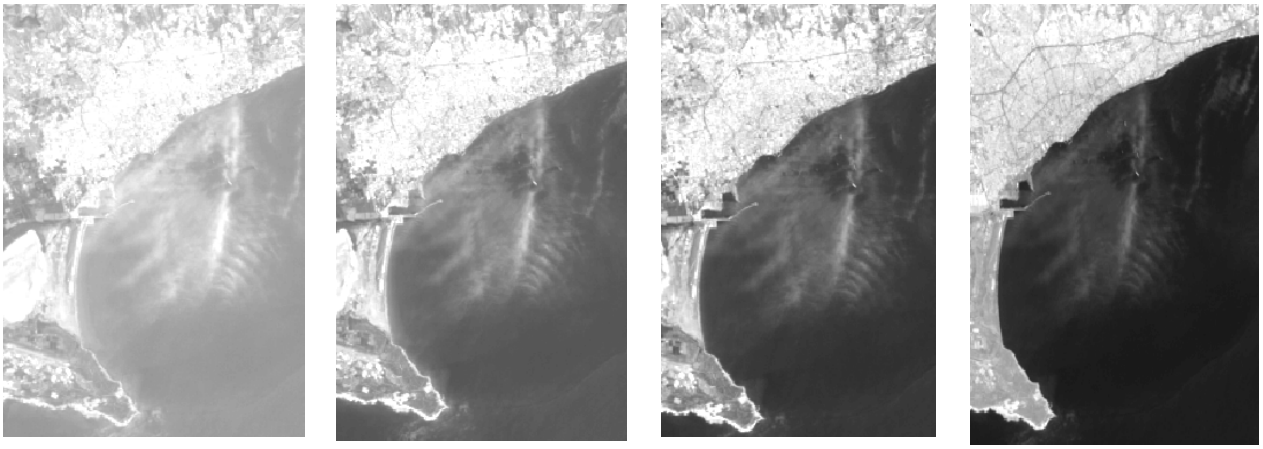

Band 1 Band 2 Band 3 Band 4

Satellite image 16/6/2010, by band, after atmospheric correction

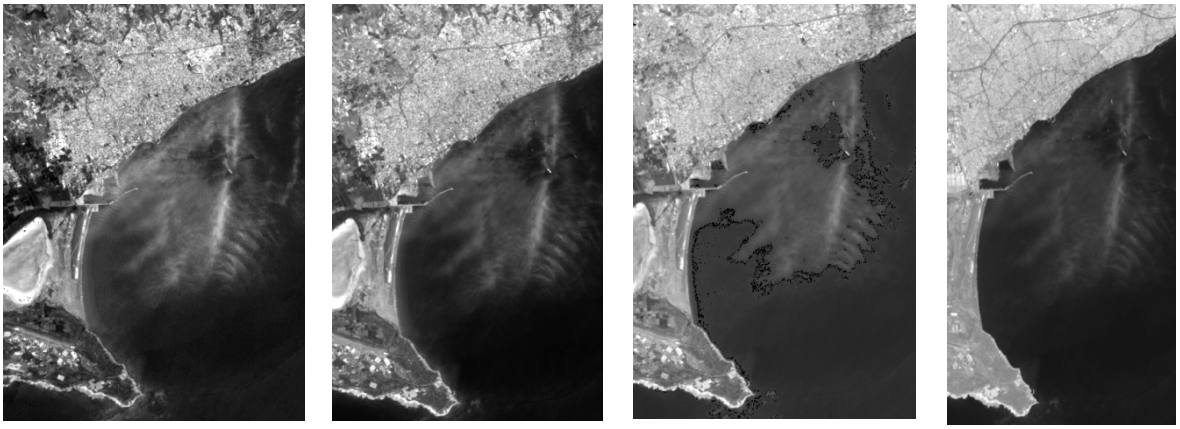

Band 1 Band 2 Band 3 Band 4

Figure 8-19 Satellite images (16/6/2010) before and after atmospheric correction by band

Figure 8-20 Satellite images acquired 16/6/2010, before (left) and after (right) atmospheric correction using DP method

Satellite image 24/6/2010, by band, before atmospheric correction

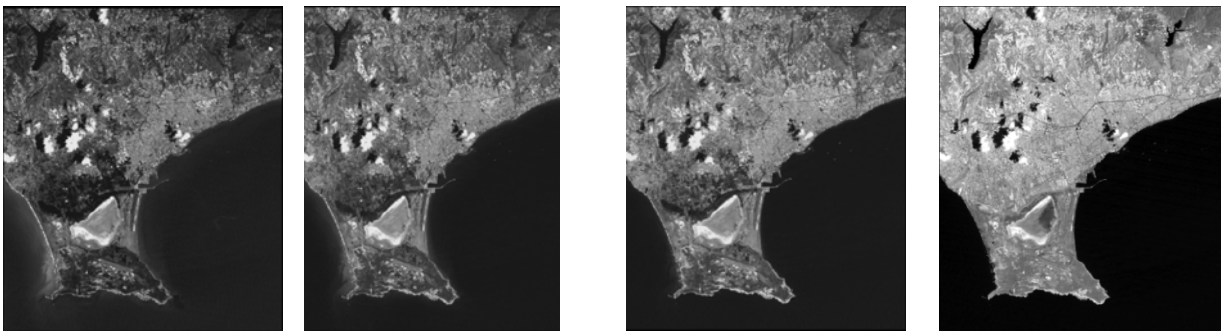

Band 1 Band 2 Band 3 Band 4

Satellite image 24/6/2010, by band, after atmospheric correction

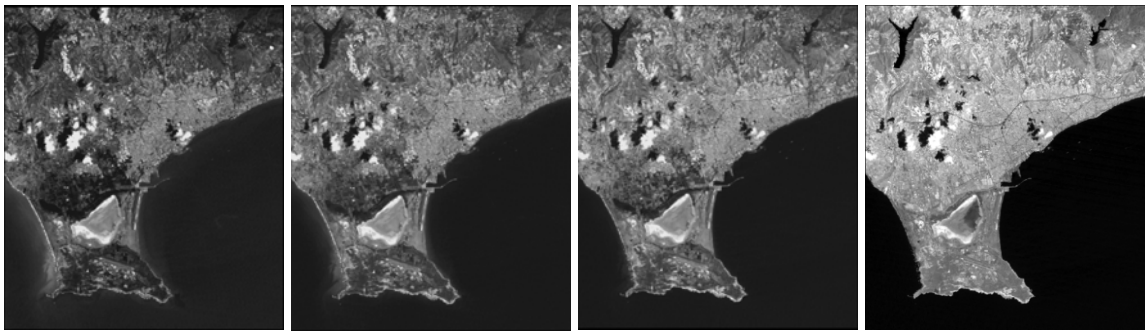

Band 1 Band 2 Band 3 Band 4

Figure 8-21 Satellite images (24/6/2010) before and after atmospheric correction by band

Figure 8-22 Satellite images acquired 24/6/2010 before (left) and after (right) atmospheric correction using DP method

Satellite image 10/7/2010, by band, before atmospheric correction

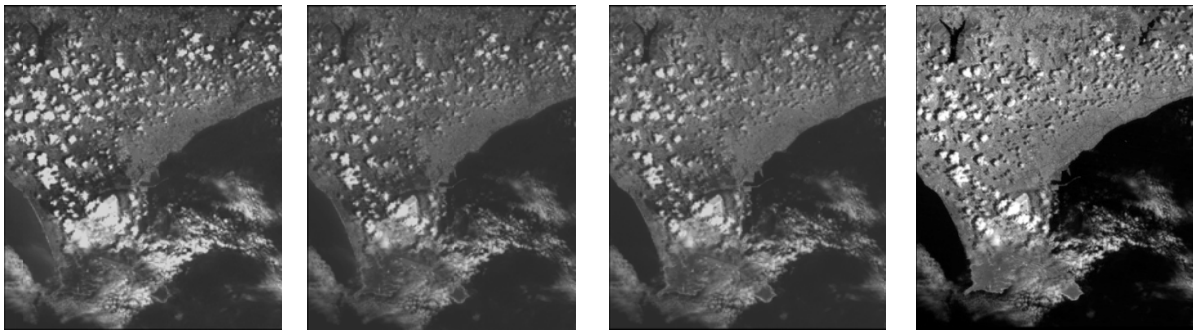

Band 1 Band 2 Band 3 Band 4

Satellite image 10/7/2010 by band, after atmospheric correction

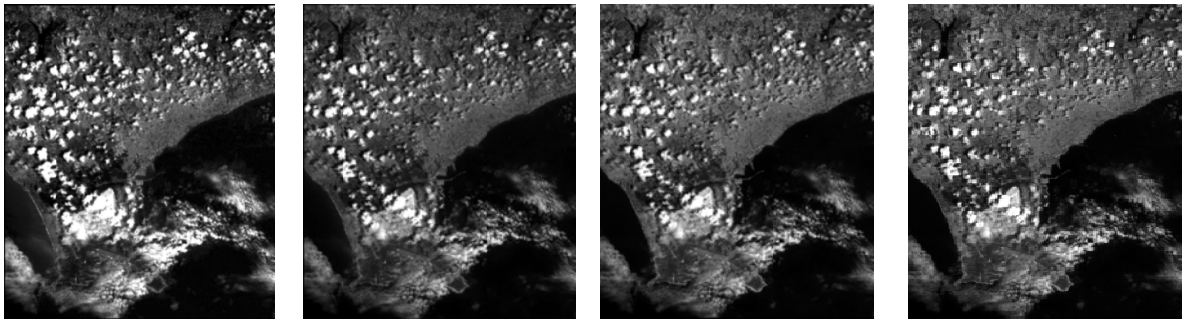

Band 1 Band 2 Band 3 Band 4

Figure 8-23 Satellite images (10/7/2010) before and after atmospheric correction by band

Figure 8-24 Satellite images acquired 10/7/2010 before (left) and after (right) atmospheric correction using DP method

Satellite image 27/8/2010, by band, before atmospheric correction

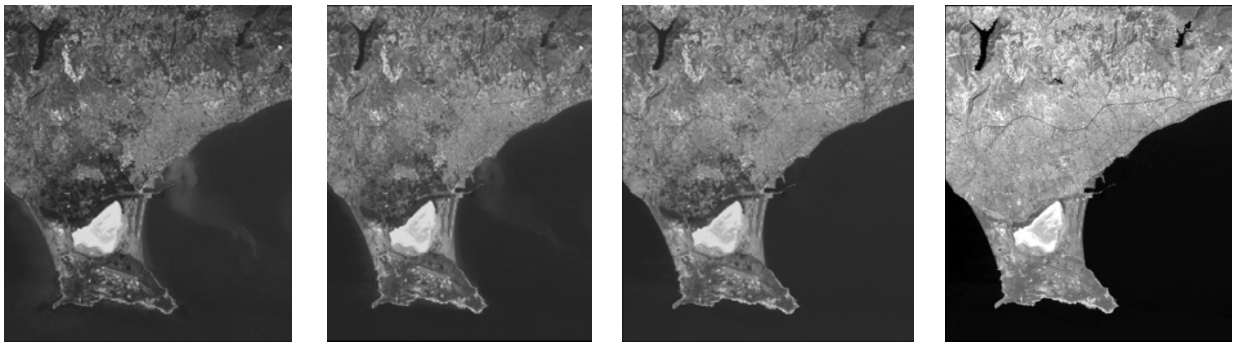

Band 1 Band 2 Band 3 Band 4

Satellite image 27/8/2010, by band, after atmospheric correction

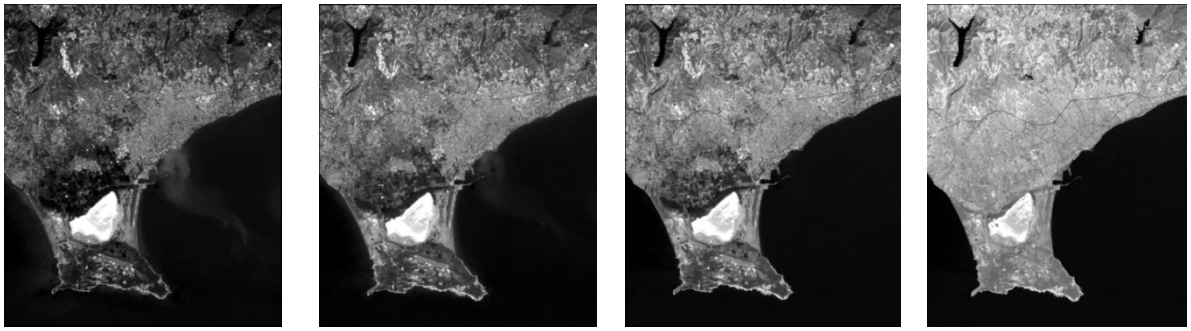

Band 1 Band 2 Band 3 Band 4

Figure 8-25 Satellite images (27/8/2010) before and after atmospheric correction by band

Figure 8-26 Satellite images acquired 27/8/2010 before (left) and after (right) atmospheric correction using DP method

Satellite image 28/9/2010, by band, before atmospheric correction

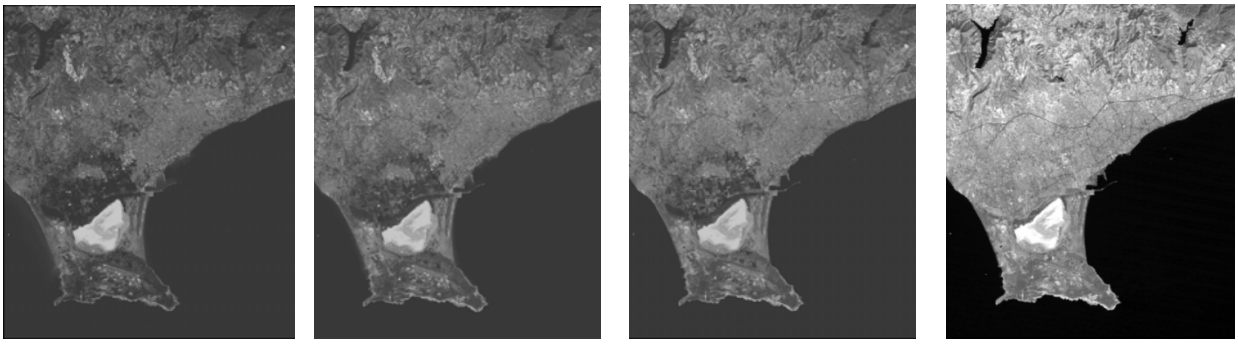

Band 1 Band 2 Band 3 Band 4

Satellite image 28/9/2010, by band, after atmospheric correction

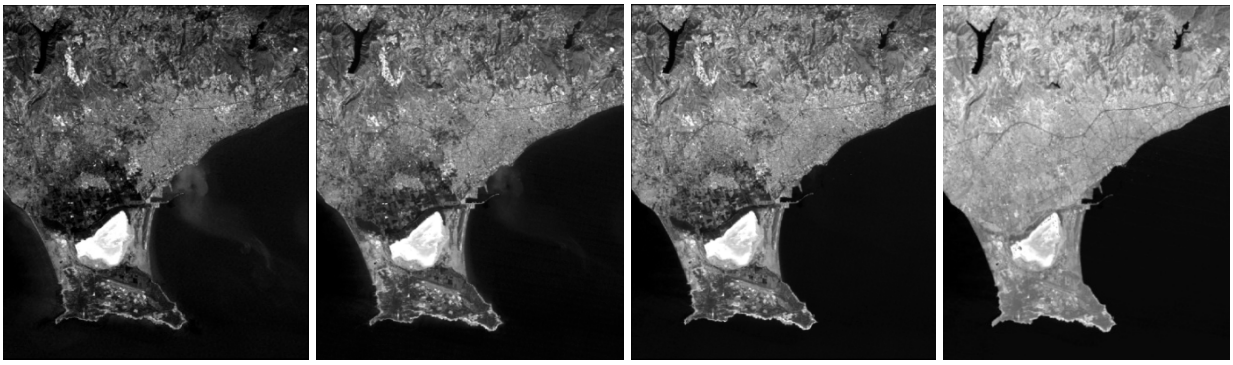

Band 1 Band 2 Band 3 Band 4

Figure 8-27 Satellite images (28/9/2010) before and after atmospheric correction by band

Figure 8-28 Satellite images acquired 28/9/2010 before (left) and after (right) atmospheric correction using DP method

Satellite image 7/11/2010, by band, before atmospheric correction

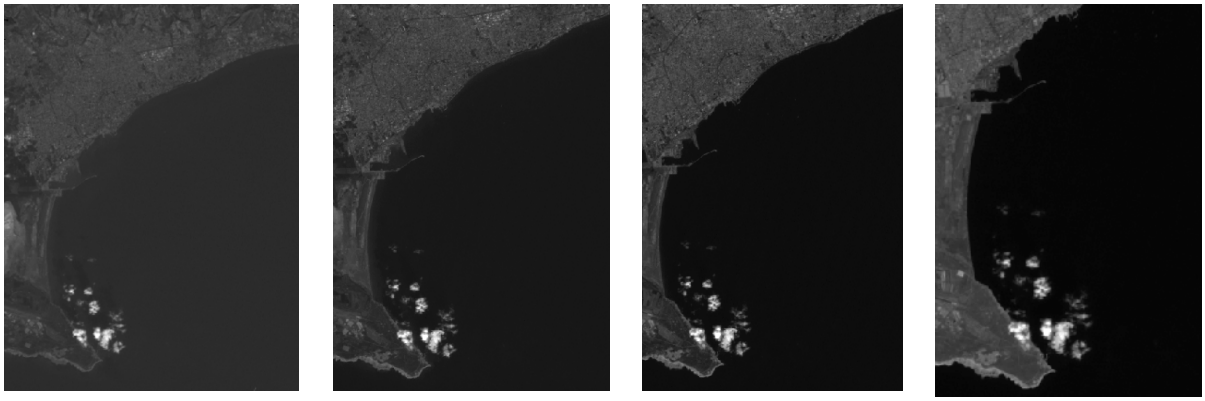

Band 1 Band 2 Band 3 Band 4

Satellite image 7/11/2010, by band, after atmospheric correction

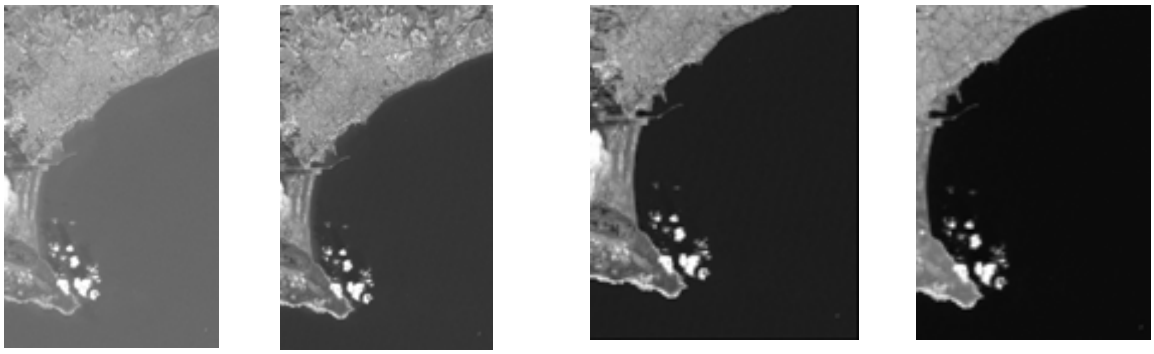

Band 1 Band 2 Band 3 Band 4

Figure 8-29 Satellite images (7/11/2010) after atmospheric correction by band

Figure 8-30 Satellite images acquired 7/11/2010 before (left) and after (right) atmospheric correction using DP method

Satellite image 9/12/2010, by band, before atmospheric correction

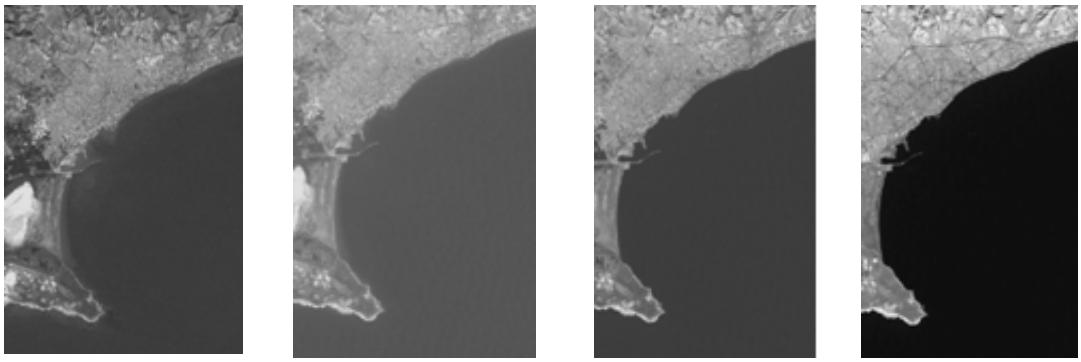

Band 1 Band 2 Band 3 Band 4

Satellite image 9/12/2010, by band, after atmospheric correction

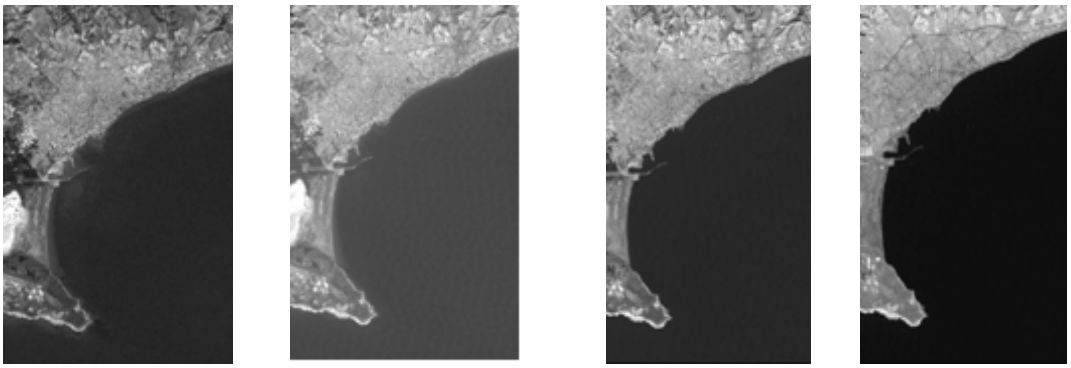

Band 1 Band 2 Band 3 Band 4

Figure 8-31 Satellite images (9/12/2010) after atmospheric correction by band

Figure 8-32 Satellite images acquired 9/12/2010 before (left) and after (right) atmospheric correction using DP method

Satellite image 2/5/2011, by band, before atmospheric correction

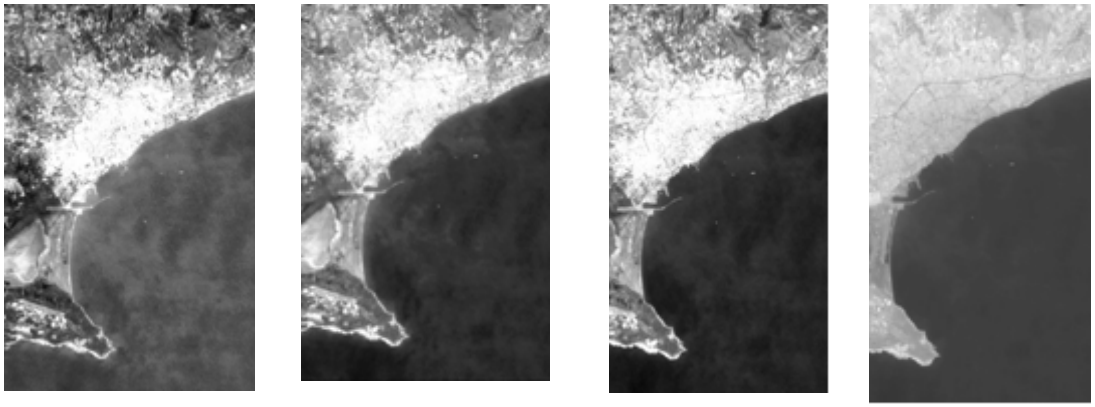

Band 1 Band 2 Band 3 Band 4

Satellite image 2/5/2011, by band, after atmospheric correction

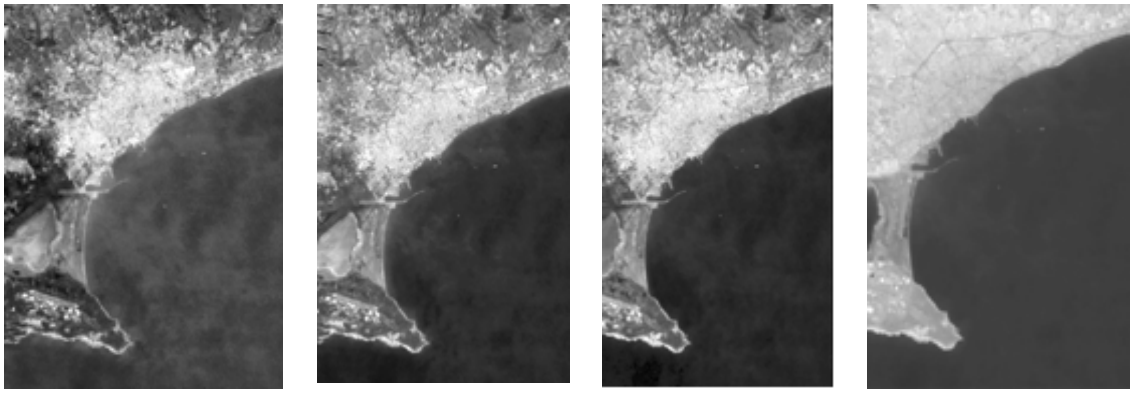

Band 1 Band 2 Band 3 Band 4

Figure 8-33 Satellite images (2/5/11) before and after atmospheric correction by band

Figure 8-34 Satellite images acquired 2/5/11 before (left) and after (right) atmospheric correction using DP method

8.5 Summary

In this chapter, the empirical line and the darkest pixel atmospheric correction methods were examined in detail and applied to eleven Landsat 5 TM and Landsat 7 ETM+ images. The results of the atmospheric correction methods, including calculated reflectance values and corrected satellite images were also presented. In the next chapter, a detailed explanation of how AOT was retrieved using the empirical line method and the darkest pixel method will be explained.

Chapter 9 AOT Retrieval and GIS Analysis

Following application of the improved PITs method and the DP method (Chapter 8), the radiative transfer (RT) equations were used to retrieve AOT values from the satellite images with as much precision as possible. This is the first time that the RT equations have been used to retrieve AOT with the proposed methodology. As a result, the "fast atmospheric correction algorithm" was developed using the RT equations, which is presented in this chapter. The algorithm is an image-based method that does not require meteorological data (Themistocleous et al., 2011). The formulas used to determine the AOT are discussed in detail in this chapter.

9.1 AOT retrieval using DP and PITs methods

To retrieve AOT using the darkest pixel and empirical line method using pseudo-invariant targets, the radiative transfer equation was used, as indicated in equation 9-1. As indicated in equation 9-1, to calculate path radiance (L_p) both the $L_{ts,}$ which is the at-satellite radiance and the ρ_{ts}, which is the at-satellite reflectance value, needs to be determined using equation 6-3. The at-satellite reflectance values can be derived through using the atmospheric correction methods of the empirical line method and darkest pixel.

In order to use the empirical line method of atmospheric correction to derive the reflectance values required for the fast atmospheric correction algorithm, the following conditions need to be met: there should exist a linear relationship between at-satellite reflectance and ground reflectance, at least two appropriate non-variant targets are identified on the image, the surface reflectance measurements should be available for the targets, the atmospheric effects other than aerosols are constant across the entire image and the targets should be homogenous. As well, the targets should be available with both high and low radiance in each of the bands to be corrected and the targets should be smooth and horizontal so they function as Lambertian, so that any errors associated with differences in geometry and illumination are minimal.

9.1.2 RT Calculations

The radiative transfer equation was described in Chapter 2 and the procedure developed in this thesis is fully described in this chapter. The procedure was applied to eleven Landsat TM/ETM+ images taken over different seasons in Cyprus. Although several researchers

(Istomina et al., 2011; Lee and Kim, 2010; Xue et al., 2008; Guanter et al., 2008; Xue et al., 2008; Remer et al., 2005; Seidel et al., 2005; Hadjimitsis et al., 2007; Hadjimitsis and Clayton, 2004; Hadjimitsis et al., 2002; Hadjimitsis, 1999; Kaufman and Sendra, 1998; Kaufman et al., 1997; Kaufman and Tanré, 1996; Forster, 1984) used the RT equation to estimate AOT values, this research proves a new perspective by using the radiative transfer equation, satellite imagery, in-situ measurements, the PITs method of atmospheric correction and the DP method of atmospheric correction to retrieve AOT. The methodology requires data that are available in satellite images, especially on dark surfaces for bands 1 (blue) and 3 (red) (Gilabert et al., 1994). As discussed in Chapter 2, AOT is considered the most significant unknown parameter in atmospheric correction since it is used to solve the radiative transfer equation and remove atmospheric effects from satellite images (Hadjimitsis et al., 2007; Hadjimitsis and Clayton, 2004; Hadjimitsis et al., 2002; Hadjimitsis, 1999; Forster, 1984). In this chapter, a detailed description of the methodology to retrieve AOT is given below. All the parameters and the nomenclature used in the fast atmospheric correction algorithm are shown in Table 9-1.

Symbol	Factors used to develop AOT equation	UNITS
d	is the correction coefficient accounting for variations in the Sun-to-Earth distance	dimensionless
DN	is the measured digital number at the satellite sensor	dimensionless
$E_{0\lambda}$	is the solar irradiance at the top of the atmosphere	$Wm^{-2}sr^{-1}$
E_G	is the global irradiance reaching the ground	$Wm^{-2}sr^{-1}$
L_{ts}	is the at-satellite radiance	$Wm^{-2}sr^{-1}$
L_p	is the atmospheric path radiance	$Wm^{-2}sr^{-1}$
L_{pa}	is the atmospheric path radiance due to Mie (aerosol) scattering	$Wm^{-2}sr^{-1}$
L_{pr}	is the atmospheric path radiance due to Rayleigh scattering	$Wm^{-2}sr^{-1}$
P'_a	is the phase function	sr^{-2}
P_r	is Rayleigh scattering phase function	sr^{-2}
ρ_{tg}	is at ground reflectance	dimensionless
ρ_{ts}	is at satellite reflectance	dimensionless
$t(\mu)\uparrow$	is the direct (upward) target-sensor atmospheric transmittance	μm
t_g	is the gaseous transmittance	dimensionless
θ_0	is the solar zenith angle	degrees
θ_v	is the sensor viewing angle	degrees
λ_c	is the central wavelength	μm
τ_a	is the aerosol optical thickness	dimensionless
$to_3\uparrow$	is the transmittance factor due to ozone in the upward direction, which is estimated as 1	dimensionless
$to_3\downarrow$	is the transmittance factor due to ozone in the downward	dimensionless

	direction, which is estimated as 1	
$t_a \uparrow$	atmospheric transmittance for aerosol-scattered radiation in the upward direction	dimensionless
$t_a \downarrow$	atmospheric transmittance for aerosol-scattered radiation in the downward direction	dimensionless
τ_r	is Rayleigh optical thickness in μm	dimensionless
ω_a	is the aerosol single scattering albedo	dimensionless
μ	is the cos (θ_0)	degree

Table 9-1 Parameters and symbols used to develop AOT equation

9.2 AOT retrieval methodology

According to Hadjimitsis and Clayton (2009), AOT can be retrieved from the path radiance through use of RT equations. The purpose of this chapter is to apply the RT equations using satellite imagery by using the DP and PITs atmospheric correction methods with non-variant targets in order to retrieve AOT from satellite images with as much precision as possible, which resulted in the fast atmospheric correction algorithm. AOT is included in path radiance and Mie scattering (L_{pa}), as indicated in equations 9-2 and 9-8. In order to calculate AOT, equation 9-1 is used.

Path radiance is the summation of Rayleigh and Mie scattering in the atmosphere, as described by Hadjimitsis and Clayton (2009), Kaufman (1993), de Haan et al. (1991), Hill and Sturm (1991), Forster (1984), and Deschamps et al. (1983).

Lp is defined below (Gilabert et al., 1994; Hill and Sturm, 1991) :

$$Lp = Lpr + Lpa \tag{9-1}$$

where

Lp is the path radiance (integrated band radiance measured in W/m^{2}sr) which is calculated using equation 9-3

Lpr is the atmospheric path radiance due to Rayleigh scattering in W/m^{2}sr which is calculated using equation 9-6

Lpa is the atmospheric path radiance due to Mie scattering in W/m^{2}sr which is calculated using equation 9-8

Step One - Calculating Path Radiance (Lp)

The atmospheric path radiance (Lp) is calculated according to equation 10-2 (Hill and Sturm, 1991; Turner and Spencer, 1972). In using the improved DP method, the Black Asphalt target reflectance value was used as the darkest pixel value (ρ_{tg}) (as discussed in Chapter 8), while in the PITs method, the reflectance values of the five non-variant targets were used as in-situ measurements using the path radiance component (c), as discussed in Chapter 8.

Lp is calculated using the following formula:

$$L_p = L_{ts} - \frac{\tau(\mu)\rho_{tg} E_G}{\pi} \tag{9-2}$$

where

Lp is the path radiance (integrated band radiance measured in W/m^{2}sr)

L_{ts} is the at-satellite radiance measured in W/(m^2 μm sr), which is calculated from equation 6-1

ρ_{tg} is the target reflectance at ground level, which is calculated based on equation 8-2

E_G is the global irradiance reaching the ground, which is calculated from equation 9-3

$\tau(\mu)$ is the direct (upward) target-sensor atmospheric transmittance, which is calculated from equation 9-4

To solve for the global irradiance reaching the ground (E_G), equation 9-3 by Hill and Strum (1991) can be used.

$$E_G = E_{0\lambda}\,\mu\, exp\left[-\left(\frac{1}{2\tau_r} + \frac{1}{6\tau_a}\right)/\mu\right] \tag{9-3}$$

where

$E_{0\lambda}$ Solar irradiance at the top of the atmosphere in the W/m^2 calculated from Table 6-1 and Table 6-2

τ_r is the Rayleigh optical thickness, calculated from equation 9-5

τ_a is the AOT, which is unknown

μ =cos (θ_0)

To solve for the direct (upward) target-sensor atmospheric transmittance $\tau(\mu)\uparrow$ equation 10-4 by Hill and Strum (1991) can be used.

$$t(\mu) \uparrow = exp\left[-(\tau_r + \tau_a)/\mu\right] \quad (9\text{-}4)$$

where

τ_r is the Rayleigh optical thickness in μm calculated from equation 9-5

τ_a is the AOT

μ =cos (θ_0)

Although several equations to calculate Rayleigh optical thickness (τ_r) have been developed, most radiative transfer equations used the equation provided by Moller, (1957) (equation 9-5), which is considered to be the most appropriate (Hadjimitsis, 1999).

$$\tau_r\ (\lambda_c) = 0.00879\ \lambda_c^{-4.09} \quad (9\text{-}5)$$

where

λ_c is the central wavelength (see Table 6-1 and Table 6-2)

Step Two - Calculating Rayleigh Scattering (*Lpr*)

The second parameter to establish path radiance is that path radiance due to Rayleigh scattering (*Lpr*) as indicated in equation 9-6. To solve equation 9-6 the following parameters are calculated: E_0, θ_0, θ_v, and τ_r . The unknown parameter is the Rayleigh scattering phase function, which can be solved through equation 9-7.

To calculate the path radiance due to Rayleigh scattering, equation 9-6 is used (Gilabert et al., 1994):

$$Lpr = \left\{ \frac{(E_{o\lambda}\ cos\theta_0\ P_r)}{4\pi\ (cos\theta_0 + cos\theta_v)} \right\} \left\{ 1 - exp\left[-\tau_r \left(1/cos\theta_0 + 1/cos\theta_v \right) \right] \right\} to_{3\uparrow}\ to_{3\downarrow} \quad (9\text{-}6)$$

where

Lpr is the atmospheric path radiance due to Rayleigh scattering in W/m^{2}sr

$E_{0\lambda}$ is the solar irradiance at the top of the atmosphere in W/m^{2}sr as found in table 6-1 and 6-2

P_r is Rayleigh scattering phase function as calculated from equation 9-7

θ_0 is the solar zenith angle, as found on the satellite header file

θ_v is the sensor viewing angle, as found on the satellite header file

τr is Rayleigh optical thickness in μm, as calculated in equation 9-5

$to_3 \uparrow$ is the transmittance factor due to ozone in the upward direction. It is solved by equation $to_3 \uparrow(\lambda)=\exp(-to_3 \uparrow(\lambda))$. According to Gilabert et al. (1994), to_3 is considered negligible and therefore is 1

$to_3 \downarrow$ is the transmittance factor due to ozone in the downward direction. It is solved by equation $to_3 \downarrow(\lambda)=\exp(-to_3 \downarrow(\lambda)/\cos\theta_0)$. According to Gilabert et al. (1994), to_3 is considered negligible and therefore is 1

The Rayleigh scattering phase function (P_r) can be calculated using equation 9-7 by solving for the single scattering phase function (Gilabert et al., 1994):

$$P_r = \frac{3}{4}\left(1+\cos^2(180-\theta_0)\right) \tag{9-7}$$

Step 3-Calculating Mie scattering

The third parameter to establish path radiance is that path radiance due to Mie scattering (L_{pa}), needs to be calculated. There are several known variables, which include ω_a, P'_a, E_0, θ_0, θ_v, and τ_r. However, the aerosol optical thickness, τ_a, is unknown.

To calculate Mie scattering, formula 10-8 can be used (Gilabert et al., 1994) is used:

$$Lpa = \left\{\frac{\left(E_{0\lambda}\ \cos\theta_0\,\omega_a\,P'_a\right)}{4\pi\left(\cos\theta_0+\cos\theta_v\right)}\right\}\left\{1-\exp\left[-\tau_a\left(\left(1/\cos\theta_0\right)+\left(1/\cos\theta_v\right)\right)\right]\right\}$$
$$\exp\left[-\tau_r\left(\left(1/\cos\theta_0\right)+\left(1/\cos\theta_v\right)\right)\right] \tag{9-8}$$

where

L_{pa} is the atmospheric path radiance due to Mie (aerosol) scattering in W/m^{2}sr

ω_a is the aerosol single scattering albedo, which is .90 for this area

P'_a is the phase function, as determined from phase function graph in Appendix 2

τ_a is the aerosol optical thickness, which is unknown

θ_0 is the solar zenith angle, as found on the satellite header file

θ_v is the sensor viewing angle, as found on the satellite header file

$E_{0\lambda}$ is the solar irradiance at the top of the atmosphere in W/m^{2}sr as indicated in table 6-1 and 6-2

τ_r is Rayleigh optical thickness in μm, as calculated in equation 9-5

As discussed in Chapter 2, ω_a refers to the single scattering albedo. According to Waggoner et al. (1981), aerosol single scattering albedo varies according to location, measuring from 0.73 to 0.87 in urban areas and from 0.89 to 0.95 in remote areas. The ω_a was also measured through AERONET, from May 2010 until October 2011. The Cimel sun photometer recorded over 540 measurements from May 2010 until October 2011, with an average value of 0.91, and standard deviation of 3%. This corresponds to the aerosol single scattering albedo for remote areas as stated by Waggoner et al (1981) and fits the location characteristics of the study area.

As discussed in Chapter 2, *P'a* refers to the phase function. As of May, 2010, AERONET also provides information regarding the phase function. AERONET recorded over 600 measurements of P'_a. The Cimel sun photometer recorded over 600 measurements for aerosol scattering phase function during 2010. The average values of *P'a* were calculated at 500 nm (to correspond to AOT at 500 nm, as measured in this study) for every scattering angle and for every month. As several researchers (Gilabert et al., 1994; Forster, 1984; Turner et al., 1971) have examined phase function in graph form, a graph was created that represented phase function in Limassol using AERONET information from the CUT station and the surrounding area. The phase function graph for each month of the year is indicated in Appendix 2.

9.3 Fast atmospheric correction algorithm calculation procedure with example

The above methodology of the fast atmospheric correction algorithm with the DP and PITs method was used to retrieve AOT from band 1 of a Landsat 5 and Landsat 7 subset, which is shown in the example below. The MATLAB program was used to retrieve the AOT values using the equations described in this chapter. The algorithm was conducted in Band 1, as the sun photometer measurements used for the accuracy assessment were in the 500 nm wavelength. The methodology used to calculate the AOT values is presented in Figure 9-1. The calculation procedure for Band 1, with the example results is summarized in the following steps. In Tables 9-1 and 9-2, the variables used for the satellite images are listed. The MATLAB program is presented in Figure 9-2.

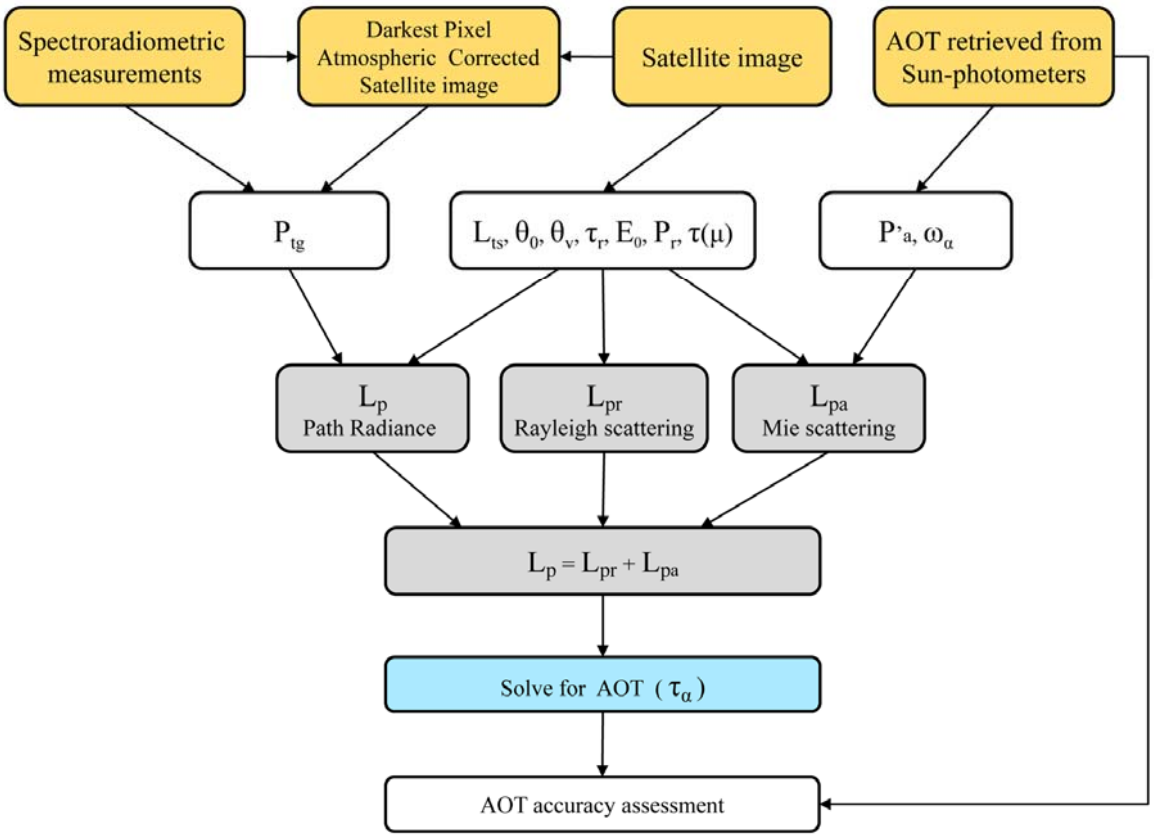

Figure 9-1 Methodology used for AOT retrieval and accuracy assessment

Step 1: Determine the date and time of the satellite overpass and the satellite number and download the Landsat image.

Date: 13/4/2010

Band: Band 1

Time: 08:15 G.M.T

Satellite number:LE71760362010103ASN00

Step 2: Calculate the solar zenith angle (θ_0) at the overpass time (according to the header file on the satellite image or through *http://solardat.uoregon.edu/SolarPosition Calculator .html*). In Landsat 7 ETM+ satellite images, the solar zenith angle (SZA) is indicated as θs on the header file of the satellite image.

$\theta_0 = 33.3382$

Step 3: Calculate the sensor viewing angle (θ_v) at the overpass time (according to the header file on the satellite image or through *http://solardat.uoregon.edu/SolarPositionCalculator.html*).

$\theta_v = 0$

Step 4: Calculate E_0 according to Tables 6-7 and 6-8.

$E_{0\lambda} =$ 1997 W/m^2

Step 5: Calculate μ , which is the cos (θ_0) using the variable derived from step 2:

$\mu = 0.835$

Step 6: Determine λ_c, using Tables 6-7 and 6-8.

$\lambda_c = 0.483$ μm

Step 7: Calculate τ_r using equation 9-5. using the variable determined in step 6:

$\tau_r =$ 0.1724 μm

Step 8: Solve for E_G using equation 9-4, using the variables derived from steps 4, 5, and 7. The τ_a (aerosol optical thickness) will be unknown.

$E_G =$ 7337594997605195/(4398046511104 x exp((4503599627370496 ta) /22574954264039217 + 2070969090799243/20066626 012479304)) W/m^2

Step 9: Find $\tau(\mu)\uparrow$ using equation 9-4, using the variables derived from steps 5 and 7. The τa (aerosol optical thickness) will be unknown.

$\tau(\mu)\uparrow$= 1/exp((9007199254740992 ta) /7524984754679739 + 2070969090799243/10033313006239652) μm
τa

Step 10: Calculate L_{ts} (which is the at-satellite radiance) from the satellite image and/or from equation 6-1 using the data found on the satellite header file.

L_{ts} = 78 W/(m^2 μmsr)

Step 11: Calculate the ρ_{tg}, from the surface reflectance measurements.

ρ_{tg} = 0.103

Step 12: Lp can be found through equation 9-2, using variables from steps 8, 9, 10 and 11.

Lp = 163/2 - 1467518999521039/(8796093022208 x pi x exp((9007199254740992 ta) /7524984754679739 + 2070969090799243/100333 13006239652) x exp((4503599627370496 ta) /22574954264039217 + 0709690907 99243/20066626012479304)) W/m^2

Step 13: Calculate P_r using equation 9-8, using variables from steps 2 and 5.

P_r = 1.2735

Step 14: Solve for Lpr using equation 9-6, using variables from step 2, 3, 4, 7, 13 and utilizing the value of 1 for $to_3\uparrow$ and $to_3\downarrow$.

Lpr = 29.0489 W/m^{2}sr

Step 15: Calculate ω_a, which is 0.73-0.87 in urban areas and 0.89 to 0.95 in remote areas. According to AERONET data, the ω_a is 0.92 in the Limassol area.

ωa = 0.91

Step 16: Enter P'_a , using phase function graph.

$P'_a = 1.1$

Step 17: Calculate Lpa using equation 10-8, using variables from step 2, 3, 4, 7, 15 and 16 and utilizing the value of 1 for $t_a\uparrow$ and $t_a\downarrow$; τ_a is unknown.

$Lpa =$ 184058110221515729239381042356253169126500570573503741758013441840581102215157292393810423562531691265005705735037417580134 4 x exp((1236785524684037 ta)/562949953421312 W/m^2sr

Step 18: Solve equation 9-1 using variables from steps 14 and 17; τ_a is unknown.

$Lp =$ 2761178067561448526414929627300131691265005705735037417580134418405811022151572923938104235625/(3169126500570573503741758013441840581102215157292393810423562531691265005705735037417580134 x exp((1236785524684037 ta)/562949953421312)) W/m^2sr

Step 19: Equation 10-1 was used to solve for τ_a .

$\tau_a = 0.262$

In this thesis, atmospheric correction was conducted with the DP method and the improved empirical line (PITs) method. Therefore, the algorithm was conducted with the reflectance values derived from the DP method (Table 9-2) and the PITs method (Table 9-3) atmospheric correction methods.

Variables used through DP Method of atmospheric correction for Band 1

Date	E_0	SZA	λc	Radiance value	Reflectance value	P'a	AOT derived
13-04-10	1997	33.34	0.483	80	0.11	1.10	0.224
29-04-10	1997	28.61	0.483	78	0.10	0.86	0.406
31-05-10	1997	23.52	0.483	75	0.10	0.71	0.284
16-06-10	1997	23.24	0.483	80	0.10	0.80	0.313
24-06-10	1983	23.85	0.485	78	0.10	0.80	0.229
10-07-10	1983	25.09	0.485	78	0.10	0.82	0.247
27-08-10	1983	32.97	0.485	79	0.09	1.10	0.338
28-09-10	1983	41.81	0.485	75	0.10	1.60	0.202
07-11-10	1997	53.99	0.483	82	0.11	3.30	0.179
09-12-10	1997	60.80	0.483	80	0.11	4.20	0.164
02-05-11	1997	27.68	0.483	78	0.10	0.86	0.319

Table 9-2 Values used for the algorithm, with reflectance values derived from the DP atmospheric correction method

Variables used through PITs Method of atmospheric correction for Band 1

Date	E_0	SZA	λc	Radiance value	Reflectance value	P'a	AOT derived
13-04-10	1997	33.34	0.483	78	0.11	1.10	0.192
29-04-10	1997	28.61	0.483	78	0.99	0.86	0.491
31-05-10	1997	23.52	0.483	75	0.95	0.71	0.194
16-06-10	1997	23.24	0.483	80	0.10	0.80	0.418
24-06-10	1983	23.85	0.485	78	0.10	0.80	0.271
10-07-10	1983	25.09	0.485	88	0.14	0.82	0.346
27-08-10	1983	32.97	0.485	83	0.09	1.10	0.357
28-09-10	1983	41.81	0.485	75	0.09	1.60	0.244
07-11-10	1997	53.99	0.483	86	0.08	3.30	0.220
09-12-10	1997	60.80	0.483	90	0.11	4.20	0.171
02-05-11	1997	27.68	0.483	106	0.10	0.86	0.340

Table 9-3 Values used for the algorithm, with reflectance values derived from the improved empirical line atmospheric correction method

9.4 Fast atmospheric correction algorithm in MATLAB

The fast atmospheric correction algorithm was inserted into the MATLAB program in order to solve for τ_a and therefore derive the AOT value from the satellite image. The MATLAB code prompted the user to insert specific values in order to calculate the AOT value, as indicated in figure 9-2.

- E_0 = input Insert value for solar irradiance on top of the atmosphere in W/(m^2*μm)
- th0 = input Insert the solar zenith angle in degrees
- lc = input Insert the band central wavelength in μm

- Lts = input Insert the at-satellite radiance in W/(m^2 x μm x sr)
- rtg = input Target reflectance at ground level

```
clc
clear
date
display '------------------------------------------------------------'
display 'Cyprus University of Technology'
display 'Remote Sensing and Geomatics'
display 'Kyriacos Themistocleous'
display '------------------------------------------------------------'
 format long

display 'Fast atmospheric correction algorithm'
display 'This file calculates AOT using RT equations'
display '------------------------------------------------------------'
display '------------------------------------------------------------'
display 'Lp=Lpr+Lpa'
display '------------------------------------------------------------'
E0=input('Insert value for solar irradiance on top of the atmosphere in
W/(m^2*μm)= ')
th0=input('Insert the solar zenith angle in degrees = ')
thv=0
lc=input('Insert the band central wavelength in μm = ')
tr=0.00879*lc^(-4.09)
th20=1
t03=1
Pr=3/4*(1+(cosd(180-th0))^2)
Lpr=(E0*cosd(th0)*Pr/(4*pi*(cosd(th0)+cosd(thv))))*(1-exp(-
tr*(1/cosd(th0)+1/cosd(thv))))

%Calculate Lpa
wa=0.91
Pa=input('Insert the phase function')
syms ta
Lpa=((wa*E0*cosd(th0)*Pa)/(4*pi*(cosd(th0)+cosd(thv))))*(1-exp(-
ta*(1/cosd(th0)+1/cosd(thv))))*exp(-tr*(1/cosd(th0)+1/cosd(thv)))

% Calculate Lp
Lts=input('Insert the at-satellite radiance in W/(m^2*μm*sr) = ')
rtg=input('Target reflectance at ground level = ')
```

```
m=cosd(th0)
tm=exp(-(tr+ta)/m)
Eg=E0*m*exp(-(tr/2+ta/6)/m)
Lp=Lts-((rtg*tm*Eg)/pi)

% Calculate ta
Lp1=Lpr+Lpa
F=Lp-Lp1
ta=solve(F)

display '------------------------------------------------------------'
```

Figure 9-2 Fast atmospheric correction algorithm in Matlab

9.5 Simplified image based AOT retrieval based on RT equation for GIS analysis

In order to solve for AOT and conduct a GIS analysis in ERDAS Imagine (see Figure 9-4), it was necessary to simplify the equation due to the complexity of the RT equations and their logarithmic components. The three equations (9-1, 9-6, and 9-8) were combined into one equation (9-18), which could be solved in MATLAB and ERDAS Imagine. The simplified formula uses the image based technique to retrieve AOT values and model them into a GIS geospatial database. In order to display AOT, a Kriging method was used to overlay the data into GIS vector maps of the city to display a spatial distribution of AOT.

It was necessary to transform the fast atmospheric correction algorithm developed in order to to retrieve AOT values from the satellite image. This was achieved by creating a model and solving the RT equation using a second order equation and solving it using the MacLaurin Taylor series. The MacLaurin Taylor series was used in order to approximate a definite integral to a desired accuracy (Greenberg, 1998; Thomas and Finney, 1996; Abramowitz and Stegun, 1970). Essentially, the MacLaurin Taylor series consists of rewriting a function as an infinite sum of other functions that are calculated from the values of the function's derivatives at a single point, with a center at zero. This algorithm is called the simplified image based AOT retrieval based on RT equation for GIS modeling. In order to run the algorithm for each satellite image, the corresponding parameters of phase function, single scattering albedo, and solar zenith angle were used depending on the date of image capture, as well as the radiance and corrected reflectance values. The equation used the parameters of L_{ts}, ρ_{tg}, L_{pr}, A, B, δ, and λ that were derived

through Mat Lab using the equations discussed below and the values were inserted into the model, as discussed in section 9-6.

In order to develop the image based AOT retrieval based on RT equation for GIS modeling, several equations were rewritten so they could be entered into the MATLAB and ERDAS Imagine model (further discussed in section 9-6). Equation 9-2 for path radiance can be written as shown below in equation 9-9:

$$L_p = L_{ts} - A\ \rho_{tg}\ e^{(-\lambda \tau_a)} \tag{9-9}$$

where

$$\lambda = \frac{7}{6\mu}$$

and

$$A = \frac{E_{0\lambda}\ \mu\ e^{\left(-\frac{3}{2}\tau_r\right)}}{\pi} \tag{9-10}$$

Following, equation 9-8 for Mie scattering can be written as shown in equation 9-11:

$$L_{pa} = B\,(1 - e^{-(\tau_\alpha\ \delta)}) \tag{9-11}$$

where

$$\delta = \frac{1}{\cos\theta_0} + \frac{1}{\cos\theta_v} \qquad \text{See equation 9-8} \tag{9-12}$$

and

$$B = \frac{\omega_a\ E_0 \cos\theta_0\ P'a}{4\pi\,(\cos\theta_0 + \cos\theta_v)} exp\,[-\tau_r \delta] \qquad \text{See equation 9-8} \tag{9-13}$$

The MacLaurin series' expansion of the exponential functions appearing in equations 9.9 to 9-13 was used to approximate a solution for τ_a up to a desired accuracy as shown in equation 9-14 (from equation 9-9) and 9-15 (from equation 9-11):

$$e^{-(\tau_a \delta)} = 1 - (\delta\ \tau_a) + \frac{\delta^2\ {\tau_a}^2}{2!} + \ldots \qquad \text{See equation 9-9} \tag{9-14}$$

$$e^{-(\lambda\ \tau_a)} = 1 - (\lambda\ \tau_a) + \frac{\lambda^2\ {\tau_a}^2}{2!} + \ldots \qquad \text{See equation 9-11} \tag{9-15}$$

Following, equations 9-14 and 9-15 can be rewritten as shown in equation 9-16 and 9-17

$$Lp = Lts - A(1 - \lambda\tau_a + \frac{\lambda^2\tau_a^2}{2}) \qquad \text{See equation 9-14} \qquad (9\text{-}16)$$

$$Lpa = B(1 - (1 - \delta\tau_a + \frac{\delta^2\tau_a^2}{2})) \qquad \text{See equation 9-15} \qquad (9\text{-}17)$$

Therefore, using the above equations, equation 9-1 can be written as shown in equation 9-18:

$$(\tau_a)^2 \ \frac{B\,\delta^2 - A\,\rho_{tg}\,\lambda^2}{2} \ - \tau_a\left(B\delta - A\,\rho_{tg}\,\lambda\right) + L_{ts} - L_{pr} - \left(A\,\rho_{tg}\right) = 0 \qquad (9\text{-}18)$$

Therefore, equation 9-18 can be written as shown in equation 9-19. The substitutions were used to rewrite the equation 9-1 as shown in equation 9-19:

$$\varphi\tau_a^2 - \vartheta\tau_a + \eta = 0 \qquad (9\text{-}20)$$

where:

$$\varphi = \frac{B\,\delta^2 - A\,\rho_{tg}\,\lambda^2}{2}$$

$$\vartheta = B\,\delta - A\,\rho_{tg}\,\lambda$$

$$\eta = L_{ts} - L_{pr} - (A\,\rho_{tg})$$

Equation 9-20 can be solved as a second order equation for τ_a through the second order equation.

$$\tau_a = \frac{\vartheta \pm \sqrt{\vartheta^2 - 4\varphi\,\eta}}{2\varphi} \qquad (9\text{-}21)$$

The equation was solved for the positive and negative sign so that only τ_a values between 0-4.0 would be calculated, which preclude the AOT found on the planet (Chin et al., 2009; Penner et al., 2010). The equation was inserted and processed through the MATLAB program, as is indicated below in Figure 9-3. For verification purposes, the algorithm was processed for the Landsat ETM+ image for 13/4/2010, in band 1, which was the same satellite image that was used as an example in section 9.3. It was found that using the

simplified image based AOT retrieval based on the RT equation for GIS modeling produced the same AOT value as the fast atmospheric correction algorithm.

```
clc
clear
date
display '------------------------------------------------------------------'
display 'Cyprus University of Technology'
display 'Remote Sensing and Geomatics'
display 'Kyriacos Themistocleous'
display '------------------------------------------------------------------'

format long

display 'Simplified image based AOT retrieval based on RT equation for
GIS modeling'
display 'This file calculates AOT for GIS use'
display '------------------------------------------------------------------'

display '------------------------------------------------------------------'
display 'Lp=Lpr+Lpa'
display '------------------------------------------------------------------'
%Lp=Lpr+Lpa
E0=input('Insert value for solar irradiance on top of the atmosphere in
W/(m^2*μm)= ')
th0=input('Insert the solar zenith angle in degrees = ')
lc=input('Insert the band central wavelength in μm = ')
thv=0

%Calculate tr
tr=0.00879*(lc^(-4.09))

%Calculate Pr
Pr=3/4*(1+(cosd(180-th0))^2)

%Calculate Lpr
Lpr=(E0*cosd(th0)*Pr/(4*pi*((cosd(th0))+(cosd(thv)))))*(1-(exp(-
tr*((1/cosd(th0))+(1/cosd(thv))))))

%Calculate B
wa=0.91
```

```
Pa=input('Insert value for Phase function = ')
syms Delta
Delta=(1/cosd(th0))+(1/cosd(thv))
syms B
B=((wa*E0*cosd(th0)*Pa)/(4*pi*((cosd(th0))+(cosd(thv)))))*(exp(-tr*
Delta))

% Calculate A
Lts=input('Insert the at-satellite radiance in W/(m^2*µm*sr) = ')
rtg=input('Target reflectance at ground level = ')
m=cosd(th0)
A=(E0*m*(exp(-(1.5*(tr/m)))))/pi

% Calculate FI, thita, Hta
syms lamvda
lamvda=7/(6*m)
syms Fi
Fi=((B*(Delta^2))-(A*rtg*(lamvda^2)))/2
syms thita
thita=(B*Delta)-(A*rtg*lamvda)
syms Hta
Hta=Lts-Lpr-(A*rtg)

% Calculate ta
syms ta
syms kappa
kappa=(thita^2)-(4*Fi*Hta)
ta=(thita-(kappa^0.5))/(2*Fi)
display '------------------------------------------------------------'
```

Figure 9-3 Simplified image based AOT retrieval based on RT equation for GIS modeling in MATLAB

9.6 GIS Analysis

The methodology as presented in Figure 6-11 was used to create GIS maps with the AOT values derived from the fast atmospheric correction algorithm presented in the thesis. The fast atmospheric correction algorithm was reconfigured to remove the exponents and power functions related to AOT retrieval in order to calculate the AOT values for every pixel in the satellite image and display them in a geo-reference GIS map with points consisting of AOT values. This provided the ability to solve for AOT by using a simplified

equation based on the RT equations. In order to conduct the GIS analysis, the "simplified image based AOT retrieval based on RT equation for GIS modeling" model was developed in MATLAB, ERDAS Imagine 2011 and ArcGIS, as indicated in Figure 9-4.

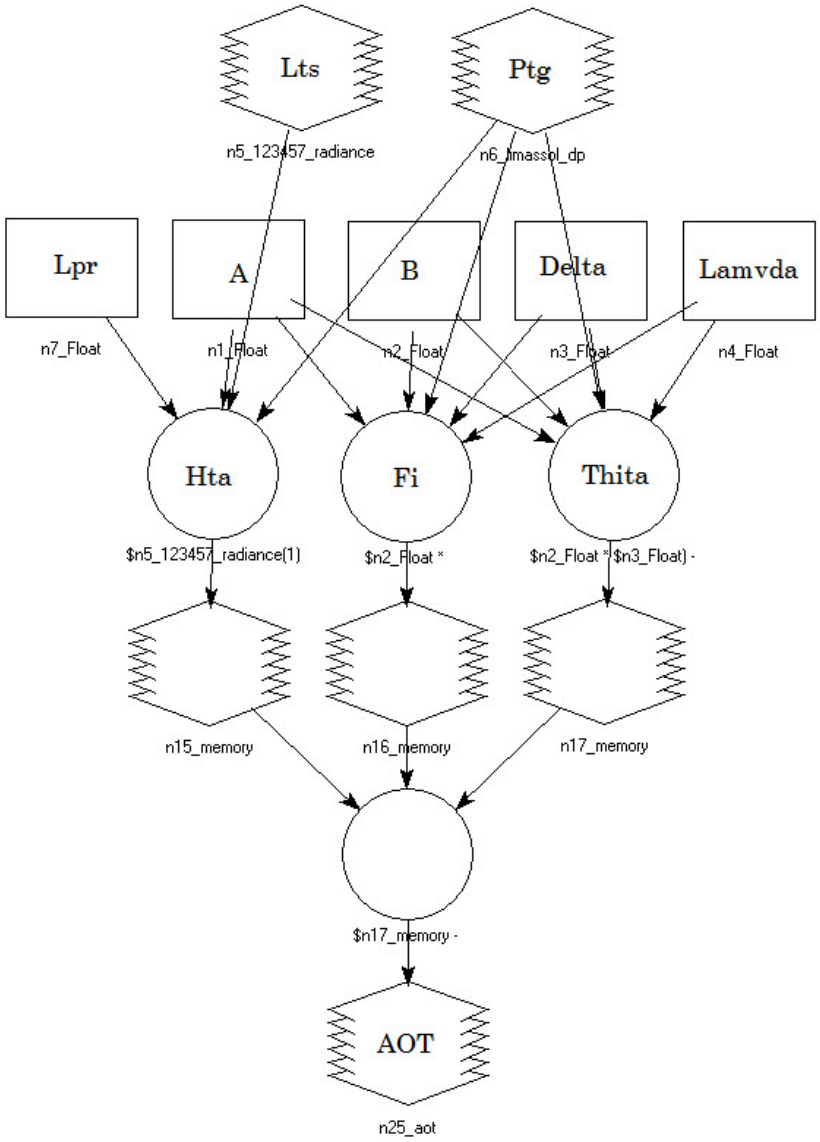

Figure 9-4 Simplified image-based AOT retrieval based on the RT equation for GIS modeling developed in ERDAS Imagine Modeller

The model was run in MATLAB and ERDAS Imagine 2011 to generate an image comprised of AOT values. Only near-Lambertian dark targets from the satellite image (Gilabert et al., 1994) were used to run the model. The model was applied to all dark surfaces in the Landsat band 1 satellite image (since the AOT required were 500 nm wavelength) and an image was created showing the AOT values for every pixel in the image, as indicated in Figure 9-4. The geo-reference image displayed the map of Limassol that met the criteria defined by the algorithm. The white areas are displayed as having no

data, due to high reflectance values of the surface, cloud presence, or surfaces that cannot be solved by the algorithm, such as non-Lambertian targets. All AOT values were exported to ASCII files to create an AOT dataset in order to exclude all the non-data values. The AOT image presented in Figure 9-5 was imported into ArcGIS.

Figure 9-5 AOT values derived from algorithm.

By using the ArcGIS software, each pixel was converted to a point creating an AOT dataset associated with each point. Figure 9-6 indicates the points generated for each pixel for the area around Tsireon stadium. The Tsireon stadium is located in a residential neighborhood just south-west of the highway. As is evident, the algorithm calculated only Lambertian or near-Lambertian surfaces, such as roads, parking lots and open areas. Non-Lambertian surfaces, such as buildings, were subtracted prior to the export of the image.

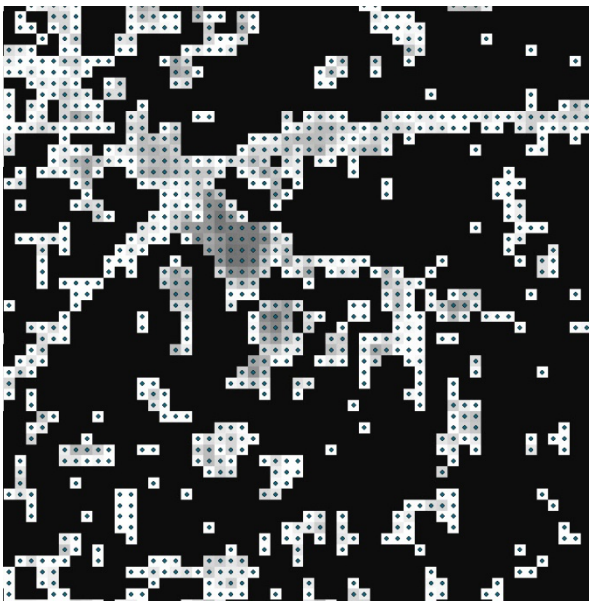

Figure 9-6 Points for the Tsireon Stadium area

Figure 9-7 shows the points and imported AOT dataset for the area around Tsireon stadium. Each point is linked with the AOT database with a specific AOT value. The white area consists of values with "no data".

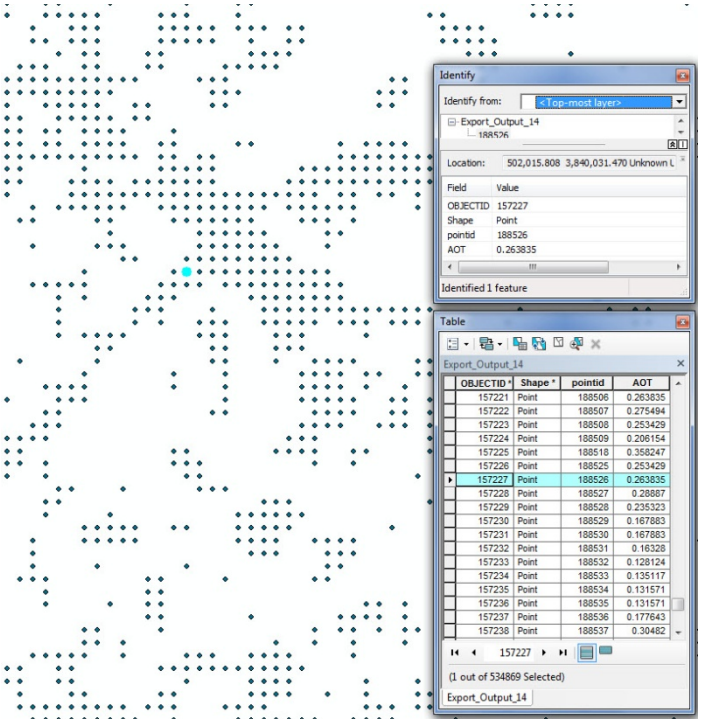

Figure 9-7 Points with AOT dataset

In order to create a GIS thematic map featuring AOT distribution throughout Limassol, interpolation was required that estimated the values missing from the "no data" area. To do so, the ordinary Kriging interpolation tool was used. Several interpolation tools were

considered and utilized, including spline, inverse distance weighting, trend surface and Theissen polygons; however, the Kriging interpolation provided the most accurate results.

Kriging is a technique for interpolating values for unknown points by utilizing the underlying spatial relationships in a data set, which is provided through variograms. A variogram refers to the variance of the difference between field values at two locations across realizations of the field (Cressie, 1993). The technique is based on regionalized variable theory, which assumes that the spatial variation in the phenomenon is statistically homogeneous throughout the surface and this provides an optimal interpolation estimate for a given coordinate location, and a variance estimate for the interpolation value (Burrough, 1986; Heine, 1986; McBratney and Webster, 1986; Oliver, 1990; Press, 1988; and Royle et al., 1981).

There are several reasons why the Kriging technique was considered the most appropriate interpolation technique. First, Kriging is the most often used geospatial technique in geo-science. Therefore, this technique is applicable to this thesis, as the in-situ spectroradiometric measurements were taken of the non-variant targets. Second, Kriging is recommended when there is a spatially correlated distance or directional bias in the data, since it assumes that the distance or direction between sample points reflects a spatial correlation that can be used to explain variation in the surface. Known measurements within a general area are typically used to derive mathematical values for locations not measured. AOT measurements tend to have a directional bias. For Kriging, data from a semivariogram, which plots the degree of spatial difference between sampled locations, are most often added to these known details. Semivariance is a principle used to derive the values on the chart. These values tend to increase with distance in relation to average sample values, up to a certain point. The estimated point values typically change in relation to the semivariance. Last, in utilizing all the GIS spatial interpolation methods available, the best results were found using the Kriging method.

The AOT dataset was calculated using Kriging, and ordinary Kriging was used, where the weighted average of neighboring samples was used to estimate the unknown values of the "no data" area. Ordinary Kriging, which assumes a constant, unknown mean, is the most general and widely used of the Kriging methods. The spherical semivariogram model was used in order to depict the spatial autocorrelation of the measured sample points. Figure 9-8 shows the results of the Kriging interpolation for the Tsireon Stadium area. The dots

indicate the points with AOT values, while the colored sections are the AOT values determined from Kriging interpolation.

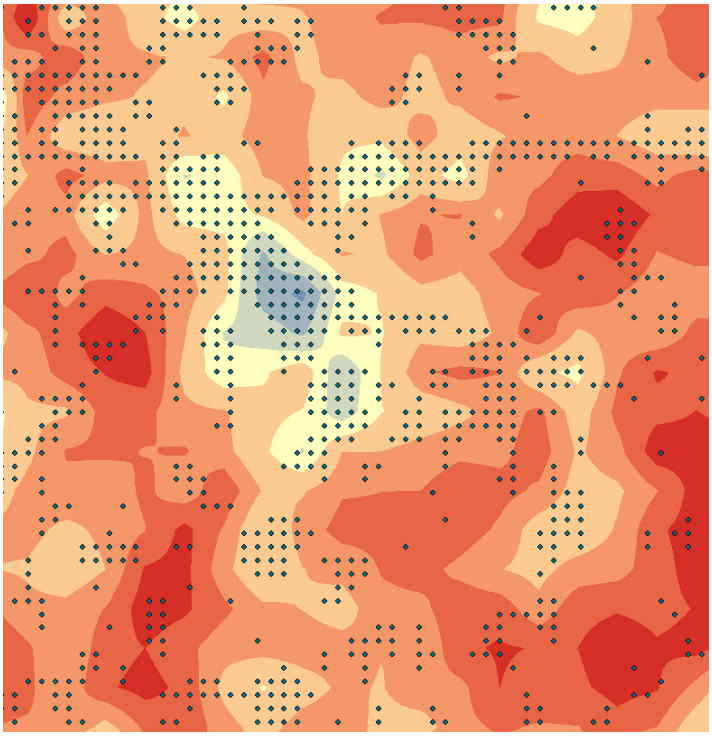

Figure 9-8 Kriging interpolation for the Tsireon Stadium area

Following the Kriging interpolation, a thematic map was generated. The map was classified according to AOT values, using different colors for the specified AOT range and a legend of the AOT values was generated. This facilitates the ability to see high and low AOT values, which makes it possible to identify high AOT levels. Figure 9-9 indicates the map of Limassol as a result of Kriging, which makes possible synoptic views of the AOT distribution.

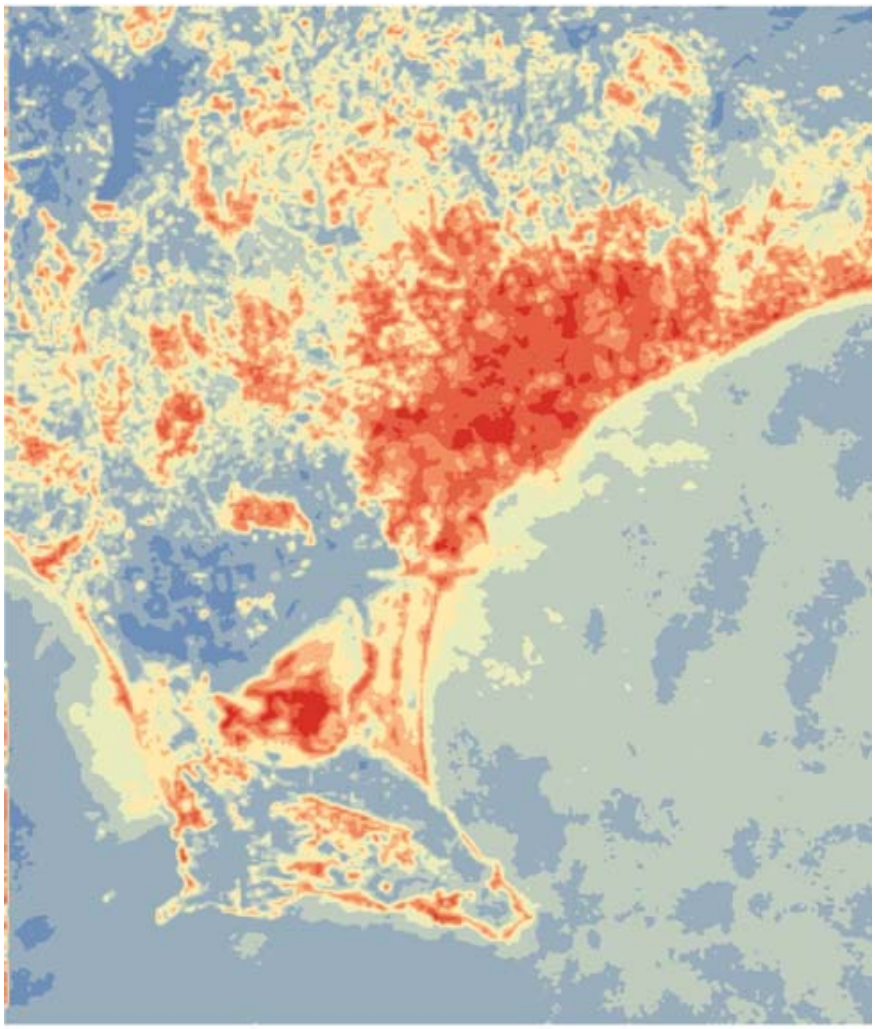

Figure 9-9 Thematic map of Limassol (2/5/2011) after Kriging interpolation, with AOT values

The thematic map was overlaid with GIS vector data from the Lands and Surveys Department for Limassol, which included roads, plots and municipality boundaries, to make it easier to identify sources of AOT values within the city and the local municipalities. Figure 9-10 indicates the thematic map with GIS vector data overlay for the Tsireon Stadium area.

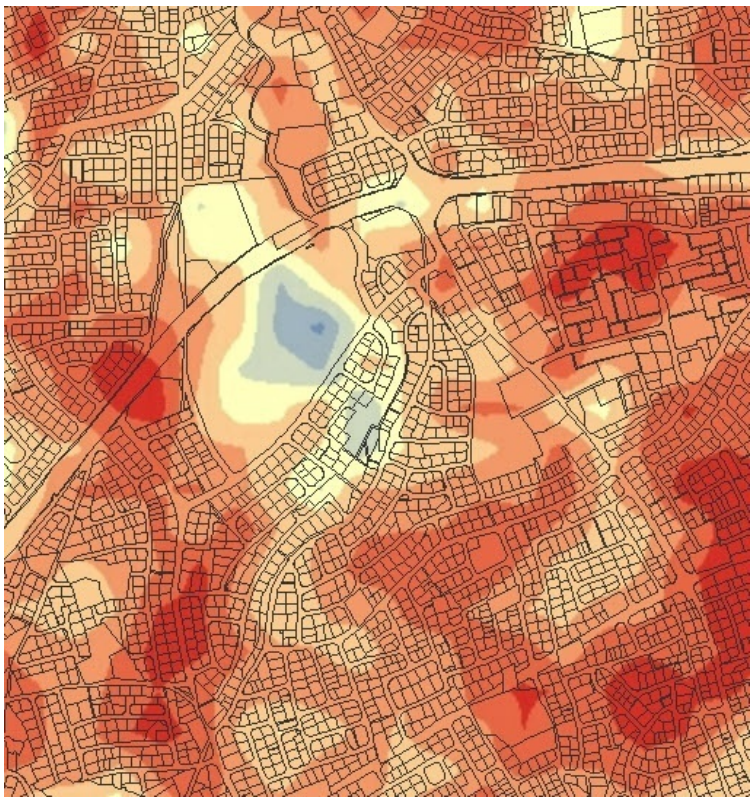

Figure 9-10 Kriging and vector overlay

Each polygon was linked to the Lands and Surveys Department database, where each plot number and characteristics were identified. This gives us the ability to use the GIS database to generate queries or create thematic maps depending on the user's search criteria. Figure 9-11 illustrates the polygon for Tsireon Stadium, which is indicative of the information associated with each vector.

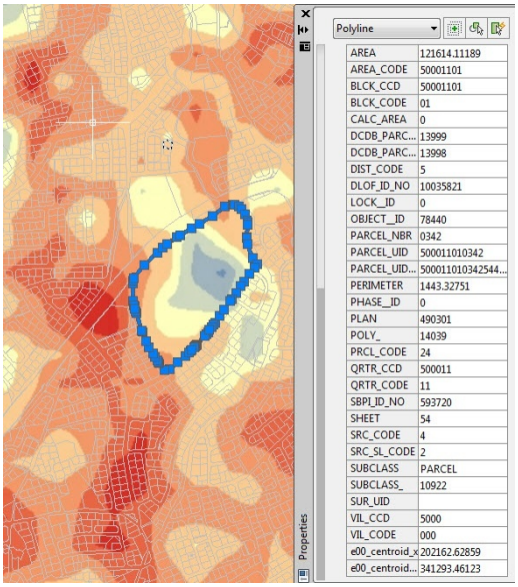

Figure 9-11 Tsireon Stadium polygon

The AOT distribution maps created using Kriging are presented in Figures 9-12 to Figure 9-22. The AOT maps with raster overlay for each date are presented in Figures 10-4 to Figures 10-14. For each map, specific areas in Limassol are indicated in order to identify trends in AOT distribution. Area #1 is Tsireon Stadium and Area #2 is the Laniteon Educational Campus, both of which are large, green areas. Both of these areas consistently display low levels of AOT. Area # 3 is the Linopetra industrial estate, which consists of light industry. Area #4 is the Cyprus University of Technology (CUT) which is located in the center of Limassol and experiences road congestion. Area #5 is the Limassol port, which is the main port in Cyprus. From examination of the maps, it is evident that Areas #3 #4 and # 5 consistently have high AOT levels in comparison with Areas #1 and #2.

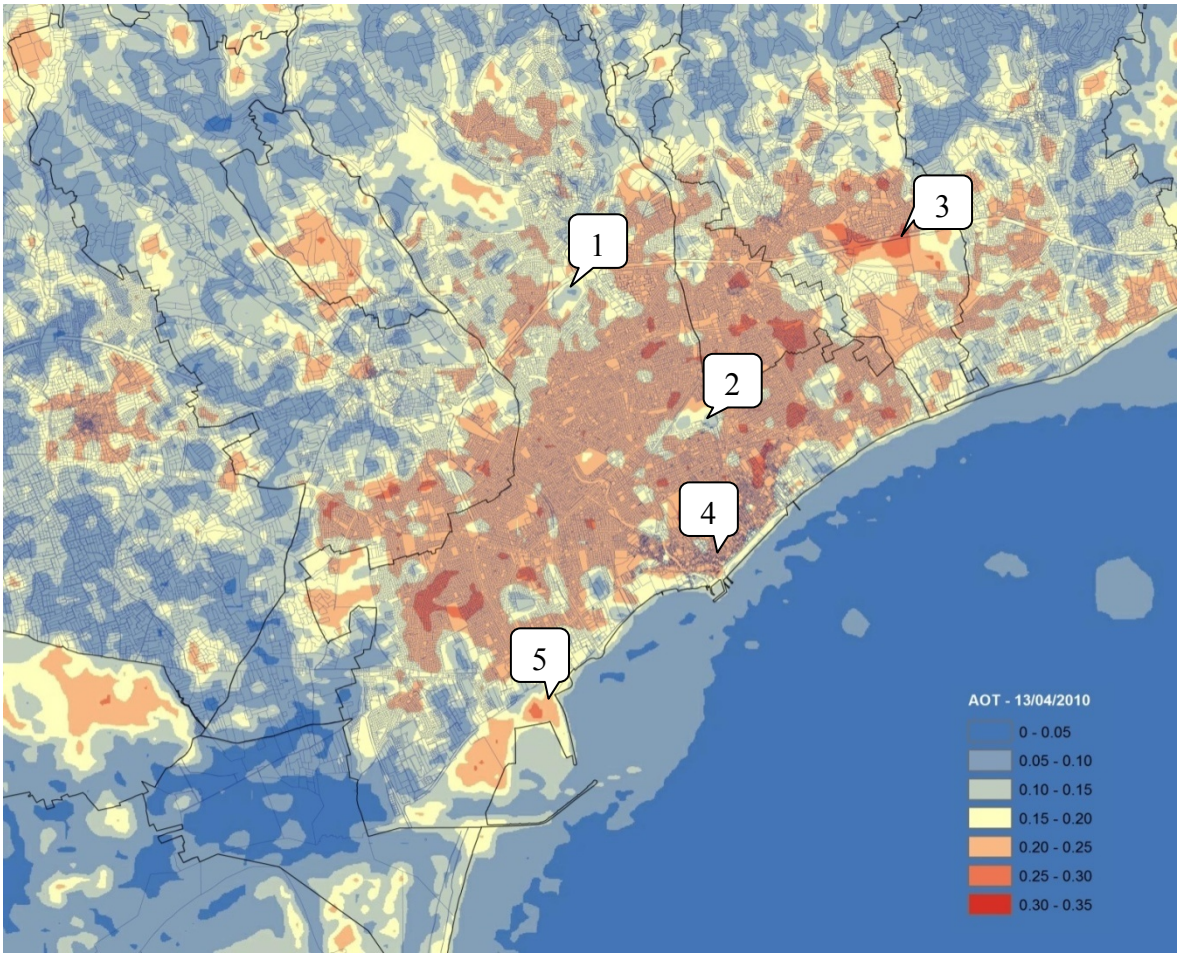

Figure 9-12 GIS Map 13/4/2010

In figure 9-12, the highest AOT levels were present in the industrial areas (#3), the CUT campus (#4) and the Limassol Port (#5). The lowest levels of AOT values in Limassol were located at the Tsireon Stadium (#1) and the Laniteon complex (#2) which are primary green, open areas. The AOT level reported by the Cimel sun photometer located at the Cyprus University of Technology (at 500 nm) is 0.256. The PM_{10} measurements reported

by the Department of Labor for Limassol (http://www.airquality.dli.mlsi.gov.cy/) that day were 35.96 μg/m^3. Overall, the map indicates moderate AOT levels, which are supported by the moderate levels of PM_{10} measurements.

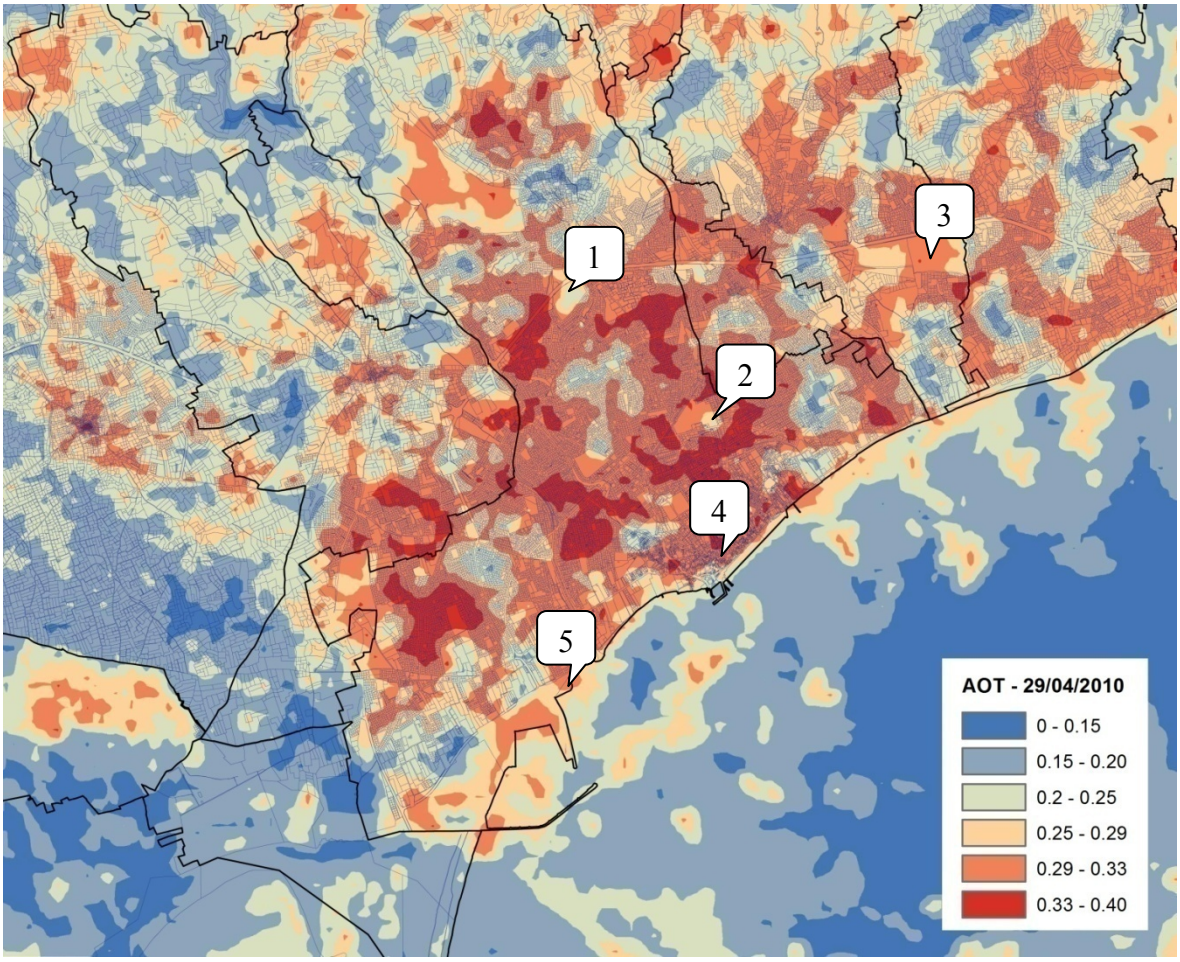

Figure 9-13 GIS Map 29/4/2010

In figure 9-13, the highest AOT levels were present in the industrial areas (#3), the CUT campus (#4) and the Limassol Port (#5). The lowest levels of AOT values in Limassol were located at the Tsireon Stadium (#1) and the Laniteon complex (#2) which are primary green, open areas. The AOT level reported by the Cimel sun photometer at the Cyprus University of Technology (at 500 nm) is 0.296. The PM_{10} measurements reported by the Department of Labor for Limassol (http://www.airquality.dli.mlsi.gov.cy/) that day were 38.26 μg/m^3. Overall, the map indicates moderate AOT levels, which are supported by the moderate levels of PM_{10} measurements.

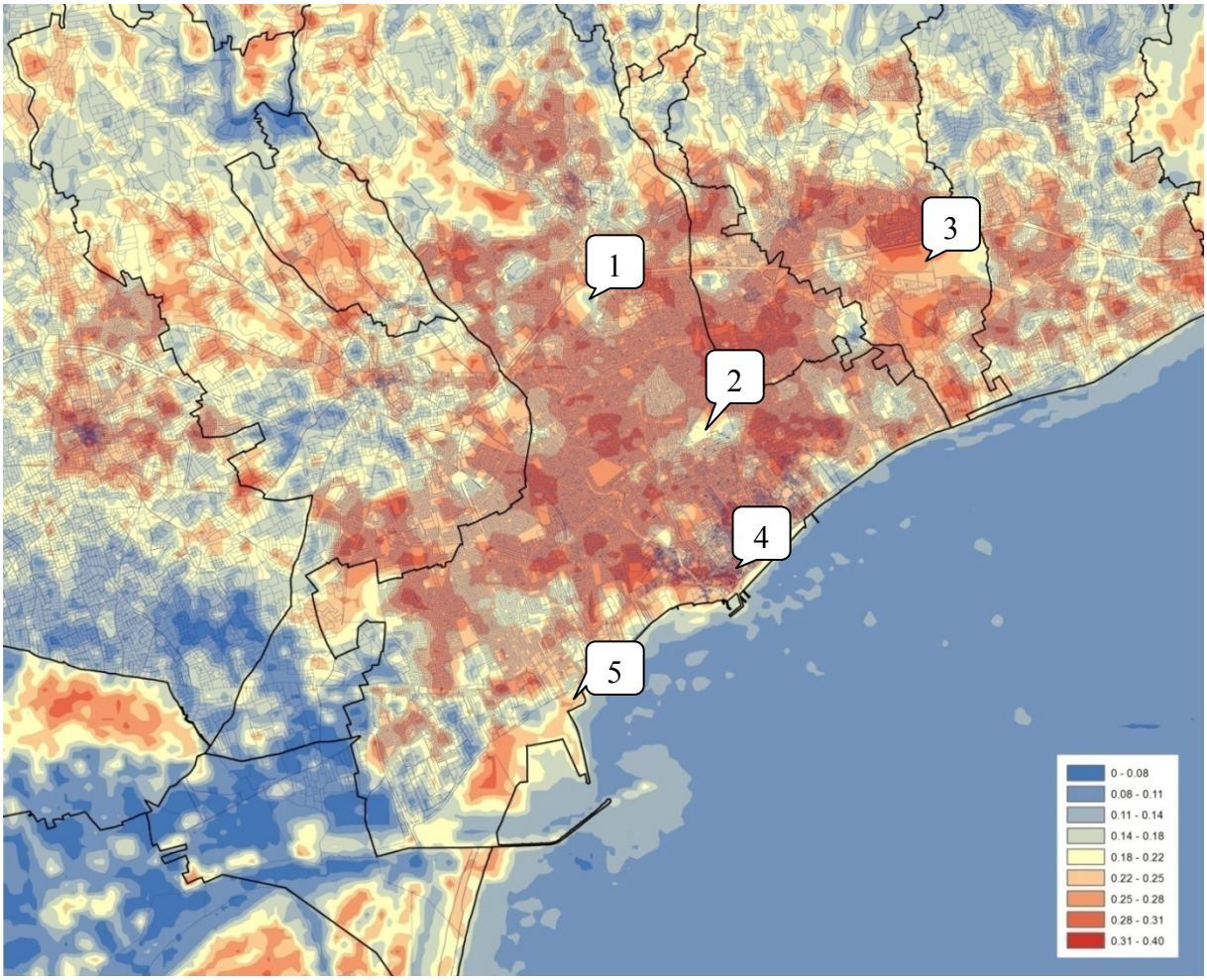

Figure 9-14 GIS map 31/5/2010

In figure 9-14, the highest AOT levels were present in the industrial areas (#3), the CUT campus (#4) and the Limassol Port (#5). The lowest levels of AOT values in Limassol were located at the Tsireon Stadium (#1) and the Laniteon complex (#2) which are primary green, open areas. The AOT level reported by the Cimel sun photometer located at the Cyprus University of Technology (at 500 nm) is 0.186. The PM_{10} measurements reported by the Department of Labor for Limassol (http://www.airquality.dli.mlsi.gov.cy/) that day were 45.5 $\mu g/m^3$. Overall, the map indicates moderate to high AOT levels, which are supported by the moderate to high levels of PM_{10} measurements.

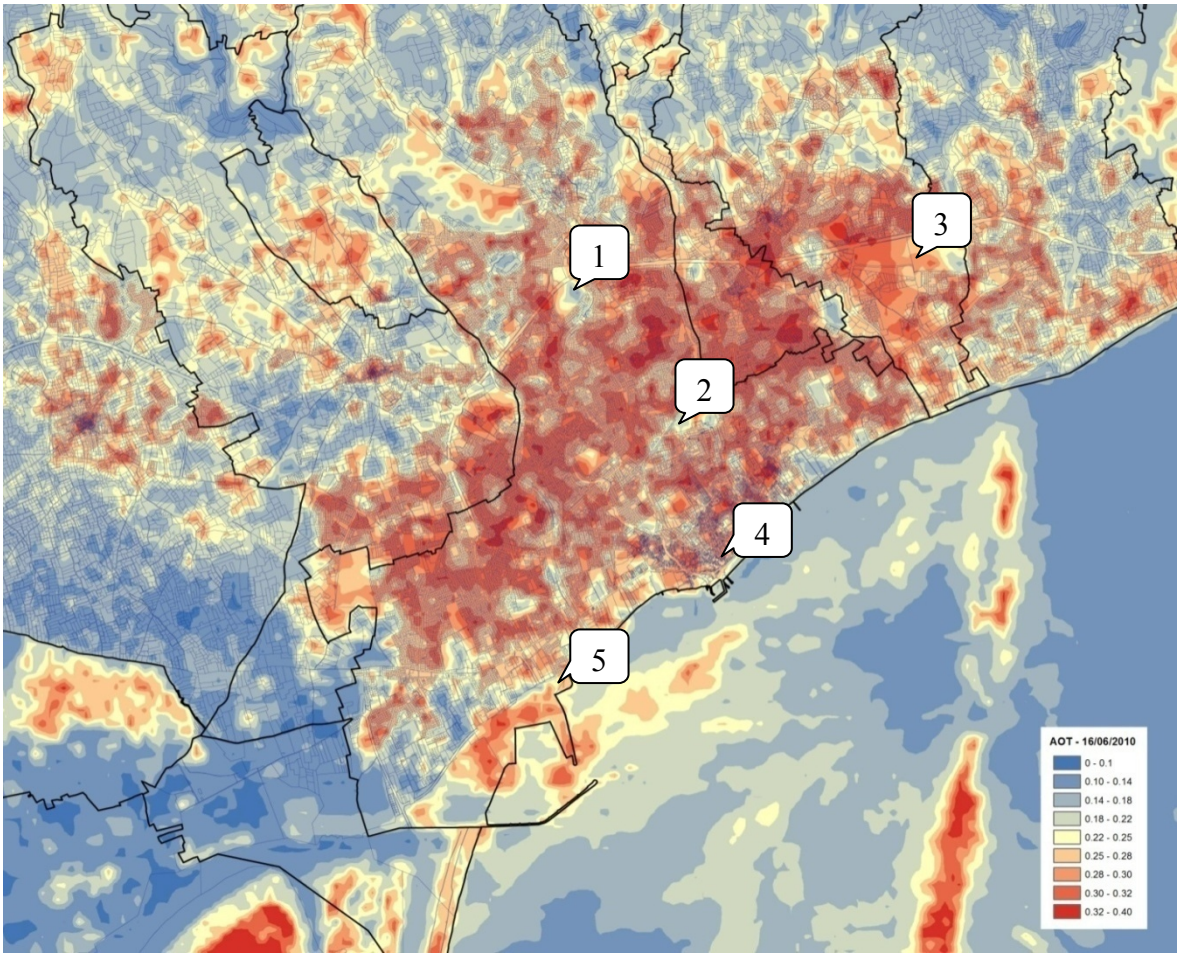

Figure 9-15 GIS map 16/6/2010

In figure 9-15, the majority of the city is presenting with elevated AOT levels. The highest AOT levels were present in the industrial areas (#3), the CUT campus (#4) and the Limassol Port (#5). The lowest levels of AOT values in Limassol were located at the Tsireon Stadium (#1) and the Laniteon complex (#2) which are primary green, open areas. The AOT level reported by the Cimel sun photometer located at the Cyprus University of Technology (at 500 nm) is 0.291. The PM_{10} measurements reported by the Department of Labor for Limassol (http://www.airquality.dli.mlsi.gov.cy/) that day were 49.84 $\mu g/m^3$. Overall, the map indicates moderate to higher AOT levels, which are supported by the moderate to high levels of PM_{10} measurements.

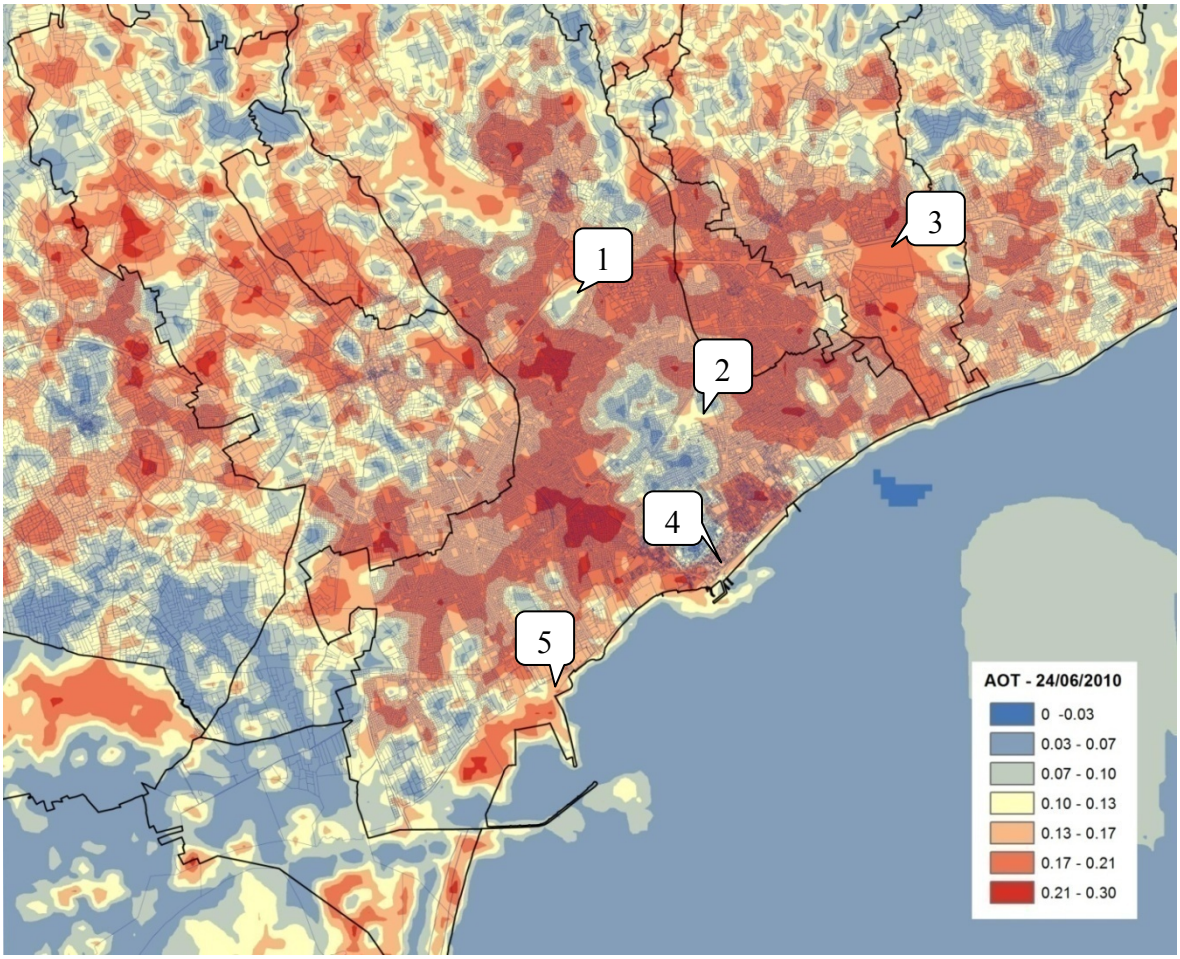

Figure 9-16 GIS Map 24/6/2010

In Figure 9-16, the majority of the city is presenting with elevated AOT levels. The highest AOT levels were present in the industrial areas (#3), the CUT campus (#4) and the Limassol Port (#5). The lowest levels of AOT values in Limassol were located at the Tsireon Stadium (#1) and the Laniteon complex (#2) which are primary green, open areas. The AOT level reported by the Cimel sun photometer located at the Cyprus University of Technology (at 500 nm) is 0.082. The AOT level reported by the Cimel sun photometer (at 500 nm) is. The PM_{10} measurements reported by the Department of Labor for Limassol (http://www.airquality.dli.mlsi.gov.cy/) that day were 32.26 $\mu g/m^3$. Overall, the map indicates moderate AOT levels, which are supported by the moderate levels of PM_{10} measurements.

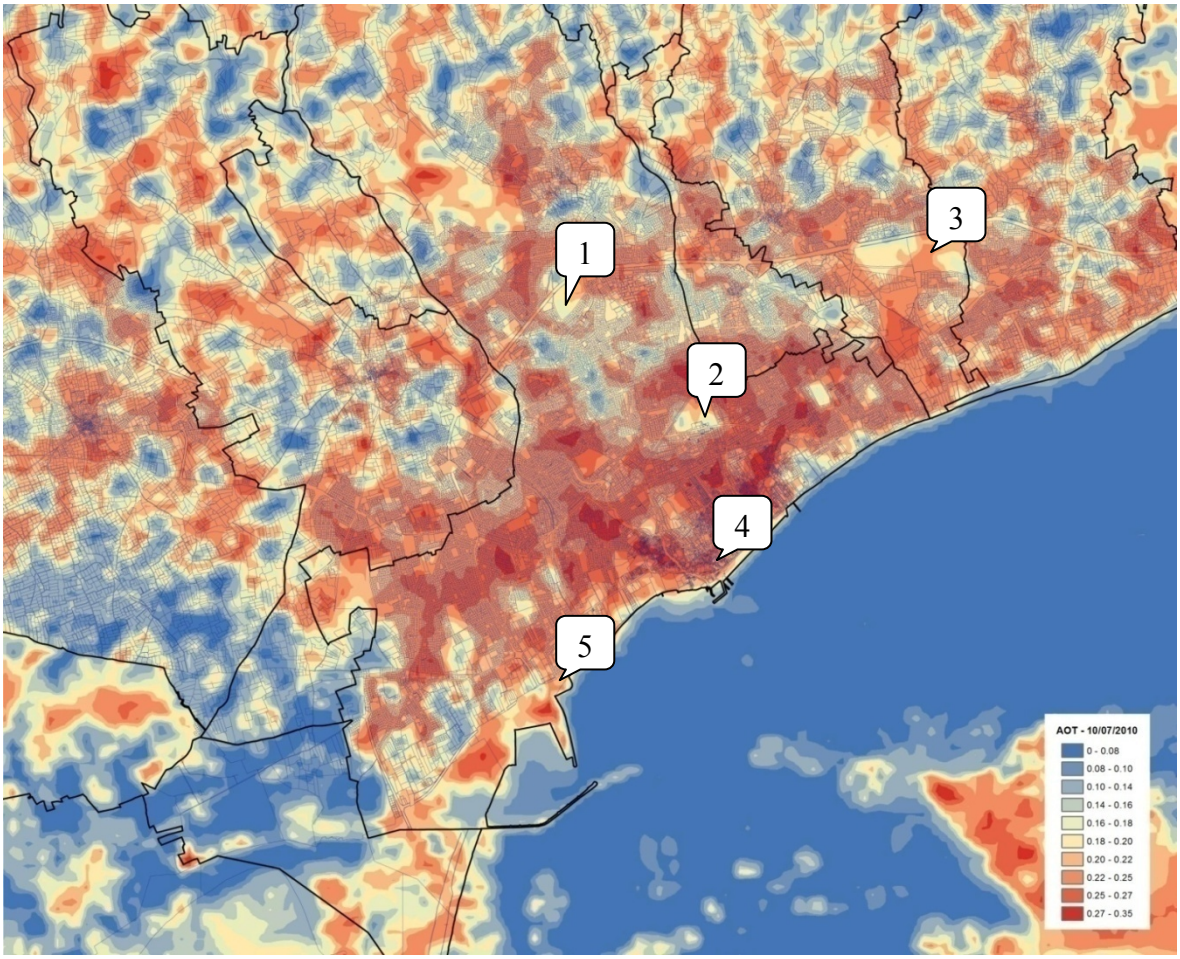

Figure 9-17 GIS map 10/7/2010

In figure 9-17, the highest AOT levels were present in the CUT campus (#4) and the Limassol Port (#5). The lowest levels of AOT values in Limassol were located at the Tsireon Stadium (#1) and the Laniteon complex (#2) which are primary green, open areas. The measurement campaign took place on Saturday, which may explain the reduced levels of AOT, due to a decrease in air pollution from automobiles. The AOT level reported by the Cimel sun photometer located at the Cyprus University of Technology (at 500 nm) is 0.123. The PM_{10} measurements reported by the Department of Labor for Limassol (http://www.airquality.dli.mlsi.gov.cy/) that day were 38.23 $\mu g/m^3$. Overall, the map indicates moderate AOT levels, which are supported by moderate levels of PM_{10} measurements.

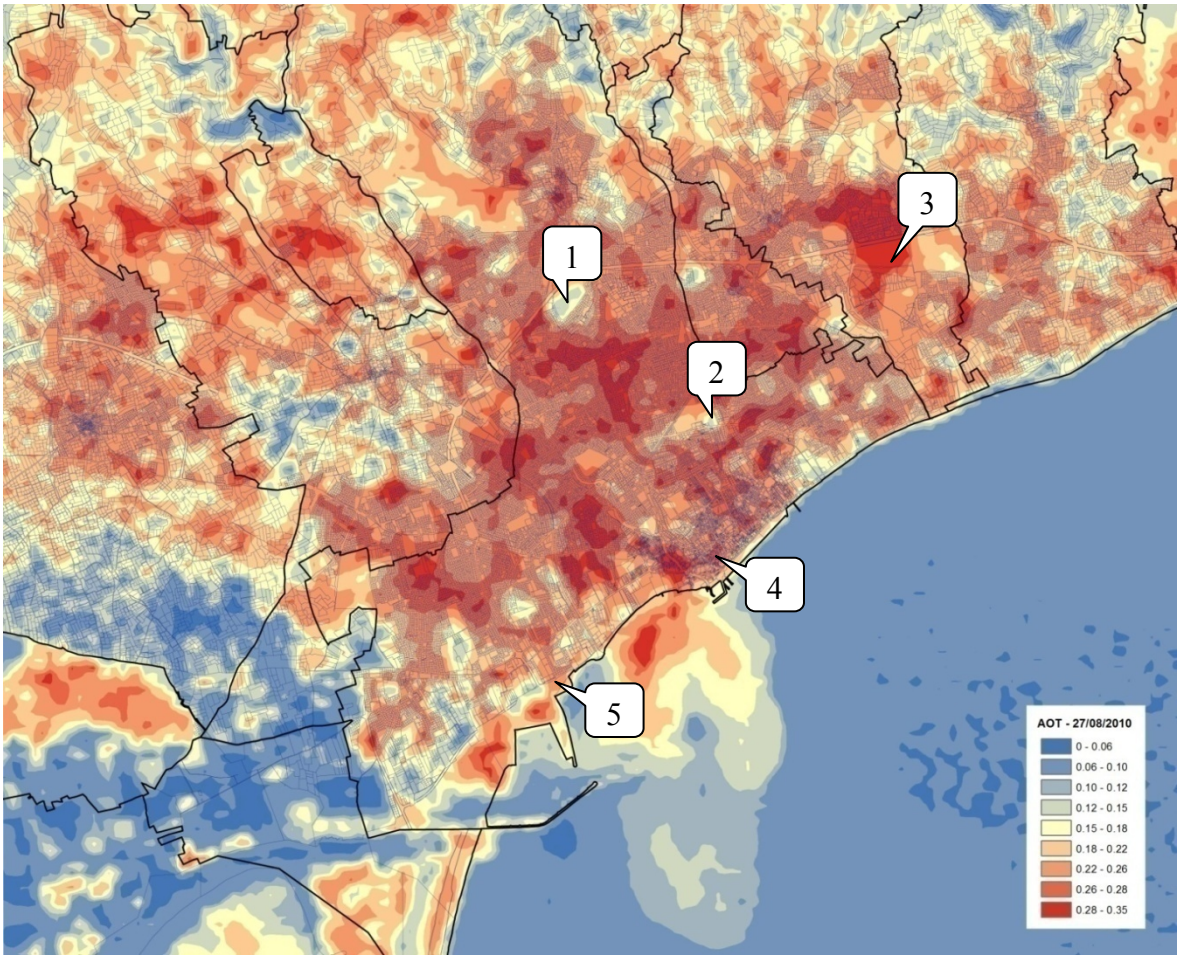

Figure 9-18 GIS map 27/8/2010

In Figure 9-18, the majority of the city is presenting with elevated AOT levels. The highest AOT levels were present in the industrial areas (#3), the CUT campus (#4) and the Limassol Port (#5). The lowest levels of AOT values in Limassol were located at the Tsireon Stadium (#1) and the Laniteon complex (#2) which are primary green, open areas. The AOT level reported by the Cimel sun photometer located at the Cyprus University of Technology (at 500 nm) is 0.179. The PM_{10} measurements reported by the Department of Labor for Limassol (http://www.airquality.dli.mlsi.gov.cy/) that day were 54.91 $\mu g/m^3$. Overall, the map indicates high AOT levels, which are supported by high levels of PM_{10} measurements.

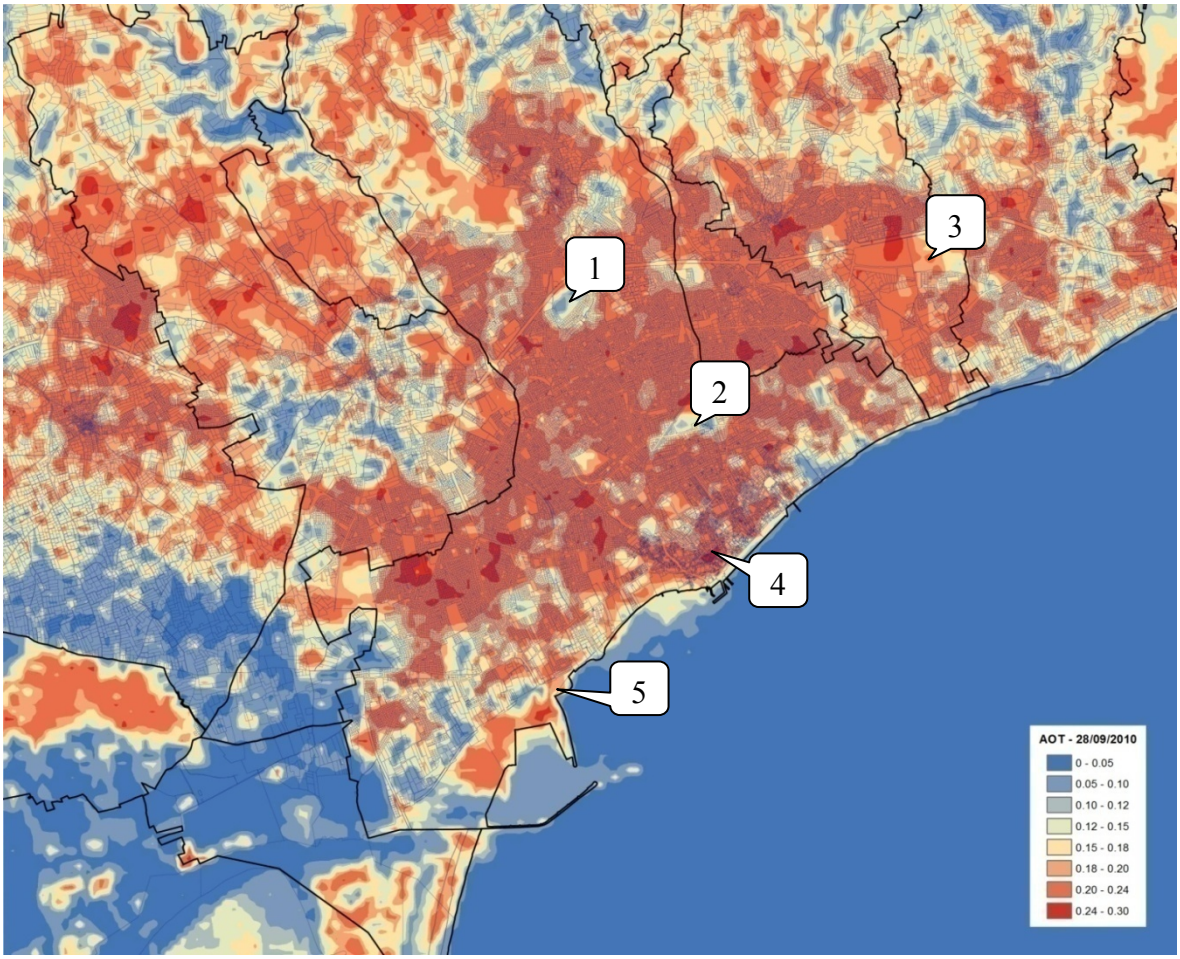

Figure 9-19 GIS map 28/9/2010

In Figure 9-19, the majority of the city is presenting with elevated AOT levels, which is correlated with the high levels of dust, as indicated by the high PM_{10} measurements. The highest AOT levels were present in industrial areas (#1) and heavily congested roads (#2). The lowest levels of AOT values in Limassol were located at the Tsireon Stadium (#3) and the Limassol Zoo (#4), which are primary green, open areas. The AOT level reported by the Cimel sun photometer located at the Cyprus University of Technology (at 500 nm) is 0.280. The PM_{10} measurements reported by the Department of Labor for Limassol (http://www.airquality.dli.mlsi.gov.cy/) that day were 43.37 $\mu g/m^3$. Overall, the map indicates moderate to high AOT levels, which are supported by moderate to high levels of PM_{10} measurements.

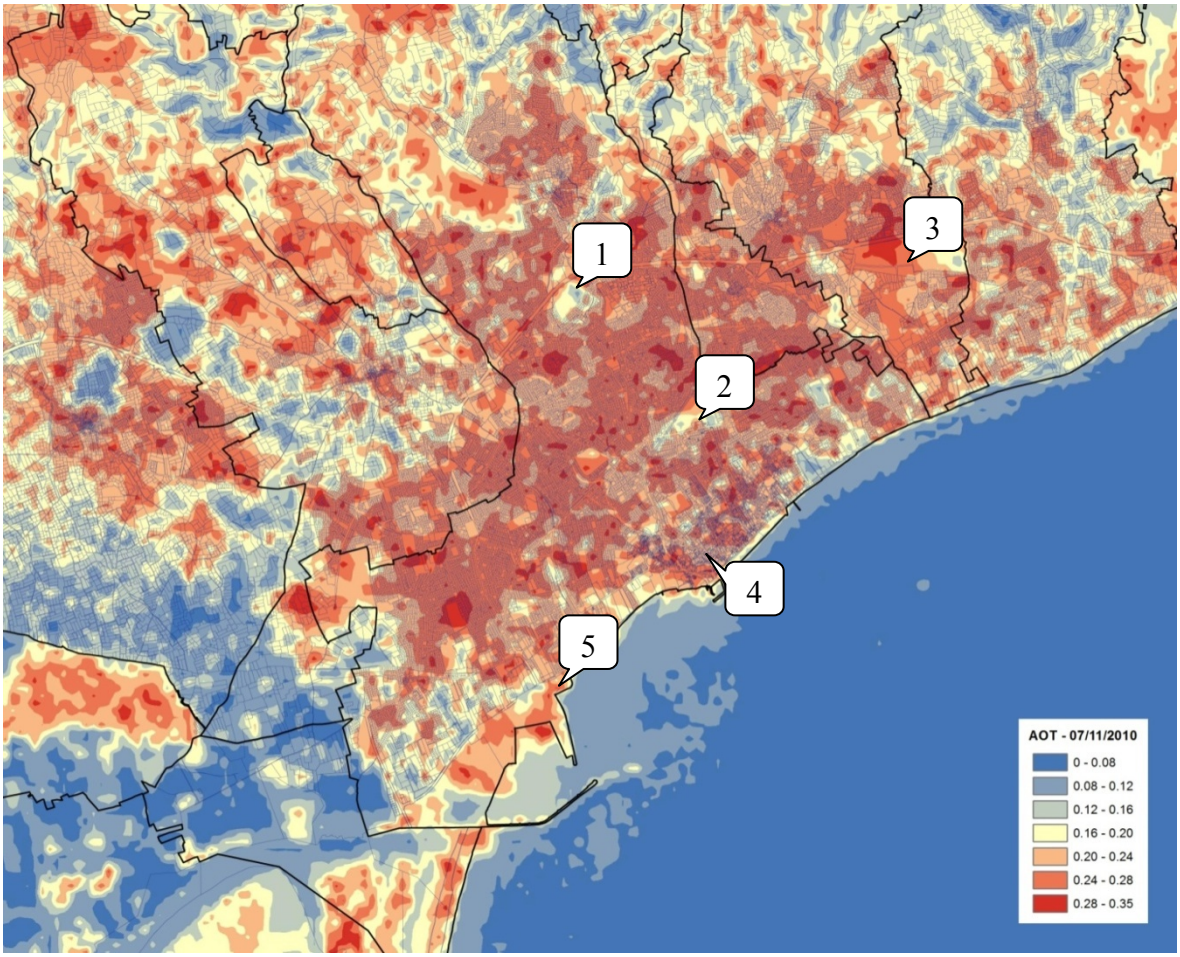

Figure 9-20 GIS map 7/11/2010

In Figure 9-20, the majority of the city is presenting with elevated AOT levels. The highest AOT levels were present in the industrial areas (#3), the CUT campus (#4) and the Limassol Port (#5). The lowest levels of AOT values in Limassol were located at the Tsireon Stadium (#1) and the Laniteon complex (#2) which are primary green, open areas. The AOT level reported by the Cimel sun photometer located at the Cyprus University of Technology (at 500 nm) is 0.088. The PM_{10} measurements reported by the Department of Labor for Limassol (http://www.airquality.dli.mlsi.gov.cy/) that day were 51.0 $\mu g/m^3$, which correlate to the high AOT values present in the region. Overall, the map indicates high AOT levels, which are supported by high levels of PM_{10} measurements.

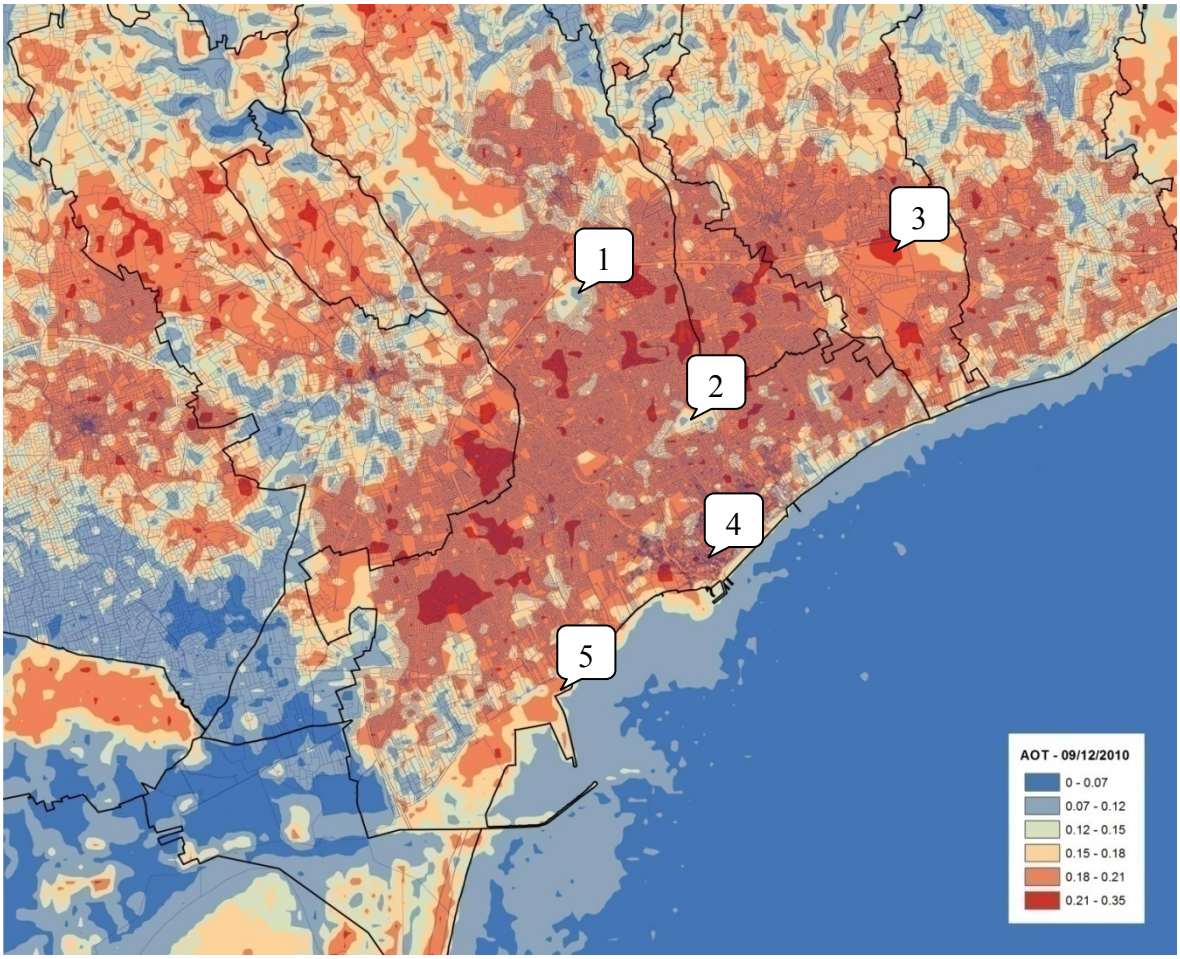

Figure 9-21 GIS map 09/12/2010

In Figure 9-21, the majority of the city is presenting with elevated AOT levels, which correlate with the high levels of dust indicated by the high PM_{10} measurements. The highest AOT levels were present in the industrial areas (#3), the CUT campus (#4) and the Limassol Port (#5). The lowest levels of AOT values in Limassol were located at the Tsireon Stadium (#1) and the Laniteon complex (#2) which are primary green, open areas. There was no data available from the AERONET network. The PM_{10} measurements reported by the Department of Labor for Limassol (http://www.airquality.dli.mlsi.gov.cy/) that day were 47.31 $\mu g/m^3$. Overall, the map indicates moderate to high AOT levels, which are supported by moderate to high levels of PM_{10} measurements.

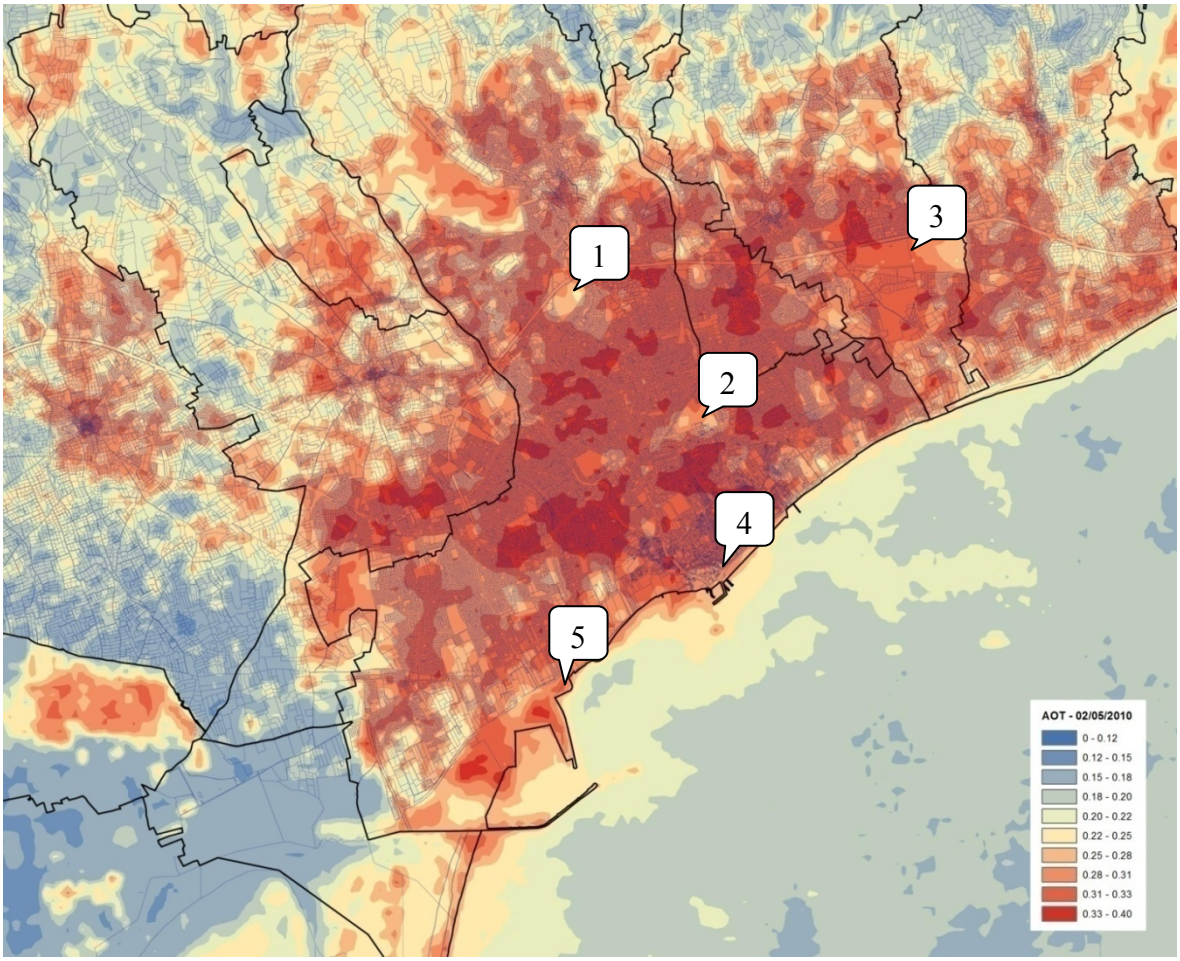

Figure 9-22 GIS map 02/05/11

In Figure 9-22, the highest AOT levels were present in the industrial areas (#3), the CUT campus (#4) and the Limassol Port (#5). In this image, the majority of the city is presenting with elevated AOT levels. There was no data available from the AERONET network nor from the air quality monitoring station. Overall, the map indicates high AOT levels.

9.7 Summary

In this chapter, a detailed explanation of the fast atmospheric correction algorithm used to retrieve AOT by applying the improved PITs method and the DP method were discussed. A detailed explanation of the parameters used in the algorithm was presented, as well as information on how the parameters can be determined. The algorithm was then reconfigured in order to enable GIS analysis to produce GIS maps featuring the AOT distribution and was named the simplified image based AOT retrieval based on RT equation for GIS modeling.

Chapter 10 Results and Accuracy Assessment

This chapter presents the results of the accuracy assessment that were done to determine the invariance of the in-situ spectroradiometric measurements, the level of agreement between the in-situ AOT measurements and the AOT measurements derived from the algorithm using the variables from the darkest pixel and the empirical line method and the agreement between the in-situ AOT values with the values derived from the algorithm as presented in the GIs maps. The accuracy assessment was indicative of several results of the study, including pseudo-invariant reflectance values, AOT retrieval values, the effects of precipitation and the accuracy of the AOT values from the GIS analysis.

10.1 Accuracy Assessment Using Pseudo-Invariant Targets

The average reflectance values derived from the improved empirical line method and the darkest pixel method were compared with the in-situ reflectance values from the SVC HR 1024 spectroradiometer. As is evident, there is strong agreement between the reflectance values derived from the atmospheric correction methods with the in-situ measurements for all targets. Table 10-1 indicates the in-situ reflectance values for all targets in compared with the DP and PITs method of atmospheric correction for Landsat band 1.

Date	Reflectance values derived from	Gray Asphalt (%)	Black Asphalt (%)	Concrete (%)	Black Sand (%)	Compacted Sand (%)
13/4/10	Empirical line method	0.13	0.11	0.19	0.12	0.11
	Darkest Pixel method	0.13	0.11	0.18	0.12	0.11
	In-situ measurements	0.12	0.11	0.18	0.12	0.12
29/4/10	Empirical line method	0.12	0.09	0.18	0.10	0.13
	Darkest Pixel method	0.11	0.10	0.15	0.10	0.12
	In-situ measurements	0.11	0.09	0.15	0.11	0.15
31/5/10	Empirical line method	0.12	0.10	0.17	0.12	0.12
	Darkest Pixel method	0.12	0.10	0.19	0.11	0.12
	In-situ measurements	0.12	0.10	0.17	0.12	0.14
16/6/10	Empirical line method	0.11	0.11	0.20	0.10	0.13

	Darkest Pixel method	0.11	0.11	0.17	0.10	0.12
	In-situ measurements	0.12	0.11	0.17	0.11	0.16
24/6/10	Empirical line method	0.13	0.10	0.17	0.11	0.18
	Darkest Pixel method	0.13	0.11	0.21	0.12	0.15
	In-situ measurements	0.13	0.11	0.18	0.14	0.19
10/7/10	Empirical line method	0.13	0.11	0.19	0.14	0.18
	Darkest Pixel method	0.13	0.11	0.19	0.12	0.18
	In-situ measurements	0.12	0.11	0.19	0.15	0.18
27/8/10	Empirical line method	0.15	0.11	0.22	0.14	0.16
	Darkest Pixel method	0.13	0.10	0.19	0.11	0.14
	In-situ measurements	0.13	0.10	0.19	0.15	0.18
28/9/10	Empirical line method	0.13	0.09	0.18	0.10	0.20
	Darkest Pixel method	0.13	0.10	0.20	0.11	0.15
	In-situ measurements	0.13	0.10	0.19	0.11	0.19
7/11/10	Empirical line method	0.13	0.10	0.20	0.09	0.13
	Darkest Pixel method	0.11	0.10	0.17	0.09	0.13
	In-situ measurements	0.11	0.10	0.18	0.10	0.16
9/12/10	Empirical line method	0.11	0.09	0.17	0.08	0.14
	Darkest Pixel method	0.13	0.11	0.18	0.10	0.13
	In-situ measurements	0.12	0.11	0.16	0.10	0.16
2/5/11	Empirical line method	0.10	0.09	0.14	0.08	0.08
	Darkest Pixel method	0.11	0.10	0.13	0.09	0.09
	In-situ measurements	0.12	0.10	0.13	0.09	0.13

Table 10-1 In-situ reflectance values for all targets in compared with the DP and PITs method of atmospheric correction for Landsat Band 1.

The results indicated that surface reflectance is affected by precipitation for all targets in varying amounts. Gray Asphalt, Black Asphalt and Concrete did not show significant differences in the average measurements and standard deviations for both wet and dry

conditions in all bands, which indicates their suitability as pseudo-invariant targets for all weather conditions. However, there were significant differences in the reflectance values of the Black Sand and Compacted Sand. The results indicated that rainfall did have a significant impact on the reflectance values, reducing them by as much as 7% after the atmospheric correction. Therefore, when using pseudo-invariant targets for image based atmospheric correction, especially sand, meteorological information such as precipitation amounts, need to be taken into consideration, as beach sand can be affected by rain. Figure 10-1 indicates the differences in average in situ reflectance values of the five targets as a function of wet and dry conditions. Table 10-2 to Table 10-6 compares the average reflectance by band for each of the five targets as a function of wet and dry conditions.

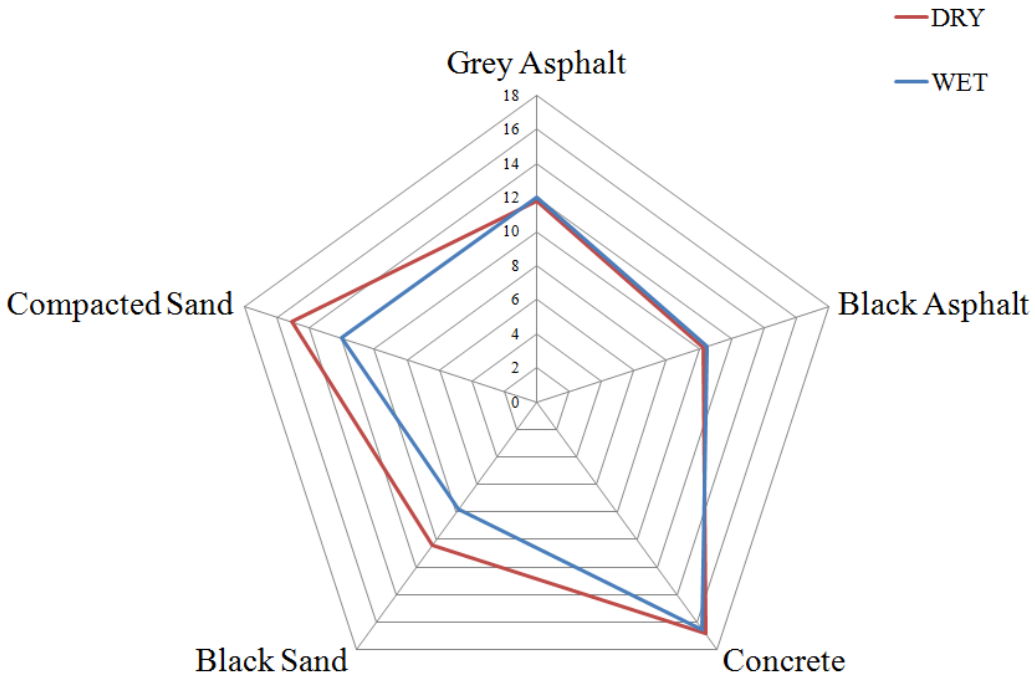

Figure 10-1 Difference in the average in situ reflectance values of the five targets as a function of wet and dry conditions

Gray Asphalt	Wet Conditions Average	Dry Conditions Average	Difference
Band 1	11.92%	11.93%	0.01%
Band 2	13.48%	13.49%	0.01%
Band 3	14.39%	14.57%	0.18%
Band 4	16.20%	16.28%	0.08%

Table10-2 Average reflectance values for Gray Asphalt for Wet and Dry conditions in Landsat TM/ETM+ bands 1-4, including difference between wet and dry conditions

Black Asphalt	Wet Conditions Average	Dry Conditions Average	Difference
Band 1	10.95%	10.25%	0.70%
Band 2	12.57%	11.76%	0.81%
Band 3	13.55%	12.87%	0.68%
Band 4	15.39%	14.96%	0.45%

Table 10-3 Average reflectance values for Black Asphalt for Wet and Dry conditions in Landsat TM/ETM+ bands 1-4, including difference between wet and dry conditions

Concrete	Wet Conditions Average	Dry Conditions Average	Difference
Band 1	16.00%	16. 92%	0.92%
Band 2	19.98%	21.22%	1.24%
Band 3	22.12%	23.78%	1.66%
Band 4	22.56%	24.48%	1.92%

Table 10-4 Average reflectance values for Concrete for Wet and Dry conditions in Landsat TM/ETM+ bands 1-4, including difference between wet and dry conditions

Black Sand	Wet Conditions Average	Dry Conditions Average	Difference
Band 1	8.28%	12.40%	4.12%
Band 2	12.08%	17.42%	5.34%
Band 3	13.22%	19.02%	5.80%
Band 4	14.45%	20.60%	6.15%

Table 10-5 Average reflectance values for Black Sand for Wet and Dry conditions in Landsat TM/ETM+ bands 1-4, including difference between wet and dry conditions

Compacted Sand	Wet Conditions Average	Dry Conditions Average	Difference
Band 1	11.59%	17.49%	5.90%
Band 2	14.87%	21.33%	6.46%
Band 3	16.07%	22.84%	5.80%
Band 4	17.08%	24.21%	7.13%

Table 10-6 Average reflectance values for Compacted Sand for Wet and Dry conditions in Landsat TM/ETM+ bands 1-4, including difference between wet and dry conditions

An assessment of precipitation effects was conducted through comparison of the atmospheric path radiance component (intercept) for both wet and dry conditions. An assessment was performed by calculating wet and dry conditions for the same satellite image in order to examine the effects of precipitation for both conditions by using the empirical line method. For example, if the in situ reflectance value corresponded to wet

conditions, the intercept was determined using the in situ reflectance values, followed by the intercept being determined by use of the average dry reflectance values. Subsequently, the difference between the intercept value for both wet and dry values was calculated. A difference from 0.03 to 0.10 in the intercept for all bands for both wet and dry conditions was found (see Table 10-7). Figure 10-2 indicates the linear regression for 7/11/2010 in Landsat bands 1-4, which corresponded to a dry condition, compared to the linear regression using average measurements for wet conditions. The arrows in Figure 10-2 indicate the difference in the atmospheric correction showing the effects of precipitation on a specific target. It was found that the proper precipitation conditions need to be considered in conducting atmospheric correction using atmospheric correction methods, as incorrect precipitation conditions can significantly affect the intercept and therefore the accuracy of the atmospheric correction.

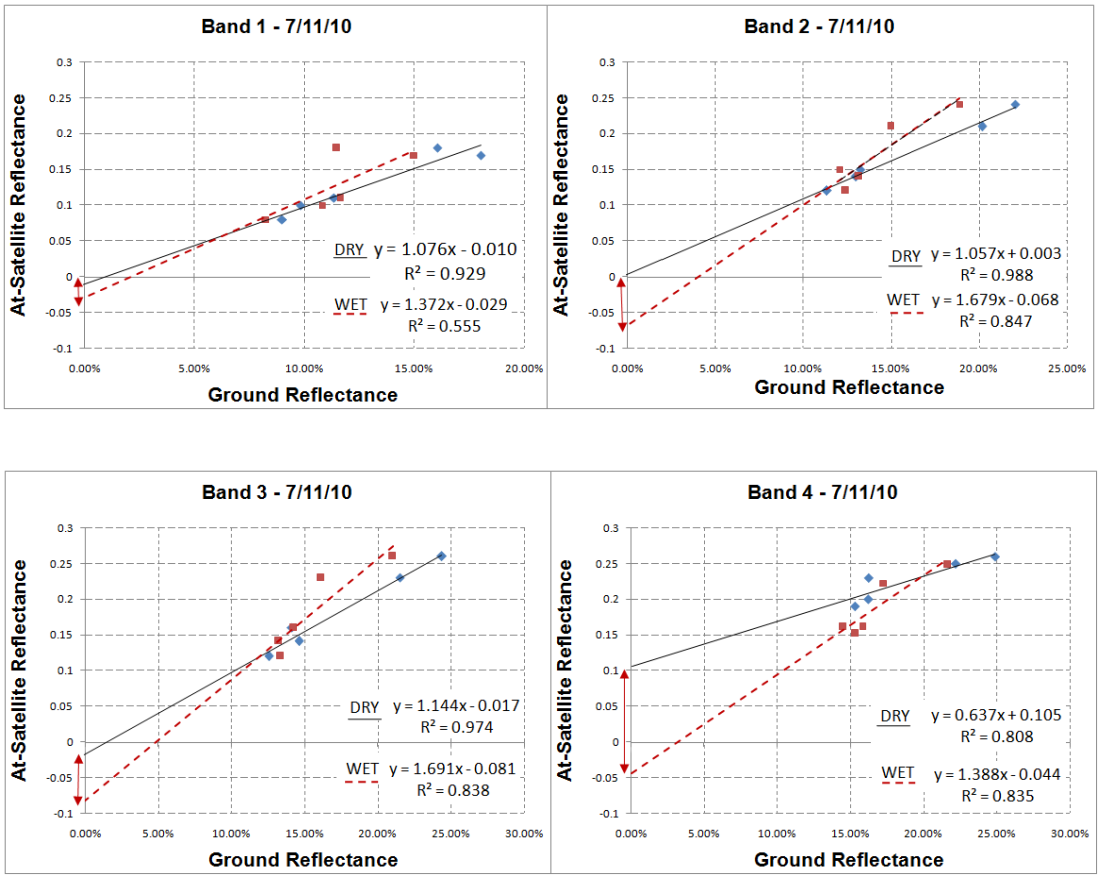

Figure 10-2 Linear regression for 7/11/2010 using the empirical line method of atmospheric correction. The arrow indicates the difference in the atmospheric path radiance component between wet and dry conditions.

Date-Condition Type of Reflectance Values	Intercept (c)			
	Landsat TM/ ETM+ band 1	Landsat TM/ ETM+ band 2	Landsat TM/ ETM+ band 3	Landsat TM/ ETM+ band 4
13/4/2010 Wet-**(in situ reflectance values)**	0.103	0.128	0.064	0.08
13/4/2010 Dry-**(averaged reflectance values)**	0.069	0.082	0.011	0.144
Difference	0.044	0.046	0.053	0.074
29/4/2010 Wet-**(in situ reflectance values)**	0.149	0.138	0.076	0.144
29/4/2010 Dry-**(averaged reflectance values)**	0.115	0.093	0.020	0.070
Difference	0.034	0.045	0.056	0.074
31/5/2010 Dry-**(in situ reflectance values)**	0.027	0.073	0.083	0.168
31/5/2010 Wet-**(averaged reflectance values)**	0.070	0.019	0.027	0.070
Difference	0.043	0.054	0.056	0.098
16/6/2010 Dry-**(in situ reflectance values)**	0.047	0.080	0.067	0.125
16/6/2010 Wet-**(averaged reflectance values)**	0.016	0.036	0.007	0.024
Difference	0.031	0.044	0.050	0.101
24/6/2010 Dry-**(in situ reflectance values)**	0.072	0.064	0.046	0.147
24/6/2010 Wet-**(averaged reflectance values)**	0.036	0.017	-0.006	0.043
Difference	0.036	0.047	0.052	0.104
10/7/2010 Dry-**(in situ reflectance values)**	0.050	0.061	0.043	0.160
10/7/2010 Wet-**(averaged reflectance values)**	0.082	0.003	-0.017	0.063
Difference	0.032	0.058	0.060	0.097
27/8/2010 Dry-**(in situ reflectance values)**	0.069	0.079	0.007	0.160
27/8/2010 Wet-**(averaged reflectance values)**	0.030	0.023	0.053	0.078
Difference	0.039	0.056	0.036	0.082
28/9/2010 Dry-**(in situ reflectance values)**	0.087	0.065	0.044	0.000
28/9/2010 Wet-**(averaged reflectance values)**	0.050	0.015	-0.013	-0.101
Difference	0.037	0.050	0.057	0.101
7/11/2010 Dry-**(in situ reflectance values)**	0.091	0.074	0.014	0.131
7/11/2010 Wet-**(averaged reflectance values)**	0.053	0.025	-0.048	0.040
Difference	0.038	0.049	0.062	0.91
9/12/2010 Wet-**(in situ reflectance values)**	0.093	0.121	0.111	0.144
9/12/2010 Dry-**(averaged reflectance values)**	0.057	0.069	0.057	0.047
Difference	0.036	0.052	0.054	0.097
2/5/2011 Dry-**(in situ reflectance values)**	0.142	0.102	0.111	0.121
2/5/2011 Wet-**(averaged reflectance values)**	0.100	0.056	0.054	0.022
Difference	0.042	0.046	0.057	0.099

Table 10-7 Atmospheric path radiance component (intercept) for both wet and dry conditions, including difference between wet and dry conditions.

10.2 Accuracy assessment of AOT values from Sun photometers

In order to conduct the accuracy assessment to determine the validity of the AOT values retrieved from the algorithm, the AOT values from the Microtops handheld sun photometer were used. The Microtops sun photometer values were downloaded using the Solar Light

software and the measurements were converted into an excel file. The measurements were then sorted according to date and target. As well, the Cimel sun photometer AOT values were downloaded from the AERONET site. As the Cimel sun photometer was part of the AERONET program, data was downloaded from the AERONET website (http://aeronet.gsfc.nasa.gov), as indicated in Figure 10-3.

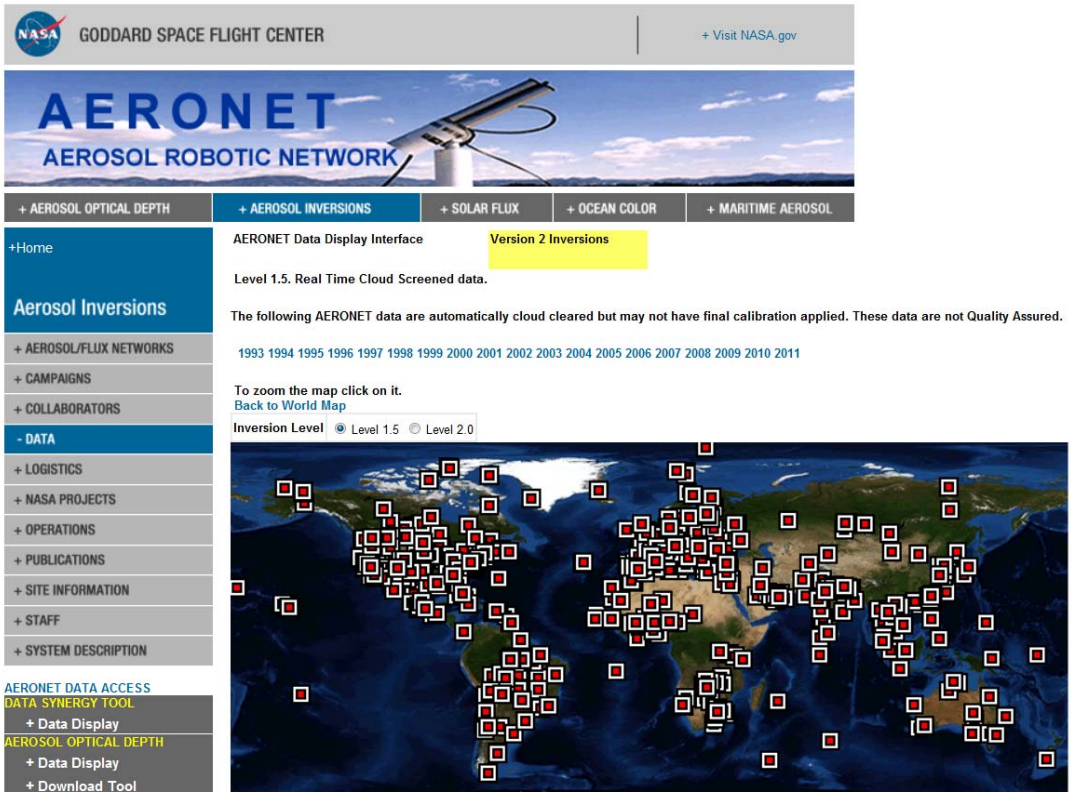

Figure 10-3 AERONET homepage for data display

There are several different data levels to choose from on the AERONET homepage. Level 1 data is considered raw data, which is Unscreened and does not have final calibration applied. Level 1.5 data is automatically cloud-screened, but does not have final calibration applied. Level 2 data are quality assured data where pre- and post-field calibration has been applied and the data has been automatically cloud cleared and manually inspected. Level 1.5 data was used, as Level 2.0 data was not available for all the satellite images. The data file was saved in an excel file for comparison with the Microtops AOT values (see Appendix 2). In order to derive the AOT values from the satellite image, the MATLAB software is used in order to solve for τ_a. Following, the AOT from the Microtops and Cimel sun photometers were compared with the derived AOT from the algorithm. As AOT varies temporally and multiple sun photometer measurements were available for each date, the sun photometer measurement that took place as close to the time of satellite overpass (08:15 G.M.T.) was used.

Using the algorithm presented in Chapter 9, AOT was derived using the reflectance values calculated through the DP method of atmospheric correction as well as the PITs method of atmospheric correction and compared with the AOT values measured by the Microtops sun photometer and the AOT values measured by the Cimel sun photometer. Table 10-1 provides a comparison of the AOT values in Band 1 retrieved with the DP method, the PITs method and the in-situ sun photometer measurements with the Microtops and Cimel sun photometer, which is presented graphically in Figure 10-4.

Date	DP AOT	PITs AOT	AOT Microtops	AOT AERONET
13/4/2010	0.224	0.192	0.263	0.192
29/4/2010	0.406	0.491	0.435	0.421
31/5/2010	0.284	0.194	0.269	0.231
16/6/2010	0.313	0.418	0.432	0.303
24/6/2010	0.230	0.271	0.294	0.118
10/7/2010	0.247	0.346	0.341	0.354
27/8/2010	0.322	0.357	0.333	0.322
28/9/2010	0.202	0.234	0.235	0.195
7/11/2010	0.179	0.22	0.221	0.173
9/12/2010	0.164	0.171	0.226	N/A
2/5/2011	0.319	0.340	0.353	N/A

Table 10-8 Comparison of AOT values derived from DP method, PITs method, Microtops and Cimel sun photometer

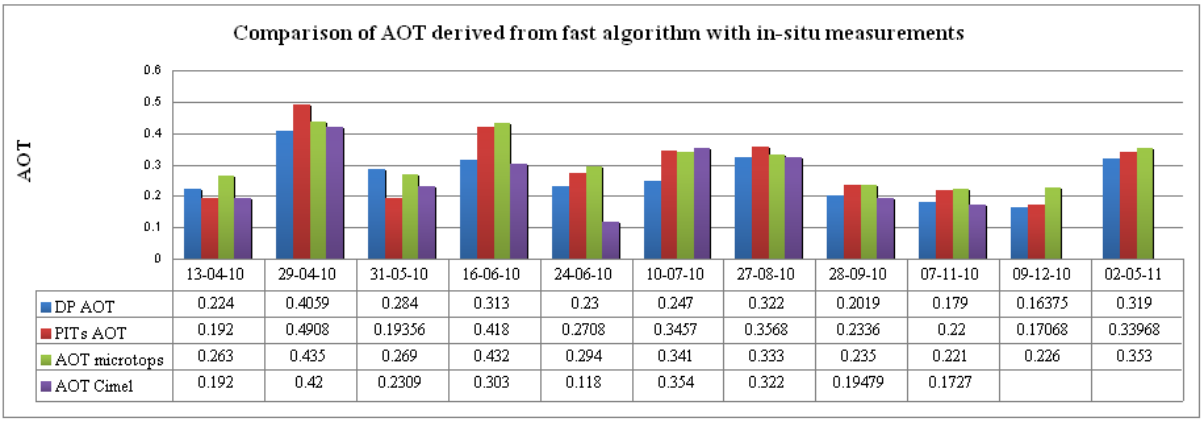

	13-04-10	29-04-10	31-05-10	16-06-10	24-06-10	10-07-10	27-08-10	28-09-10	07-11-10	09-12-10	02-05-11
DP AOT	0.224	0.4059	0.284	0.313	0.23	0.247	0.322	0.2019	0.179	0.16375	0.319
PITs AOT	0.192	0.4908	0.19356	0.418	0.2708	0.3457	0.3568	0.2336	0.22	0.17068	0.33968
AOT microtops	0.263	0.435	0.269	0.432	0.294	0.341	0.333	0.235	0.221	0.226	0.353
AOT Cimel	0.192	0.42	0.2309	0.303	0.118	0.354	0.322	0.19479	0.1727		

Figure 10-4 Comparison graph for AOT derived from DP method, PITs method, Microtops and Cimel sun photometer

It is apparent that there is a close agreement between the AOT values derived from the algorithm and the in-situ AOT measurements derived from the Microtops and Cimel sun photometer, as the correlation coefficient (R^2) values are between 0.73 to 0.99.

10.3 Accuracy Assessment from GIS maps

The simplified image based AOT retrieval based on RT equation for GIS analysis algorithm described in Chapter 9 was used to produce GIS maps indicating the AOT distribution over Limassol. A thematic map was generated using different colors for the specified AOT range, which provided the ability to see high and low AOT values (Figures 10-5 to 10-15). The AOT values generated were compared with the in-situ AOT values from the Microtops and Cimel sun photometers at the five pseudo-invariant targets and at the Cyprus University of Technology, where the Cimel sun photometer is located, as indicated in Tables 10-4 to Tables 10-14. As research (Gupta and Christopher, 2009) indicates a relationship between AOT values and PM_{10} measurements to determine air quality, the PM_{10} as determined from the air quality monitoring stations from the Department of Labor are also presented synoptically in Table 10-15 and in details in Tables 10-4 to Table 10-14.

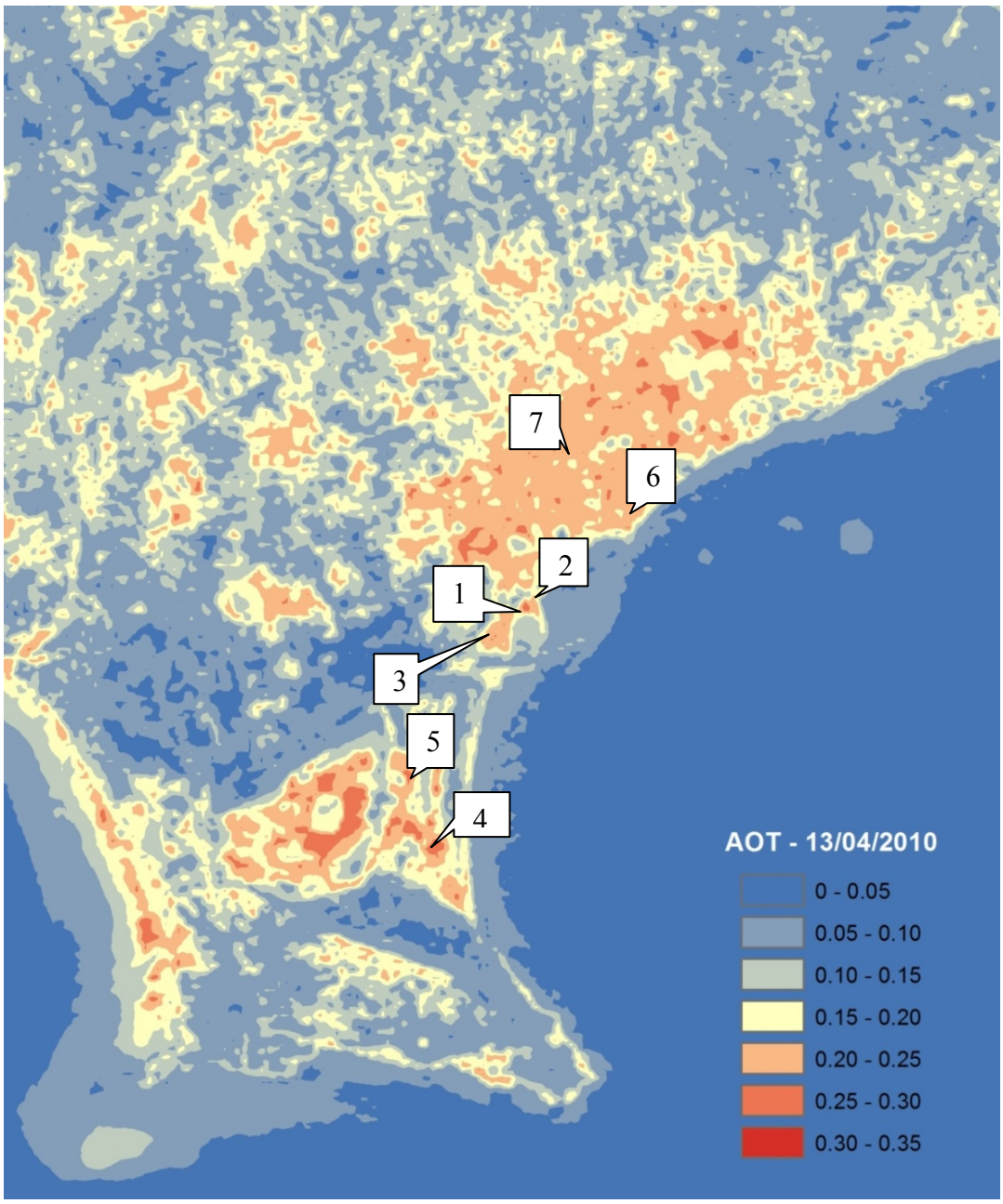

Figure 10-5 Kriging Map 13/4/2010

#	Location	AOT in-situ	AOT from GIS
1	Gray Asphalt	0.265	0.261
2	Black Asphalt	0.263	0.261
3	Concrete	0.257	0.256
4	Black Sand	0.254	0.252
5	Compacted Sand	0.260	0.258
6	CUT (Cimel Sun photometer)	0.256	0.252

#	Location	PM_{10}	AOT from GIS
7	Department of Labor air quality monitoring site	35.96 $\mu g/m^3$	0.259

Table 10-8 In-Situ AOT measurements 13/4/2010

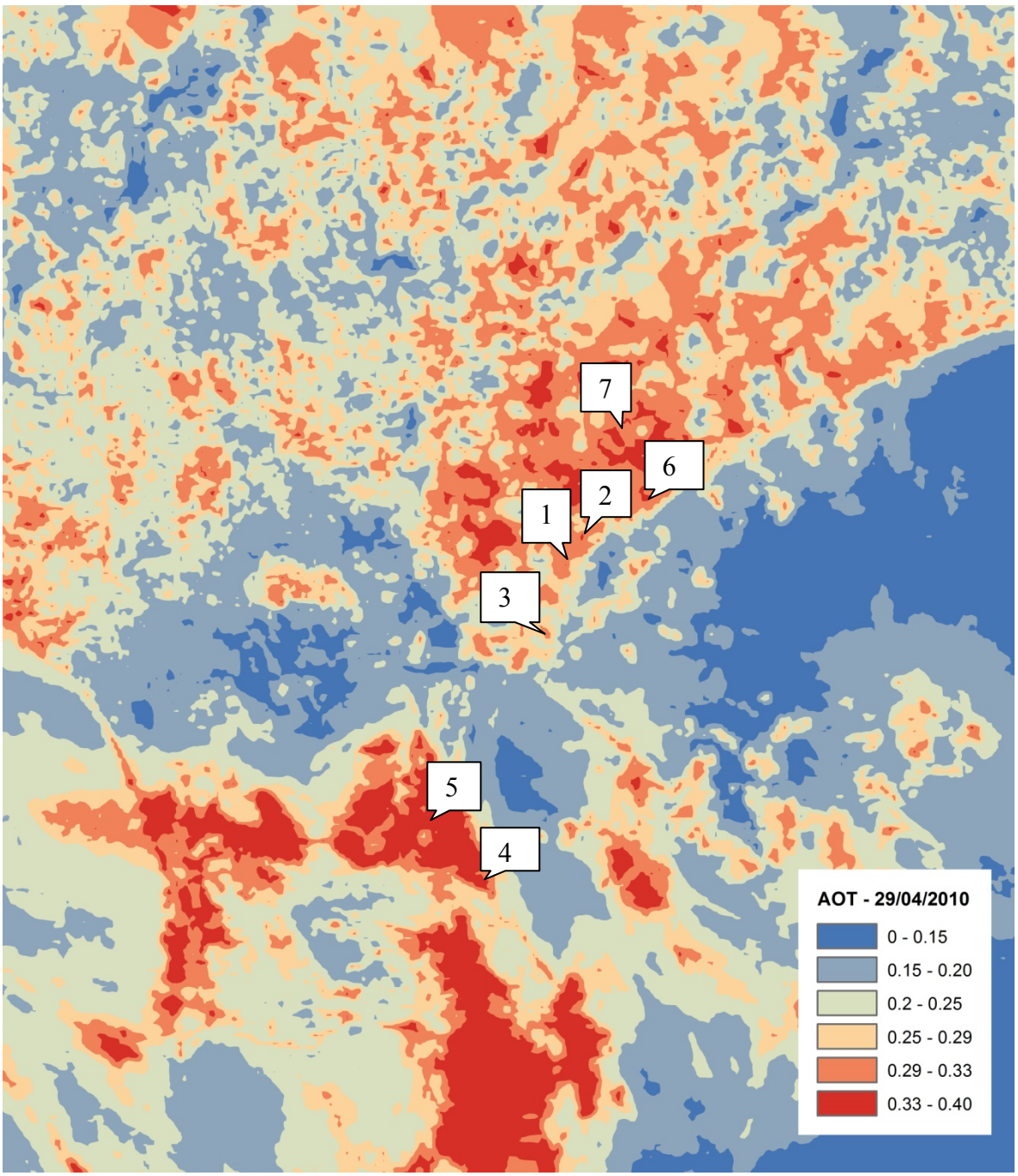

Figure 10-6 Kriging Map 29/4/2010

#	Location	AOT in-situ	AOT from GIS
1	Gray Asphalt	0.328	0.320
2	Black Asphalt	0.435	0.400
3	Concrete	0.310	0.315
4	Black Sand	0.393	0.390
5	Compacted Sand	0.391	0.390
6	CUT (Cimel Sun photometer)	0.421	0.400

#	Location	PM_{10}	AOT from GIS
7	Department of Labor air quality monitoring site	38.26 $\mu g/m^3$	0.276

Table 10-10 In-Situ AOT measurements 29/4/2010

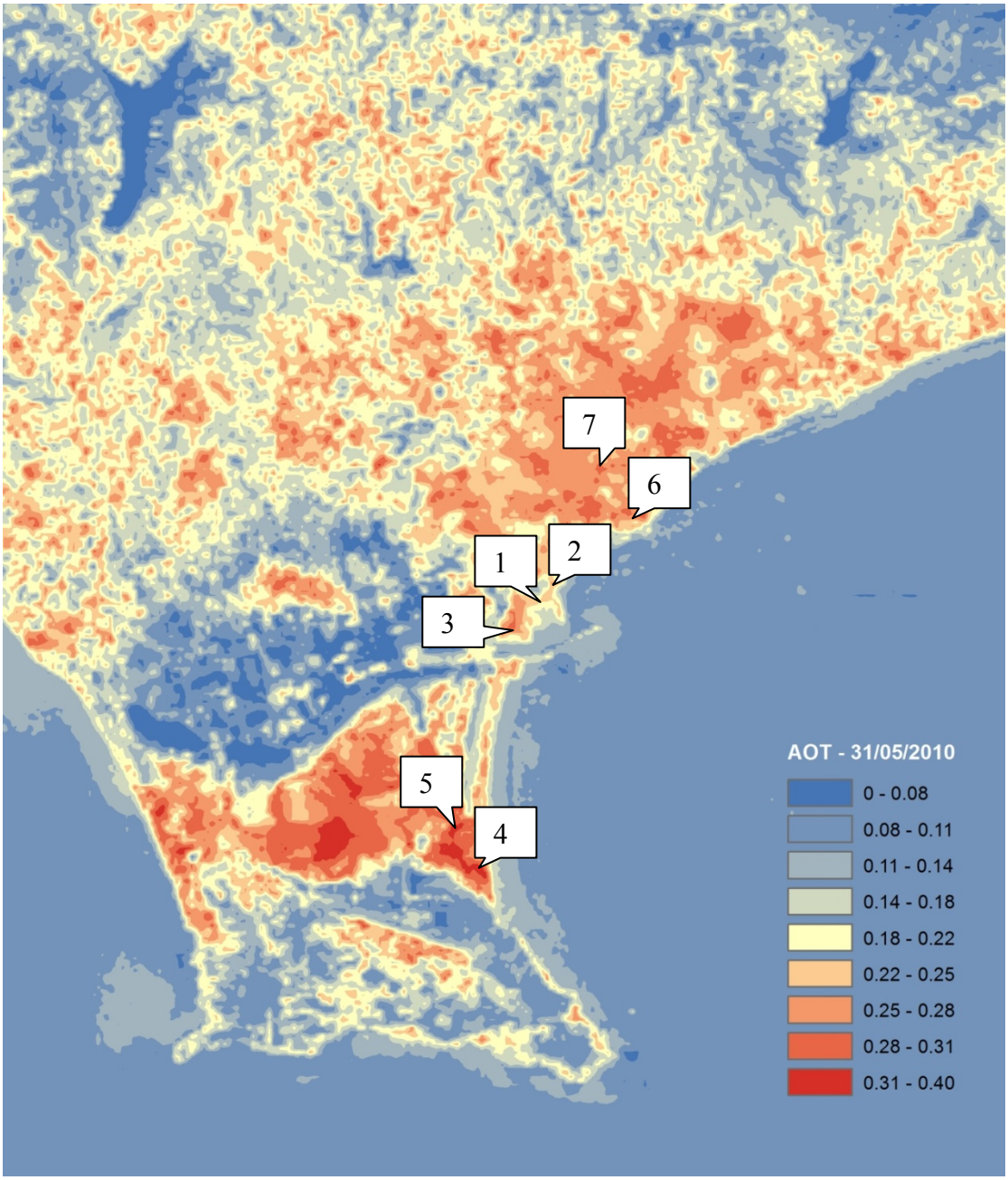

Figure 10-7 GIS map 31/5/2010

#	Location	AOT in-situ	AOT from GIS
1	Gray Asphalt	0.269	0.268
2	Black Asphalt	0.271	0.272
3	Concrete	0.449	0.400
4	Black Sand	0.360	0.359
5	Compacted Sand	0.321	0.320
6	CUT (Cimel Sun photometer)	0.186	0.220

#	Location	PM_{10}	AOT from GIS
7	Department of Labor air quality monitoring site	45.5 $\mu g/m^3$	0.337

Table 10-11 In-Situ AOT measurements 31/5/2010

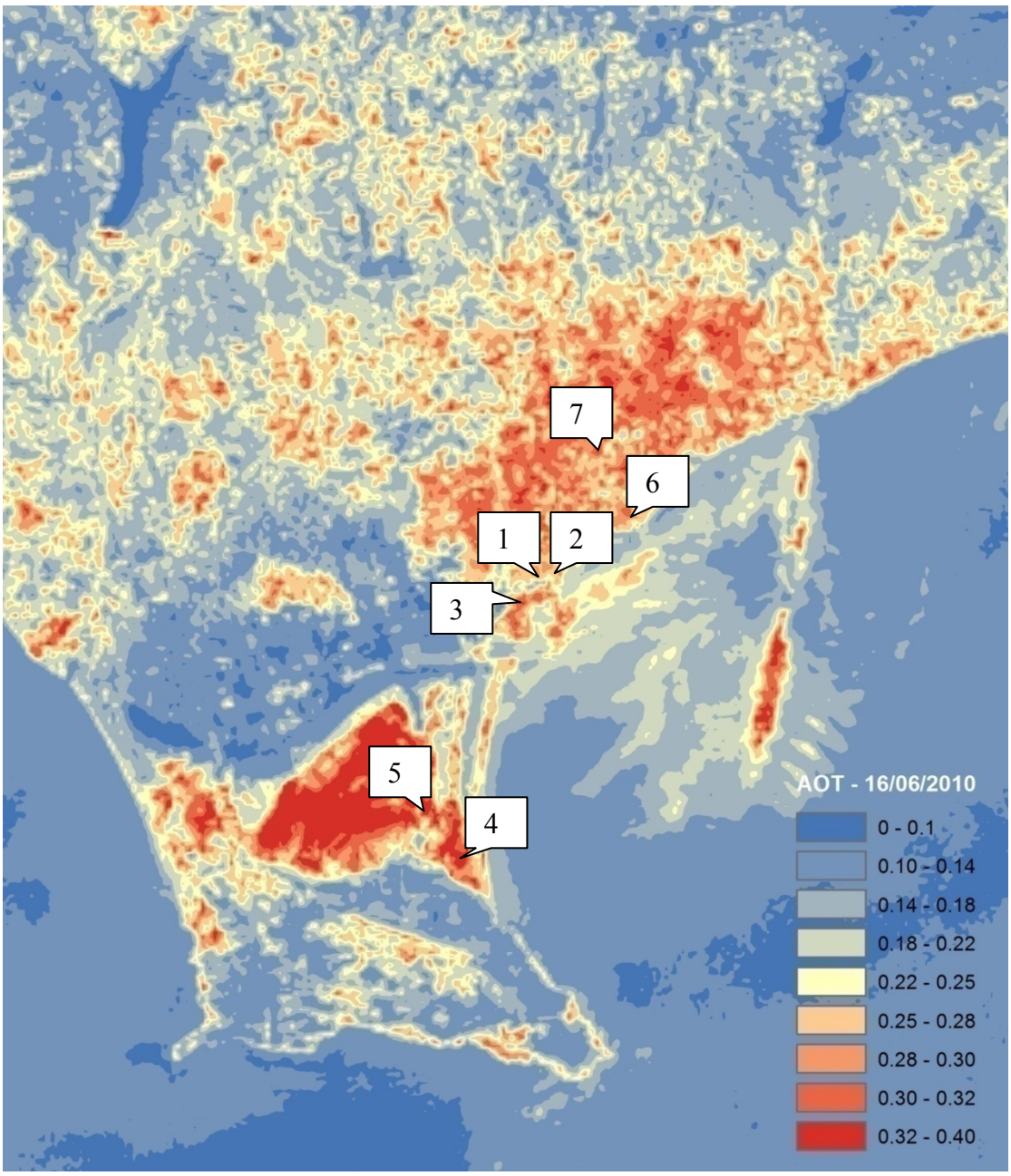

Figure 10-8 Kriging map 16/6/2010

#	Location	AOT in-situ	AOT from GIS
1	Gray Asphalt	0.290	0.292
2	Black Asphalt	0.295	0.296
3	Concrete	0.324	0.325
4	Black Sand	0.344	0.345
5	Compacted Sand	0.321	0.322
6	CUT (Cimel Sun photometer)	0.291	0.290

#	Location	PM_{10}	AOT from GIS
7	Department of Labor air quality monitoring site	49.84 $\mu g/m^3$	0.358

Table 10-12 In-Situ AOT measurements 16/6/2010

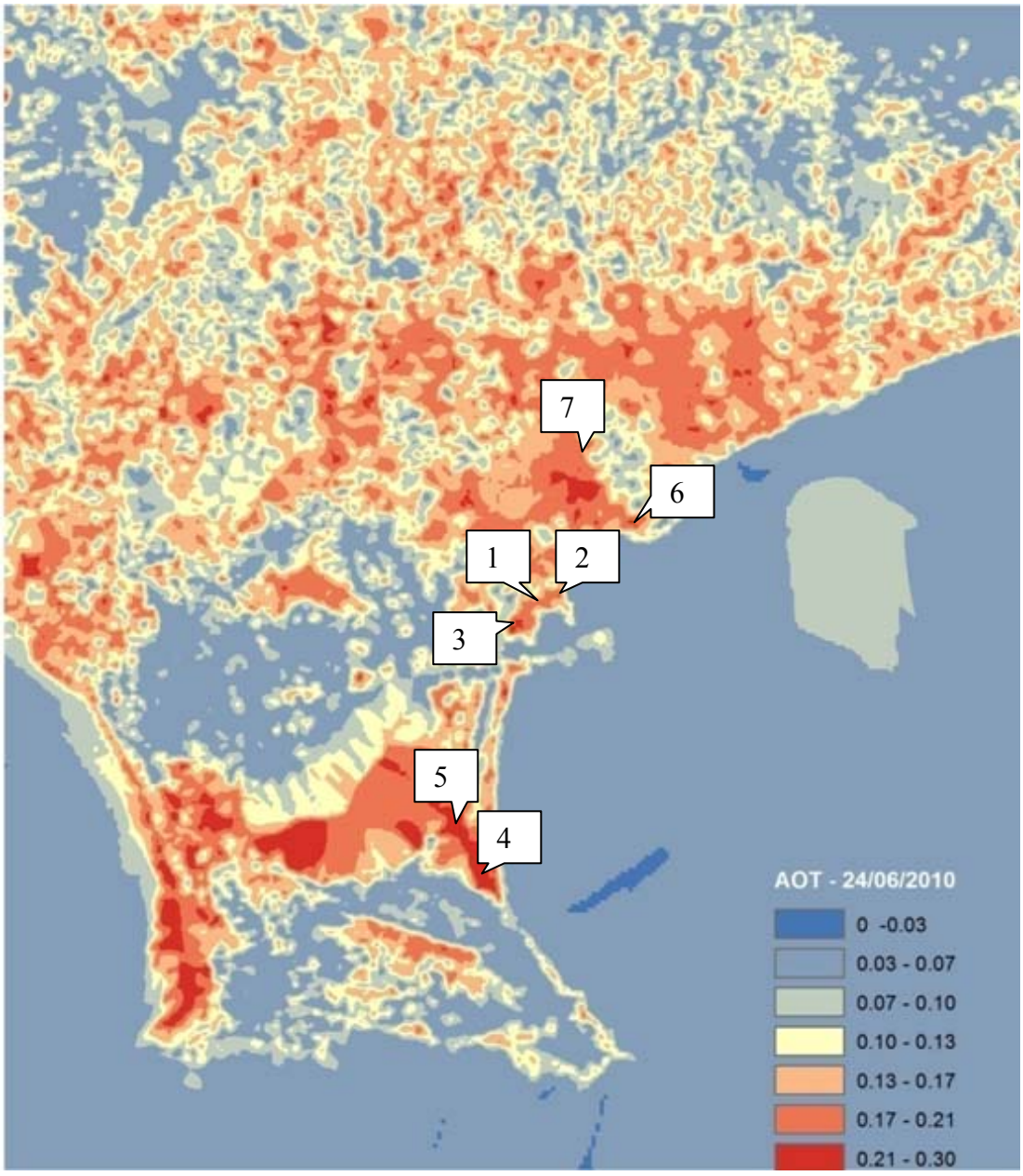

Figure 10-9 Kriging Map 24/6/2010

#	Location	AOT in-situ	AOT from GIS
1	Gray Asphalt	0.292	0.293
2	Black Asphalt	0.294	0.295
3	Concrete	0.288	0.290
4	Black Sand	0.299	0.300
5	Compacted Sand	0.290	0.291
6	CUT (Cimel Sun photometer)	0.118	0.120

#	Location	PM_{10}	AOT from GIS
7	Department of Labor air quality monitoring site	32.26 $\mu g/m^3$	0.224

Table 10-13 In-Situ AOT measurements 24/6/2010

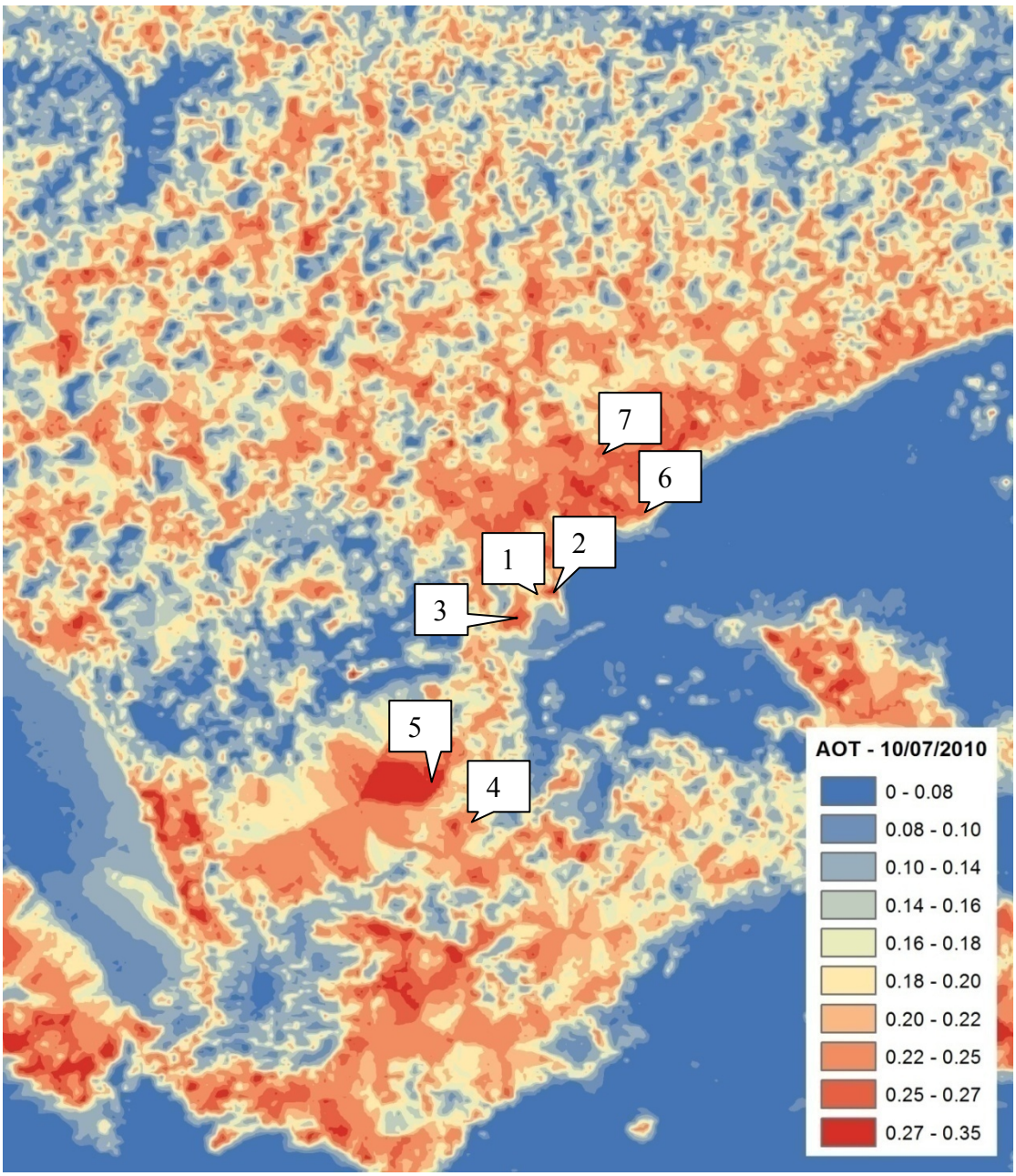

Figure 10-10 Kriging map 10/7/2010

#	Location	AOT in-situ	AOT from GIS
1	Gray Asphalt	0.271	0.270
2	Black Asphalt	0.339	0.350
3	Concrete	0.339	0.350
4	Black Sand	0.270	0.270
5	Compacted Sand	0.341	0.350
6	CUT (Cimel Sun photometer)	0.354	0.350

#	Location	PM_{10}	AOT from GIS
7	Department of Labor air quality monitoring site	38.23 $\mu g/m^3$	0.274

Table 10-14 In-Situ AOT measurements 10/7/2010

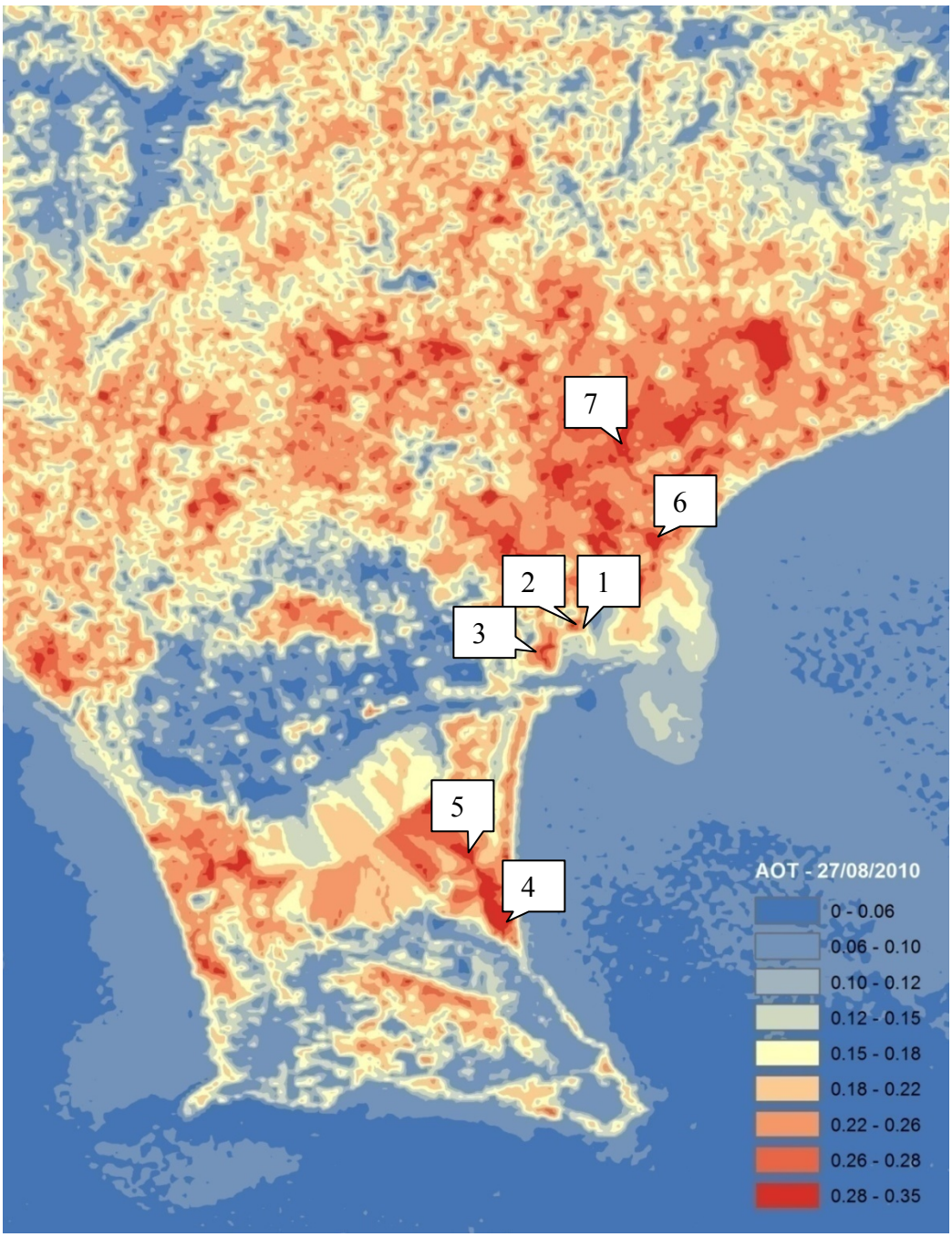

Figure 10-11 GIS map 27/8/2010

#	Location	AOT in-situ	AOT from GIS
1	Gray Asphalt	0.282	0.280
2	Black Asphalt	0.333	0.340
3	Concrete	0.320	0.325
4	Black Sand	0.347	0.350
5	Compacted Sand	0.333	0.335
6	CUT (Cimel Sun photometer)	0.322	0.325

#	Location	PM_{10}	AOT from GIS
7	Department of Labor air quality monitoring site	54.91 $\mu g/m^3$	0.341

Table 10-15 In-Situ AOT measurements 27/8/2010

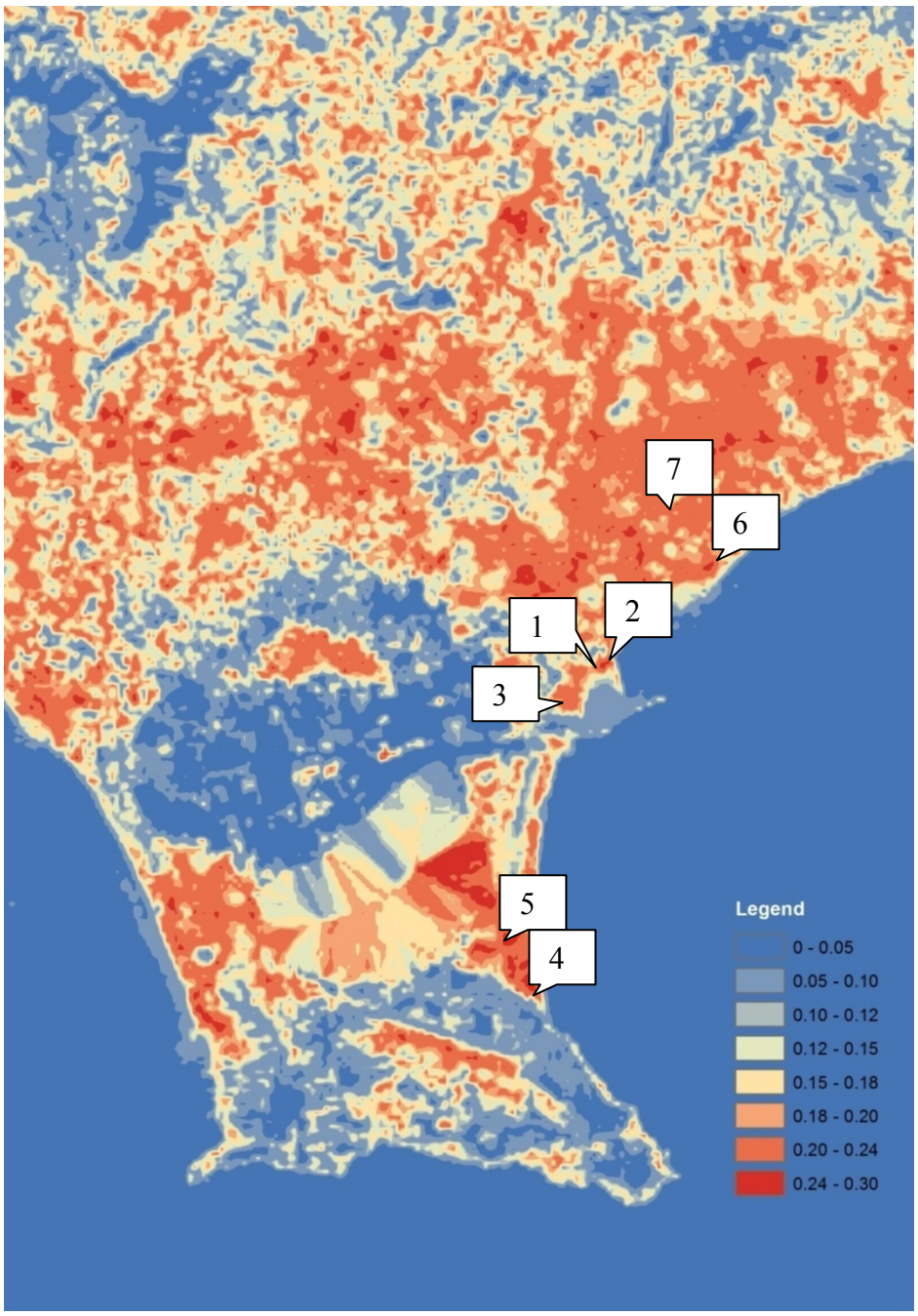

Figure 10-12 Kriging map 28/9/2010

#	Location	AOT in-situ	AOT from GIS
1	Gray Asphalt	0.208	0.200
2	Black Asphalt	0.235	0.234
3	Concrete	0.200	0.202
4	Black Sand	0.235	0.240
5	Compacted Sand	0.263	0.265
6	CUT (Cimel Sun photometer)	0.195	0.200

#	Location	PM_{10}	AOT from GIS
7	Department of Labor air quality monitoring site	43.37 $\mu g/m^3$	0.273

Table 10-16 In-Situ AOT measurements 28/9/2010

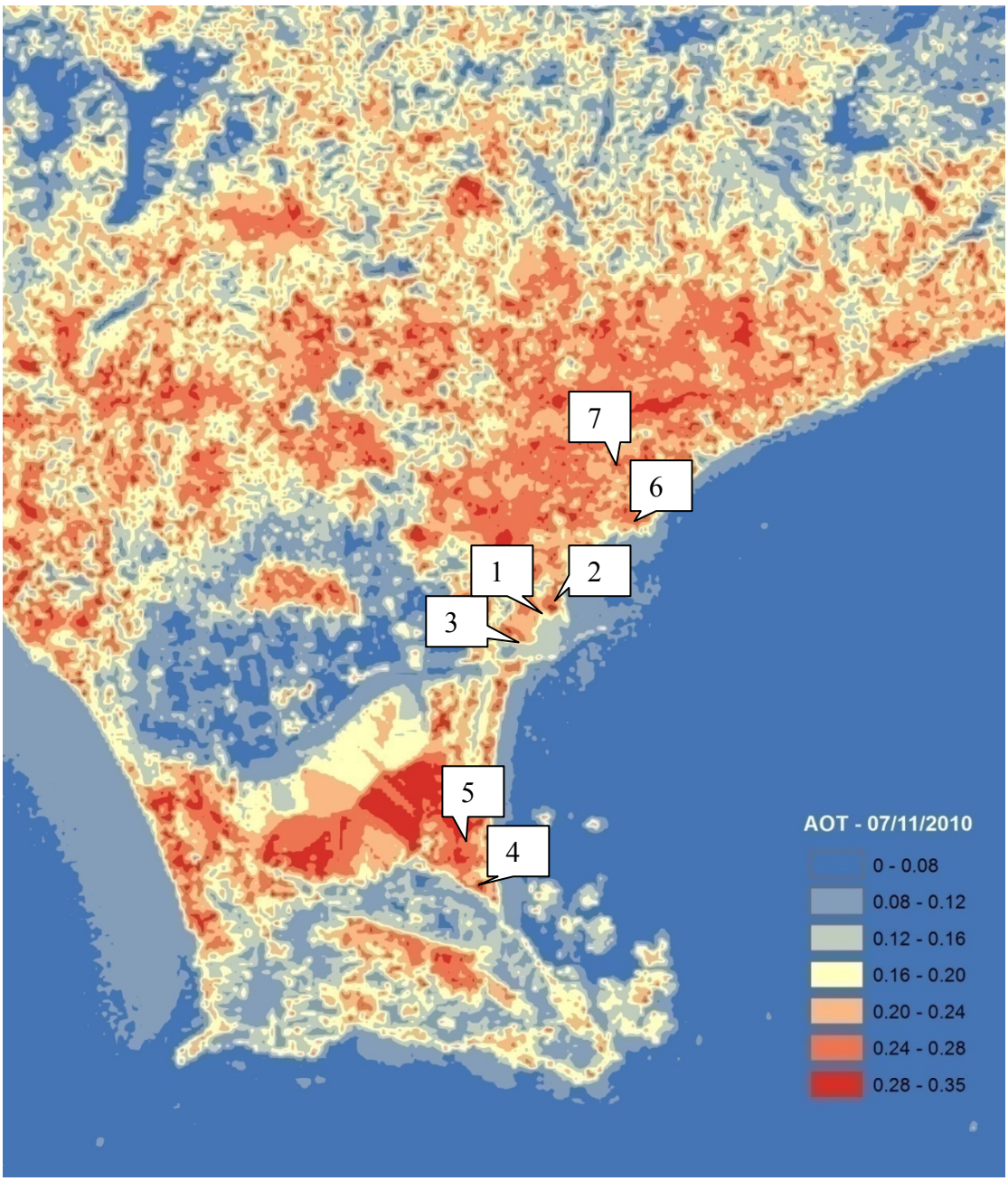

Figure 10-13 Kriging map 7/11/2010

#	Location	AOT in-situ	AOT from GIS
1	Gray Asphalt	0.235	0.238
2	Black Asphalt	0.221	0.225
3	Concrete	0.231	0.235
4	Black Sand	0.290	0.295
5	Compacted Sand	0.232	0.240
6	CUT (Cimel Sun photometer)	0.173	0.200

#	Location	PM_{10}	AOT from GIS
7	Department of Labor air quality monitoring site	51.0 $\mu g/m^3$	0.317

Table 10-17 In-Situ AOT measurements 7/11/2010

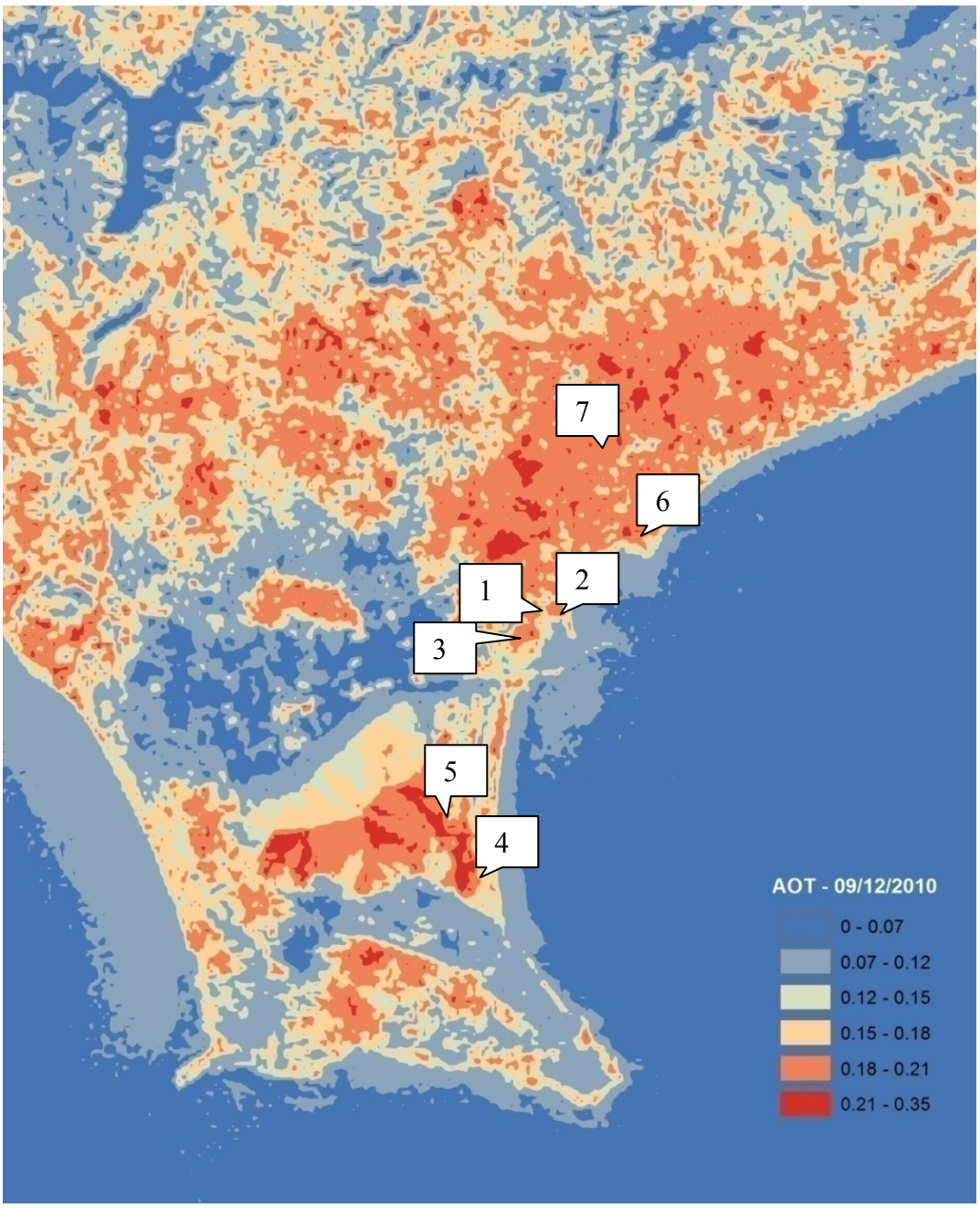

Figure 10-14 Kriging map 09/12/2010

#	Location	AOT in-situ	AOT from GIS
1	Gray Asphalt	0.200	0.205
2	Black Asphalt	0.232	0.228
3	Concrete	0.228	0.230
4	Black Sand	0.244	0.245
5	Compacted Sand	0.260	0.263
6	CUT (Cimel Sun photometer)	N/A	0.210

#	Location	PM_{10}	AOT from GIS
7	Department of Labor air quality monitoring site	47.31 $\mu g/m^3$	0.320

Table 10-18 In-Situ AOT measurements 9/12/2010

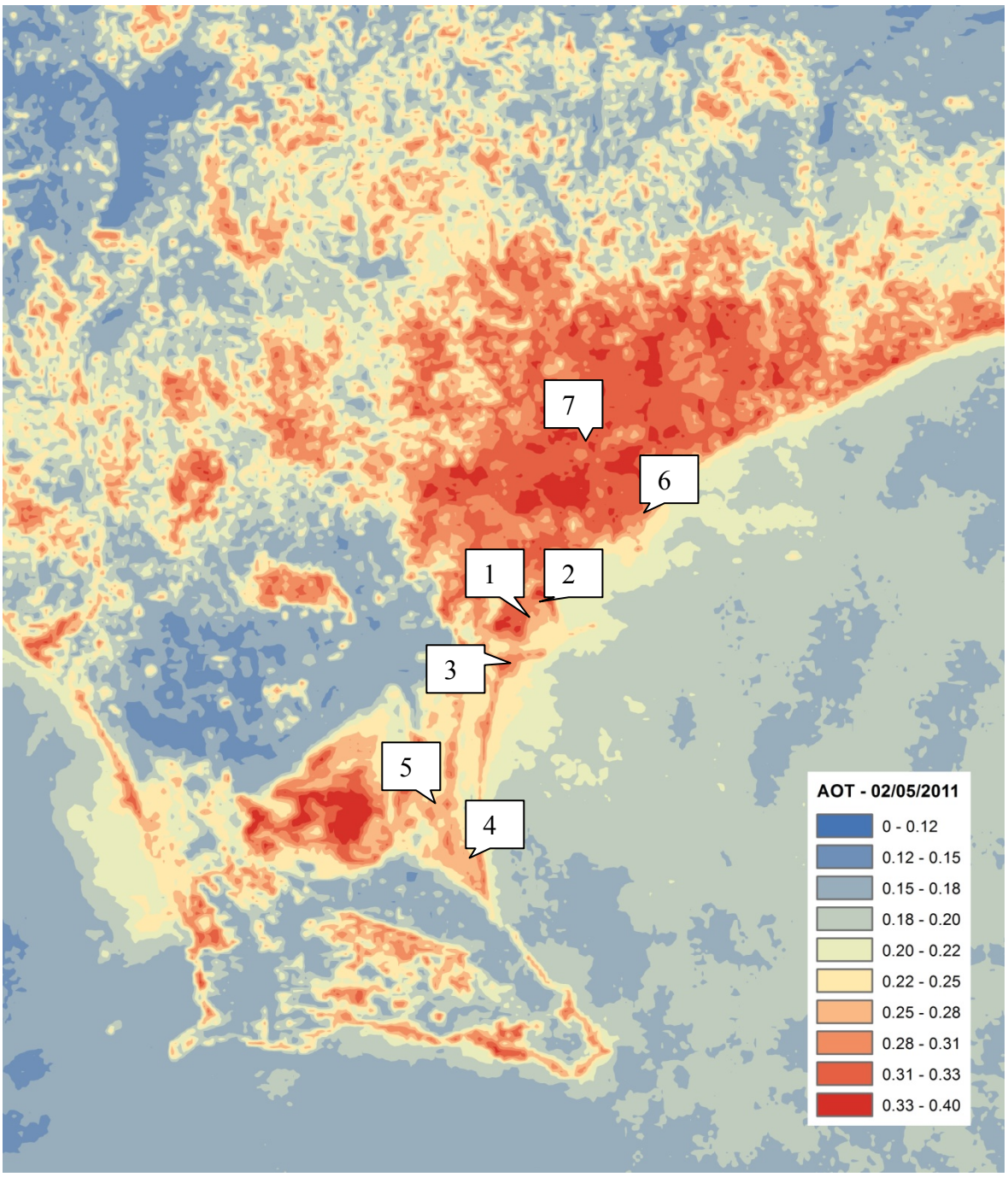

Figure 10-15 Kriging map 02/05/11

#	Location	AOT in-situ	AOT from GIS
1	Gray Asphalt	0.313	0.310
2	Black Asphalt	0.355	0.355
3	Concrete	0.349	0.350
4	Black Sand	0.248	0.250
5	Compacted Sand	0.283	0.285
6	CUT (Cimel Sun photometer)	N/A	0.330

#	Location	PM_{10}	AOT from GIS
7	Department of Labor air quality monitoring site	N/A	0.331

Table 10-19 In-Situ AOT measurements 2/05/2011

A linear regression was conducted of all the in-situ AOT values against AOT values derived from the GIS analysis, as indicated in Figure 10-16. The correlation co-efficient was 0.977, which is indicative of a strong correlation between the in-situ AOT values and the AOT values derived from the GIS analysis.

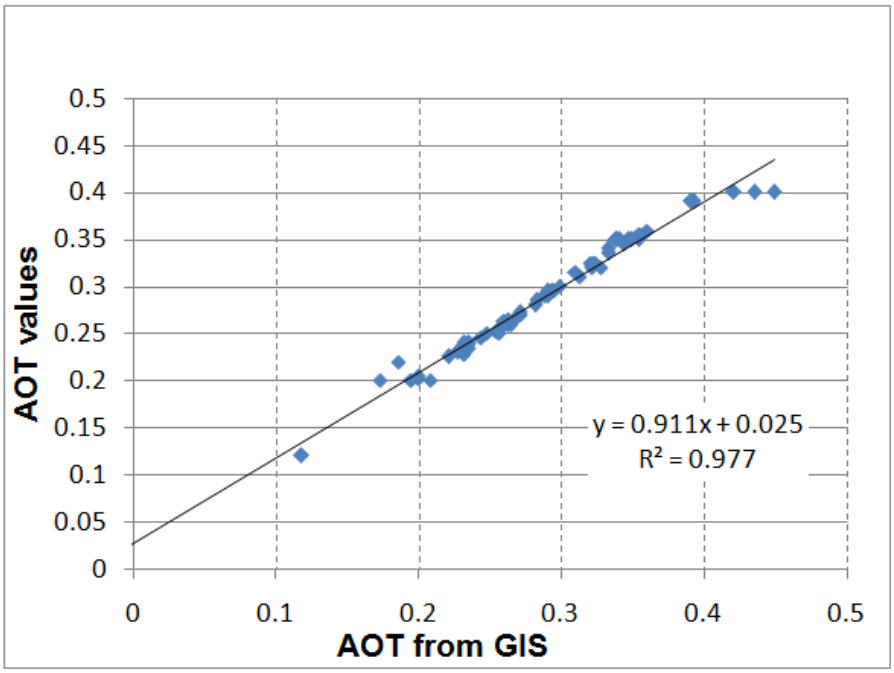

Figure 10-16 Linear regression of in-situ AOT values against AOT values derived from the GIS analysis

Using the five pseudo-invariant targets discussed in Chapter 4 and the atmospherically corrected satellite images discussed in Chapter 8, a verification of the methodology to retrieve AOT values was conducted for the Paphos area (Hadjimitsis et al., 2009a, 2009b). For the verification, in-situ AOT values were taken using the Microtops sun photometer at three different locations in the Paphos area during the same time as satellite overpass. The fast atmospheric correction algorithm was applied in the MATLAB program in order to retrieve the AOT values from the Pafos area using the five pseudo-invariant targets in Limassol for the empirical line atmospheric correction method. In order to check the accuracy of the method, three AOT measurements during the satellite overpass were undertaken. The derived AOT values from the fast atmospheric correction algorithm using the empirical line method were found to be very close with the three AOT values found from the sun photometer, as indicated in Table 10-20. Figure 10-17 shows the partial scene of the atmospherically corrected Landsat TM satellite image of Paphos and Limassol acquired on 24/6/2010, with the location of the three in-situ AOT measurements for the

Paphos area indicated in purple, using the five pseudo-invariant targets in the Limassol area for atmospheric correction, which are indicated in red.

Figure 10-17 Atmospherically corrected satellite image of Paphos and Limassol acquired on 24/6/2010

In-situ AOT - Paphos	AOT retrieved
0.35	0.35
0.43	0.43
0.43	0.42

Table 10-20 Comparison of in-situ AOT with AOT retrieved with the fast atmospheric correction algorithm using the empirical line method for Paphos for 24/6/2010

Although it was not a part of this thesis, a comparison was conducted of the AOT measurements from the air quality monitoring stations with the PM_{10} measurements recorded by the air quality monitoring stations, as this data was available to the author. The AOT measurements were assessed with the PM_{10} measurements that corresponded to the time of the satellite overpass (see table 10-21). AOT values can vary significantly from PM_{10} data since AOT values indicate the thickness of the atmosphere, while PM_{10} values are locally distributed. The linear correlation between AOT levels and PM_{10} measurements as indicted in figure 10-17 is promising and can be further studied in future work. To date, several researchers have also found a relationship between AOT values and PM_{10} measurements (Amanollahi et al, 2011; Othman et al, 2009; Jiang et al, 2007; Kalivitis et al, 2007; Hashim et al, 2006; Yahi et al, 2004).

Date	AOT measurement near air quality monitoring station	PM_{10} measurement in $\mu g/m^3$
13/4/2010	0.259	35.96
29/4/2010	0.276	38.26
31/5/2010	0.337	45.5
16/6/2010	0.358	49.84
24/6/2010	0.224	32.26
10/7/2010	0.274	38.23
27/8/2010	0.341	54.91
28/9/2010	0.273	43.37
7/11/2010	0.317	51.0
9/12/2010	0.320	47.31
2/5/2011	0.331	N/A

Table 10-21 Comparison table of AOT and PM_{10} measurements

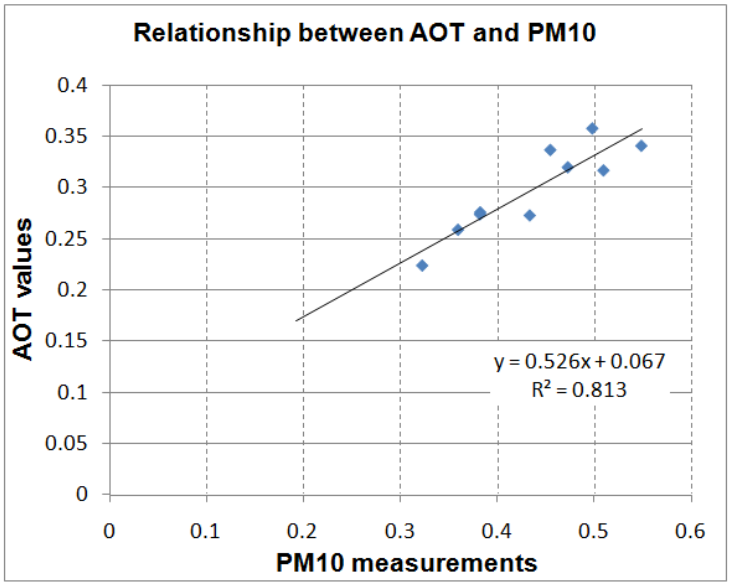

Figure 10-18 Linear regression of AOT and PM_{10} measurements

10.4 Summary

In this chapter, the results of the study were presented. An accuracy assessment was conducted to determine if the five targets examined in the thesis are indeed pseudo-invariant, by examining their reflectance values over time. The reflectance values of the five targets were also examined to see if precipitation affected the reflectance values of the pseudo-invariant targets. As well, using the algorithm presented in Chapter 9, AOT values derived from the DP method and the PITs method were compared with the in-situ AOT measurements from the Microtops and Cimel sun photometers. Finally, the simplified image based AOT retrieval based on RT equation for GIS modeling was used to create a choropeth map indicating the distribution of AOT values over Limassol, which was

compared with the in-situ AOT measurements calculated from the sun photometers and PM_{10} measurements from the local air quality monitoring stations.

Chapter 11 Conclusions and Future Work

The objective of this chapter is to briefly present the conclusions of the study and recommendations for future work in this area. The fast atmospheric correction algorithm for AOT retrieval developed in this thesis used the improved empirical line method using five PITs was found to provide a good alternative to the more complex and sophisticated methods when, as is common, meteorological or atmospheric input data are not available. Further, the simplified image based AOT retrieval based on RT equation for GIS modeling provided an accurate calculation of the AOT values distributed over Limassol when compared with in-situ AOT values.

11.1 Innovation and contribution to scientific community

The innovation of this thesis focuses on the retrieval of AOT after applying the darkest pixel and empirical line atmospheric correction methods. Novel contributions to this thesis include the employment of pseudo-invariant targets for conducting accuracy assessment of both atmospheric correction methods and the improvement of the empirical line method using more than three PITS. It is the first time that a field campaign was conducted measuring the reflectance values of pseudo-invariant targets for an extended time period throughout the year examining how wet and dry ground conditions affect the reflectance values for atmospheric correction. A further innovation of this thesis is the integrated use of field spectroscopy, GIS and remote sensing for atmospheric correction of satellite imagery and AOT retrieval.

This thesis provides an important contribution to the field of remote sensing as it improves the empirical line atmospheric correction method by using five pseudo-invariant targets of varying spectral characteristics. The effects of wet and dry conditions on the pseudo-invariant targets were also assessed and it was found that sand was significantly affected by rainfall; therefore, precipitation needs to be considered when using sand as a pseudo-invariant target. Further, a fast atmospheric correction algorithm was developed using the DP and empirical line method to derive AOT measurements directly from satellite images and GIS analysis was used to map AOT distribution.

11.2 Conclusions

The objectives of this research, as established in Chapter 1, were reached, as described below:

Objective 1: Improvement of the Empirical Line Method using Pseudo-Invariant Targets for atmospheric correction and application of the Darkest Pixel method and Empirical Line Method using Pseudo-Invariant Targets.

In this study, the empirical line method was improved by using five pseudo-invariant targets of varying spectral characteristics instead of the three targets used in most empirical line methods of atmospheric correction. From January 2010 until May 2011, over 2,000 measurements were taken on 46 different field campaign in both wet and dry conditions, which established that the reflectance values of the targets did not vary significantly, making them suitable for the empirical line method. One of the significant findings of the study is that sand has a lower reflectance value when wet. Therefore, it is recommended that the reflectance value of wet sand and the reflectance value of dry sand be used separately. The darkest pixel method of atmospheric correction was modified by using the reflectance value of the darkest target (Black Asphalt), instead of zero, to adjust for the atmospheric correction, as recommended by Hadjimitsis and Clayton (2008). Both the darkest pixel and empirical line (PITs) method were used to conduct atmospheric correction of eleven Landsat satellite images. As found in objective 3, there exists a high level of agreement between the satellite reflectance values after atmospheric correction with the in-situ measurements reported from the sun photometer, as indicated in Chapters 8 and 10.

Objective 2: Aerosol optical thickness (AOT) retrieval based on the application of the atmospheric correction method.

Using the radiative transfer equation, in combination with the darkest pixel and the empirical line method using five pseudo-invariant targets, the fast atmospheric correction algorithm was created to retrieve AOT from satellite images, as described in Chapter 9. The algorithm was used on eleven Landsat satellite images in order to determine the AOT levels that were present in the target area during the time of satellite overpass on those specific dates. In order to verify the validity of the algorithm, the AOT values derived using the algorithm were compared with the AOT values from the sun photometer measurements taken on the specific days. As found in objective 3, there exists a strong

agreement between the in-situ AOT values and the AOT derived from the fast atmospheric correction algorithm, indicating that this algorithm can be used for image-based atmospheric correction methods, including archived satellite images, where in-situ AOT levels are not available. As discussed in Chapter 10, the in-situ AOT values were compared with the AOT values retrieved from the algorithm for the Paphos area of Cyprus.

Objective 3: Accuracy assessment based on the in-situ measurement using spectroradiometers and sun photometers.

In order to determine if the atmospheric correction and the AOT algorithm were successful, an accuracy assessment comparing satellite-derived measurements with in-situ measurements. The in-situ reflectance values measured from the spectroradiometer were compared to the satellite reflectance value derived following the darkest pixel and empirical line methods of atmospheric correction methods, as presented in Table 10-1. Both atmospheric correction methods produced a high level of agreement between the in-situ and satellite reflectance values, with the empirical line method being slightly more accurate. As well, the radiance values determined from the darkest pixel and empirical line method of atmospheric correction were used in the AOT algorithm in order to retrieve AOT values. These values were compared with the in-situ AOT measurements determined using the Microtops and Cimel sun photometers, as presented in Table 10-8 and Figure 10-3. There was high agreement between the AOT values determined using the AOT algorithm with the AOT values determined with the sun photometer.

Objective 4: Use of Geographic Information Systems (GIS) analysis to map atmospheric pollution in urban areas based on retrieved AOT values.

The simplified image based AOT retrieval based on RT equation for GIS modeling algorithm was developed in order to produce a GIS map indicating the AOT value distribution over Limassol. The AOT values derived from the algorithm were compared with the in-situ AOT values from the Microtops and Cimel sun photometer, as indicated in Tables 4-14. There was strong agreement between the in-situ AOT measurements and the AOT values indicated on the GIS map, which indicated the accuracy of the algorithm.

The most significant finding of this thesis concerns the five pseudo-invariant targets which were utilized in improving the empirical line method. Pseudo-invariant targets are critical in remote sensing, as their stable reflectance values can be used when in-situ measurements

cannot be made concurrent with the imagery acquisition. The pseudo-invariant targets used in the study are surfaces that are commonly found in most places around the world. Therefore, researchers can identify similar pseudo-invariant targets in their study area, in order to establish standardized ground measurements, which can be used simultaneously with satellite image acquisition or for archived satellite images. In this study, it was determined that the asphalt and concrete reference targets were non-variant, regardless of precipitation. This study found that Black Asphalt, Gray Asphalt and Concrete surfaces can successfully be used as pseudo-invariant targets for use with the empirical line method of atmospheric correction throughout the year. However, for the Black Sand and Compacted Sand targets, the results indicated that rainfall did impact the reflectance values. Based on the results of this thesis, asphalt, concrete and sand are all recommended as pseudo-invariant targets, as their reflectance values do not change significantly over time. However, it is recommended that if sand is used as a pseudo-invariant target, the moisture condition of the sand be noted. It appears that sand exhibits a consistent reflectance value, which is dependent on the moisture in the sand. Black sand, especially when wet, has a low reflectance value and can be considered as a dark target. Sand, when dry, especially following months of dry conditions, can be used as a light target. This thesis found that volcanic black beach sand can also be used as a pseudo-invariant target; however, precipitation condition need to be taken into consideration to avoid errors when conducting the atmospheric correction.

The second most significant finding of this thesis is the validation that the fast atmospheric correction algorithm was able to retrieve AOT measurements using satellite images. Comparisons of retrieved AOT measurements with the Microtops II and Cimel sun-photometers found significant agreement between the AOT measurement retrieved from the sun-photometers and the AOT measurements retrieved from the algorithm. As well, the results indicate that the darkest pixel and empirical line method of atmospheric correction can be successfully used for AOT retrieval by using the proposed algorithm. This method allows for AOT values to be retrieved even from archived images where no in-situ measurements are available. Overall, the AOT values retrieved through the algorithm were comparable to the AOT values from the sun photometers. It is important to note that several parameters of the algorithm were estimated, such as the ↑ and ↓ transmittance of ozone, as featured in Chapter 9. Therefore, the algorithm can be considered as an acceptable image-based method of retrieving AOT from satellite images.

The results indicate that the AOT retrieved after applying an atmospheric correction from the images was very near to those found from the sun-photometers acquired simultaneous during the satellite overpass. This thesis found that simultaneous acquisition of satellite imagery, sun-photometer measurements and spectroradiometric measurements are useful in developing a more effective method of retrieving aerosol optical thickness. As indicated in this thesis, the determined atmospheric path radiance can be used to retrieve the aerosol optical thickness as a method of assessing atmospheric pollution. The results reported in Chapter 10 are indicative that the AOT retrieved after applying an atmospheric correction from the images was very near to those found from the sun-photometers acquired simultaneous during the satellite overpass.

The proposed method has a number of advantages, including:

- Simplicity and ease of computation.
- The proposed PITs are generally large in size and distinctive in shape and spectral characteristics, and can thus usually be easily identified.
- Such features occur in many geographical areas.
- The application in urban areas improves the accuracy of the method in determining the AOT values using RT equations.
- The method can be used to map AOT levels by use of a GIS.

The effective results obtained from applying the proposed method using the atmospheric correction algorithm presented in Chapter 10 for determining the aerosol optical thickness within the values obtained from the hand-held sun-photometer, increase the potential of the method. Meanwhile, common surfaces around the world can be used as pseudo-variant targets to conduct the empirical line atmospheric correction method. The retrieval of AOT values from the atmospheric path reflectance component (intercept) provides a novel revised version of the existing empirical line atmospheric correction method.

11.3 Future Work

Future research is necessary to validate the algorithm by using more measurements in a wider area with more targets throughout the seasons in order to provide more accurate validation results and estimates of possible errors that may be encountered. As discussed in Chapter 2, research have found a relationship between AOT values and PM_{10} measurement regarding air pollution. Future work can imclude examining the relationship between AOT values, PM_{10} measurements and atmospheric pollution. Although this research focused on

Landsat TM/ETM+ satellite images, the retrieved reflectance values for the proposed pseudo-invariant targets can be used for images acquired from other sensors such as ASTER, ALOS, QuickBird, CHRIS-PROBA, etc.

PUBLICATIONS ASSOCIATED WITH THIS PHD THESIS

Chapter in Book

Hadjimitsis, D.G.**, Themistocleous K.,** and Nisantzi A., (2011). *Chapter: Air Pollution Monitoring Using Earth Observation & GIS, Air Pollution* / Book 1, ISBN 979-953-307-228-8, (Ed.) Dr. Mukesh Khare.

Journal Articles

Themistocleous, K., Hadjimitsis, D.G., Retalis, A., Chrysoulakis, N. and Michaelides, S. (Accepted). *Precipitation effects on the selection of suitable non-variant targets intended for atmospheric correction of satellite remotely sensed imagery.* Atmospheric Research: Perspectives of Precipitation Science.

Themistocleous, **K.**, Nisantzi, A., Hadjimitsis, D.G., Retalis, A., Paronis, D., Michaelides, S., Chrysoulakis, N., Agapiou A., Giorgousis, G., Perdikou, S., (Accepted). *Long term monitoring of air pollution in the vicinity of cultural heritage sites in Cyprus using remote sensing techniques.* International Journal of Digital Heritage.

Hadjimitsis, D.G**.;** Retalis, A.; Chrysoulakis, N.; Michaelides, S.; **Themistocleous, K.,** Clayton, C.R.I. (2010). Atmospheric correction for satellite remotely sensed data intended for hydrological cycle applications: impact on vegetation indices, *Natural Hazards and Earth System Sciences Journal, 10* (1), pp. 89-95.

Hadjimitsis, D.G**.** ,**Themistocleous K.,** and Agapiou A. (2009). Monitoring archaeological site landscapes in Cyprus using multitemporal atmospheric corrected image data. *International Journal of Architectural Computing, 7* (1) 121-138. Doi:10.1260/147807709788549376, Scopus.

Themistocleous, K., Hadjimitsis, D.G., Retalis, A., and Chrysoulakis, N. (submitted, under review). *The identification of pseudo-invariant targets using ground field spectroscopy measurements intended for the removal of atmospheric effects from satellite imagery: the case study of Limassol area in Cyprus.* International Journal of Remote Sensing.

Themistocleous, K., Hadjimitsis, D.G., Retalis, A.; and Chrysoulakis, N. (submitted, under review). *Fast atmospheric correction algorithm based on the darkest pixel approach for retrieving the aerosol optical thickness: comparison with in-situ AOT measurements.* International Journal of Applied Remote Sensing.

International Conferences with Peer Review

2012

Themistocleous, K., Hadjimitsis, D.G., Retalis, A., Chrysoulakis, N. and Michaelides, S. (2012). *Aerosol optical thickness retrieval and GIS distribution analysis using the fast atmospheric correction method: a case study in Cyprus.* European Geosciences Union, Vienna, Austria, 22 – 27 April 2012. (Abstract).

Agapiou A., Lysandrou V., Hadjimitsis D. G., Alexakis D.D., **Themistocleous K.** and Michaelides S. (2012) *Long term monitoring of open-air monuments under threat: the case study of the "Tombs of the Kings", Nea Paphos, Cyprus.* European Geosciences Union, Vienna, Austria, 22 – 27 April 2012. (Abstract).

Themistocleous, K., Hadjimitsis, D.G., Demetriades, C., Retalis, A., Chrysoulakis, N. (2012). *Image-based fast atmospheric model for AOT retrieval intended for generating air pollution maps: a case study of Limassol, Cyprus.* 32nd EARSeL Symposium 2012, Mykonos – Greece, 21 - 24 May 2012. (Abstract).

Papageorgiou, K., Hadjimitsis, D. G., Agapiou, A., **Themistocleous, K.,** Koutsias, N. (2012). *Spectral Signatures of Pinus brutia post fire regeneration in Paphos forest, using ground spectroradiometers.* 32nd EARSeL Symposium 2012, Mykonos – Greece, 21 - 24 May 2012. (Abstract).

Agapiou, A., Hadjimitsis, D.G., Nisantzi, A. , Alexakis, D. D. , **Themistocleous**, **K.,** Papadavid G. (2012). *Variability of field spectroradiometric measurements using nearly Lambertian surfaces and auxiliary Lidar observations.* 32nd EARSeL Symposium 2012, Mykonos – Greece, 21 - 24 May 2012. (Abstract).

2011

Themistocleous, K., Hadjimitsis, D.G., and Alexakis, D. (2011). *Fast atmospheric correction algorithm based on the darkest pixel approach for retrieving the aerosol optical thickness: comparison with in-situ AOT measurements.* In: CD-ROM of Proceedings of SPIE 8177, 81770B (2011); 20-23 September, Prague, Czech Republic, doi:10.1117/12.898593.

Themistocleous, K., Chrysoulakis, N., Hadjimitsis, D.G., Retalis, A., and Alexakis, D. *Determination of the aerosol optical thickness through the atmospheric path radiance component obtained from the application of the pseudo-invariant target atmospheric correction method*. In: CD-ROM of Proceedings of the 31st EARSeL Symposium and 35th General Assembly 2011, Prague, Czech Republic, May 30 - June 2. (abstract).

2010

Themistocleous, K., Nisantzi, A., Hadjimitsis, D.G., Retalis, A., Paronis, D., Michaelides, S., Chrysoulakis, N., Giorgousis, G. and S. Perdikou, (2010). *Monitoring air pollution in the vicinity of cultural heritage sites in Cyprus using remote sensing techniques.* In: Ioannides, M (Ed): Euromed 2010, LNCS 6436, Springer, pp. 536 – 547.

Hadjimitsis, D. G., **Themistocleous, K.,** Trigkas, V., Matsas A., Retalis A., and Chrysoulakis N., (2010). *Spectro-radiometric measurements of non-variant targets intended for the removal of atmospheric effects from satellite images: the case study of Lemesos area in Cyprus*. Proceedings of SPIE Vol. 7827, 78270D. doi:10.1117/12.864806.

Themistocleous, K., Hadjimitsis, D. G., Retalis, A., and Chrysoulakis, N. (2010). *Accuracy assessment of atmospheric correction algorithms using Sun-photometers (AERONET), Lidar system and in-situ spectroradiometers*. Proceedings of SPIE Vol. 7827, 78270E . doi:10.1117/12.864825.

Hadjimitsis, D. G., Nisantzi, A., **Themistocleous, K.,** Matsas, A., and Trigkas, V. P. (2010). *Satellite remote sensing, GIS and Sun-photometers for monitoring PM10 in Cyprus: issues on public health*. Proceedings of SPIE Vol. 7826, 78262C . doi:10.1117/12.865120.

Hadjimitsis, D. G., **Themistocleous, K.,** Nisantzi, A., and Matsas, A. (2010). *The study of atmospheric correction of satellite remotely sensed images intended for air pollution using Sun photometers (AERONET) and Lidar system in Lemesos*. Cyprus Proceedings of SPIE Vol. 7832, 78320V. doi:10.1117/12.864822.

Themistocleous, **K.** (2010). *Air Pollution Monitoring in Cyprus Using Satellite Remote Sensing.* Space Applications for Cyprus and the Mediterranean Region. Hilton Hotel, Nicosia, April 15, 2010.

Matsas, A., Hadjimitsis, D.G, **Themistocleous**, **K.** and Retalis, A. (2010). *Use of LIDAR system and Sun-photometers for supporting satellite remote sensing measurements of atmospheric pollution.* 10th International Conference on Meteorology – Climatology and Atmospheric Physics (10th COMECAP), organized by: The Laboratory of Atmospheric Physics of the University of Patras and the Hellenic Meteorological Society, 15-21/5/2010, University of Patras .

Themistocleous, **K.,** Trigkas, V. and Hadjimitsis, D.G. (2010). *Aerosol optical thickness measurements and monitoring using remote sensing and GIS over Cyprus,* 10th International Conference on Meteorology – Climatology and Atmospheric Physics (10th COMECAP), organized by: The Laboratory of Atmospheric Physics of the University of Patras and the Hellenic Meteorological Society, 15-21/5/2010, University of Patras .

Nisantzi, A., **Themistocleous**, **K.** and Hadjimitsis, D.G. (2010). *Use of meteorological data for supporting the removal of atmospheric effects from satellite imagery in the areas located in the vicinity of existing meteorological stations in Cyprus*, 10th International Conference on Meteorology – Climatology and Atmospheric Physics (10th COMECAP), organized by: The Laboratory of Atmospheric Physics of the University of Patras and the Hellenic Meteorological Society, 15-21/5/2010, University of Patras.

2009

Hadjimitsis, D.G., and **Themistocleous**, **K.** (2009). *Assessment of the effectiveness of atmospheric correction methods using standard calibration targets, ground measurements and ASTER images*. Proc. SPIE 7475, 74750V, SPIE Remote Sensing Europe, Berlin. doi:10.1117/12.830555

Themistocleous, **K.,** and Hadjimitsis, D.G. (2009). *Air pollution monitoring through the application of atmospheric correction for ASTER imagery*, Proc. SPIE, Vol. 7478, 74780T, SPIE Remote Sensing Europe, Berlin. doi:10.1117/12.830581

Hadjimitsis, D.G, **Themistocleous K.,** Agapiou, A., Hadjimitsis, M., and Papadavid, G. (2009). *Application of the empirical line atmospheric correction using non-variant targets for ASTER images*. Proceedings of the Remote Sensing and Photogrammetric Society-UK, Annual Conference, Leicester, UK. p. 296-302.

Hadjimitsis, D.G, **Themistocleous**, **K.,** Agapiou, A., Hadjimitsis, M., and Papadavid, G. (2009). *Atmospheric correction algorithms intended for air pollution monitoring in Cyprus using satellite remotely sensed data.* Proceedings of the Remote Sensing and Photogrammetric Society-UK, Annual Conference, Leicester, UK, p. 309-314.

Hadjimitsis, D.G and **Themistocleous**, **K.** (2009). *Aerosol optical thickness determination over Cyprus using satellite remote sensing and ground measurements*. Proceedings of the 29th EARSeL Symposium: Imagin(e/g) Europe - Chania, Crete, Greece, 15-18/6/2009.

Hadjimitsis, D.G., **Themistocleous**, **K.** and Hadjimitsis, M. (2009). *Application of satellite remote sensing and Sun-photometers to determine the aerosol optical thickness over Cyprus.* Proceedings of the Second International Conference on Environmental Management, Engineering, Planning and Economics (CEMEPE 09) and SECOTOX Conference, 21-26 June 2009, Mykonos-Greece.

2008

Hadjimitsis, D.G. and **Themistocleous**, **K.** (2008). *Integrated use of Satellite Remote Sensing and GIS for monitoring atmospheric pollution in Cyprus*. 5th PanHellenic Conference 2008, 4-5 December 2008, Athens, Greece-ERDAS Solutions Session.

Hadjimitsis, D.G. and **Themistocleous**, **K.** (2008). *The importance of considering atmospheric correction in the pre-processing of satellite remote sensing data*

intended for the management and detection of cultural sites: a case study of the Cyprus area. 14th International Conference on Virtual Systems and Multimedia (dedicated to culture heritage)- VSMM 2008, 20-25 October 2008, Limassol, Cyprus.

Hadjimitsis, D.G., **Themistocleous**, **K.** and Papadavid, G. (2008). *The application of atmospheric correction algorithms for monitoring atmospheric pollution using Landsat TM images*. Proceedings of SPIE Europe Remote Sensing, 15 - 18 September 2008 University of Wales Institute, Cardiff, UK . doi:10.1117/12.800346.

Hadjimitsis, D.G. , **Themistocleous, K.** , Papadavid, G. , Retalis, A. , Chrysoulakis, N. ,Michaelides, S. , Toulios, L. , and Clayton, C.R.I. (2008). *Atmospheric correction for satellite remotely sensed data intended for hydrological applications using in-situ spectroradiometric and Sun-photometer measurements*. EGU Topical Conference Series, 10th Plinius Conference on Mediterranean Storms, Nicosia, Cyprus, 22 – 24 September 2008 .

Hadjimitsis, D.G. , **Themistocleous, K.** , Papadavid, G. , Retalis, A. , Chrysoulakis, N. , Michaelides, S. , Toulios, L. , and Clayton, C.R.I. (2008). *Comparison between visibility measurements obtained from satellites and ground.* EGU Topical Conference Series, 10th Plinius Conference on Mediterranean Storms, Nicosia, Cyprus, 22 – 24 September 2008 .

Hadjimitsis, D.G., **Themistocleous**, **K.** and Onoufriou, T. (2008). *Remote sensing measurements and GIS application for evaluation of air pollution in an industrial area in Limassol,* Cyprus. Proceedings of the International Conference 'PRE9: Protection and Restoration of the Environment IX', 29 June-3 July 2008, Kefalonia-Greece.

Themistocleous, K. and Hadjimitsis, D.G. (2008). *Atmospheric correction algorithms intended for the assessment of atmospheric pollution using satellite remote sensing. 9th Conference of Meteorology, Climatology and Atmospheric Physics, 9th COMECAP2008*, Thessaloniki, 28-31 May 2008, p.267 .

References

Abramowitz, M. and Stegun, I. A. (1970). *Handbook of Mathematical Functions with Formulas, Graphs, and Mathematical Tables, 9th edition*, New York: Dover Publications.

Adam, S., Vitse I, Johanssen, C., and Monbaliu, J. (2006). Sediment type unsupervised classification of the Molenplaat, Westerschelde estuary, the Netherlands. *EARSeL eProceedings* 5/2006, 146-1604.

Afoldi, T.T., Munday J.C. (1978). Water quality analysis by digital chromaticity mapping of Landsat data. *Canadian Journal of Remote Sensing*, *4,* 108-126.

Al-Saadi, J., Szykman, J., Pierce, B., Kittala, C., Neul, D., Chu, D.A., Remer, L., Gumley, L., Crins, E, Weinstock, L., McDonald, C., Wayland, R, and Dimmeck, F. (2005). Improving national air quality forecasts with satellite aerosol observations. *Bulletin of the Atmospheric Meteorological Society, 86* (9), 1249-1261.

Amanollahi, J., Abdullah, A.M., Farzanmanesh, R., Ramli, M.F., and Pirastek, S. (2011). PM10 distribution using remotely sensed data and GIS techniques; Klang Valley, Malaysia. *Environment Asia, 4* (1), 47-52.

Anderson, T., Charlson, R., Schwartz, S., Knutti, R., Boucher, O., Rodhe, H., and Heintzenberg, J. (2003). Climate forcing by aerosol- a hazy picture. *Science, 300,* 1103-1104.

Apresyan, L.A., and Kratsov, Y.A. (1996). Radiative Transfer: Statistical and Wave Aspects. Boca Raton, FL: CRC Press.

Bartlett, B.D., and Schott, J.R. (2007). Atmospheric inversion in the presence of clouds: an adaptive ELM approach, *Proceedings of the SPIE, SPIE, Imaging Spectrometry XII, 6661, 66610H, San Diego, California, United States.*

Baugh, W.M. and Groeneveld, D.P.(2008). Empirical proof of the empirical line. *International Journal of Remote Sensing. 29*(3), 665-672.

Baumgardner, M.F., Silva, L.F., Biehl, L.L, Stoner, E.R. (1985). Reflectance properties of soils. Adv. Agron., 38, 1-44.

Ben-dor, E., Kruse, F.A., Lefkoss, A.B., and Banin, A. (1994). Comparison of three calibration techniques for the utilization of GER 63-chemical scanner data of Makhtesh, Ramon, Negev, Israel, *Photogrammetric Engineering and Remote Sensing, 60,* 1339-1354.

Berger, F.H. (2001). Bestimmung des Energiehaushalts am Erdboden mit Hilfe von Satellitendaten. *Tharandter Klimaprotokol, Band 5*, 206.

Berger, HF. (1989). Multi-temporal analysis of forest areas in the surroundings of Innsbruck, Austria. In: Guyenne, T.D. Calabrese, G. (Eds.), *A Pilot Project Campaign on Landsat Thematic Mapper Applications*. (ESA SP-1102). 293-298.

Berk, A., Bernstein, L. S., and Robertson., D. C. (1989). *MODTRAN: A Moderate Resolution Model for LOWTRAN 77 GL-TR-89-0122*.

Berk, A., Anderson, G.P., Acharya, P.K., Bernstein, L.S., Muratov, L., Lee, J., Fox, M. Adler-Golden, S. M., Chetwynd, J.H., Hoke, M.L., Lockwood, R.B., Gardner, J.A., Cooley, T.W., Borel, C.C., and Lewis, P.E. (2005). MODTRAN 5: a reformulated atmospheric band model with auxiliary species and practical multiple scattering options: update. Proceedings of the PIE 5806, 662, doi: 10.1117/12.606026.

Bogrekci, I., W. S. Lee. (2006). Effects of Soil Moisture Content on Absorbance Spectra of Sandy Soils in Sensing Phosphorus Concentrations Using UV-VIS-NIR Spectroscopy. Trans. of ASAE 49(4): 1175-1180.

Bowers, S.A. and Hanks, R.J. (1965). Reflection of radiant energy from soils. Soil Science, 2, 130-138.

Brest, C. L., and Goward, S. N. (1987). Deriving surface albedo measurements from narrow band satellite data. *International Journal of Remote Sensing,* 8**,** 351–367.

Burrough, P.A. (1986). *Principles of Geographic Information Systems for Land Assessment.* New York: Oxford University Press.

Campbell J.B. (2008) *Introduction To Remote Sensing*, 4th ed. Guildford Press: London.

Canty, M.J., Nielsen, A.A, and Schmidt, M. (2004). Automatic radiometric normalization of multi-spectral imagery. *Remote Sensing of the Environment 91* (34), 441-451.

Caprioli, M., Figorito, B., and Tarantino, E. (2008). Radiometric normalization of Landsat ETM+ Data for Multitemporal Analysis. *International Archives of the Photogrammetry Remote Sensing and Spatial Information Sciences*, Vol. XXVII, Part B8, Beijing, China, 397-402.

Caselles, V., and Garcia, M.J.L. (1989). An alternative simple approach to estimate atmospheric correction in multi-temporal studies. *International Journal of Remote Sensing 10* (6)1127-1134.

Cervino, M., Torricella, F., Costa, M.J., Levizzani, V., Bartoloni, A., Mochi, M. Colandrea, P. Zappitelli, E. (2011). *Validation of Aerosol Properties Retrieved from GOME Measurements*. Institute of Atmospheric Sciences and Climate. Accessed 11/9/2011 at www.isac.cnr.it.

Chahine, M.T. (1983). *Interaction mechanisms within the atmosphere (Chapter 5)*, In: Manual of Remote Sensing (ed. Colwell, R.N.), 2nd edition, Falls Church, Virginia: American Society of Photogrammetry, 165-230.

Chander, G., Markham, B. L., and Barsi, J. A. (2007a). Revised Landsat 5 Thematic Mapper radiometric calibration. *IEEE Transactions on Geoscience and Remote Sensing, 44*, 490−494.

Chander G, Markham BL, and Helder DL (2009). Summary of current radiometric calibration coefficients for Landsat MSS, TM, ETM+, and EO-1 ALI sensors, , *Remote Sensing of Environment, 113*(5), 893-903

Chander, G. Haque, M.O. Micijevic, E. and Barsi, J.A. (2010). A Procedure for Radiometric Recalibration of Landsat 5 TM Reflective-Band Data*, IEEE Transactions on Geoscience and Remote Sensing, 48* (1) 556 – 574.

Chandrasekhar, S. (1960). *Radiative Transfer*, Dover Publications, New York.

Chavez, P.S. (1975). Atmospheric, solar and MTF corrections for ERTS digital imagery. *Proceedings of the American Society of Photogrammetry*, 69-69a.

Chavez, P.S. (1988) An improved dark-object subtraction technique for atmospheric scattering correction of multi-spectral data, *Remote Sensing Environment, 24,* 458-479.

Chavez, P.S. (1989). Radiometric calibration of Landsat Thematic Mapper multispectral Images*. Photogrammetric Engineering and Remote Sensing*, 24, 459-479.

Cheng, P., Gσmez, F. Weber, M. and Flingelli, C. (2008). Correcting the Data Mapping of IKONOS Images. *Geo-informatics,* March, 2008.

Cheng, K.S. and Lei, T.C., (2001). Reservoir Trophic state evaluation using Landsat TM images. *Journal of the American Water Resources Association, 37*, 1321–1334.

Chepfer, H., Goloub, P., Riedi, J., Dehaan, J. F., Hovenier, J. W., and Flamant, P. (2001). Ice crystal shapes in cirrus clouds derived from POLDER/ADEOS-1, *Journal of Geophysical Research, 106* (D8), 7955–7966.

Chin, M. (2009). Atmospheric aerosol properties and Climate impacts-synthesis and assessment product 2.3. *Report by the US Climate Change Science Program and the subcommittee on Global Change Research.* Washington, D.C.

Chin, M., Ginoux, P., Kinne, S., Torres, O., Holben, B.N., Duncan, B.N., Martin, R.V., Logan, J.A., Higurashi, A., and Nakajima, T. (2002). Tropospheric aerosol optical thickness from the GOCART model and comparisons with satellite and Sun photometer measurements. *Journal of the Atmospheric Sciences; 59*, 461–483.

Chrysoulakis, N., Abrams, M., Feidas, H., and Arai, K. (2010). Comparison of atmospheric correction methods using ASTER data for the area of Crete, Greece. *International Journal of Remote Sensing, 31* (24), 6347-6385.

Chu, D. A., Kaufman, Y. J., Ichoku, C., Remer, L. A., Tanré, D., Holben, B. N. (2002). *Validation of MODIS aerosol optical depth retrieval over land*, Geophys. Res. Lett., 29(12), pp. 8007.

Chuvieco, E. and Huete, A. (2009). *Fundamentals of Remote Sensing.* New York, USA: Taylor Francis.

Clark, R. N., Swayze, G. A., Livo, K. E., Kokaly, R. F., King, J. B., Dalton, J. S., Rockwell, B. W., Hoefen, T. & Mcdougal, R. R. (2003) Surface reflectance calibration of terrestrial imaging spectroscopy data: a tutorial using AVIRIS. *AVIRIS Workshop Proceedings.* http://speclab.cr.usgs.gov/PAPERS.calibration.tutorial/

Cracknell, A.P., and Hayes, L.W. (1993) *Introduction to Remote Sensing*, Taylor and Francis, London, 116-158.

Crane R.B. (1971). Pre-processing techniques to reduce atmospheric and sensor variability in multi-spectral scanner data. Proceedings of the *7th International Symposium on Remote Sensing of Environment,* Ann Arbor, MI, USA (Michigan: Environmental Research Institute of Michigan), 1345.

Cressie, N. (1993). *Statistics For Spatial Data*. New York: Wiley Interscience.

Crippen, R.E. (1987). The regression intersection method of adjusting image data for band rationing. *International Journal of Remote Sensing, 8*(2),137–155.

D'Almeida, G. A.(1987). On the variability of desert Aerosol Radiative characteristics, Journal of Geophysical Research, 92(D3), 3017–3026.

Datt, B., Mcvicar, T.R., Van Niel, T.G., Jupp, D.L.B., and Pearlman, J.S. (2003). Preprocessing EO-1 hyperion hyperspectral data to support the application of agricultural indexes. *IEEE Transactions on Geoscience and Remote Sensing, 41* (6), 1246-1259.

De Haan, Hovenier, J.W, Kokke J.M.M, and Van Stokkom H.T.C (1991). Removal of atmospheric influences on satellite-borne imagery: A radiative transfer approach, *Remote Sensing Environment, 37,* 1-21.

DeLeeuw, G., Neele, F.P., Hill, M., Smith, M.H., Vignati, E. (2000). Sea spray aerosol production by waves breaking in the surf zone. *Journal of Geophysical Research, 105* (D2), 29397-29409.

Deirmendjian, D. (1964). Scattering and polarization of water clouds and hazes on the visible and infrared. *Applied Optics, 3,* 187-196.

Deschamps, P.Y., Herman, M., and Tanré, D. (1983a). Modeling of the atmospheric effects and its application to the remote sensing of ocean colour, *Applied Optics, 23,* 3751-3758.
Dobos, E., (2003). Albedo, Encyclopedia of Soil Science, 1-3. DOI: 10.1081/E-ESS 120014334.

Du, Y., Cihlar J. Beaubien J, and Latifovic, R. (2001). Radiometric normalization, compositing and quality control for satellite high resolution image mosaics over large areas. *IEEE Transactions on Geoscience and Remote Sensing* 39 (3) 623-634.

Du, Y., Teillet, PM, and Cihlar J. (2002). Radiometric normalization of multi-temporal, High resolution satellite images with quality control for land cover change detection. *Remote Sensing of Environment 82,* 123-134.

Dubovik, O., Smirnov, A., Holben, B.N., King, M.D., Kaufman, Y.J., Eck, T.F., and Slutsker, I. (2000). Accuracy assessments of aerosol optical properties retrieved from AERONET Sun and sky radiance measurements. *Journal of Geophysical Research*. *2000,* 105, 9791-9806.

Dubovik, O., Holben, B., Eck, T., Smirnov, A., Kaufman, Y., King, M., Tanré, D., and Slutsker, I. (2002). Variability of absorption and optical properties of key aerosol types observed in worldwide locations. *Journal of Atmospheric Science, 59,* 590-608.

Dubovik, O, and King, M. (2000). A flexible inversion algorithm for retrieval of aerosol optical properties from Sun and sky radiance measurements. *Journal of Geophysical Research*. *105,* 20673-20696.

Eck ,T., Holben, B., Reid, J., Dubovik, O., Smirnov, A., O'Neill, N., Slutsker, I., and Kinne, S. (1999). Wavelength dependence of the optical depth of biomass burning, urban and desert dust aerosols. *Journal of Geophysical Research*, *104,* 31333-31350.

Eck, T., Holben, B. N., Reid, J. S., Sinyuk, A., Dubovik, O., Smirnov, A., Giles, D., O'Neill, N., Tsay, S. C., Ji, Q., Schafer, J. S., Sorokine, M., Newcomb, W., and Slutsker, I. (2008). Spatial and temporal variability of column integrated aerosol optical properties in the southern Arabian Gulf and United Arab Emirates in summer, *Journal of Geophysical Research,*113, D01204, doi:10.1029/2007JD008944.

Eckhardt, D.W., Verdin, J.P., Lyford, G.R. (1990). Automated update of an irrigated lands GIS using SPOT HRV imagery. *Photogrammetry Engineering and Remote Sensing, 61,* 1515-1522.

Emery, D.R., Milton, E.J., and Felstead, R. (1998). Optimising data collection for Heathland remote sensing. *Proceedings of the 24th Annual Conference of the Remote Sensing Society, Developing International Connections.* University of Greenwich, 483-489.

ERDAS. (2010). ERDAS Imagine Field Guide, ERDAS Inc. Atlanta, GA, USA.

Escadafal, R., Bacha, S., and Delaitre, E. (1997). *Remote Sensing '96-Integrated Applications for Risk Assessment and Disaster Prevention for the Mediterranean.* (Ed. Spiteri A). Ballema, Rotterdam, 35-40.

Evans, K. F., and Wiscombe, W., (2003). Improvements to the SHDOM radiative transfer modeling package. *Proceedings of the 13th Atmospheric Radiation Measurement ARM Science Team Meeting Proceedings,* Broomfield, Colorado, March 31-April 4.

Ferrier, G. and Wadge, G. (1996). The application of imagery spectrometry data to mapping alteration zones associated with gold mineralization in Southern Spain. *International Journal of Remote Sensing, 17,* 331-350.

Forster, B.C. (1984). Derivation of atmospheric correction procedures for Landsat MSS with particular reference to urban data. *International Journal of Remote Sensing 5* (5): 799-817.

Forster, B.C. (1989). An introduction to Modern Remote Sensing techniques and their implication for Surveying practice, *The Australian Surveyor, 34* (8), 763-779.

Fraser, R. S., Ferrare, R. A., Kaufman, Y. J., Markham, B. L., & Mattoo, S. (1992). Algorithm for atmospheric corrections of aircraft and satellite imagery. *International Journal of Remote Sensing, 13,* 541–557.

Fraser, R.S., and Kaufman, Y.J., (1985). The relative importance of scattering and absorption in remote sensing, *IEE Transactions of Geo-science and Remote Sensing, 23,* 625-633.

Fraser, R.S., Kaufman, Y.J., and Mahoney R.L. (1984). Satellite measurements of aerosol mass and transport, *Atmospheric Environment*, 18, 2577-2584.

Ganesh, K.E., Umesh, T.K., Narasimtiamurthy, B. (2010). Interannual variability in time scale characteristics of aerosol optical thickness over Mysore, India. *Indian Journal of Radio and Space Physics, 39,* 80-91.

García Rodríguez, J. N., (2011). Changes in Spectral Slope due to the Effect of Grain Size and Moisture in Beach Sand of Western Puerto Rico. Accessed 21 October, 2011: http://gers.uprm.edu/pdfs/topico_johanna2.pdf.

Gaut, N.E., Reifenstein, III, E.C., and Sievery, H. (1975). Interaction mechanisms within the atmosphere. In RG Reeves (eds.) *Manual of remote sensing, 1st edition. American Society of Photogrammetry.* Falls Church, VA, USA: Keuffel and Esser Company.

Gilabert, M.A., Conese, C., and Maselli, F. (1994). An atmospheric correction method for the automatic retrieval of surface reflectances from TM images. *International Journal of Remote Sensing, 15* (10), 2065–2086.

Gill, T.K. Danasher, T., Gillingham, S.S., Mitchell, R.M., (2012). Comparing bright target surface spectral reflectance estimates obtained from IRS P6 LIS111 to those obtained from Landsat 5TM and Landsat 7 ETM+. Remote Sensing Letters, 3,2,121-130.

Gordon, H.R., Clark, D.K., Brown, J.W., Evans, R.H., and Broenkow, W.W. (1983).Phytoplankton pigment concentrations in the Middle Atlantic Bight: Comparison of ship determinations and CZCS estimates, *Applied Optics, 22* (1), 20-36.

Goward, S.N., and Williams, D.L. (1997). Landsat and Earth Systems Science: Development of terrestrial monitoring. *Photogrammetric Engineering and Remote Sensing*, *63* (7), 887-900.

Greenberg, M. (1998), *Advanced Engineering Mathematics (2nd ed.)*. New York: Prentice Hall.

Guang, J., Xue, Y., Li, X., Bai, L., Wang, Y. Li, Y., Wan, W., and Guo, J. (2008). Multi-spatial scale aerosol optical thickness mapping for Beijing using remote sensing technique. Proceedings of the ISPRS., XXXVII, p. 485-490.

Guanter, L. (2006). New Algorithms for Atmospheric Correction Retrieval of Biophysical Parameters in Earth's Observation Application to Envisat/MERIS Data. Doctoral Thesis: *University of Valencia, Spain*.

Gupta, P., and Christopher, S.A. (2008). Seven Year Particulate Matter Air Quality Assessment from Surface and Satellite Measurements, *Atmospheric Chemistry and Physics, 8* (12), 2008, pp.3311-3324.

Gupta, P. and Christopher, S.A. (2009). Particulate matter, air quality assessment using integrated surface, satellite and meteorological products: 2. A neural network approach. Journal of Geophysical Research, 114, D20205, doi: 10.1029/2008JD011497.

Hadjimitsis, D.G. (1999). The application of atmospheric correction algorithms in the satellite remote sensing of reservoirs. PhD thesis. *University of Surrey, School of Engineering in the Environment, Department of Civil Engineering, Guildford*.

Hadjimitsis, D.G. (2008). Description of a new method for retrieving the aerosol optical thickness from satellite remotely sensed imagery using the maximum contract value principle and the darkest pixel approach. *Transactions in GIS Journal, 12* (5), 633-644.

Hadjimitsis, D.G. (2009). Aerosol optical thickness (AOT) retrieval over land using satellite image-based algorithm. *Air Quality Atmosphere and Health-An International Journal, 2* (2), 89-97.

Hadjimitsis, D.G., and Clayton, C.R.I. (2004). Determination of the aerosol optical thickness and assessment of atmospheric conditions using satellite image-based processing algorithm and radiative transfer theory. *Proceedings of the 7th Pan-Hellenic International Conference of Meteorology, Climatology and Atmospheric Physics,* University of Cyprus, Nicosia, Cyprus, 28-30 September.

Hadjimitsis, D.G., and Clayton, C.R.I. (2006). Detecting air pollution from space using image-based method. *Proceedings of the International Conference: Protection and Restoration of the Environment, VIII,* Crete, July 2006, p. 313.

Hadjimitsis, D.G., and Clayton, C.R.I. (2008). The use of an improved atmospheric correction algorithm for removing atmospheric effects from remotely sensed images using an atmosphere-surface simulation and meteorological data, *Meteorological Applications,* 381-387. http://dx.doi.org/10.1002/met.80.

Hadjimitsis, D.G., Clayton, C.R.I., Hope, V.S. (2004). An assessment of the effectiveness of atmospheric correction algorithms through the remote sensing of some reservoirs. *International Journal of Remote Sensing, 25* (18):3651–3674.

Hadjimitsis, D.G., Clayton, C.R.I., Hope, V.S., and, Retalis, A. (1999b) A new method of removing atmospheric effects using pseudo-invariant targets, In: *Earth observations from data to information, Proceedings of the 25th Annual Conference and Exhibition of the RSS,* University of Wales and Swansea, 633-641.

Hadjimitsis D.G., Clayton CRI and Retalis A. (2003). Darkest pixel atmospheric correction algorithm: a revised procedure for environmental applications of satellite remotely sensed imagery, *Proceedings of the 10th International Symposium on Remote Sensing,* 8-12/9/2003, Barcelona - Spain , organised by NASA, SPIE Conference, 414.

Hadjimitsis D.G., Clayton CRI and Retalis A., (2009). The use of selected pseudo-invariant targets for the application of atmospheric correction in multi-temporal studies using satellite remotely sensed imagery. *International Journal of Applied Earth Observation and Geoinformation, 11* (3), 192-200.

Hadjimitsis, D.G., Hope, V.S., and Clayton C.R.I. (1998) The suitability of simple statistical techniques to remove the atmospheric effects from satellite multi-spectral remote sensing data from inland waters. In: *Developing Space '98, Proceedings of the 1998 Remote Sensing Society Student Conference, Observations and Interactions,* University of Oxford, Department of Zoology, 116-122.

Hadjimitsis, D.G., Papadavid, G., Agapiou, A., Themistocleous, K., Hadjimitsis, M.G., Retalis, A., Michaelides, S., Chrysoulakis, N., Toulios, L., and Clayton, C.R.I. (2010). Atmospheric correction for satellite remotely sensed data intended for agricultural applications: impact on vegetated indices. *National Hazards Earth System Science, 10,* 89-95.

Hadjimitsis, D.G., Retalis, A., and Clayton, C.R.I. (2002). The assessment of atmospheric pollution using satellite remote sensing techniques in large cities in the vicinity of airports. *Water, Air and Soil Pollution: Focus, An International Journal of Environmental Pollution, 2* (5-6), 631-640.

Hadjimitsis, D.G., Themistocleous, K., Vryonides, P., Toulios, L., and Clayton, C.R.I. (2007). Applications of satellite remote sensing and GIS to urban air-quality monitoring: potential solutions and suggestions for the Cyprus area. In Ranjeet S. Sohki and M. Neophytou (Eds.): *Proceeding of the 6th International Conference on Urban Air Quality*. Limassol, Cyprus, 27-29 March, 2007, 144.

Hadjimitsis, D.G and Themistocleous, K. (2009a). *Aerosol optical thickness determination over Cyprus using satellite remote sensing and ground measurements*. Proceedings of the 29th EARSeL Symposium: Imagin(e/g) Europe -Chania, Crete, Greece, 15-18/6/2009.

Hadjimitsis, D.G, Themistocleous, K., Agapiou, A., Hadjimitsis, M., and Papadavid, G. (2009b). *Atmospheric correction algorithms intended for air pollution monitoring in Cyprus using satellite remotely sensed data.* Proceedings of the Remote Sensing and Photogrammetric Society-UK, Annual Conference, Leicester, UK, p. 309-314.

Hall, F.G., Strebel, D.E., Nickeson, J.E., and Goetz, S.J. (1991). Radiometric rectification: Toward a common radiometric response among multidate, multisensor images, *Remote Sensing Environment.*, *35,* 11–27.

Hall, A., Lamb, D.W., Holzapfel, B. and Louis, J. (2002). Optical remote sensing applications for viticulture – a review. *Australian Journal of Grape and Wine Research, 8,* 36–47.

Hansen, J. E., and Lacis, A. A. (1990). Sun and dust versus greenhouse gases: an assessment of their relative roles in global climate change. *Nature, 336*, 713-719.

Hashim, S.A., Alsultan, S., MatJafri, M.Z., Abdullah, K., and Salleh, N.M., (2006). The measurement of aerosol optical thickness in Mina during the Hajj season, 1426H. *Proceedings of the XXXVI conference of the International Society for Photogrammetry and Remote Sensing, part 7.* May 8-11, 2006. Enschede, The Netherlands.

Hauser, A., Oesch D., and Wunderle, S. (2004). NOAA AVHRR derived Aerosol Optical Depth (AOD) over Land: A comparison with AERONET Data. *Óptica Pura Y Aplicada*, 37, 3131-3135.

Haywood, J. M. (2003). Radiative properties and direct radiative effect of Saharan dust measured by the C-130 aircraft during Saharan Dust Experiment (SHADE). 1: Solar spectrum. *Journal of Geophysical Research, (108)* 8577-8593. doi:10.1029/2002JD002687.

Heo, J., and Fitzhugh, T.W. (2000). A standardized radiometric normalization method for change detection using remotely sensed imagery. *Photogrammetry Engineering and Remote Sensing, 66,* 173-181.

Heine, G.W. (1986). A Controlled Study of Some Two-Dimensional Interpolation Method. *COGS Computer Contributions*, 3, 60-67.

Hess, T., Stephens, W. and Thomas, G., (1996). Modeling NDVI from decadal rainfall data in the North East Arid Zone of Nigeria. *Journal of Environmental Management, 48*, 249-261.

Hill, J., and Aifadopoulou, J.D. (1990) Comparative analysis of Landsat-5 TM and Spot HRV-1 sensors for the use in multiple sensor approaches, *Remote Sensing of Environment, 34,* 55-70.

Hill, J., and Sturm, B. (1991). Radiometric correction of multi-temporal Thematic Mapper data for use in agricultural land cover classification and vegetation monitoring. *International Journal of Remote Sensing, 12* (7) 1471-1491.

Holben, B., Eck, T., Slutsker, I., Tanré, D., Buis, J.P., Setzer. A., Vermote, E., Reagan, J. A., Kaufman, Y. J., Nakajima, T., Lavenu, F., Jankowiak, I., and Smirnov, A. (1998). AERONET-a federated instrument network and data archive for aerosol characterization. *Remote Sensing of the Environment (66),* 1-16.

Holben, B. N., Smirnov, A., Eck, T. F.,Slutsker, I., Abuhassan, N., Newcomb, W. , Schafer, J. S., Tanré, D., Chatenet, B., and Lavenu, F. (2001). An emerging ground-based aerosol climatology: aerosol optical depth from AERONET. *Journal of Geophysical Research, 106,* 12067-12098.

Hsu C. N., Tsay S.C., King, M.D., and Herman, J.R. (2004). Aerosol Properties Over Bright-Reflecting Source Regions, *IEEE Transactions on Geoscience and Remote Sensing, 42,* 3, 557-569.

Huang, C., Wylie, B., Yang, L., Homer, C., and Zylstra, G. (2002). Derivation of a tasselled cap transformation based on Landsat 7 at-satellite reflectance. *International Journal of Remote Sensing*, *23,* 1741-1748.

Huang, C., Yang, L., Homer, C., Wylie, B., Vogelman, J., and DeFelice, T. (2000). *At-satellite reflectance: a first order normalization of Landsat 7 ETM+ images.* http://kndcover.usgs.gov/pdf/huang.pdf. (Retrieved 30/12/2010).

Hummel, P. (2011). Remotely Sensed Ground Control Points: *Field tests verify accuracy* of satellite imagery. Accessed on 30/12/2011 at http://www.compassdatainc.com/

Ishida, T. Ando, H., Fukuhra, M., (1991). Estimation of complex refractive index of soil particles and its dependence on soil chemical properties. Remote Sensing of Environment, 38, 173-182.

Istomina, L.G. von Hoyningen-Huene, W., Kokhanovsky, A.A., Schultz, E. and Burrows, J.P. (2011). Remote sensing of aerosols over snow using infrared AATSR observation, Atmospheric Measurement Techniques, 4, 1133-1145, doi. 10.51941.amt-4-1133-2011.

Jackson, R., Clarke, T., and Moran, S. (1992). Bidirectional direction results for 11 Spectralon and 16BaSO4 reference reflectance panels. *Remote Sensing of Environment, 40,* 231-239.

Janzen, D., Fredeen, A., and Wheate, R. (2006). Radiometric correction techniques and accuracy assessment for Landsat TM data in remote forested regions. *Canadian Journal of Remote Sensing 32* (5) 330-340.

Jensen, H. W., Legakis, J., and Dorsey, J. (1999). Rendering of Wet Materials. Rendering Techniques '99. Eds. D. Lischinski and G. W. Larson. Springer-Verlag**,** pages 273-282, 1999.

Jenness, J. and Singer, J. (2007). Technical Brief: Color and Contract of Detectable Warnings. Federal Highway Administration, Washington D.C. Accessed at: http://www.access-board.gov/research/dw-fhwa/summary.htm, 19/12/2011.

Jensen, J.R. (1996) *Introductory digital image processing*, Newark, New Jersey, USA: Prentice Hall.

Jiang, X., Liu, Y., Yu, B., and Jiang, M. (2007). Comparison of MISR aerosol optical thickness with AERONET measurements in Beijing metropolitan area. *Remote Sensing of Environment, 107, 4*5-53.

Kahn R., Gaitley, R., Martonchik, J., Diner, D., Crean, K., and Holben, B. (2005a). MISR global aerosol optical depth validation based on two years of coincident AERONET observations.*Journal of Geophysical Research*, 110. D10S04, doi:10.1029/2004JD004706.

Kaleita, A.L., Tian, L.F., Hirschi, M.C. (2005). Relationship between soil moisture content and soil surface reflectance. Transactions of the American Society of Agricultural Engineers, (48) 5, 1979-1986.

Kalivitis, N., Gerasopoulos, E., Vrekoussis, M., Kouvarakis, G., Kubilay, N., Hatzianastassiou, N., Vardavas, I., and Mihalopoulos, N. (2007). Dust transport over the eastern Mediterranean derived from Total Ozone Mapping Spectrometer, Aerosol Robotic Network, and surface measurements, *Journal of Geophysical Research, 112,* D03202, doi:10.1029/2006JD007510.

Kanaroglou, P.S., Soulakellis, N.A., and Sifakis, N.I. (2002). Improvement of satellite derived pollution maps with the use of a geostatistical interpolation method. *Journal of Geographical Systems, 4,* 193-208.

Karpouzli, E. and Malthus, T. (2003). The empirical line method for the atmospheric correction of IKONOS imagery. *International Journal of Remote Sensing, 24* (5), 1143-1150.

Kaufman, Y.J. (1985) The atmospheric effect on the separability of field classes measured from satellites, *Remote Sensing of Environment, 18,* 21-34.

Kaufman YJ (1989). The atmospheric effect on remote sensing and its correction. In: Asrar G (ed) *Theory and applications of optical remote sensing*. New York City, New York, USA: Wiley and Sons.

Kaufman, Y.J, and Fraser, R.S. (1983) Light extinction by aerosols during summer air pollution. *Journal of Applied. Meteorology, 22,* 1694-1706.

Kaufman YJ, Fraser RS, Ferrare, RA. (1990). Satellite remote sensing of large scale air pollution method. *Journal of Geophysical. Research*. *95,* 9895-9909.

Kaufman Y., Haywood, J., Hobbs, P., Hart, W., Kleidman, R., and Schmid, B., (2003). Remote sensing of vertical distributions of smoke aerosol off the coast of Africa. *Geophysical. Research Letters, 30*:1831, doi:10.1029/2003GL017068.

Kaufman, Y.J., and Sendra, C. (1988). Algorithm for automatic atmospheric corrections to visible and near-IR satellite imagery*, International Journal of Remote Sensing, 9* (8), 1357-1381.

Kaufman, Y. J., and Tanré D. (1996). Direct and Indirect Methods for Correcting the Aerosol Effect on Remote Sensing, *Remote Sensing of Environment*, *55*, 65-79.

Kaufman, Y. J., Tanré, D., Remer, L. A., Vermote, E. F., Chu, A., and Holben, B. N., (1997). Operational remote sensing of tropospheric aerosol over land from EOS moderate resolution imaging spectroradiometer. *Journal of Geophysical Research 102,* 17051–17067.

Kaufman, Y.J., Tanré, D, and Boucher, O. (2002a). A satellite view of aerosols in the climate system. *Nature (419),* doi 10.1038/nature 01091.

Kimes, D.S. (1983). Dynamics of directional reflectance factor distribution for vegetation canopies. *Applied Optics, 22* (9), 1364-1372.

King, M.D., Kaufman, Y.J., Tanré, D., Nakajima, T. (1999). *Remote Sensing of Tropospheric Aerosols from Space: Past, Present, and Future*, Bulletin of the American Meteorological Society 80, pp. 2229--2259

Kneizys, F.X., Shettle, E.P., Abreu, L.W., Chetwynd, J.H., Anderson, G.P., Gallery, W.O., Selby, J.E.A., and Clough, S.A. (1988). *User's guide to LOWTRAN 7*. Air Force Geophysics Laboratory, Hanscom AFB Environmental Research Report ERP No. 1010.

Kokhanovsky, A. A., Breon, F.-M., Cacciari, A., Carboni, E., Diner, D., Di Nicolantonio, W., Grainger, R. G. Grey, W. M. F., Holler, R., Lee, K.-H., Li, Z., North, P. R. J., Sayer, A., Thomas, G., and von Hoyningen-Huene,W. (2007). Aerosol remote sensing over land: A comparison of satellite retrievals using different algorithms and instruments, *Atmospheric Research, 85,* 372–294.

Kokhanovsky, A. A., Cornet, C., Duan, M., Emde, C., Katsev, I. L., Labonnote, L.-C., Min, Q., Nakajima, T., Ota, Y., Prikhach, A. S., Rozanov, V. V., Yokota, T., and Zege, E. P. (2010a). Benchmark results in vector radiative transfer, *Journal of Quantitive Spectroscopy and Radiance,* doi:10.1016/j.jqsrt.2010.03.005.

Kokhanovsky, A. A., Deuz´e, J. L., Diner, D. J., Dubovik, O., Ducos, F., Emde, C., Garay, M. J., Grainger, R. G., Heckel, A., Herman, M., Katsev, I. L., Keller, J., Levy, R., North, P. R. J., Prikhach, A. S., Rozanov, V. V., Sayer, A. M., Ota, Y., Tanr´e, D., Thomas, G. E., and Zege, E. P. (2010b). The inter-comparison of major satellite aerosol retrieval algorithms using simulated intensity and polarization characteristics of reflected light, *Atmospheric Measurement Techniques,* 3, 909–932, doi:10.5194/amt-3-909-2010.

Kotchenova S. Y. and Vermote E. F. (2007). Validation of a vector version of the 6S radiative transfer code for atmospheric correction of satellite data. Part II: Homogeneous Lambertian and anisotropic surfaces. *Applied Optics, 46,* 4455-4464.

Kruse, F.A., Kierein-Young, K.S, and Boardman, J.W. (1990). Mineral Mapping at Cuprite, Nevada with 63-Channel Imaging Spectrometer. *Photogrammetric Engineering and Remote Sensing, 56,* 83-92.

Lach, S.R. and Kerekes, J.P. (2008). Atmospheric compensation using a geometrically-compensated empirical line method. *IGARSS (3),* 664-667.

Landsat 7 Science Data Users Handbook, (2011) National Aeronautics and Space Administration, accessed at:
http://landsathandbook.gsfc.nasa.gov/pdfs/Landsat7_Handbook.pdf (retrieved 4/2/2010).

Leahy, L., Anderson, T., Eck, T., and Bergstrom, R. (2007). A synthesis of single scattering albedo of biomass burning aerosol over southern Africa during SAFARI 2000. *Geophysical. Research Letters,* 34:L12814, doi:10.1029/2007GL029697.

Lee, K. H, and Kim, Y. J. (2010). Satellite remote sensing of Asian aerosols: a case study of clean, polluted and dust storm days. *Atmospheric Measurement Techniques Discussions, 3,* 2651-2680. doi10.5194/amtd-3-2651-2010.

Lee, K. H., Li, Z. and Kim, Y. J. (2009). Atmospheric aerosol monitoring from satellite observations: A history of three decades of atmospheric and biological environmental monitoring, *Environmental Monitor,* 13, doi:10.1007/978-1-4020-9674-7.

Leon, J., Chazette, P., and Dulac, F. (1995). Direct and indirect methods for correcting the aerosol effect on remote sensing. *Remote Sensing and Environment, 55,* 65-79.

Lesaignoux, A., Fabre, S., Briottet, X., Olioso, A., Belin, E., Cedex, T. (2009). *Influence of surface soil moisture on spectral reflectance of bare soil in the 0.4 - 15µm domain.* Proceedings of the 6th EARSeL SIG IS workshop imaging spectroscopy.

Liang S, Fang H, and Chen M (2001). Atmospheric correction of Landsat ETM+ Land surface imagery-Part 1: Methods. *IEEE Transactions on Geoscience and remote sensing, 39* (11), 2490-2498.

Liang, S., H. Fang, J. Morisette, M. Chen, C. Walthall, C. Daughtry, and C. Shuey, (2002), Atmospheric Correction of Landsat ETM+ Land Surface Imagery: II. Validation and Applications, *IEEE Transactions on Geosciences and Remote Sensing, 40*(12): 2736-2746.

Lillesand, T.M., and Kiefer, R.W. (2004). *Remote Sensing and image interpretation,* 3rd edition, John Wiley and Sons, USA.

Lim H. S., MatJafri M. Z., Abdullah K., Saleh N. M., and Al-Sultan, S. (2004). determination of aerosol optical thickness from spectral sky transmittance, *25th ACRS 2004* Chiang Mai, Thailand, p 133-138

Lindell, T., Karlsson, B.K., Rosengren, M., and Afoldi, T. (1986). A further development of the chromaticity technique for satellite mapping of suspended sediment load. *Photogrammetric Engineering and Remote Sensing, 52,* 1521-1529.

Liu, W., Baret F., Gu, X., Tong, Q., Zheng, L. and Zhang, B. (2002). Relating soil surface moisture to reflectance. *Remote Sensing of Environment*, 81, pp.238-246.

Lu, D., Mausel, P., Brondizio, E., and Moran, E. (2002) Assessment of atmospheric correction methods for Landsat TM data applicable to Amazon basin LBA research. *International Journal of Remote Sensing, 23* (13) 2651-2671.

Lyons, T.J. and Scott, W.D. (1990). Principles of Air Pollution Meteorology. Boca Raton, FL: CRC Press.

Mahiny AS and Turner BJ. (2007). A comparison of four common atmospheric correction methods. *Photogrammetric Engineering and Remote Sensing, 73* (4), 361-368.

Mahmoud, E.H., Begue, A., LaFrance, B. Itagolle, O., Dedieu, G. and Rumeau, M. (2008). Relative radiometric normalization and atmospheric correction of a SPOT 5 Time series. *Sensors, (8),* 2774-2791.

Magi B., Hobbs, P., Kirchstetter, T., Novakov, T., Hegg, D., Gao, S., Redemann, J., and Schmid, B., (2005). Aerosol properties and chemical apportionment of aerosol optical depth at locations off the United States East Coast in July and August 2001. *Journal of Atmospheric Science, 62,* 919-933.

Mätzler, C, Ed. (2006). *Thermal microwace radiation: applications for remote sensing*. IET electromagnetic waves series. London: The Institution of Engeneering and Technology.

Maracci, G., and Aifadopoulou, D. (1990). Multi-temporal remote sensing study of spectral signatures of crops in the Thessaloniki test site, *International Journal of Remote Sensing, 11* (9), 1609-1615.

Maracci, G., Andreoli, G., and Hosgood, B. (1986). Measurements of spectral signatures in less favoured areas (LFA): a contribution to the definition of a remote sensing multi-temporal experiment. *ESA/EARSel Symposium on Europe from Space, Lyngby, D*K, 25-28 June 1986, ESA SP-258, 215-218.

Marchuk, G.I., Kondratyev, K.Y., Kozodervo, V.V., and Khvorostyanov, V.I. (1986). *Clouds and Climate.* Gidrometeoizdat. Leningrad (in Russian).

Markham, B.L. and Barker, J.L. (1985). Spectral characterization of the Landsat Thematic Mapper sensors. *International Journal of Remote Sensing, 6,* 697-716.

Mather, P.M. (1987). *Computer Processing of Remotely-Sensed Images. An Introduction, 1st Edition*. Chichester, UK: John Wiley.

Mather, P. and Koch, M. (2011). *Computer Processing of Remotely Sensed Images, 4th edition,*. Chichester, UK: John Wiley.

McBratney, A.B. and Webster, R. (1986). Choosing Functions For Semi-Variograms of Soil Properties and Fitting Them to Sampling Estimates, *Journal of Soil Science, 37,* 617-639.

McCoy, K.R. (2005). *Resource Management information systems*, London, UK: Taylor and Francis.

Miesch, C. and Briottet, X. (2002). Bidirectional reflectance of a rough anisotropic surface. *International Journal of Remote Sensing Letters, 23,* 3107-4114.

Miesch, C., Briottet, X., and Kerr, Y.H. (2004). Phenomenological analysis of simulated signals observed over shaded areas in an urban scene. *IEEE Transactions in Geoscience Remote Sensing, 42,* 434-442.

Miesch, C., Briottet, X., Kerr, Y.H., and Cabot, F. (1999). Monte Carlo approach for solving the radiative transfer equation over mountainous and heterogeneous areas. *Applied Optics, 38,* 7419-7430.

Mishchenko, M. I., Geogdzhayev, I. V., Cairns, B , Carlson, B. E., Chowdhary, J., Lacis, A. A., Liu, L., Rossow, W. B., and Travis, L. D. (2007)Past, present, and future of global aerosol climatologies derived from satellite observations: A perspective. *Journal of Quantitative Spectroscopy and Radiative Transfer*, *106*(1-3), 325–347.

Milton, E. J. (1987). Review Article Principles of field spectroscopy. *International Journal of Remote Sensing, (8)* 12,1807 -1827.

Milton, E.J., Fox, N., and Chapman, M.E. (2006). Progress in field spectroscopy, *Proceedings 2006 IEEE International Geoscience and Remote Sensing Symposium. IGARSS '06*, 2006-07-31-08-04- Denver, pp.1966-1968.

Milton, E.J., Rollin, E.M., and Emery, D.R. (1995). Advances in field spectroscopy. In: Danson, F.M. and Plummer, S.E. (Eds.). *Advances in Environmental Remote Sensing.* Chichester, UK: John Wiley and Sons, p. 9-32.

Meroni M. and Colombo R. (2009). 3S: A novel program for field spectroscopy *Computers and Geosciences, (35)* 7, 1491-1496.

Moran, M. S., and Bryant, R. (2001). A refined empirical line approach for reflectance factor retrieval from Landsat-5 TM and Landsat-7 ETM+. *Remote Sensing of Environment, 78,* 71-82.

Moran, M.S., Jackson, D., Slate, P.N., and Teillet, P.M. (1992). Evaluation of simplified procedures for retrieval of land surface reflectance factors from satellite sensor output. *Remote sensing of Environment, 41,* 169-184.

Morillo-Contreras, S., Vélez-Reyes, M., and Hunt, S.D. (2004). Effects of Resolution Enhancement and Atmospheric Correction Pre-Processing in Classification of Hyperspectral Imager. In *Algorithms and Technologies Miguel Vélez-Reyes, for Multispectral, Hyperspectral, and Ultraspectral Imagery X, Proceedings of SPIE Vol. 5425.*

Munday, J.C.M. (1983). Chromaticity of path radiance and atmospheric correction of Landsat data. *Remote Sensing of Environment*, *13,* 525-538.

Neckel, H., and Labs, D. (1984). The solar radiation between 3300 and 12500 nm, *Solar Physics, 90,* 250-258.

Nisantzi A., Hadjimitsis D.G., and Alexakis D. (2011). Estimating the relationship between aerosol optical thickness and PM10 using lidar and meteorological data in Limassol,

Cyprus. Proceedings Vol. 8182, SPIE Remote Sensing 2011, Prague, Czech Republic (2011) DOI: 10.1117/12.898357.

North, P., Grey, W., Heckel, A., Fischer, J., Preusker, R., and Brockmann, C. (2009). MERIS/AATSR synergy algorithms for cloud screening, aerosol retrieval and atmospheric correction. Synergy-Aerosol and Land Surface

Novack, K. (1992). Rectification of digital imagery, *Photogrammetric Engineering and Remote Sensing, 58* (3), 339-344.

Nunes, A. and Marçal A.R.S. (2004). Atmospheric correction of high resolution multi-spectral satellite images using a simplified method based on the 6S code, *Proceedings of the 4th Remote Sensing and Photogrammetry Society Annual Conference - "Mapping and Resources Management",* Aberdeen, Scotland, UK, CD-ROM.

O'Neill, S., Tsay, C., Ji, Q., Schafer, J. S., Sorokine, M., Newcomb, W., and Slutsker, I. (2008). Spatial and temporal variability of column integrated aerosol optical properties in the southern Arabian Gulf and United Arab Emirates in summer, *Journal of Geophysical Research,113,* D01204, doi:10.1029/2007JD008944.

Oliver, M.A. (1990). Kriging: A Method of Interpolation for Geographical Information Systems, *International Journal of Geographic Information Systems, 4,* 313-332.

Ormeci, O. and Ekercin, S. (2008). Use of real-time remote sensing data for evaluating soil moisture and salinity effects on light penetration depth. *International Society For Photogrammetry and Remote Sensing XXI Congress 3-11 July 2008.* Beijing, China, Proceedings Vol. XXXVII, Part B2-1, Chen, J. , Jiang, J. Boudoin, A., 167-174.

Othman, N., MatJafri, M.Z., Lim, H.S., and Abdullah, K. (2009). Retrieval of aerosol optical thickness (AOT) and its relativity to air pollution particulate matter (PM10). CGIV'09, Sixth International Conference on Computer Graphics Imagery and Visualization. doi: 10.1109/CGIV.2009.22.

Ouillon, S., Lucas, Y, Gaggelli, J. (2002). Hyperspectral detection of sand. *Presentation at the Seventh International Conference on remote sensing and coastal environments*. Miami Florida, May 20-22, 2002.

Paronis, D. and Sifakis, N.I. (2003). Satellite aerosol optical thickness retrieval over land with contrast reduction analysis using a variable window size. *Geoscience and Remote Sensing Symposium, IGARSS Proceedings, IEEE, Intl 2,* 1276-1278.

Penner, J. E., and Coauthors, (2001). Aerosols, their direct and indirect effects. *Climate Change 2001: The Scientific Basis,* J. T. Houghton, et al., Eds., Cambridge University Press, 289–348.

Philpot, W. (2010). Spectral Reflectance of Wetted Soils. *Proceedings of ASD and IEEE GRS; Art, Science and Applications of Reflectance Spectroscopy Symposium*, Vol. II.

Pincus, R., and Evans, K. F. (2009). Computational cost and accuracy in calculating three dimensional radiative transfer: Results for new implementations of Monte Carlo and SHDOM. *Journal of Atmospheric Science, 66,* 3131–3146.

Potter, J.F., and Mendolowitz, M. (1975). On the determination of the haze levels from Landsat data. *10th International Symposium on Remote Sensing of Environment. Ann Arbor, MI, Environmental Research Institute of Michiga*n (Ann Arbor, MI: ERIM), 695-703.

Press, W.H. (1988). *Numerical Recipes in C, The Art of Scientific Computing,* New York: Cambridge University Press.

Price J.C., Anger, C.D., and Mah, S. (1995). Preliminary evaluation of casi pre-processing techniques. In *Proceedings of the 17th Canadian Symposium on Remote Sensing,* 694-697.

Prospero, J.M., Ginoux, P., Torres, O., Nicholson, S., and Gill, T. (2002). Environmental Characterization of Global Sources of Atmospheric Soil Dust Identified with the NIMBUS7 Total Ozone Mapping Spectrometer (TOMS) Absorbing Aerosol Product, *Review of Geophysics*, *40*, 1, 1002, doi:10.1029/2000RG000095.

Quaife, T, and Bransley, M. (1999a). Comparison of SMAC and 6S for atmospheric correction of multi-angle image data sets. *Earth Observations from Data to Information, Proceedings of the 25th Annual Conference and Exhibition of the RSS University of Wales and Swansea* (Nottingham, UK: Remote Sensing Society) 811-818.

Radke, L. F., Hegg, D. A. Hobbs, P. V. Nance, J. D. Lyons, J. H. Laursen, K. K. Weiss, R. E. Riggan, P. J. and Ward, D. E. (1991). *Particulate and trace gas emissions from large biomass fires in North America*. In Global Biomass Burning: Atmospheric, Climate and Biospheric Implications, ed. J. S. Levine, pp. 209-224, MIT Press, Cambridge, MA.

Rahman, H. and Dedieu, G. (1994). SMAC: a simplified method for atmospheric correction of satellite measurements in the solar spectrum. *International Journal of Remote Sensing*, 15, 123-143.

Raju, P.L.N. (2003). The fundamentals of Geographical Information Systems. Satellite Remote Sensing and GIS applications in Agricultural Meteorology, 103-120.

Remer, L., Kaufman, Y., Tanré, D., Mattoo, S., Chu, D., Martins, J., Li, R., Ichoku, C., Levy, R., Kleidman, R., Eck, T., Vermote, E., and Holben, B. (2005). MODIS aerosol algorithm, products and validation. *Journal of Atmospheric Science, 62,* 947-973.

Retalis, A,, Hadjimitsis, D.G., Michaelides, S., Tymvios, F., Chrysoulakis, N., Toulios, L., Clayton, C.R.I., and Themistocleous, K. (2010). Comparisons of aerosol optical thickness with in-situ visibility data over Cyprus. *Natural Hazards Earth System Science, 10* (3) 421-428.

Retalis A., Sifakis N., Grosso N. and Paronis D. (2003). Aerosol optical thickness retrieval from AVHRR images over the Athens urban area. *In Proceedings of IEEE International Geoscience and Remote Sensing Symposium (IGARSS) 2003*, vol. 4, 2182-2184, doi: 10.1109/IGARSS.2003.1294381

Retalis A., Cartalis C., and Athanassiou E. (1999). Assessment of the distribution of aerosols in the area of Athens with the use of LANDSAT Thematic Mapper data. *International Journal of Remote Sensing*, 20 (5), 939-945.

Richards, JA. (2005). *Remote Sensing Digital Image Analysis: An introduction.* 4th edition, Springler-Verlag: Berlin.

Richter, R. (1990) A fast atmospheric correction algorithm applied to Landsat TM images, *International Journal of Remote Sensing, 11* (1), 159-166.

Richter, R. (1996). A spatially adaptive fast atmospheric correction algorithm. *International Journal of Remote Sensing*, 11, pp. 159-166.

Richter, R. (2009). *Atmospheric / Topographic Correction for Airborne Imagery* (ATCOR-4 User Guide, Version 5.0). DLR-IB 565-02/09, 145.

Roder, A., Kuemmerle, T., and Hill, J. (2005). Extension of retrospective datasets using multiple sensors. An approach to radiometric intercalibration of Landsat TM and MSS data. *Remote Sensing of Environment, 95,* (2), 195-210

Rollin, E.M. and Milton, E.J., (1998). Processing of high spectral resolution reflectance data for the retrieval of canopy water content information. *Remote Sensing of Environment, 65,* 86-92.

Royle, A.G., Clausen, F.L. and Frederiksen, P. (1981). Practical Universal Kriging and Automatic Contouring, *Geoprocessing, 1,* 377-394.

Sabins, F.F. (1987). *Remote Sensing Principles and Interpretation.* New York: W.H. Freeman and Co.

Schott J.R. (2007). *Remote Sensing: The image chain approach*. Oxford, UK: Oxford University Press.

Schott, J.R., Salvaggio, C., and Wolchock, W.J. (1988). Radiometric scene normalisation using pseudo-invariant features. *Remote Sensing of Environment*, *26,* 1–16.

Schowengerdt, R.A. (2007). *Remote Sensing, 3rd edition.* New York City, New York, USA: Academic Press.

Schuman, R.A., and Rea, D.K. (1981). Determination of beach sand parameters using remotely sensed aircraft reflectance data. *Remote Sensing Of Environment*, II, 295-310.

Schroeder, T.A., Cohen, W.B., Song, C., Canty, M.J., and Yang, Z. (2006). Radiometric correction of multi-temporal Landsat data for characterization of early successional forest patterns in western Oregon. *Remote Sensing of Environment*. *103,* 16-26

Seidel, F., Schlapfer, D., Nieke, J., and Itten, K.I. (2008). Sensor Performance Requirements for the Retrieval of Atmospheric Aerosols by Airborne Optical Remote Sensing, *Sensors* 2008, *8*, 1901-1914.

Sifakis, N., and Deschamps, P.Y. (1992). Mapping of air pollution using SPOT satellite data, *Photogrammetric Engineering and Remote Sensing, 58,* 1433-1437.

Sifakis, N., Soulakellis, N., and Paronis, D. (1998). Quantitative mapping of air pollution density using Earth observations: a new processing method and application to an urban area. *International Journal of Remote Sensing 19* (17), 3289–3300.

Sinyuk, A., Dubovik O., Holben, B., Eck, T., Breon, F., Martonchik, J., Kahn, R, Diner, D J, Vermote, E F, Roger J, Lapyonok T, and Slutsker I. (2007). Simultaneous retrieval of aerosol and surface properties from a combination of AERONET and satellite data. *Remote Sensing of Environment, 107* (1-2), 90-108.

Slater, P.N.(1980). *Remote sensing optics and optical systems.* Reading, Massachusetts, USA: Addison-Wesley Publishing.

Slater, P.N., Biggar, S.F., Holm, R.G., Jackson, R.D., Mao, Y., Moran, M.S., Palmer, M., and Yuan, B. (1986). Absolute radiometric calibration of the Thematic Mapper, *SPIE, 660,* 2-8.

Slater, P.N., Biggar, S.F., Holm, R.G., Jackson, R.D., Mao, Y., Moran, M.S., Palmer, M., and Yuan, B. (1987) Reflectance- and radiance-based methods for the in-flight absolute calibration of multi-spectral sensors. *Remote Sensing of Environment, 22,* 11-37.

Smith, G.M. and Milton, E.J. (1999). The use of the empirical line method to calibrate remotely sensed data to reflectance. *International Journal of Remote Sensing, 20,* 2653-2662.

Smirnov, A., Holben, B.N., Eck, T.F., Dubovik, O., and Slutsker, I. (2000). Cloud screening and quality control algorithms for the AERONET database. *Remote Sensing of Environment, 73,* 337-349.

Song, C., and Woodcock, C. E. (2003). Monitoring forest succession with multitemporal Landsat images: Factors of uncertainty. *IEEE Transactions on Geoscience and Remote Sensing, 41*(11), 2557−2567.

Soufflet, V., Tanré, D. Royer, A. and O'Neill, N. T. (1997). Remote sensing of aerosols over boreal forest and lake water from AVHRR data. *Remote Sensing of Environment*, 60, 22-34.

Soulakellis N., Kousoulakou A., Sarafidis D., Sifakis N., Sarigiannis D. (2002). *Synergistic use of GIS and satellite remote sensing data in urban air pollution mapping.* Workshop on Social practices and spatial information: European and Greek experience in using GIS, 27-28 June 2002, Thessaloniki, Greece, 9 p.

Soulakellis N., and Sifakis N. (1997). *Mapping airborne pollution with Landsat TM satellite imagery and spatial analysis with GIS.* Proceedings of the 4th National Conference in Cartography: Cartography and Mapping in Environmental Protection, 16-17 October 1997, Kastoria, Greece.

Stow, D., Hope, A., Hgugen, A.T., Phinn, S., and Benkelman, C.A. (1996) Monitoring detailed land surface changes using an airborne multi-spectral digital camera system. *IEE transactions in Geo-science and Remote Sensing, 34,* 1191-1203.

Switzer, P., Kowalik, W.S., and Lyon, R.J.P. (1981). Estimation of atmospheric path radiance by the Covariance Matrix method. *Photogrammetric Engineering and Remote Sensing*, *47,* 1469-1476.

Tan F., Lim H.S., Mat Jafri, M.Z. and Abdullah K. (2011). Aerosol Optical Thickness and PM10 Study by Using a Handheld Spectroradiometer Over Penang, Monitoring, Control and Effects of Air Pollution, Andrzej G. Chmielewski (Ed.), ISBN: 978-953-307-526-6, InTech, Available from: http://www.intechopen.com/articles/show/title/aerosol-optical-thickness-and-pm10-study-by-using-a-handheld-spectroradiometer-over-penang

Tang, J., Xue, T., Yuc, T., Guen, Y.N. (2005). Aerosol optical thickness determination by exploiting the synergy of TERRRA and AQUA MODIS. *Remote Sensing and Environment, 94,* 327-334.

Tanre, D., P. Y. Deschamps, C. Devaux, and M. Herman (1988). Estimation of Saharan aerosol optical thickness from blurring effects in thematic mapperd data. *Journal of Geophysical Research,93*, 15,955-964.

Tanré, D., Deroo, C., Dahaut, P., Herman, M., and Morcrette, J.J. (1990). Description of a computer code to simulate the satellite signal in the solar spectrum: the 5S code, *International Journal of Remote Sensing, 11,* 659-688.

Tanré D., Y. Kaufman, M. Herman, and S. Mattoo, (1997). Remote sensing of aerosol properties over oceans using the MODIS/EOS spectral radiances. *Journal of Geophysical Research*, *102,* 16971-16988.

Tanré, D., Remer L. A., Kaufman Y. J., Mattoo S., Hobbs P. V., Livingston J. M., Russell P. B, and Smirnov A., (1999). Retrieval of aerosol optical thickness and size distribution over ocean from the MODIS Airborne Simulator during TARFOX. *Journal of Geophysical Research, 104*, 2261-2278.

Tassan, S. (1992). An algorithm for the identification of benhtic algae in the Venice lagoon from Thematic Mapper data, *International Journal of Remote Sensing, 13 (15),* 2887-2909.

Teillet, P.M. (1992). An algorithm for the radiometric and atmospheric correction of AVHRR data in the solar reflective channels, *Remote sensing of Environment, 41,* 185-195.

Teillet, P.M. and Fedosejevs (1995). *On the dark target approach to atmospheric correction of remotely sensed data*, Canadian Journal of Remote Sensing, 21(4), 375-381.

Themistocleous, K., Hadjimitsis, D.G., and Alexakis, D. (2011). *Fast atmospheric correction algorithm based on the darkest pixel approach for retrieving the aerosol optical thickness: comparison with in-situ AOT measurements.* In: CD-ROM of Proceedings of SPIE 8177, 81770B (2011); 20-23 September, Prague, Czech Republic, doi:10.1117/12.898593.

Thomas, C., Doz, S., Briottet, X., and Lacherade, S. (2011). AMARTIS v2: 3D radiative transfer code in the (0.4;2.5µm) spectral domain dedicated to urban areas. *Remote Sensing, 3,* 1914-1942.

Thomas, G. B.. and Finney, R. L. (1996). *Calculus and Analytic Geometry (9th ed.)*, Chicago, IL:Addison Wesley Publishing.

Thomas, G.E. and Stamnes, K. (1999). *Radiative Transfer in the Atmosphere and Ocean*. Cambridge: Cambridge University Press.

Toril, K., Mase, T., and Hoshi, T. (1995). Effects of atmospheric correction on satellite image data by Lowtran model. http://www.geospatialworld.net/index.php?option =com_contentandview=articleandid=14467andcatid=89%3Atechnology-image-processingandItemid=50. Accessed 29/7/2010.

Twomey, S.A., Bohren, C.F., Mergenthaler, J.L., (1986). Reflectances and albedo diferences between wet and dry surfaces. *Applied Optics, 25,* 431-437.

Tulloch, M. and Li, J. (2004). Applications of satellite remote sensing to urban air-quality monitoring: status and potential solutions to Canada. *Environ Inform Arch,* 2, 846–854.

Turner. R. E., Malila W. A. and Nalepka, R. F. (1971). Importance o-f atmospheric scattering in remote sensing, or everything you've always wanted to know about atmospheric scattering but were afraid to ask. *Proc. of the Seventh International Symposium on Remote Sensing of Environment III: 16 51-1697.*

Turner, R. E. (1975). *Atmospheric effects in multispectral remote sensor data.* Contract No. NAS9-14123. Final Report 109600-15-F. 5-15-74 to 3-14-75.

Turner, R.E., and Spencer, M.M. (1972). Atmospheric model for correction of spacecraft data. In *Proceedings of the Eight International Symposium on Remote Sensing of the Environment, II.* Michigan. Ann Arbor; 895-934.

Tyagi, P. and Bhosle, U. (2010). Image Based Atmospheric Correction of Remotely Sensed Images", In *Proceedings of International Conference on Computer Applications and Industrial Applications (ICCAIE2010), Institution of Electrical and Electronics(IEEE)*, Kuala Lumpur, Malasyia, Pages 56 -61.

van Der Meer, F. (1994). Extraction of mineral absorption features from high-spectral resolution data using non-parametric geo-statistical techniques. *International Journal of Remote Sensing, 15,* 2193-2214.

Vermote, E. F., El Saleous, N. Z., and Justice, C. O. (2002). Operational atmospheric correction of the MODIS data in the visible to middle infrared: first results. *Remote Sensing of Environment, 83* (1), 97-111.

Vermote, E. (1996). *Atmospheric Correction Algorithm: Spectral Reflectances (MOD09),* Algorithm Technical Background Document, NASA5-96062.

Vermote, E.F., Tanré, D, Deuze, J.L., Herman, M., and Morcrette, J.J. (1997) Second Simulation of the Satellite Signal in the Solar Spectrum, 6S: An overview, *IEEE. Transactions in Geoscience Remote Sensing. GE-35,* 675–686.

Volchok, W.J., and Schott, J.R. (1986). Scene to scene radiometric normalization of the reflected bands of the Landsat Thematic Mapper. In *Proceedings of the SPIE Symposium, Earth Remote Sensing Using the Landsat Thematic Mapper and Spot Sensor Systems.* Innsbruck Austria, vol. 660 (ed. PN Slater). Bellingham, WA: The International Society for Optical Engineering, 9-17.

Waggoner, A.P., Weiss, R.E., Ahlquist, N.C., Covert, D.S., Wills, S., and Charlson, R.J. (1981). Optical characteristics of atmospheric aerosols. *Atmospheric Environment, 15,* 1891-1909.

Wald, L., Basly, L., and Balleynaud, J.M. (1999). Satellite data for the air pollution mapping, Proceedings of the 18th EARseL symposium on operational sensing for sustainable development (Enschede, Netherlands, 11-14 May 1998), In: *Operational*

Remote Sensing for Sustainable Development (edited by Nieeuwenhuis, G.J.A, Vaugham, R.A., Molenaar, M.), 133-139.

Wang, Y. Q., Traber, M., Milstead, B., and Stevers, S. (2007). Terrestrial and submerged aquatic vegetation mapping in Fire Island National Seashore using high spatial resolution remote sensing data. *Marine Geodesy, 30,* 77−95.

Wang, M. and Gordon, H.R. (1993). Retrieval of the columnar aerosol phase function and single scattering albedo from sky radiance over the ocean: simulations. *Applied Optics, 32*, 4598-4609.

Wang. J., and Christopher, S.A. (2003). Intercomparison between satellite derived aerosol optical thickness and PM 2.5 mass: implications for air quality studies. *Geophysical Research Letters, 30* (21), 2095.

Wehrli, C.J. (2008). *Remote sensing of aerosol optical depth in a global surface network.* Ph.D. Dissertation. ETH Werhli, Werhli, Switzerland.

Wen, G., Cahalan, R. F., Tsay, S. C. and Oreopoulos, L. (1999). *Aerosol Optical Thickness Retrieval from Landsat TM Image over SGP Site of the ARM Program.* Ninth ARM Science Team Meeting Proceedings, San Antonio, Texas, March 22-26, 1999.

Weng, Q. (2010). Remote sensing and GIS integration: theories, methods and applications. New York, NY: McGraw-Hill.

Whiting, M.L., Li, L., Ustin, S.L., (2003). Estimating surface soil moisture in simulated AVIRIS spectra. Twelfth Annual Airborne Earth Science and Application Workshop. Jet Propulsion Laboratory, California Institute of Technology, Pasadena, California, February 25-28.

Wilhelmi, O., Betancourt, T., Boehnert, J. Shipley, S. and Breman, J. (2009). ArcGIS atmospheric data model. Accessed 1/12/2011, www.gisand science.com/2009/06/030/atmospheric_data_model_for_arcgis.

Wilson, A.K. (1988) The critical dependence of remote sensing on sensor calibration and atmosphere transparency, In: *Proceedings of the NERC 1987 Airborne Campaign Workshop, NERC, Swindon-UK*, 29-58.

Wilson, R.T. and Milton, E.J. (2010). Automated selection of suitable atmospheric calibration sites for satellite imagery. *Proceedings of the RSPSoc Annual Conference*.

Wong M.S., Nichol, J.E., and Lee, K.H (2009) Modeling of Aerosol Vertical Profiles Using GIS and Remote Sensing. *Sensors, 9*, 4380-4389.

Wu, J.,Wang, D., and Bauer, M E. (2005) Image-based atmospheric correction of QuickBird imagery of Minnesota cropland *Remote Sensing of Environment, 99,* 315 – 325.

Xue, Y., Wan W., Li, Y.J., Guang, J., Bai, L.Y., Wang Y. and Ai, J.W. (2008). A Data Intensive Scientific Computing Framework for Quantitative Retrieval of Geophysical Parameters using Satellite Data, *IEEE Computer*, Vol. 41(4), 33-40.

Yahi, H., Santer, R., Weill, A., Crepin, M. and Thiria, S. (2010). Exploratory study for estimating atmospherically low level particle pollution based on vertical integrated optical measurements. *Atmospheric Environment, 45,* 3891-3902.

Yu, H., Dickinson, R., Chin, M., Kaufman, Y., Zhou, M., Zhou, L., Tian, Y., Dubovik, O., and Holben, B., (2004). The direct radiative effect of aerosols as determined from a combination of MODIS retrievals and GOCART simulations. *Journal of. Geophysical Research, 109*.D03206, doi:10.1029/2003JD003914.

Yu, H., Kaufman, Y., Chin, M., Feingold, G., Remer, L., Anderson, T., Balkanski, Y., Bellouin, N., Boucher, O., Christopher, S., DeCola, P., Kahn, R., Koch, D., Loeb, N., Reddy, M. S., Schulz, M., Takemura, T., and Zhou, M. (2006). A review of measurement-based assessments of aerosol direct radiative effect and forcing. *Atmospheric Chemistry and Physics. 6,* 613-666.

Yuan, D. and Elvidge C.D. (1996). Comparison of relative radiometric normalization techniques. *ISPRS Journal of Photometry and Remote Sensing*, 51, 117-126.

Yuen, P. and Bishop, G. (2004). Adaptive Feature Extraction Techniques for Subpixel Target Detections in Hyperspectral Remote Sensing. *SPIE proceeding: Military remote sensing,* 5613 99-110.

Yuen, P., Killey, A., Hobson, S., and Bishop, G. (2004). Atmospheric correction preprocessing techniques in hyperspectral remote sensing. *1st EMRS DTC Technical conference*.

Zhou, Q. (1995). The integration of GIS and remote sensing for land resource and environment management. In Proceedings of United Nations ESCAP Workshop on Remote Sensing and GIS for Land and Marine Resources and Environment Management, 13-17 February, Sura, Fiji, 43-55.

APPENDICES

This part consists the following appencides:

Appendix 1

- SVC spectroradiometric in-situ measurements, wet and dry measurements
- Radiance values at-satellite before atmospheric correction
- Reflectance values at-satellite before atmospheric correction
- RSR example

Appendix 2

- Microtops Sun photometer measurements
- Cimel Sun photometer measurements
- Single Scattering Albedo, derived from AERONET
- Phase function

Appendix 3

- Earth-Date correction table
- Log sheet for Microtops Sun-photometer field campaign

Appendix 1

- SVC spectroradiometric in-situ measurements, wet and dry measurements
- Radiance values at-satellite before atmospheric correction
- Reflectance values at-satellite before atmospheric correction
- RSR example

SVC spectroradiometric in-situ measurements

	BAND1				BAND2			
DATE	**Min**	**Max**	**Average**	**SD**	**Min**	**Max**	**Average**	**SD**
19/03/10	11.82	13.78	12.80	0.98	13.26	15.76	14.51	1.25
20/03/10	11.24	13.65	12.44	1.21	12.64	15.53	14.08	1.44
22/03/10	10.69	12.28	11.49	0.79	12.06	14.02	13.04	0.98
23/03/10	11.81	13.46	12.63	0.82	13.28	15.24	14.26	0.98
22/04/10	10.69	12.28	11.49	0.79	12.06	14.02	13.04	0.98
23/04/10	10.66	11.51	11.08	0.42	11.92	12.74	12.33	0.41
26/04/10	10.92	12.87	11.89	0.98	12.29	14.79	13.54	1.25
09/12/10	11.04	12.05	11.55	0.51	12.49	13.54	13.01	0.53
average	**11.11**	**12.74**	**11.92**	**0.81**	**12.50**	**14.45**	**13.48**	**0.98**

	BAND3				BAND4			
DATE	**Min**	**Max**	**Average**	**SD**	**Min**	**Max**	**Average**	**SD**
19/03/10	14.09	16.84	15.47	1.38	15.58	18.53	17.06	1.48
20/03/10	13.55	16.52	15.03	1.48	15.45	18.28	16.86	1.41
22/03/10	12.68	15.02	13.85	1.17	13.96	16.84	15.40	1.44
23/03/10	14.17	16.08	15.13	0.96	15.92	17.64	16.78	0.86
22/04/10	12.68	15.02	13.85	1.17	13.96	16.84	15.40	1.44
23/04/10	12.57	14.25	13.41	0.84	13.89	14.49	14.19	0.30
26/04/10	12.96	16.01	14.48	1.525	14.40	18.09	16.25	1.85
09/12/10	13.30	14.46	13.88	0.582	15.02	20.28	17.65	2.63
average	**13.25**	**15.53**	**14.39**	**1.137**	**14.77**	**17.62**	**16.20**	**1.43**

Appendix 1 Table 1 Gray Asphalt SVC HR 1024 In-situ measurements Bands 1-4, wet

	BAND1				BAND2			
DATE	**Min**	**Max**	**Average**	**SD**	**Min**	**Max**	**Average**	**SD**
16/2/2010	11.28	12.78	12.03	0.75	12.85	14.63	13.74	0.89
24/2/2010	11.47	12.85	12.16	0.69	12.91	14.65	13.78	0.87
3/3/2010	12.72	12.75	12.73	0.02	14.33	14.54	14.43	0.10
4/3/2010	10.69	12.98	11.84	1.14	11.94	14.74	13.34	1.40
9/3/2010	9.49	12.23	10.86	1.37	10.71	13.93	12.32	1.61
10/3/2010	10.64	12.42	11.53	0.89	12.05	14.04	13.05	1.00
12/3/2010	11.35	13.21	12.28	0.93	12.93	15.18	14.05	1.12
15/3/2010	12.73	14.69	13.71	0.98	14.54	17.02	15.78	1.24
17/3/2010	9.98	12.66	11.32	1.34	11.18	14.24	12.71	1.53
4/4/2010	9.40	11.97	10.68	1.28	10.53	13.48	12.00	1.48
13/4/2010	11.07	13.55	12.31	1.24	12.52	15.69	14.10	1.59
19/4/2010	10.62	12.32	11.47	0.85	12.01	13.96	12.98	0.98
27/4/2010	11.00	12.56	11.78	0.78	12.24	14.24	13.24	1.00
28/4/2010	10.69	12.28	11.49	0.79	12.06	14.02	13.04	0.98
29/4/2010	8.46	12.55	10.51	2.04	9.14	14.17	11.65	2.52
30/4/2010	10.60	13.00	11.80	1.20	11.95	14.89	13.42	1.47
10/5/2010	10.99	13.24	12.12	1.13	12.38	14.97	13.67	1.29
31/5/2010	10.69	12.28	11.49	0.79	12.06	14.02	13.04	0.98
24/6/2010	11.32	14.96	13.14	1.82	12.77	17.27	15.02	2.25
10/7/2010	11.05	13.40	12.23	1.18	12.48	15.49	13.99	1.50
27/8/2010	10.91	14.96	12.94	2.03	12.42	14.75	13.59	1.16
28/9/2010	11.24	12.78	12.01	0.77	12.82	14.87	13.84	1.02
average	**10.84**	**13.02**	**11.93**	**1.09**	**12.22**	**14.76**	**13.49**	**1.27**

	BAND3				BAND4			
DATE	**Min**	**Max**	**Average**	**SD**	**Min**	**Max**	**Average**	**SD**
16/2/2010	13.72	15.67	14.70	0.97	15.60	17.73	16.66	1.07
24/2/2010	13.52	15.76	14.64	1.12	14.83	17.78	16.31	1.47
3/3/2010	13.24	15.67	14.45	1.22	17.19	17.99	17.59	0.40
4/3/2010	14.50	15.85	15.18	0.68	13.90	17.88	15.89	1.99
9/3/2010	11.42	14.92	13.17	1.75	14.76	16.56	15.66	0.90
10/3/2010	12.84	15.00	13.92	1.08	14.36	16.63	15.50	1.14
12/3/2010	13.89	16.26	15.08	1.18	15.56	18.20	16.88	1.32
15/3/2010	15.60	18.57	17.08	1.48	17.63	21.09	19.36	1.73
17/3/2010	11.86	15.03	13.44	1.58	13.07	16.46	14.76	1.69
4/4/2010	11.14	14.42	12.78	1.64	12.43	16.08	14.25	1.83
13/4/2010	13.22	16.86	15.04	1.82	14.48	18.93	16.70	2.22
19/4/2010	12.79	14.70	13.74	0.96	14.18	16.09	15.14	0.96
27/4/2010	12.79	15.25	14.02	1.23	14.05	17.03	15.54	1.49
28/4/2010	12.68	15.02	13.85	1.17	13.96	16.84	15.40	1.44
29/4/2010	11.34	15.09	13.21	1.88	13.00	16.80	14.90	1.90
30/4/2010	12.74	16.13	14.44	1.69	14.28	18.24	16.26	1.98
10/5/2010	14.02	15.83	14.92	0.91	14.23	17.49	15.86	1.63
31/5/2010	12.68	15.02	13.85	1.17	13.96	16.84	15.40	1.44
24/6/2010	13.59	18.67	16.13	2.54	14.96	20.74	17.85	2.89

10/7/2010	13.26	16.84	15.05	1.79	14.61	18.79	16.70	2.09
27/8/2010	13.88	17.81	15.84	1.96	15.41	20.49	17.95	2.54
28/9/2010	13.67	18.21	15.94	2.27	15.10	20.10	17.60	2.50
average	**13.11**	**16.03**	**14.57**	**1.46**	**14.62**	**17.94**	**16.28**	**1.66**

Appendix 1 Table 2 Gray Asphalt SVC HR 1024 In-situ measurements Bands 1-4, dry

	BAND1				BAND2			
DATE	Min	Max	Average	SD	Min	Max	Average	SD
19/03/10	10.35	11.42	10.89	0.54	11.79	12.93	12.36	0.57
22/03/10	10.19	11.33	10.76	0.57	11.58	13.03	12.30	0.73
20/04/10	10.61	11.39	11.00	0.39	12.20	13.19	12.69	0.49
21/04/10	9.62	11.77	10.69	1.07	11.19	13.56	12.37	1.18
23/04/10	10.06	12.10	11.08	1.02	11.66	13.88	12.77	1.11
09/12/10	10.58	12.01	11.30	0.71	12.08	13.78	12.93	0.85
average	**10.23**	**11.67**	**10.95**	**0.72**	**11.75**	**13.39**	**12.57**	**0.822**

	BAND3				**BAND4**			
DATE	**Min**	**Max**	**Average**	**SD**	**Min**	**Max**	**Average**	**SD**
19/03/10	12.63	13.73	13.18	0.55	14.27	15.35	14.81	0.54
22/03/10	12.46	13.85	13.15	0.69	14.19	15.43	14.81	0.62
20/04/10	13.17	14.24	13.71	0.54	15.07	16.14	15.60	0.54
21/04/10	12.25	14.58	13.41	1.17	14.28	16.57	15.43	1.15
23/04/10	12.74	14.86	13.80	1.06	14.85	16.89	15.87	1.02
09/12/10	13.20	14.95	14.07	0.87	15.20	16.44	15.82	0.62
average	**12.74**	**14.37**	**13.55**	**0.81**	**14.643**	**16.14**	**15.39**	**0.75**

Appendix 1 Table 3 Black Asphalt SVC HR 1024 In-situ measurements Bands 1-4, wet

	BAND1				BAND2			
DATE	**Min**	**Max**	**Average**	**SD**	**Min**	**Max**	**Average**	**SD**
07/11/10	8.83	10.86	9.84	1.01	10.21	12.54	11.37	1.17
03/03/10	8.74	10.20	9.47	0.73	9.89	11.78	10.84	0.94
04/03/10	8.98	11.25	10.12	1.14	10.21	12.76	11.48	1.27
09/03/10	9.82	11.06	10.44	0.62	11.36	12.68	12.02	0.66
10/03/10	9.67	11.28	10.48	0.80	11.09	12.82	11.95	0.87
12/03/10	8.14	10.80	9.47	1.33	9.48	12.53	11.01	1.53
15/03/10	9.41	10.16	9.78	0.38	11.02	11.76	11.39	0.37
17/03/10	9.55	10.54	10.05	0.49	10.84	12.03	11.43	0.59
04/04/10	8.99	11.00	9.99	1.01	10.28	12.55	11.42	1.13
13/04/10	9.83	11.36	10.59	0.77	11.39	13.03	12.21	0.82
19/04/10	9.49	10.93	10.21	0.72	10.92	12.50	11.71	0.79
26/4/2010	9.41	10.76	10.08	0.68	10.90	12.35	11.63	0.72
27/04/10	10.37	11.79	11.08	0.71	10.99	13.55	12.27	1.28
28/04/10	9.08	11.64	10.36	1.28	10.56	13.38	11.97	1.41
07/05/10	8.86	11.15	10.00	1.15	10.20	12.75	11.48	1.27
31/05/10	9.35	10.85	10.10	0.75	10.90	11.97	11.44	0.54
16/06/10	10.05	11.56	10.81	0.75	11.64	13.35	12.49	0.85
24/06/10	9.99	11.72	10.85	0.87	11.65	13.63	12.64	0.99
10/07/10	10.18	11.72	10.95	0.77	11.77	13.47	12.62	0.85
27/08/10	8.90	11.40	10.15	1.25	10.89	12.29	11.59	0.70
28/9/2010	8.86	11.75	10.31	1.45	10.78	13.22	12.00	1.22
average	**9.36**	**11.13**	**10.25**	**0.89**	**10.81**	**12.71**	**11.76**	**0.95**

	BAND3				BAND4			
DATE	**Min**	**Max**	**Average**	**SD**	**Min**	**Max**	**Average**	**SD**
07/11/10	11.39	13.79	12.59	1.20	14.13	16.49	15.31	1.18
03/03/10	10.64	12.67	11.66	1.01	12.35	14.53	13.44	1.09
04/03/10	11.03	13.67	12.35	1.32	12.71	15.49	14.10	1.39
09/03/10	12.58	13.70	13.14	0.56	13.88	15.89	14.89	1.01
10/03/10	12.04	13.68	12.86	0.82	13.88	15.43	14.66	0.77
12/03/10	10.56	13.76	12.16	1.60	13.76	15.49	14.62	0.87
15/03/10	12.26	12.95	12.60	0.35	14.66	15.16	14.91	0.25
17/03/10	11.66	13.00	12.33	0.67	13.37	14.91	14.14	0.77
04/04/10	11.29	13.35	12.32	1.03	13.34	14.99	14.16	0.82
13/04/10	12.40	14.02	13.21	0.81	14.37	16.01	15.19	0.82
19/04/10	11.87	13.36	12.62	0.74	13.75	15.80	14.77	1.02
26/4/2010	12.00	13.39	12.69	0.69	14.15	15.39	14.77	0.62
27/04/10	13.23	14.59	13.91	0.68	15.54	16.63	16.08	0.55
28/04/10	11.88	14.41	13.15	1.26	14.45	16.30	15.37	0.92
07/05/10	11.36	13.62	12.49	1.13	13.64	15.40	14.52	0.88
31/05/10	12.13	12.27	12.20	0.07	14.50	14.69	14.60	0.09
16/06/10	12.75	14.52	13.63	0.89	14.56	16.48	15.52	0.96
24/06/10	13.00	14.95	13.98	0.98	15.18	17.22	16.20	1.02
10/07/10	12.96	14.54	13.75	0.79	15.11	16.34	15.72	0.62
27/08/10	11.97	14.67	13.32	1.35	14.64	16.59	15.62	0.97
28/9/2010	11.68	14.94	13.31	1.63	15.00	16.21	15.61	0.60
average	**11.94**	**13.80**	**12.87**	**0.93**	**14.14**	**15.78**	**14.96**	**0.82**

Appendix 1 Table 4 Black Asphalt SVC HR 1024 In-situ measurements Bands 1-4, dry

	BAND1				BAND2			
DATE	Min	Max	Average	SD	Min	Max	Average	SD
26/02/10	14.42	15.77	15.10	0.67	19.18	19.32	19.25	0.07
19/03/10	15.76	17.01	16.38	0.62	19.44	21.22	20.33	0.89
22/03/10	14.89	15.71	15.30	0.41	18.24	19.59	18.91	0.67
23/03/10	15.46	16.91	16.18	0.73	19.11	20.60	19.86	0.74
20/04/10	16.13	17.44	16.78	0.66	20.29	21.75	21.02	0.73
21/04/10	15.35	15.59	15.47	0.12	19.33	19.62	19.47	0.14
22/04/10	14.98	16.96	15.97	0.99	19.34	21.00	20.17	0.83
23/04/10	16.68	17.98	17.33	0.65	20.96	22.19	21.57	0.62
26/04/10	15.04	17.06	16.05	1.01	18.66	21.34	20.00	1.34
09/12/10	14.74	16.07	15.40	0.66	18.56	19.92	19.24	0.68
average	**15.34**	**16.65**	**16.00**	**0.65**	**19.31**	**20.65**	**19.98**	**0.67**

	BAND3				BAND4			
DATE	Min	Max	Average	SD	Min	Max	Average	SD
26/02/10	21.18	21.86	21.52	0.34	22.25	21.70	21.97	0.28
19/03/10	21.49	23.58	22.54	1.05	23.04	23.24	23.14	0.10
22/03/10	19.82	21.73	20.77	0.95	21.24	21.63	21.43	0.20
23/03/10	20.87	22.44	21.66	0.78	22.37	21.77	22.07	0.30
20/04/10	22.65	23.95	23.30	0.65	24.11	23.67	23.89	0.22
21/04/10	21.40	21.63	21.52	0.12	22.42	20.75	21.58	0.83
22/04/10	21.73	23.41	22.57	0.84	23.15	23.22	23.18	0.04
23/04/10	23.19	24.40	23.79	0.61	24.20	23.85	24.03	0.18
26/04/10	20.79	23.37	22.08	1.29	21.90	22.74	22.32	0.42
09/12/10	20.76	22.10	21.43	0.67	21.95	21.96	21.95	0.00
average	**21.39**	**22.85**	**22.12**	**0.73**	**22.66**	**22.45**	**22.56**	**0.26**

Appendix 1 Table 5 Concrete SVC HR 1024 In-situ measurements Bands 1-4, wet

	BAND1				BAND2			
DATE	**Min**	**Max**	**Average**	**SD**	**Min**	**Max**	**Average**	**SD**
7/11/2010	16.26	19.79	18.03	1.76	20.20	23.98	22.09	1.89
3/3/2010	15.73	18.14	16.94	1.21	19.67	22.65	21.16	1.49
4/3/2010	15.52	18.97	17.25	1.73	19.36	24.05	21.71	2.35
9/3/2010	16.92	17.90	17.41	0.49	21.03	22.10	21.56	0.54
10/3/2010	15.17	16.65	15.91	0.74	18.69	20.92	19.81	1.12
12/3/2010	15.56	17.27	16.42	0.85	20.13	22.31	21.22	1.09
15/3/2010	16.01	16.18	16.10	0.09	20.04	20.57	20.31	0.26
17/3/2010	15.57	15.76	15.67	0.09	19.66	20.56	20.11	0.45
4/4/2010	15.06	16.59	15.83	0.77	19.10	20.68	19.89	0.79
13/4/2010	17.43	19.18	18.31	0.88	21.95	23.77	22.86	0.91
19/4/2010	17.41	18.20	17.80	0.40	22.18	22.98	22.58	0.40
27/4/2010	15.30	16.92	16.11	0.81	19.38	21.18	20.28	0.90
29/4/2010	15.24	17.24	16.24	1.00	19.57	21.66	20.62	1.04
30/4/2010	15.54	18.99	17.27	1.73	19.34	23.43	21.38	2.05
7/5/2010	14.73	17.63	16.18	1.45	18.33	22.43	20.38	2.05
31/5/2010	14.99	17.18	16.08	1.10	18.60	20.99	19.79	1.20
16/6/2010	15.32	19.11	17.22	1.89	19.12	23.99	21.56	2.44
24/6/2010	15.31	17.57	16.44	1.13	18.77	22.54	20.65	1.88
10/7/2010	17.30	18.50	17.90	0.60	21.78	23.47	22.62	0.84
3/8/2010	16.38	18.27	17.33	0.95	20.74	22.78	21.76	1.02
27/8/2010	17.75	20.23	18.99	1.24	20.55	25.56	23.05	2.50
28/9/2010	15.23	18.62	16.92	1.70	19.45	23.52	21.48	2.03
average	**15.90**	**17.95**	**16.92**	**1.03**	**19.89**	**22.55**	**21.22**	**1.33**

	BAND3				BAND4			
DATE	**Min**	**Max**	**Average**	**SD**	**Min**	**Max**	**Average**	**SD**
7/11/2010	22.63	26.12	24.38	1.74	24.08	25.74	24.91	0.83
3/3/2010	21.81	25.33	23.57	1.76	23.33	25.22	24.28	0.95
4/3/2010	22.67	26.98	24.83	2.16	24.47	26.69	25.58	1.11
9/3/2010	23.45	24.45	23.95	0.50	25.01	24.26	24.64	0.38
10/3/2010	20.80	23.40	22.10	1.30	22.37	23.48	22.92	0.56
12/3/2010	22.67	25.17	23.92	1.25	24.17	25.21	24.69	0.52
15/3/2010	22.26	22.81	22.53	0.27	23.83	23.32	23.58	0.25
17/3/2010	22.00	23.57	22.79	0.79	23.73	23.63	23.68	0.05
4/4/2010	21.25	22.92	22.08	0.84	22.76	23.52	23.14	0.38
13/4/2010	24.51	26.34	25.43	0.92	26.16	26.05	26.10	0.06
19/4/2010	24.86	25.80	25.33	0.47	26.53	25.46	26.00	0.53
27/4/2010	21.94	23.36	22.65	0.71	23.74	22.99	23.37	0.37
29/4/2010	22.22	24.05	23.13	0.92	23.83	23.38	23.60	0.23
30/4/2010	21.41	25.79	23.60	2.19	22.80	25.54	24.17	1.37
7/5/2010	20.41	25.06	22.73	2.32	21.52	24.67	23.10	1.57
31/5/2010	20.67	23.17	21.92	1.25	21.99	22.85	22.42	0.43
16/6/2010	21.34	26.71	24.03	2.68	22.78	26.07	24.42	1.64
24/6/2010	20.77	25.41	23.09	2.32	22.17	25.23	23.70	1.53
10/7/2010	24.44	26.56	25.50	1.06	26.34	26.51	26.42	0.09

3/8/2010	23.51	25.23	24.37	0.86	25.24	24.78	25.01	0.23
27/8/2010	25.31	28.65	26.98	1.67	27.23	28.37	27.80	0.57
28/9/2010	22.07	26.30	24.19	2.11	23.82	26.06	24.94	1.12
average	**22.41**	**25.15**	**23.78**	**1.37**	**24.00**	**24.96**	**24.48**	**0.67**

Appendix 1 Table 6 Concrete SVC HR 1024 In-situ measurements Bands 1-4, dry

	BAND1				BAND2			
DATE	Min	Max	Average	SD	Min	Max	Average	SD
4/3/2010	6.75	8.43	7.59	0.84	9.76	12.11	10.94	1.17
9/3/2010	7.58	8.63	8.11	0.53	11.66	12.83	12.24	0.59
10/3/2010	6.23	8.21	7.22	0.99	9.11	12.41	10.76	1.65
12/3/2010	7.58	8.42	8.00	0.42	11.78	12.41	12.10	0.31
15/3/2010	8.61	9.62	9.12	0.50	12.74	14.39	13.56	0.83
17/3/2010	7.98	10.38	9.18	1.20	11.35	14.87	13.11	1.76
20/3/2010	7.15	7.94	7.55	0.40	10.52	11.76	11.14	0.62
22/3/2010	8.04	9.26	8.65	0.61	11.67	13.39	12.53	0.86
23/3/2010	6.33	9.80	8.07	1.73	9.15	13.68	11.42	2.26
4/4/2010	8.72	10.63	9.67	0.95	12.85	14.77	13.81	0.96
21/4/2010	7.80	8.88	8.34	0.54	11.64	13.17	12.41	0.77
22/4/2010	6.97	7.71	7.34	0.37	10.50	11.49	11.00	0.49
23/4/2010	6.21	8.14	7.18	0.97	9.24	11.97	10.60	1.36
26/4/2010	8.47	10.96	9.71	1.24	12.40	15.03	13.71	1.31
9/12/2010	7.30	9.70	8.50	1.20	10.03	13.65	11.84	1.81
average	**7.45**	**9.12**	**8.28**	**0.83**	**10.96**	**13.19**	**12.08**	**1.12**

	BAND3				BAND4			
DATE	Min	Max	Average	SD	Min	Max	Average	SD
4/3/2010	10.38	13.04	11.71	1.33	10.98	13.91	12.45	1.46
9/3/2010	13.02	13.94	13.48	0.46	14.39	15.13	14.76	0.37
10/3/2010	9.73	13.69	11.71	1.98	10.60	15.20	12.90	2.30
12/3/2010	13.18	13.53	13.36	0.18	14.73	14.81	14.77	0.04
15/3/2010	14.01	16.00	15.00	1.00	15.31	17.62	16.46	1.16
17/3/2010	12.07	16.33	14.20	2.13	13.16	17.96	15.56	2.40
20/3/2010	11.42	12.67	12.05	0.63	12.58	13.92	13.25	0.67
22/3/2010	12.58	14.46	13.52	0.94	13.70	15.76	14.73	1.03
23/3/2010	10.37	14.77	12.57	2.20	11.84	15.96	13.90	2.06
4/4/2010	14.19	16.68	15.44	1.25	15.66	17.92	16.79	1.13
21/4/2010	12.73	14.44	13.59	0.86	13.99	15.88	14.94	0.94
22/4/2010	11.51	12.45	11.98	0.47	12.70	13.68	13.19	0.49
23/4/2010	9.89	13.16	11.53	1.63	10.71	14.45	12.58	1.87
26/4/2010	13.60	16.06	14.83	1.23	15.00	17.50	16.25	1.25
9/12/2010	11.85	14.79	13.32	1.47	12.70	15.84	14.27	1.57
average	**12.04**	**14.40**	**13.22**	**1.18**	**13.20**	**15.70**	**14.45**	**1.25**

Appendix 1 Table 7 Black Sand SVC HR 1024 In-situ measurements Bands 1-4, wet

	BAND1				BAND2			
DATE	**Min**	**Max**	**Average**	**SD**	**Min**	**Max**	**Average**	**SD**
3/3/2010	8.66	14.94	11.80	3.14	11.39	20.21	15.80	4.41
13/4/2010	11.58	13.38	12.48	0.90	16.66	19.30	17.98	1.32
19/4/2010	10.34	13.64	11.99	1.65	14.40	18.55	16.47	2.08
20/4/2010	11.16	12.21	11.68	0.52	16.05	17.33	16.69	0.64
29/4/2010	11.44	15.43	13.43	2.00	16.63	22.06	19.34	2.71
30/4/2010	10.90	13.08	11.99	1.09	15.57	18.43	17.00	1.43
7/5/2010	9.20	11.75	10.47	1.27	13.17	16.37	14.77	1.60
31/5/2010	10.94	12.67	11.81	0.86	15.54	17.77	16.66	1.12
16/6/2010	8.71	10.92	9.82	1.11	13.35	15.63	14.49	1.14
24/6/2010	13.20	13.86	13.53	0.33	18.48	18.89	18.69	0.21
10/7/2010	15.16	15.40	15.28	0.12	20.97	21.23	21.10	0.13
3/8/2010	14.72	15.37	15.05	0.33	20.28	21.24	20.76	0.48
27/8/2010	14.03	14.96	14.50	0.47	19.68	20.75	20.21	0.54
28/9/2010	11.05	13.52	12.28	1.23	14.89	18.75	16.82	1.93
7/11/2010	9.00	10.87	9.93	0.94	13.28	15.59	14.44	1.15
average	**11.34**	**13.47**	**12.40**	**1.06**	**16.02**	**18.81**	**17.42**	**1.39**

	BAND3				BAND4			
DATE	**Min**	**Max**	**Average**	**SD**	**Min**	**Max**	**Average**	**SD**
3/3/2010	12.28	22.22	17.25	4.97	13.11	23.51	18.31	5.20
13/4/2010	18.11	21.31	19.71	1.60	19.87	23.30	21.58	1.71
19/4/2010	15.30	19.90	17.60	2.30	16.48	21.62	19.05	2.57
20/4/2010	17.67	18.85	18.26	0.59	19.50	20.68	20.09	0.59
29/4/2010	18.32	24.41	21.36	3.04	20.22	26.84	23.53	3.31
30/4/2010	16.98	20.08	18.53	1.55	18.72	22.08	20.40	1.68
7/5/2010	14.44	18.00	16.22	1.78	13.74	19.62	16.68	2.94
31/5/2010	16.78	19.42	18.10	1.32	17.06	21.02	19.04	1.98
16/6/2010	15.00	17.13	16.07	1.07	16.81	18.86	17.84	1.02
24/6/2010	20.26	20.38	20.32	0.06	21.86	21.92	21.89	0.03
10/7/2010	22.83	23.55	23.19	0.36	24.61	25.69	25.15	0.54
3/8/2010	22.20	23.29	22.75	0.54	23.92	25.04	24.48	0.56
27/8/2010	21.53	22.81	22.17	0.64	23.32	24.49	23.91	0.59
28/9/2010	15.63	20.40	18.02	2.38	17.52	22.06	19.79	2.27
7/11/2010	14.63	16.88	15.75	1.12	16.22	18.25	17.23	1.02
average	**17.47**	**20.57**	**19.02**	**1.55**	**18.86**	**22.33**	**20.60**	**1.73**

Appendix 1 Table 8 Black Sand SVC HR 1024 In-situ measurements Bands 1-4, dry

	BAND1				BAND2			
DATE	**Min**	**Max**	**Average**	**SD**	**Min**	**Max**	**Average**	**SD**
03/03/10	11.382	12.106	11.744	0.3621	16.565	17.973	17.269	0.7037
04/03/10	10.27	12.373	11.322	1.0511	13.239	16.12	14.679	1.4405
09/03/10	11.184	11.359	11.272	0.0876	14.399	15.084	14.741	0.3425
10/03/10	10.196	11.305	10.75	0.5545	13.402	14.7	14.051	0.649
12/03/10	7.7821	8.441	8.1115	0.3294	10.529	11.394	10.962	0.4325
15/03/10	11.554	12.827	12.19	0.6362	14.543	16.447	15.495	0.952
17/03/10	11.931	12.768	12.349	0.4183	15.068	16.112	15.59	0.522
19/03/10	11.859	12.785	12.322	0.4628	15.034	15.814	15.424	0.3901
20/03/10	12.713	14.17	13.442	0.7288	15.695	17.132	16.414	0.7184
22/03/10	12.984	15.059	14.021	1.0374	15.589	17.807	16.698	1.1089
19/04/10	14.521	14.698	14.609	0.0886	17.921	18.088	18.004	0.0834
21/04/10	9.8114	10.581	10.196	0.385	12.733	13.443	13.088	0.3548
22/04/10	9.1524	9.7124	9.4324	0.28	12.032	12.564	12.298	0.2661
23/04/10	9.8729	11.051	10.462	0.5893	12.753	14.14	13.447	0.6937
average	**11.09**	**12.09**	**11.59**	**0.50**	**14.25**	**15.49**	**14.87**	**0.62**

	BAND3				BAND4			
DATE	**Min**	**Max**	**Average**	**SD**	**Min**	**Max**	**Average**	**SD**
03/03/10	18.033	19.27	18.652	0.6185	19.823	20.683	20.253	0.4302
04/03/10	14.725	17.938	16.331	1.6069	16.007	19.343	17.675	1.6679
09/03/10	15.28	16.449	15.865	0.5844	16.042	17.524	16.783	0.7409
10/03/10	14.881	16.506	15.693	0.8123	16.111	17.842	16.977	0.8656
12/03/10	11.899	12.805	12.352	0.4527	13.052	13.944	13.498	0.4463
15/03/10	15.415	18.188	16.802	1.3865	16.159	19.591	17.875	1.7162
17/03/10	16.103	17.494	16.798	0.6952	17.316	18.42	17.868	0.5523
19/03/10	16.17	16.86	16.515	0.3453	17.117	17.676	17.397	0.2795
20/03/10	17.122	18.421	17.772	0.6498	18.056	19.175	18.616	0.5596
22/03/10	16.525	18.6	17.563	1.0376	17.189	19.205	18.197	1.008
19/04/10	19.181	19.355	19.268	0.0868	20.327	20.638	20.483	0.1557
21/04/10	13.607	14.274	13.941	0.3334	14.385	15.07	14.727	0.3423
22/04/10	12.811	13.377	13.094	0.2829	13.45	14.136	13.793	0.3429
23/04/10	13.513	15.126	14.32	0.8065	14.283	15.745	15.014	0.7307
average	**15.38**	**16.76**	**16.07**	**0.69**	**16.38**	**17.79**	**17.08**	**0.70**

Appendix 1 Table 9 Compacted Sand SVC HR 1024 In-situ measurements Bands 1-4, wet

	BAND1				BAND2			
DATE	**Min**	**Max**	**Average**	**SD**	**Min**	**Max**	**Average**	**SD**
07/11/10	16.068	16.364	16.216	0.1484	20.183	20.32	20.252	0.0684
23/03/10	16.938	21.519	19.229	2.2906	20.551	25.021	22.786	2.2348
04/04/10	14.479	16.07	15.274	0.7955	17.31	18.91	18.11	0.7996
13/04/10	11.729	18.944	15.337	3.6074	14.95	23.47	19.21	4.2596
26/04/10	14.285	15.128	14.706	0.4212	17.29	17.899	17.594	0.3042
27/04/10	15.096	16.23	15.663	0.5673	18.009	19.255	18.632	0.6231
20/04/10	17.021	21.883	19.452	2.4313	21.696	27.136	24.416	2.7198
28/04/10	17.854	19.73	18.792	0.9379	20.468	22.861	21.664	1.1964
29/04/10	14.863	16.308	15.585	0.7225	17.96	18.771	18.365	0.4055
30/04/10	15.743	19.055	17.399	1.656	19.046	21.965	20.505	1.4596
07/05/10	19.567	21.026	20.297	0.7296	23.275	24.568	23.921	0.6464
31/05/10	13.545	16.927	15.236	1.691	16.92	20.62	18.77	1.8498
16/06/10	15.932	18.377	17.154	1.2228	19.829	22.179	21.004	1.1751
24/06/10	19.274	20.006	19.64	0.3658	23.849	24.344	24.097	0.2472
10/07/10	17.735	17.843	17.789	0.0542	22.789	22.823	22.806	0.0168
03/08/10	18.233	18.273	18.253	0.0198	22.651	23.383	23.017	0.3658
27/08/10	17.79	20.084	18.937	1.1473	22.723	25.086	23.905	1.1813
28/09/10	19.175	20.662	19.918	0.7437	24.309	25.599	24.954	0.6449
average	**16.41**	**18.58**	**17.49**	**1.086**	**20.21**	**22.46**	**21.33**	**1.12**

	BAND3				BAND4			
DATE	**Min**	**Max**	**Average**	**SD**	**Min**	**Max**	**Average**	**SD**
07/11/10	21.522	21.854	21.688	0.166	22.199	23.139	22.669	0.4698
23/03/10	21.846	26.298	24.072	2.2257	23.255	27.514	25.384	2.1297
04/04/10	17.964	19.697	18.831	0.8666	18.661	20.446	19.554	0.8924
13/04/10	16.025	25.364	20.694	4.6694	17.074	27.683	22.378	5.3044
26/04/10	18.117	18.674	18.396	0.2786	18.773	19.488	19.131	0.3575
27/04/10	18.833	20.192	19.512	0.6795	19.341	20.973	20.157	0.8159
20/04/10	23.522	29.54	26.531	3.009	25.485	32.145	28.815	3.33
28/04/10	21.173	24.072	22.622	1.4495	21.776	25.216	23.496	1.7201
29/04/10	18.971	19.277	19.124	0.1527	19.914	19.772	19.843	0.0713
30/04/10	20.111	22.844	21.478	1.3665	21.071	23.779	22.425	1.3541
07/05/10	24.523	25.747	25.135	0.6118	25.801	26.851	26.326	0.5248
31/05/10	18.316	22.039	20.177	1.8615	19.328	23.203	21.265	1.9373
16/06/10	21.299	24.221	22.76	1.4612	22.629	25.315	23.972	1.3431
24/06/10	25.949	26.313	26.131	0.1818	27.43	28.084	27.757	0.3272
10/07/10	25.374	25.435	25.404	0.0304	27.349	27.692	27.52	0.1718
03/08/10	24.764	25.925	25.345	0.5808	26.469	28.275	27.372	0.9035
27/08/10	25.014	27.133	26.073	1.0593	27.351	29.433	28.392	1.0407
28/09/10	26.642	27.581	27.112	0.4698	29.03	29.688	29.359	0.3287
average	**21.67**	**24.01**	**22.84**	**1.17**	**22.94**	**25.48**	**24.21**	**1.28**

Appendix 1 Table 2 Compacted Sand SVC HR 1024 In-situ measurements Bands 1-4, dry

Radiance

RADIANCE		Asphalt 1				Asphalt 2			
Date	band	Min	Max	mean	st. dev	Min	Max	mean	st. dev
13-04-10	1	91	95	92.50	1.64	76.00	85.00	80.92	2.84
13-04-10	2	79	81	79.67	0.82	62.00	71.00	65.67	2.54
13-04-10	3	66	70	67.67	1.63	51.00	60.00	54.33	2.90
13-04-10	4	49	57	52.67	3.20	39.00	46.00	41.17	2.59
29-04-10	1	104	131	111.83	10.03	94.00	102.00	97.42	2.39
29-04-10	2	87	109	93.33	8.34	83.00	87.00	84.58	1.38
29-04-10	3	71	95	78.83	8.52	69.00	76.00	71.00	1.95
29-04-10	4	53	73	59.83	7.57	51.00	57.00	53.75	1.82
31-05-10	1	100	104	102.33	1.37	87.00	94.00	90.17	1.95
31-05-10	2	87	91	88.67	1.86	71.00	79.00	74.17	2.37
31-05-10	3	74	79	75.83	1.94	60.00	66.00	62.08	2.23
31-05-10	4	54	60	55.83	2.40	45.00	55.00	48.08	3.40
16-06-10	1	99	106	103.00	3.16	95.00	108.00	100.75	4.12
16-06-10	2	89	93	90.67	1.86	80.00	91.00	84.08	3.45
16-06-10	3	76	78	76.83	0.98	66.00	74.00	69.67	2.71
16-06-10	4	53	59	56.17	2.23	47.00	54.00	49.75	1.87
24-06-10	1	93	98	96.33	2.58	78.00	90.00	84.42	3.00
24-06-10	2	84	92	88.83	3.19	69.00	79.00	73.58	2.58
24-06-10	3	70	80	75.83	3.43	57.00	69.00	61.00	3.05
24-06-10	4	50	59	54.50	3.21	42.00	54.00	46.58	4.06
10-07-10	1	98	100	98.67	0.82	85.00	94.00	89.92	2.81
10-07-10	2	85	91	88.33	1.97	72.00	82.00	77.33	3.03
10-07-10	3	73	76	74.67	1.37	59.00	68.00	63.17	2.92
10-07-10	4	51	58	54.50	2.74	41.00	53.00	46.25	3.84
27-08-10	1	88	101	95.17	4.79	75.00	85.00	79.83	3.19
27-08-10	2	78	91	85.33	5.13	63.00	76.00	68.83	4.15
27-08-10	3	67	76	72.00	3.52	51.00	63.00	56.92	3.48
27-08-10	4	49	57	52.00	2.83	36.00	49.00	41.50	3.37
28-09-10	1	77	85	81.33	3.50	65.00	71.00	68.00	2.00
28-09-10	2	69	78	73.00	3.35	55.00	63.00	57.92	2.43
28-09-10	3	58	65	61.00	2.45	45.00	53.00	48.58	2.19
28-09-10	4	40	46	42.67	2.34	31.00	40.00	35.50	3.00
07-11-10	1	65	72	68.17	2.48	57.00	62.00	59.17	1.53
07-11-10	2	54	58	56.33	1.37	41.00	49.00	45.75	2.09
07-11-10	3	43	49	45.67	2.34	31.00	40.00	37.58	2.47
07-11-10	4	31	35	33.83	1.60	26.00	30.00	27.50	1.45
09-12-10	1	56	58	57.17	0.98	51.00	55.00	52.25	1.36
09-12-10	2	44	48	46.17	1.60	38.00	43.00	40.33	1.61
09-12-10	3	37	39	38.00	0.89	30.00	34.00	31.83	1.19
09-12-10	4	26	27	26.33	0.52	21.00	26.00	23.08	1.62
02-05-11	1	101	102	101.67	0.52	94.00	102.00	97.42	2.39
02-05-11	2	89	90	89.17	0.41	83.00	87.00	84.58	1.38
02-05-11	3	75	77	76.00	0.63	69.00	76.00	71.00	1.95
02-05-11	4	57	63	59.67	2.16	51.00	57.00	53.75	1.82

Appendix 1 Table 11 Radiance values Gray and Black Asphalt

RADIANCE		Concrete			
Date	band	Min	Max	mean	st. dev
13-04-10	1	116.00	124.00	119.71	3.59
13-04-10	2	109.00	123.00	115.57	4.47
13-04-10	3	97.00	109.00	102.57	4.20
13-04-10	4	70.00	78.00	74.57	2.94
29-04-10	1	111.00	153.00	132.29	16.46
29-04-10	2	91.00	135.00	112.14	15.85
29-04-10	3	73.00	113.00	93.00	14.57
29-04-10	4	57.00	86.00	72.57	10.47
31-05-10	1	134.00	147.00	138.86	4.85
31-05-10	2	127.00	143.00	136.29	4.89
31-05-10	3	113.00	130.00	121.43	5.97
31-05-10	4	80.00	87.00	84.57	2.51
16-06-10	1	131.00	141.00	137.14	4.10
16-06-10	2	127.00	139.00	133.57	4.83
16-06-10	3	107.00	126.00	117.86	7.34
16-06-10	4	75.00	87.00	82.71	4.35
24-06-10	1	134.00	143.00	139.00	3.46
24-06-10	2	131.00	147.00	140.14	4.85
24-06-10	3	114.00	128.00	122.71	4.82
24-06-10	4	81.00	90.00	84.86	2.73
10-07-10	1	130.00	140.00	136.14	3.53
10-07-10	2	131.00	143.00	137.29	4.42
10-07-10	3	113.00	127.00	121.14	4.49
10-07-10	4	84.00	88.00	85.86	1.68
27-08-10	1	119.00	129.00	124.71	3.50
27-08-10	2	121.00	134.00	127.00	4.83
27-08-10	3	104.00	114.00	109.71	3.25
27-08-10	4	73.00	79.00	76.29	2.22
28-09-10	1	107.00	117.00	112.43	3.55
28-09-10	2	107.00	118.00	113.29	3.68
28-09-10	3	94.00	104.00	98.29	3.82
28-09-10	4	65.00	71.00	67.00	2.38
07-11-10	1	83.00	91.00	87.29	2.93
07-11-10	2	79.00	87.00	83.29	2.87
07-11-10	3	70.00	78.00	74.43	2.88
07-11-10	4	48.00	55.00	52.00	2.45
09-12-10	1	67.00	75.00	72.57	2.88
09-12-10	2	61.00	71.00	66.14	3.53
09-12-10	3	55.00	61.00	58.71	2.36
09-12-10	4	36.00	42.00	39.57	1.90
02-05-11	1	111.00	116.00	114.57	1.72
02-05-11	2	102.00	112.00	107.43	3.05
02-05-11	3	88.00	95.00	92.43	2.30
02-05-11	4	70.00	72.00	71.14	0.90

Appendix 1 Table 12 Radiance Values Concrete

RADIANCE		sand 1				sand 2			
Date	band	Min	Max	mean	st. dev	Min	Max	mean	st. dev
13-04-10	1	81.00	90.00	86.00	2.32	81.00	85.00	82.68	1.02
13-04-10	2	75.00	87.00	82.73	2.64	72.00	75.00	72.82	0.86
13-04-10	3	66.00	78.00	73.80	3.01	60.00	64.00	60.89	1.07
13-04-10	4	49.00	58.00	54.07	1.80	42.00	46.00	43.07	0.90
29-04-10	1	101.00	106.00	103.57	1.43	115.00	119.00	116.64	1.03
29-04-10	2	86.00	90.00	87.23	1.01	95.00	99.00	97.46	1.07
29-04-10	3	68.00	74.00	71.27	1.39	79.00	82.00	80.43	0.88
29-04-10	4	50.00	54.00	51.70	0.95	55.00	57.00	55.86	0.65
31-05-10	1	90.00	101.00	95.87	2.79	97.00	104.00	100.89	1.87
31-05-10	2	90.00	100.00	94.77	2.58	89.00	98.00	93.39	2.42
31-05-10	3	79.00	91.00	84.30	3.14	77.00	88.00	81.11	2.51
31-05-10	4	56.00	65.00	60.47	2.42	54.00	62.00	56.75	1.99
16-06-10	1	95.00	103.00	98.43	2.11	104.00	113.00	108.39	2.63
16-06-10	2	93.00	103.00	97.50	2.43	98.00	108.00	103.04	2.72
16-06-10	3	83.00	91.00	86.40	2.53	85.00	96.00	91.04	2.91
16-06-10	4	58.00	66.00	61.27	2.21	60.00	70.00	64.39	2.46
24-06-10	1	85.00	97.00	90.00	2.79	101.00	110.00	106.29	1.94
24-06-10	2	89.00	102.00	92.80	3.37	101.00	111.00	106.64	2.48
24-06-10	3	76.00	89.00	80.90	3.34	89.00	96.00	92.25	1.92
24-06-10	4	54.00	64.00	57.47	2.37	63.00	68.00	65.25	1.24
10-07-10	1	86.00	110.00	96.27	5.45	109.00	155.00	128.71	13.61
10-07-10	2	78.00	102.00	88.93	6.10	99.00	147.00	122.96	12.62
10-07-10	3	61.00	87.00	73.80	6.31	86.00	128.00	106.18	10.88
10-07-10	4	41.00	61.00	51.03	5.04	59.00	91.00	75.21	8.45
27-08-10	1	79.00	87.00	82.83	2.04	92.00	103.00	97.93	2.87
27-08-10	2	82.00	92.00	85.33	2.17	92.00	107.00	99.57	3.26
27-08-10	3	72.00	82.00	74.23	2.43	81.00	94.00	88.18	2.92
27-08-10	4	51.00	59.00	53.03	2.28	58.00	66.00	63.14	2.22
28-09-10	1	69.00	78.00	72.93	2.61	81.00	93.00	87.61	2.64
28-09-10	2	72.00	82.00	74.80	2.52	82.00	95.00	89.46	3.06
28-09-10	3	61.00	71.00	64.83	2.52	72.00	85.00	79.32	3.01
28-09-10	4	44.00	51.00	46.43	2.00	51.00	60.00	57.00	2.18
07-11-10	1	56.00	61.00	57.43	1.31	65.00	72.00	69.61	1.75
07-11-10	2	48.00	55.00	50.03	1.71	57.00	66.00	61.79	1.75
07-11-10	3	38.00	47.00	41.20	2.19	48.00	56.00	52.46	1.92
07-11-10	4	26.00	33.00	28.60	1.94	34.00	39.00	37.04	1.17
09-12-10	1	45.00	50.00	48.47	1.31	54.00	57.00	55.89	0.79
09-12-10	2	37.00	43.00	39.83	1.49	46.00	49.00	46.93	1.12
09-12-10	3	29.00	34.00	32.33	1.45	37.00	40.00	38.79	0.69
09-12-10	4	19.00	23.00	21.57	1.28	25.00	27.00	26.00	0.39
02-05-11	1	89.00	95.00	91.70	1.77	91.00	96.00	93.32	1.54
02-05-11	2	83.00	90.00	85.30	1.97	81.00	85.00	83.82	1.09
02-05-11	3	70.00	79.00	73.77	2.16	68.00	73.00	70.93	1.51
02-05-11	4	53.00	59.00	54.57	1.65	49.00	53.00	51.07	0.98

Appendix 1 Table 13 Radiance values Black and compacted sand

At-satellite reflectance (before correction)

Image date	TM bands	Gray Asphalt minimum	Gray Asphalt maximum	Gray Asphalt average
13/4/2010	1	0.17	0.18	0.18
	2	0.16	0.17	0.17
	3	0.16	0.17	0.17
	4	0.18	0.21	0.19
29/4/2010	1	0.19	0.23	0.20
	2	0.17	0.21	0.18
	3	0.16	0.22	0.18
	4	0.18	0.25	0.20
31/5/2010	1	0.18	0.18	0.18
	2	0.17	0.18	0.17
	3	0.17	0.18	0.17
	4	0.18	0.20	0.19
16/6/2010	1	0.18	0.19	0.18
	2	0.17	0.18	0.18
	3	0.18	0.18	0.18
	4	0.18	0.20	0.19
24/6/2010	1	0.17	0.18	0.17
	2	0.17	0.18	0.18
	3	0.16	0.19	0.18
	4	0.17	0.20	0.19
10/7/2010	1	0.18	0.18	0.18
	2	0.17	0.18	0.18
	3	0.17	0.18	0.17
	4	0.18	0.20	0.19
27/8/2010	1	0.17	0.20	0.18
	2	0.17	0.19	0.18
	3	0.17	0.19	0.18
	4	0.18	0.21	0.19
28/9/2010	1	0.16	0.18	0.17
	2	0.16	0.18	0.17
	3	0.16	0.18	0.17
	4	0.16	0.19	0.18
7/11/2010	1	0.17	0.19	0.18
	2	0.16	0.17	0.16
	3	0.15	0.17	0.16
	4	0.16	0.18	0.17
9/12/2010	1	0.18	0.18	0.18
	2	0.15	0.17	0.16
	3	0.16	0.16	0.16
	4	0.16	0.16	0.16
2/5/2011	1	0.18	0.18	0.18
	2	0.18	0.18	0.18
	3	0.18	0.18	0.18
	4	0.20	0.22	0.21

Appendix 1 Table 14 Reflectance values Gray Asphalt

Image date	TM bands	Black asphalt minimum	Black asphalt maximum	Black asphalt average
13/4/2010	1	0.14	0.16	0.15
	2	0.13	0.15	0.14
	3	0.13	0.15	0.13
	4	0.14	0.17	0.15
29/4/2010	1	0.17	0.18	0.18
	2	0.16	0.17	0.17
	3	0.16	0.18	0.17
	4	0.18	0.20	0.19
31/5/2010	1	0.15	0.17	0.16
	2	0.14	0.15	0.14
	3	0.14	0.15	0.14
	4	0.15	0.19	0.16
16/6/2010	1	0.17	0.19	0.18
	2	0.16	0.18	0.16
	3	0.15	0.17	0.16
	4	0.16	0.18	0.17
24/6/2010	1	0.14	0.16	0.15
	2	0.14	0.16	0.15
	3	0.13	0.16	0.14
	4	0.15	0.19	0.16
10/7/2010	1	0.15	0.17	0.16
	2	0.14	0.16	0.15
	3	0.14	0.16	0.15
	4	0.14	0.18	0.16
27/8/2010	1	0.15	0.16	0.15
	2	0.13	0.16	0.15
	3	0.13	0.16	0.14
	4	0.13	0.18	0.15
28/9/2010	1	0.14	0.15	0.15
	2	0.13	0.15	0.14
	3	0.12	0.15	0.13
	4	0.13	0.16	0.15
7/11/2010	1	0.15	0.16	0.16
	2	0.12	0.14	0.13
	3	0.11	0.14	0.13
	4	0.13	0.15	0.14
9/12/2010	1	0.16	0.17	0.16
	2	0.13	0.15	0.14
	3	0.12	0.14	0.13
	4	0.13	0.16	0.14
2/5/2011	1	0.17	0.18	0.18
	2	0.16	0.17	0.17
	3	0.16	0.18	0.17
	4	0.18	0.20	0.19

Appendix 1 Table 15 Reflectance values Black asphalt

Image date	TM bands	Concrete minimum	Concrete maximum	Concrete average
13/4/2010	1	0.22	0.24	0.23
	2	0.23	0.26	0.24
	3	0.24	0.27	0.25
	4	0.26	0.28	0.27
29/4/2010	1	0.20	0.27	0.24
	2	0.18	0.26	0.22
	3	0.17	0.26	0.22
	4	0.20	0.29	0.25
31/5/2010	1	0.24	0.26	0.25
	2	0.25	0.28	0.26
	3	0.26	0.30	0.28
	4	0.27	0.30	0.29
16/6/2010	1	0.23	0.25	0.24
	2	0.25	0.27	0.26
	3	0.25	0.29	0.27
	4	0.26	0.30	0.28
24/6/2010	1	0.24	0.26	0.25
	2	0.26	0.29	0.28
	3	0.26	0.30	0.28
	4	0.28	0.31	0.29
10/7/2010	1	0.24	0.25	0.25
	2	0.26	0.29	0.27
	3	0.26	0.30	0.28
	4	0.29	0.31	0.30
27/8/2010	1	0.23	0.25	0.24
	2	0.26	0.29	0.27
	3	0.26	0.28	0.27
	4	0.27	0.29	0.28
28/9/2010	1	0.23	0.25	0.24
	2	0.25	0.28	0.27
	3	0.26	0.29	0.27
	4	0.27	0.29	0.28
7/11/2010	1	0.22	0.24	0.23
	2	0.23	0.25	0.24
	3	0.24	0.27	0.26
	4	0.24	0.28	0.26
9/12/2010	1	0.21	0.24	0.23
	2	0.21	0.25	0.23
	3	0.22	0.25	0.24
	4	0.22	0.25	0.24
2/5/2011	1	0.20	0.21	0.21
	2	0.20	0.22	0.21
	3	0.21	0.22	0.22
	4	0.24	0.25	0.25

Appendix 1 Table 16 Reflectance values Concrete

Image date	TM bands	Black Sand minimum	Black Sand maximum	Black Sand average
13/4/2010	1	0.15	0.17	0.16
	2	0.16	0.18	0.17
	3	0.16	0.19	0.18
	4	0.18	0.21	0.20
29/4/2010	1	0.18	0.19	0.18
	2	0.17	0.18	0.17
	3	0.16	0.17	0.17
	4	0.16	0.18	0.17
31/5/2010	1	0.17	0.19	0.18
	2	0.18	0.21	0.19
	3	0.19	0.22	0.21
	4	0.26	0.31	0.28
16/6/2010	1	0.17	0.18	0.17
	2	0.18	0.20	0.19
	3	0.19	0.21	0.20
	4	0.20	0.22	0.21
24/6/2010	1	0.15	0.17	0.16
	2	0.18	0.20	0.18
	3	0.18	0.21	0.19
	4	0.19	0.22	0.20
10/7/2010	1	0.16	0.20	0.17
	2	0.16	0.20	0.18
	3	0.14	0.20	0.17
	4	0.14	0.21	0.18
27/8/2010	1	0.15	0.17	0.16
	2	0.18	0.20	0.18
	3	0.18	0.20	0.19
	4	0.19	0.22	0.20
28/9/2010	1	0.15	0.17	0.16
	2	0.17	0.19	0.18
	3	0.17	0.20	0.18
	4	0.18	0.21	0.19
7/11/2010	1	0.15	0.16	0.15
	2	0.14	0.16	0.15
	3	0.13	0.16	0.14
	4	0.13	0.17	0.14
9/12/2010	1	0.14	0.16	0.15
	2	0.13	0.15	0.14
	3	0.12	0.14	0.13
	4	0.11	0.14	0.13
2/5/2011	1	0.16	0.18	0.17
	2	0.16	0.18	0.17
	3	0.17	0.19	0.17
	4	0.18	0.21	0.19

Appendix 1 Table 17 Reflectance values Black sand

Image date	TM bands	Compacted Sand minimum	Compacted Sand maximum	Compacted Sand average
13/4/2010	1	0.15	0.16	0.16
	2	0.15	0.16	0.15
	3	0.15	0.16	0.15
	4	0.15	0.17	0.16
29/4/2010	1	0.20	0.21	0.21
	2	0.19	0.19	0.19
	3	0.18	0.19	0.19
	4	0.19	0.20	0.19
31/5/2010	1	0.17	0.18	0.18
	2	0.17	0.19	0.18
	3	0.18	0.20	0.19
	4	0.18	0.21	0.19
16/6/2010	1	0.18	0.20	0.19
	2	0.19	0.21	0.20
	3	0.19	0.22	0.21
	4	0.20	0.24	0.22
24/6/2010	1	0.18	0.20	0.19
	2	0.20	0.22	0.21
	3	0.21	0.22	0.21
	4	0.22	0.23	0.23
10/7/2010	1	0.20	0.28	0.23
	2	0.20	0.29	0.25
	3	0.20	0.30	0.25
	4	0.21	0.32	0.26
27/8/2010	1	0.18	0.20	0.19
	2	0.20	0.23	0.21
	3	0.20	0.23	0.22
	4	0.22	0.25	0.23
28/9/2010	1	0.17	0.20	0.19
	2	0.19	0.22	0.21
	3	0.20	0.23	0.22
	4	0.21	0.25	0.23
7/11/2010	1	0.17	0.19	0.18
	2	0.17	0.19	0.18
	3	0.16	0.19	0.18
	4	0.17	0.20	0.19
9/12/2010	1	0.17	0.18	0.18
	2	0.16	0.17	0.16
	3	0.15	0.16	0.16
	4	0.15	0.16	0.16
2/5/2011	1	0.16	0.17	0.17
	2	0.16	0.17	0.17
	3	0.16	0.17	0.17
	4	0.17	0.18	0.18

Appendix 1 Table 18 Reflectance values Compacted sand

DP corrected		Gray Asphalt			
13-04-10	band	Min	Max	mean	st. dev
	1	0.125	0.133	0.128	0.003
	2	0.150	0.154	0.151	0.002
	3	0.161	0.171	0.165	0.004
	4	0.180	0.209	0.194	0.012
29-04-10	band	Min	Max	mean	st. dev
	1	0.096	0.144	0.110	0.018
	2	0.102	0.144	0.114	0.016
	3	0.104	0.160	0.122	0.020
	4	0.117	0.186	0.141	0.026
31-05-10	band	Min	Max	mean	st. dev
	1	0.118	0.125	0.122	0.002
	2	0.140	0.147	0.143	0.004
	3	0.149	0.161	0.153	0.004
	4	0.166	0.186	0.172	0.008
16-06-10	band	Min	Max	mean	st. dev
	1	0.105	0.117	0.112	0.006
	2	0.134	0.142	0.137	0.004
	3	0.151	0.156	0.153	0.002
	4	0.166	0.187	0.177	0.008
24-06-10	band	Min	Max	mean	st. dev
	1	0.124	0.133	0.130	0.005
	2	0.147	0.163	0.157	0.006
	3	0.160	0.184	0.174	0.008
	4	0.173	0.204	0.189	0.011
10-07-10	band	Min	Max	mean	st. dev
	1	0.124	0.127	0.125	0.001
	2	0.142	0.154	0.149	0.004
	3	0.161	0.168	0.165	0.003
	4	0.174	0.198	0.186	0.010
27-08-10	band	Min	Max	mean	st. dev
	1	0.117	0.142	0.131	0.009
	2	0.135	0.163	0.151	0.011
	3	0.158	0.180	0.170	0.009
	4	0.184	0.214	0.195	0.010
28-09-10	band	Min	Max	mean	st. dev
	1	0.122	0.139	0.132	0.007
	2	0.147	0.168	0.156	0.008
	3	0.159	0.178	0.167	0.007
	4	0.174	0.199	0.185	0.010
07-11-10	band	Min	Max	mean	st. dev
	1	0.105	0.125	0.114	0.006
	2	0.154	0.177	0.160	0.006
	3	0.167	0.195	0.178	0.007
	4	0.191	0.219	0.201	0.008
09-12-10	band	Min	Max	mean	st. dev
	1	0.125	0.131	0.129	0.003
	2	0.142	0.156	0.149	0.006

DP corrected		Gray Asphalt			
	3	0.161	0.170	0.166	0.004
	4	0.176	0.182	0.178	0.003
	band	Min	Max	mean	st. dev
	1	0.106	0.108	0.107	0.001
07-05-11	2	0.125	0.127	0.125	0.001
	3	0.136	0.141	0.139	0.001
	4	0.160	0.181	0.169	0.007

Appendix 1 Table 18 DP correction for Gray Asphalt

DP corrected		Black Asphalt			
	band	Min	Max	mean	st. dev
	1	0.097	0.114	0.106	0.005
13-04-10	2	0.115	0.133	0.122	0.005
	3	0.124	0.146	0.132	0.007
	4	0.144	0.169	0.152	0.009
	band	Min	Max	mean	st. dev
	1	0.093	0.108	0.100	0.004
29-04-10	2	0.113	0.121	0.116	0.003
	3	0.122	0.139	0.127	0.005
	4	0.139	0.160	0.149	0.006
	band	Min	Max	mean	st. dev
	1	0.095	0.108	0.101	0.003
31-05-10	2	0.109	0.124	0.115	0.005
	3	0.117	0.131	0.122	0.005
	4	0.136	0.169	0.146	0.012
	band	Min	Max	mean	st. dev
	1	0.098	0.121	0.108	0.007
16-06-10	2	0.117	0.138	0.125	0.007
	3	0.128	0.147	0.137	0.006
	4	0.146	0.170	0.155	0.006
	band	Min	Max	mean	st. dev
	1	0.097	0.119	0.109	0.005
24-06-10	2	0.118	0.137	0.127	0.005
	3	0.130	0.158	0.140	0.007
	4	0.146	0.187	0.161	0.014
	band	Min	Max	mean	st. dev
	1	0.100	0.116	0.109	0.005
10-07-10	2	0.116	0.136	0.127	0.006
	3	0.128	0.149	0.138	0.007
	4	0.139	0.181	0.157	0.013
	band	Min	Max	mean	st. dev
	1	0.092	0.111	0.101	0.006
27-08-10	2	0.103	0.131	0.115	0.009
	3	0.118	0.148	0.133	0.009
	4	0.136	0.184	0.156	0.012

DP corrected		Black Asphalt			
	band	Min	Max	mean	st. dev
28-09-10	1	0.097	0.110	0.103	0.004
	2	0.114	0.132	0.121	0.006
	3	0.123	0.145	0.133	0.006
	4	0.137	0.174	0.156	0.012
	band	Min	Max	mean	st. dev
07-11-10	1	0.093	0.106	0.099	0.004
	2	0.099	0.123	0.113	0.006
	3	0.103	0.134	0.126	0.008
	4	0.145	0.166	0.153	0.007
	band	Min	Max	mean	st. dev
09-12-10	1	0.109	0.122	0.113	0.004
	2	0.121	0.139	0.129	0.006
	3	0.133	0.149	0.14	0.005
	4	0.145	0.176	0.158	0.010
	band	Min	Max	mean	st. dev
07-05-11	1	0.093	0.108	0.100	0.004
	2	0.113	0.121	0.116	0.003
	3	0.122	0.139	0.127	0.005
	4	0.139	0.160	0.149	0.006

Appendix 1 Table 19 DP correction for Black Asphalt

DP corrected		Concrete			
	band	Min	Max	mean	st. dev
13-04-10	1	0.173	0.188	0.180	0.007
	2	0.212	0.241	0.226	0.009
	3	0.237	0.267	0.251	0.010
	4	0.257	0.286	0.273	0.011
	band	Min	Max	mean	st. dev
29-04-10	1	0.108	0.183	0.146	0.029
	2	0.109	0.195	0.151	0.031
	3	0.109	0.202	0.155	0.034
	4	0.131	0.230	0.184	0.036
	band	Min	Max	mean	st. dev
31-05-10	1	0.178	0.201	0.187	0.009
	2	0.217	0.248	0.235	0.009
	3	0.239	0.278	0.258	0.014
	4	0.254	0.278	0.270	0.008
	band	Min	Max	mean	st. dev
16-06-10	1	0.162	0.179	0.172	0.007
	2	0.208	0.232	0.221	0.009
	3	0.223	0.266	0.248	0.017
	4	0.241	0.282	0.267	0.015
	band	Min	Max	mean	st. dev
24-06-10	1	0.197	0.213	0.206	0.006
	2	0.240	0.272	0.258	0.010

	3	0.262	0.294	0.282	0.011
	4	0.280	0.311	0.293	0.009
10-07-10	band	Min	Max	mean	st. dev
	1	0.182	0.200	0.193	0.006
	2	0.234	0.258	0.246	0.009
	3	0.254	0.287	0.273	0.010
	4	0.288	0.302	0.295	0.006
27-08-10	band	Min	Max	mean	st. dev
	1	0.177	0.196	0.188	0.007
	2	0.226	0.254	0.239	0.010
	3	0.250	0.275	0.264	0.008
	4	0.273	0.295	0.285	0.008
28-09-10	band	Min	Max	mean	st. dev
	1	0.186	0.208	0.198	0.008
	2	0.236	0.262	0.251	0.009
	3	0.258	0.286	0.270	0.011
	4	0.277	0.302	0.285	0.010
07-11-10	band	Min	Max	mean	st. dev
	1	0.162	0.183	0.173	0.008
	2	0.210	0.233	0.222	0.008
	3	0.237	0.264	0.252	0.010
	4	0.257	0.292	0.277	0.012
09-12-10	band	Min	Max	mean	st. dev
	1	0.160	0.185	0.177	0.009
	2	0.201	0.235	0.218	0.012
	3	0.235	0.259	0.250	0.010
	4	0.236	0.272	0.257	0.011
07-05-11	band	Min	Max	mean	st. dev
	1	0.124	0.133	0.131	0.003
	2	0.150	0.170	0.161	0.006
	3	0.167	0.183	0.177	0.005
	4	0.205	0.212	0.209	0.003

Appendix 1 Table 20 DP correction for Concrete

DP corrected		Black sand			
13-04-10	band	Min	Max	mean	st. dev
	1	0.106	0.123	0.116	0.004
	2	0.142	0.167	0.158	0.005
	3	0.161	0.190	0.180	0.007
	4	0.180	0.213	0.199	0.007
29-04-10	band	Min	Max	mean	st. dev
	1	0.090	0.099	0.095	0.003
	2	0.100	0.107	0.102	0.002
	3	0.097	0.111	0.105	0.003
	4	0.107	0.121	0.113	0.003
31-05-10	band	Min	Max	mean	st. dev
	1	0.101	0.120	0.111	0.005
	2	0.145	0.165	0.155	0.005
	3	0.161	0.188	0.173	0.007
	4	0.173	0.203	0.188	0.008
16-06-10	band	Min	Max	mean	st. dev
	1	0.098	0.112	0.104	0.004
	2	0.142	0.162	0.151	0.005
	3	0.167	0.186	0.175	0.006
	4	0.183	0.210	0.194	0.008
24-06-10	band	Min	Max	mean	st. dev
	1	0.110	0.131	0.119	0.005
	2	0.157	0.183	0.165	0.007
	3	0.174	0.204	0.186	0.008
	4	0.187	0.221	0.199	0.008
10-07-10	band	Min	Max	mean	st. dev
	1	0.102	0.145	0.121	0.010
	2	0.128	0.176	0.150	0.012
	3	0.133	0.194	0.163	0.015
	4	0.139	0.208	0.174	0.018
27-08-10	band	Min	Max	mean	st. dev
	1	0.100	0.115	0.107	0.004
	2	0.143	0.165	0.151	0.005
	3	0.170	0.195	0.176	0.006
	4	0.191	0.221	0.199	0.008
28-09-10	band	Min	Max	mean	st. dev
	1	0.105	0.125	0.114	0.006
	2	0.154	0.177	0.16	0.006
	3	0.167	0.195	0.178	0.007
	4	0.191	0.219	0.201	0.008
07-11-10	band	Min	Max	mean	st. dev
	1	0.091	0.104	0.094	0.003
	2	0.120	0.140	0.126	0.005
	3	0.127	0.158	0.138	0.007
	4	0.145	0.181	0.159	0.010
09-12-10	band	Min	Max	mean	st. dev
	1	0.091	0.106	0.102	0.004
	2	0.118	0.139	0.128	0.005

	3	0.129	0.149	0.142	0.006
	4	0.133	0.157	0.149	0.008
07-05-11	band	Min	Max	mean	st. dev
	1	0.084	0.095	0.089	0.003
	2	0.113	0.127	0.117	0.004
	3	0.124	0.146	0.133	0.005
	4	0.146	0.167	0.152	0.006

Appendix 1 Table 21 DP correction for Black Sand

DP corrected		Compacted Sand			
13-04-10	band	Min	Max	mean	st. dev
	1	0.106	0.114	0.109	0.002
	2	0.136	0.142	0.137	0.002
	3	0.146	0.156	0.148	0.003
	4	0.155	0.169	0.159	0.003
29-04-10	band	Min	Max	mean	st. dev
	1	0.115	0.122	0.118	0.002
	2	0.117	0.125	0.122	0.002
	3	0.123	0.130	0.126	0.002
	4	0.124	0.131	0.127	0.002
31-05-10	band	Min	Max	mean	st. dev
	1	0.113	0.125	0.120	0.003
	2	0.143	0.161	0.152	0.005
	3	0.156	0.181	0.165	0.006
	4	0.166	0.193	0.175	0.007
16-06-10	band	Min	Max	mean	st. dev
	1	0.114	0.130	0.122	0.005
	2	0.152	0.171	0.162	0.005
	3	0.172	0.197	0.186	0.007
	4	0.190	0.224	0.205	0.008
24-06-10	band	Min	Max	mean	st. dev
	1	0.138	0.154	0.148	0.003
	2	0.181	0.201	0.192	0.005
	3	0.204	0.221	0.212	0.004
	4	0.218	0.235	0.226	0.004
10-07-10	band	Min	Max	mean	st. dev
	1	0.144	0.227	0.179	0.025
	2	0.170	0.266	0.218	0.025
	3	0.191	0.289	0.238	0.025
	4	0.201	0.313	0.258	0.029
27-08-10	band	Min	Max	mean	st. dev
	1	0.125	0.146	0.136	0.006
	2	0.165	0.197	0.181	0.007
	3	0.193	0.225	0.211	0.007
	4	0.217	0.247	0.236	0.008

	band	Min	Max	mean	st. dev
28-09-10	1	0.131	0.157	0.145	0.006
	2	0.177	0.208	0.195	0.007
	3	0.197	0.233	0.218	0.008
	4	0.219	0.256	0.244	0.009
	band	Min	Max	mean	st. dev
07-11-10	1	0.114	0.133	0.126	0.005
	2	0.146	0.172	0.160	0.005
	3	0.161	0.189	0.177	0.007
	4	0.186	0.211	0.201	0.006
	band	Min	Max	mean	st. dev
09-12-10	1	0.119	0.128	0.125	0.002
	2	0.149	0.159	0.152	0.004
	3	0.161	0.174	0.169	0.003
	4	0.170	0.182	0.176	0.002
	band	Min	Max	mean	st. dev
07-05-11	1	0.088	0.097	0.092	0.003
	2	0.109	0.117	0.114	0.002
	3	0.102	0.131	0.127	0.004
	4	0.132	0.146	0.140	0.003

Appendix 1 Table 22 DP correction for Compacted Sand

wavelength (every 1nm)	Interpolated real spectrum	100% spectrum	RSR (filter function)	GER*Filter	Filter*100
(nm)	ρ %				
435	9.85	100	0.016	0.15760	1.6
436	9.88	100	0.027	0.26676	2.7
437	9.92	100	0.048	0.47616	4.8
438	9.95	100	0.094	0.93530	9.4
439	9.98	100	0.167	1.66666	16.7
440	10.01	100	0.287	2.87287	28.7
441	10.04	100	0.459	4.60836	45.9
442	10.08	100	0.605	6.09840	60.5
443	10.11	100	0.728	7.36008	72.8
444	10.14	100	0.769	7.79766	76.9
445	10.17	100	0.792	8.05464	79.2
446	10.20	100	0.821	8.37420	82.1
447	10.23	100	0.857	8.76711	85.7
448	10.25	100	0.857	8.78425	85.7
449	10.28	100	0.862	8.86136	86.2
450	10.31	100	0.839	8.65009	83.9
451	10.33	100	0.845	8.72885	84.5
452	10.35	100	0.810	8.38350	81.0
453	10.38	100	0.802	8.32476	80.2
454	10.40	100	0.804	8.36160	80.4
455	10.43	100	0.779	8.12497	77.9
456	10.46	100	0.798	8.34708	79.8
457	10.48	100	0.816	8.55168	81.6
458	10.51	100	0.876	9.20676	87.6
459	10.53	100	0.888	9.35064	88.8
460	10.55	100	0.901	9.50555	90.1
461	10.57	100	0.918	9.70326	91.8
462	10.60	100	0.896	9.49760	89.6
463	10.61	100	0.903	9.58083	90.3
464	10.63	100	0.888	9.43944	88.8
465	10.65	100	0.890	9.47850	89.0
466	10.67	100	0.863	9.20821	86.3
467	10.69	100	0.860	9.19340	86.0
468	10.70	100	0.842	9.00940	84.2
469	10.72	100	0.866	9.28352	86.6
470	10.74	100	0.875	9.39750	87.5
471	10.77	100	0.881	9.48837	88.1
472	10.79	100	0.888	9.58152	88.8
473	10.81	100	0.898	9.70738	89.8
474	10.83	100	0.879	9.51957	87.9
475	10.84	100	0.884	9.58256	88.4
476	10.86	100	0.907	9.85002	90.7
477	10.88	100	0.928	10.09664	92.8
478	10.90	100	0.932	10.15880	93.2
479	10.92	100	0.955	10.42860	95.5
480	10.94	100	0.958	10.48052	95.8
481	10.96	100	0.948	10.39008	94.8
482	10.98	100	0.952	10.45296	95.2

wavelength (every 1nm)	Interpolated real spectrum	100% spectrum	RSR (filter function)	GER*Filter	Filter*100
483	11.00	100	0.956	10.51600	95.6
484	11.02	100	0.980	10.79960	98.0
485	11.04	100	0.980	10.81920	98.0
486	11.06	100	0.975	10.78350	97.5
487	11.09	100	0.973	10.79057	97.3
488	11.11	100	0.977	10.85447	97.7
489	11.13	100	0.958	10.66254	95.8
490	11.15	100	0.965	10.75975	96.5
491	11.16	100	0.957	10.68012	95.7
492	11.18	100	0.952	10.64336	95.2
493	11.20	100	0.973	10.89760	97.3
494	11.22	100	0.974	10.92828	97.4
495	11.24	100	0.995	11.18380	99.5
496	11.26	100	0.986	11.10236	98.6
497	11.29	100	0.986	11.13194	98.6
498	11.31	100	0.994	11.24214	99.4
499	11.33	100	1.000	11.33000	100.0
500	11.36	100	0.990	11.24640	99.0
501	11.38	100	0.990	11.26620	99.0
502	11.40	100	0.976	11.12640	97.6
503	11.43	100	0.983	11.23569	98.3
504	11.45	100	0.976	11.17520	97.6
505	11.47	100	0.983	11.27501	98.3
506	11.50	100	0.960	11.04000	96.0
507	11.52	100	0.973	11.20896	97.3
508	11.55	100	0.964	11.13420	96.4
509	11.57	100	0.975	11.28075	97.5
510	11.60	100	0.960	11.13600	96.0
511	11.62	100	0.932	10.82984	93.2
512	11.65	100	0.853	9.93745	85.3
513	11.67	100	0.684	7.98228	68.4
514	11.69	100	0.486	5.68134	48.6
515	11.71	100	0.293	3.43103	29.3
516	11.73	100	0.150	1.75950	15.0
517	11.76	100	0.073	0.85848	7.3
518	11.78	100	0.036	0.42408	3.6
519	11.80	100	0.019	0.22420	1.9
520	11.83	100	0.009	0.10647	0.9
		SUM	67.204	733.6303	6720
Average	**10.88534884**		**In-band reflectance(%) Band1**	**10.91647**	

Appendix 1, Table 23 RSR example, band 1

wavelength (every 1nm)	Interpolated real spectrum	100% spectrum	RSR (filter function)	GER*Filter	Filter*100
(nm)	ρ %				
500	11.36	100	0.0006	0.006816	0.06
501	11.38	100	0.0009	0.010242	0.09
502	11.40	100	0.0010	0.011400	0.10
0503	11.43	100	0.0020	0.022860	0.20
504	11.45	100	0.0020	0.022900	0.20
505	11.47	100	0.0030	0.034410	0.30
506	11.50	100	0.0050	0.057500	0.50
507	11.52	100	0.0090	0.103680	0.90
508	11.55	100	0.0145	0.167475	1.45
509	11.57	100	0.0236	0.273052	2.36
510	11.60	100	0.0260	0.301600	2.60
511	11.62	100	0.0410	0.476420	4.10
512	11.65	100	0.0600	0.699000	6.00
513	11.67	100	0.0880	1.026960	8.80
514	11.69	100	0.1260	1.472940	12.6
515	11.71	100	0.1740	2.037540	17.4
516	11.73	100	0.2360	2.768280	23.6
517	11.76	100	0.3080	3.622080	30.8
518	11.78	100	0.3880	4.570640	38.8
519	11.80	100	0.4720	5.569600	47.2
520	11.83	100	0.5520	6.530160	55.2
521	11.85	100	0.6210	7.358850	62.1
522	11.87	100	0.6760	8.024120	67.6
523	11.89	100	0.7160	8.513240	71.6
524	11.91	100	0.7430	8.849130	74.3
525	11.93	100	0.7590	9.054870	75.9
526	11.95	100	0.7690	9.189550	76.9
527	11.97	100	0.7790	9.324630	77.9
528	11.99	100	0.7900	9.472100	79.0
529	12.01	100	0.8050	9.668050	80.5
530	12.02	100	0.8220	9.880440	82.2
531	12.04	100	0.8420	10.137680	84.2
532	12.07	100	0.8610	10.392270	86.1
533	12.09	100	0.8780	10.615020	87.8
534	12.10	100	0.8930	10.805300	89.3
535	12.12	100	0.9050	10.968600	90.5
536	12.14	100	0.9160	11.120240	91.6
537	12.16	100	0.9240	11.235840	92.4
538	12.17	100	0.9330	11.354610	93.3
539	12.19	100	0.9420	11.482980	94.2
540	12.21	100	0.9470	11.562870	94.7
541	12.23	100	0.9510	11.630730	95.1
542	12.24	100	0.9530	11.664720	95.3
543	12.26	100	0.9520	11.671520	95.2
544	12.28	100	0.9510	11.678280	95.1
545	12.29	100	0.9520	11.700080	95.2
546	12.31	100	0.9510	11.706810	95.1
547	12.33	100	0.9510	11.725830	95.1

wavelength (every 1nm)	Interpolated real spectrum	100% spectrum	RSR (filter function)	GER*Filter	Filter*100
548	12.34	100	0.9520	11.74768	95.2
549	12.36	100	0.9520	11.76672	95.2
550	12.38	100	0.9530	11.79814	95.3
551	12.40	100	0.9510	11.79240	95.1
552	12.41	100	0.9500	11.78950	95.0
553	12.42	100	0.9500	11.79900	95.0
554	12.43	100	0.9510	11.82093	95.1
555	12.45	100	0.9540	11.87730	95.4
556	12.47	100	0.9600	11.97120	96.0
557	12.48	100	0.9660	12.05568	96.6
558	12.49	100	0.9680	12.09032	96.8
559	12.51	100	0.9650	12.07215	96.5
560	12.52	100	0.9590	12.00668	95.9
561	12.54	100	0.9510	11.92554	95.1
562	12.55	100	0.9440	11.84720	94.4
563	12.57	100	0.9370	11.77809	93.7
564	12.58	100	0.9320	11.72456	93.2
565	12.59	100	0.9330	11.74647	93.3
566	12.60	100	0.9350	11.78100	93.5
567	12.62	100	0.9370	11.82494	93.7
568	12.63	100	0.9400	11.87220	94.0
569	12.64	100	0.9450	11.94480	94.5
570	12.65	100	0.9510	12.03015	95.1
571	12.67	100	0.9550	12.09985	95.5
572	12.68	100	0.9570	12.13476	95.7
573	12.69	100	0.9560	12.13164	95.6
574	12.70	100	0.9570	12.15390	95.7
575	12.71	100	0.9550	12.13805	95.5
576	12.72	100	0.9520	12.10944	95.2
577	12.72	100	0.9540	12.13488	95.4
578	12.73	100	0.9580	12.19534	95.8
579	12.74	100	0.9630	12.26862	96.3
580	12.76	100	0.9730	12.41548	97.3
581	12.76	100	0.9810	12.51756	98.1
582	12.77	100	0.9880	12.61676	98.8
583	12.78	100	0.9950	12.71610	99.5
584	12.79	100	1.0000	12.79000	100.0
585	12.80	100	1.0000	12.80000	100.0
586	12.81	100	0.9940	12.73314	99.4
587	12.81	100	0.9830	12.59223	98.3
588	12.82	100	0.9690	12.42258	96.9
589	12.83	100	0.9540	12.23982	95.4
590	12.84	100	0.9420	12.09528	94.2
591	12.85	100	0.9360	12.02760	93.6
592	12.85	100	0.9320	11.97620	93.2
593	12.86	100	0.9280	11.93408	92.8
594	12.86	100	0.9240	11.88264	92.4
595	12.87	100	0.9120	11.73744	91.2
596	12.89	100	0.8830	11.38187	88.3
597	12.90	100	0.8340	10.75860	83.4

wavelength (every 1nm)	Interpolated real spectrum	100% spectrum	RSR (filter function)	GER*Filter	Filter*100
598	12.91	100	0.7630	9.850330	76.3
599	12.92	100	0.6740	8.708080	67.4
600	12.93	100	0.5740	7.421820	57.4
601	12.93	100	0.4730	6.115890	47.3
602	12.94	100	0.3800	4.917200	38.0
603	12.95	100	0.3000	3.885000	30.0
604	12.95	100	0.2350	3.043250	23.5
605	12.95	100	0.1850	2.395750	18.5
606	12.95	100	0.1460	1.890700	14.6
607	12.96	100	0.1170	1.516320	11.7
608	12.97	100	0.0940	1.219180	9.40
609	12.98	100	0.0770	0.999460	7.70
610	12.99	100	0.0620	0.805380	6.20
611	12.99	100	0.0520	0.675480	5.20
612	12.99	100	0.0420	0.545580	4.20
613	13.00	100	0.0330	0.429000	3.30
614	13.01	100	0.0260	0.338260	2.60
615	13.01	100	0.0210	0.273210	2.10
616	13.01	100	0.0158	0.205558	1.58
617	13.02	100	0.0124	0.160797	1.24
618	13.02	100	0.0094	0.122388	0.94
619	13.02	100	0.0072	0.093353	0.72
620	13.02	100	0.0048	0.062496	0.48
621	13.02	100	0.0037	0.048174	0.37
622	13.01	100	0.0026	0.033826	0.26
623	13.00	100	0.0017	0.022100	0.17
624	13.00	100	0.0014	0.018200	0.14
			77.5985	968.437207	7759.85
Average	**12.42704**		**In-band reflectance(%) Band2**	**12.4800989**	

Appendix 1, Table 23 RSR example, band 2

wavelength (every 1nm)	Interpolated real spectrum	100% spectrum	RSR (filter function)	GER*Filter	Filter*100
(nm)	ρ %				
	□				
614	13.01	100	0.0005	0.006505	0.05
615	13.01	100	0.0001	0.001301	0.01
616	13.01	100	0.0000	0	0
617	13.02	100	0.0005	0.00651	0.05
618	13.02	100	0.0006	0.007812	0.06
619	13.02	100	0.0014	0.018228	0.14
620	13.02	100	0.0020	0.026040	0.2
621	13.02	100	0.0030	0.039060	0.3
622	13.01	100	0.0060	0.078060	0.6
623	13.00	100	0.0130	0.169000	1.3
624	13.00	100	0.0250	0.325000	2.5
625	13.01	100	0.0470	0.611470	4.7
626	13.01	100	0.0830	1.079830	8.3
627	13.01	100	0.1370	1.782370	13.7
628	13.01	100	0.2110	2.745110	21.1
629	13.02	100	0.3060	3.984120	30.6
630	13.03	100	0.4190	5.459570	41.9
631	13.04	100	0.5450	7.106800	54.5
632	13.05	100	0.6740	8.795700	67.4
633	13.05	100	0.7880	10.28340	78.8
634	13.06	100	0.8730	11.40138	87.3
635	13.06	100	0.9210	12.02826	92.1
636	13.07	100	0.9410	12.29887	94.1
637	13.09	100	0.9430	12.34387	94.3
638	13.09	100	0.9420	12.33078	94.2
639	13.09	100	0.9390	12.29151	93.9
640	13.09	100	0.9370	12.26533	93.7
641	13.10	100	0.9350	12.24850	93.5
642	13.11	100	0.9350	12.25785	93.5
643	13.11	100	0.9380	12.29718	93.8
644	13.12	100	0.9430	12.37216	94.3
645	13.13	100	0.9490	12.46037	94.9
646	13.14	100	0.9530	12.52242	95.3
647	13.15	100	0.9610	12.63715	96.1
648	13.16	100	0.9680	12.73888	96.8
649	13.17	100	0.9710	12.78807	97.1
650	13.17	100	0.9730	12.81441	97.3
651	13.17	100	0.9740	12.82758	97.4
652	13.18	100	0.9720	12.81096	97.2
653	13.19	100	0.9690	12.78111	96.9
654	13.20	100	0.9630	12.71160	96.3
655	13.20	100	0.9580	12.64560	95.8
656	13.21	100	0.9560	12.62876	95.6
657	13.22	100	0.9550	12.62510	95.5
658	13.25	100	0.9550	12.65375	95.5
659	13.25	100	0.9560	12.66700	95.6
660	13.26	100	0.9620	12.75612	96.2
661	13.27	100	0.9690	12.85863	96.9
662	13.28	100	0.9770	12.97456	97.7
663	13.29	100	0.9830	13.06407	98.3

wavelength (every 1nm)	Interpolated real spectrum	100% spectrum	RSR (filter function)	GER*Filter	Filter*100
664	13.31	100	0.9880	13.15028	98.8
665	13.33	100	0.9930	13.23669	99.3
666	13.34	100	0.9960	13.28664	99.6
667	13.36	100	0.9970	13.31992	99.7
668	13.37	100	0.9990	13.35663	99.9
669	13.37	100	1.0000	13.37000	100.0
670	13.39	100	1.0000	13.39000	100.0
671	13.40	100	0.9980	13.37320	99.8
672	13.42	100	0.9960	13.36632	99.6
673	13.43	100	0.9950	13.36285	99.5
674	13.45	100	0.9930	13.35585	99.3
675	13.47	100	0.9920	13.36224	99.2
676	13.49	100	0.9910	13.36859	99.1
677	13.50	100	0.9890	13.35150	98.9
678	13.50	100	0.9880	13.33800	98.8
679	13.50	100	0.9840	13.28400	98.4
680	13.49	100	0.9770	13.17973	97.7
681	13.50	100	0.9700	13.09500	97.0
682	13.51	100	0.9600	12.96960	96.0
683	13.51	100	0.9490	12.82099	94.9
684	13.52	100	0.9400	12.70880	94.0
685	13.53	100	0.9320	12.60996	93.2
686	13.53	100	0.9190	12.43407	91.9
687	13.55	100	0.8980	12.16790	89.8
688	13.55	100	0.8630	11.69365	86.3
689	13.56	100	0.8090	10.97004	80.9
690	13.57	100	0.7290	9.89253	72.9
691	13.58	100	0.6250	8.48750	62.5
692	13.59	100	0.5060	6.87654	50.6
693	13.60	100	0.3820	5.19520	38.2
694	13.61	100	0.2720	3.70192	27.2
695	13.62	100	0.1830	2.49246	18.3
696	13.63	100	0.1200	1.63560	12.0
697	13.65	100	0.0790	1.07835	7.90
698	13.66	100	0.0530	0.72398	5.30
699	13.66	100	0.0360	0.49176	3.60
700	13.67	100	0.0250	0.34175	2.50
701	13.68	100	0.0196	0.26813	1.96
702	13.69	100	0.0142	0.19440	1.42
703	13.71	100	0.0101	0.13847	1.01
704	13.71	100	0.0075	0.10283	0.75
		SUM	**60.0105**	**798.17158**	**6001.05**
Average	**13.29406593**		**In-band reflectance(%) TM 3**	**13.300532**	

Appendix 1, Table 24 RSR example, band 3

wavelength (every 1nm)	Interpolated real spectrum	100% spectrum	RSR (filter function)	GER*Filter	Filter*100
(nm)	ρ %				
740	14.15	100	0.0004	0.005660	0.04
741	14.18	100	0.0037	0.052466	0.37
742	14.20	100	0.0010	0.014200	0.10
743	14.21	100	0.0144	0.204624	1.44
744	14.21	100	0.0182	0.258622	1.82
745	14.23	100	0.0216	0.307368	2.16
746	14.24	100	0.0269	0.383056	2.69
747	14.26	100	0.0315	0.449190	3.15
748	14.27	100	0.0377	0.537979	3.77
749	14.29	100	0.0474	0.677346	4.74
750	14.31	100	0.0562	0.804222	5.62
751	14.32	100	0.0688	0.985216	6.88
752	14.34	100	0.0690	0.989460	6.90
753	14.35	100	0.0830	1.191050	8.30
754	14.37	100	0.0990	1.422630	9.90
755	14.39	100	0.1210	1.741190	12.1
756	14.40	100	0.1460	2.102400	14.6
757	14.42	100	0.1750	2.523500	17.5
758	14.41	100	0.2090	3.011690	20.9
759	14.42	100	0.2480	3.576160	24.8
760	14.44	100	0.2940	4.245360	29.4
761	14.47	100	0.3460	5.006620	34.6
762	14.49	100	0.4020	5.824980	40.2
763	14.47	100	0.4630	6.699610	46.3
764	14.48	100	0.5230	7.573040	52.3
765	14.51	100	0.5880	8.531880	58.8
766	14.52	100	0.6490	9.423480	64.9
767	14.55	100	0.7050	10.257750	70.5
768	14.57	100	0.7570	11.029490	75.7
769	14.59	100	0.7970	11.628230	79.7
770	14.61	100	0.8270	12.082470	82.7
771	14.62	100	0.8530	12.470860	85.3
772	14.64	100	0.8710	12.751440	87.1
773	14.65	100	0.8840	12.950600	88.4
774	14.66	100	0.8920	13.076720	89.2
775	14.69	100	0.8990	13.206310	89.9
776	14.70	100	0.9030	13.274100	90.3
777	14.71	100	0.9080	13.356680	90.8
778	14.72	100	0.9110	13.409920	91.1
779	14.74	100	0.9160	13.501840	91.6
780	14.77	100	0.9200	13.588400	92.0
781	14.78	100	0.9250	13.671500	92.5
782	14.79	100	0.9260	13.695540	92.6
783	14.81	100	0.9270	13.728870	92.7
784	14.82	100	0.9270	13.738140	92.7
785	14.84	100	0.9290	13.786360	92.9
786	14.85	100	0.9320	13.840200	93.2
787	14.85	100	0.9300	13.810500	93.0
788	14.86	100	0.9260	13.760360	92.6
789	14.88	100	0.9260	13.778880	92.6

wavelength (every 1nm)	Interpolated real spectrum	100% spectrum	RSR (filter function)	GER*Filter	Filter*100
790	14.90	100	0.9250	13.78250	92.5
791	14.90	100	0.9280	13.82720	92.8
792	14.92	100	0.9250	13.80100	92.5
793	14.94	100	0.9260	13.83444	92.6
794	14.94	100	0.9280	13.86432	92.8
795	14.96	100	0.9280	13.88288	92.8
796	14.97	100	0.9280	13.89216	92.8
797	14.99	100	0.9230	13.83577	92.3
798	14.99	100	0.9200	13.79080	92.0
799	14.98	100	0.9190	13.76662	91.9
800	14.98	100	0.9140	13.69172	91.4
801	14.99	100	0.9100	13.64090	91.0
802	15.02	100	0.9080	13.63816	90.8
803	15.04	100	0.9050	13.61120	90.5
804	15.05	100	0.9030	13.59015	90.3
805	15.05	100	0.9040	13.60520	90.4
806	15.06	100	0.9020	13.58412	90.2
807	15.08	100	0.9090	13.70772	90.9
808	15.08	100	0.9170	13.82836	91.7
809	15.09	100	0.9200	13.88280	92.0
810	15.11	100	0.9280	14.02208	92.8
811	15.10	100	0.9380	14.16380	93.8
812	15.13	100	0.9460	14.31298	94.6
813	15.13	100	0.9530	14.41889	95.3
814	15.12	100	0.9620	14.54544	96.2
815	15.11	100	0.9690	14.64159	96.9
816	15.11	100	0.9710	14.67181	97.1
817	15.16	100	0.9710	14.72036	97.1
818	15.15	100	0.9700	14.69550	97.0
819	15.16	100	0.9690	14.69004	96.9
820	15.16	100	0.9690	14.69004	96.9
821	15.16	100	0.9700	14.70520	97.0
822	15.20	100	0.9670	14.69840	96.7
823	15.19	100	0.9690	14.71911	96.9
824	15.18	100	0.9680	14.69424	96.8
825	15.17	100	0.9630	14.60871	96.3
826	15.17	100	0.9650	14.63905	96.5
827	15.20	100	0.9670	14.69840	96.7
828	15.21	100	0.9650	14.67765	96.5
829	15.22	100	0.9630	14.65686	96.3
830	15.22	100	0.9580	14.58076	95.8
831	15.24	100	0.9500	14.47800	95.0
832	15.26	100	0.9490	14.48174	94.9
833	15.27	100	0.9430	14.39961	94.3
834	15.27	100	0.9330	14.24691	93.3
835	15.26	100	0.9290	14.17654	92.9
836	15.27	100	0.9280	14.17056	92.8
837	15.28	100	0.9250	14.13400	92.5
838	15.28	100	0.9240	14.11872	92.4
839	15.28	100	0.9270	14.16456	92.7
840	15.30	100	0.9320	14.25960	93.2
841	15.31	100	0.9340	14.29954	93.4

wavelength (every 1nm)	Interpolated real spectrum	100% spectrum	RSR (filter function)	GER*Filter	Filter*100
842	15.32	100	0.9430	14.44676	94.3
843	15.32	100	0.9520	14.58464	95.2
844	15.31	100	0.9560	14.63636	95.6
845	15.31	100	0.9660	14.78946	96.6
846	15.31	100	0.9770	14.95787	97.7
847	15.32	100	0.9850	15.09020	98.5
848	15.29	100	0.9900	15.13710	99.0
849	15.31	100	0.992	15.18752	99.2
850	15.31	100	0.9930	15.20283	99.3
851	15.31	100	0.9940	15.21814	99.4
852	15.31	100	0.9980	15.27938	99.8
853	15.32	100	0.9960	15.25872	99.6
854	15.31	100	0.9920	15.18752	99.2
855	15.32	100	0.9910	15.18212	99.1
856	15.33	100	0.9920	15.20736	99.2
857	15.31	100	0.9940	15.21814	99.4
858	15.30	100	0.9930	15.19290	99.3
859	15.31	100	0.9970	15.26407	99.7
860	15.33	100	0.9970	15.28401	99.7
861	15.34	100	0.9960	15.27864	99.6
862	15.33	100	0.9980	15.29934	99.8
863	15.32	100	0.9990	15.30468	99.9
864	15.33	100	1.0000	15.33000	100.0
865	15.34	100	0.9990	15.32466	99.9
866	15.34	100	0.9960	15.27864	99.6
867	15.34	100	0.9910	15.20194	99.1
868	15.32	100	0.9900	15.16680	99.0
869	15.32	100	0.9910	15.18212	99.1
870	15.36	100	0.9850	15.12960	98.5
871	15.35	100	0.9780	15.01230	97.8
872	15.36	100	0.9690	14.88384	96.9
873	15.36	100	0.9550	14.66880	95.5
874	15.37	100	0.9370	14.40169	93.7
875	15.37	100	0.9160	14.07892	91.6
876	15.36	100	0.8920	13.70112	89.2
877	15.34	100	0.8680	13.31512	86.8
878	15.37	100	0.8450	12.98765	84.5
879	15.37	100	0.8240	12.66488	82.4
880	15.36	100	0.8110	12.45696	81.1
881	15.37	100	0.8070	12.40359	80.7
882	15.35	100	0.8190	12.57165	81.9
883	15.33	100	0.8410	12.89253	84.1
884	15.37	100	0.8680	13.34116	86.8
885	15.36	100	0.8920	13.70112	89.2
886	15.36	100	0.8920	13.70112	89.2
887	15.39	100	0.8540	13.14306	85.4
888	15.35	100	0.7700	11.81950	77.0
889	15.36	100	0.6440	9.89184	64.4
890	15.39	100	0.5010	7.71039	50.1
891	15.40	100	0.3650	5.62100	36.5
892	15.39	100	0.2560	3.93984	25.6
893	15.38	100	0.1770	2.72226	17.7

wavelength (every 1nm)	Interpolated real spectrum	100% spectrum	RSR (filter function)	GER*Filter	Filter*100
894	15.36	100	0.1220	1.873920	12.20
895	15.39	100	0.0850	1.308150	8.50
896	15.39	100	0.0610	0.938790	6.10
897	15.44	100	0.0440	0.679360	4.40
898	15.43	100	0.0320	0.493760	3.20
899	15.41	100	0.0250	0.385250	2.50
900	15.37	100	0.0190	0.292030	1.90
901	15.38	100	0.0140	0.215320	1.40
902	15.44	100	0.0110	0.169840	1.10
903	15.44	100	0.0107	0.165208	1.07
904	15.39	100	0.0080	0.123120	0.80
905	15.38	100	0.0061	0.093818	0.61
906	15.42	100	0.0052	0.080184	0.52
907	15.40	100	142.5576	2195.3870	14255.76
908	15.39	100	143.5576	2209.3515	14355.76
909	15.37	100	144.5576	2221.8503	14455.76
910	15.44	100	145.5576	2247.4093	14555.76
911	15.41	100	146.5576	2258.4526	14655.76
912	15.44	100	147.5576	2278.2893	14755.76
913	15.40	100	148.5576	2287.787	14855.76
914	15.44	100	149.5576	2309.1693	14955.76
			1289.1786	**19832.144**	**128917.9**
Average	**15.04908571**		**In-band reflectance(%) TM 4**	**15.38355**	

Appendix 1, Table 25 RSR example, band 4

Appendix 2

- Microtops Sun photometer measurements
- Cimel Sun photometer measurements
- Single Scattering Albedo, derived from AERONET
- Phase function

Microtops Sun photometer measurements

TARGET	DATE	AOT440	AOT500	AOT675	AOT870	AOT936
Gray Asphalt	13/4/2010	0.290	0.254	0.182	0.133	0.121
Gray Asphalt	13/4/2010	0.291	0.246	0.163	0.120	0.109
Gray Asphalt	13/4/2010	0.287	0.245	0.163	0.121	0.110
Gray Asphalt	13/4/2010	0.290	0.265	0.212	0.154	0.141
Gray Asphalt	13/4/2010	0.288	0.249	0.167	0.132	0.120
Gray Asphalt	13/4/2010	0.288	0.258	0.197	0.143	0.130
Gray Asphalt	29/4/2010	0.383	0.328	0.268	0.201	0.150
Gray Asphalt	29/4/2010	0.387	0.335	0.266	0.203	0.152
Gray Asphalt	29/4/2010	00.86	0.338	0.267	0.204	0.141
Gray Asphalt	31/5/2010	0.284	0.305	0.204	0.237	0.215
Gray Asphalt	31/5/2010	0.264	0.274	0.185	0.217	0.197
Gray Asphalt	31/5/2010	0.267	0.269	0.184	0.216	0.196
Gray Asphalt	31/5/2010	0.334	0.350	0.249	0.274	0.250
Gray Asphalt	31/5/2010	0.270	0.311	0.221	0.266	0.242
Gray Asphalt	24/6/2010	0.308	0.271	0.188	0.146	0.130
Gray Asphalt	24/6/2010	0.296	0.265	0.183	0.143	0.127
Gray Asphalt	24/6/2010	0.324	0.376	0.202	0.172	0.154
Gray Asphalt	10/7/2010	0.444	0.388	0.243	0.291	0.265
Gray Asphalt	10/7/2010	0.462	0.397	0.264	0.296	0.269
Gray Asphalt	10/7/2010	0.437	0.396	0.249	0.308	0.281
Gray Asphalt	28/9/2010	0.222	0.199	0.126	0.152	0.138
Gray Asphalt	28/9/2010	0.211	0.208	0.135	0.198	0.180
Gray Asphalt	28/9/2010	0.225	0.200	0.127	0.150	0.136
Gray Asphalt	9/12/2010	0.226	0.199	0.127	0.086	0.078
Gray Asphalt	9/12/2010	0.225	0.199	0.130	0.087	0.080
Gray Asphalt	9/12/2010	0.225	0.200	0.135	0.091	0.083
Gray Asphalt	2/5/2011	0.327	0.313	0.260	0.242	0.210
Gray Asphalt	2/5/2011	0.346	0.354	0.327	0.272	0.238
Gray Asphalt	2/5/2011	0.327	0.314	0.262	0.239	0.208
Gray Asphalt	2/5/2011	0.329	0.314	0.265	0.244	0.212
Black Asphalt	13/4/2010	0.295	0.276	0.217	0.160	0.146
Black Asphalt	13/4/2010	0.293	0.263	0.184	0.133	0.121
Black Asphalt	13/4/2010	0.293	0.265	0.195	0.140	0.128
Black Asphalt	29/4/2010	0.485	0.435	0.381	0.360	0.310
Black Asphalt	29/4/2010	0.497	0.480	0.384	0.310	0.255
Black Asphalt	31/5/2010	0.322	0.358	0.254	0.282	0.257
Black Asphalt	31/5/2010	0.312	0.361	0.256	0.286	0.260
Black Asphalt	31/5/2010	0.319	0.355	0.250	0.279	0.254
Black Asphalt	16/6/2010	0.254	0.214	0.113	0.136	0.106
Black Asphalt	16/6/2010	0.390	0.356	0.233	0.264	0.223
Black Asphalt	16/6/2010	0.321	0.292	0.178	0.206	0.170
Black Asphalt	16/6/2010	0.311	0.295	0.205	0.206	0.170
Black Asphalt	16/6/2010	0.312	0.305	0.219	0.215	0.178
Black Asphalt	16/6/2010	0.261	0.250	0.168	0.178	0.144

TARGET	DATE	AOT440	AOT500	AOT675	AOT870	AOT936
Black Asphalt	24/6/2010	0.332	0.306	0.232	0.203	0.185
Black Asphalt	24/6/2010	0.374	0.327	0.272	0.218	0.198
Black Asphalt	24/6/2010	0.333	0.294	0.229	0.204	0.185
Black Asphalt	24/6/2010	0.333	0.294	0.235	0.212	0.193
Black Asphalt	24/6/2010	0.330	0.290	0.231	0.198	0.180
Black Asphalt	24/6/2010	0.330	0.289	0.230	0.177	0.161
Black Asphalt	10/7/2010	0.461	0.367	0.313	0.245	0.205
Black Asphalt	10/7/2010	0.333	0.284	0.238	0.195	0.168
Black Asphalt	10/7/2010	0.350	0.339	0.283	0.202	0.165
Black Asphalt	27/8/2010	0.331	0.267	0.240	0.191	0.129
Black Asphalt	27/8/2010	0.345	0.282	0.256	0.188	0.126
Black Asphalt	27/8/2010	0.309	0.248	0.211	0.179	0.118
Black Asphalt	27/8/2010	0.301	0.234	0.222	0.172	0.111
Black Asphalt	27/8/2010	0.284	0.222	0.198	0.153	0.094
Black Asphalt	27/8/2010	0.284	0.222	0.198	0.153	0.094
Black Asphalt	27/8/2010	0.388	0. 333	0.310	0.266	0.206
Black Asphalt	28/9/2010	0.223	0.202	0.134	0.153	0.139
Black Asphalt	28/9/2010	0.246	0.219	0.159	0.159	0.145
Black Asphalt	28/9/2010	0.217	0.199	0.130	0.158	0.144
Black Asphalt	10/11/2010	0.239	0.231	0.186	0.144	0.131
Black Asphalt	10/11/2010	0.245	0.235	0.180	0.143	0.130
Black Asphalt	10/11/2010	0.252	0.242	0.188	0.148	0.135
Black Asphalt	10/11/2010	0.258	0.249	0.197	0.154	0.140
Black Asphalt	10/11/2010	0.224	0.214	0.155	0.125	0.114
Black Asphalt	10/11/2010	0.234	0.224	0.170	0.134	0.122
Black Asphalt	9/12/2010	0.241	0.213	0.132	0.086	0.078
Black Asphalt	9/12/2010	0.250	0.220	0.138	0.090	0.081
Black Asphalt	9/12/2010	0.247	0.218	0.140	0.091	0.082
Black Asphalt	9/12/2010	0.260	0.232	0.143	0.089	0.081
Black Asphalt	9/12/2010	0.258	0.231	0.143	0.089	0.081
Black Asphalt	9/12/2010	0.258	0.232	0.148	0.092	0.084
Black Asphalt	2/05/2011	0.405	0.355	0.281	0.241	0.202
Black Asphalt	2/05/2011	0.410	0.404	0.379	0.345	0.305
Black Asphalt	2/05/2011	0.422	0.378	0.305	0.266	0.224
Concrete	29/4/2010	0.342	0.310	0.255	0.232	0.165
Concrete	29/4/2010	0.355	0.319	0.271	0.253	0.175
Concrete	29/4/2010	0.335	0.313	0.279	0.243	0.212
Concrete	29/4/2010	0.341	0.317	0.281	0.208	0.162
Concrete	31/5/2010	0.453	0.478	0.373	0.382	0.348
Concrete	31/5/2010	0.450	0.482	0.373	0.383	0.349
Concrete	31/5/2010	0.440	0.480	0.373	0.386	0.351
Concrete	31/5/2010	0.284	0.301	0.201	0.233	0.212
Concrete	16/6/2010	0.327	0.332	0.228	0.247	0.215
Concrete	16/6/2010	0.314	0.324	0.217	0.239	0.208
Concrete	16/6/2010	0.311	0.323	0.216	0.240	0.209

TARGET	DATE	AOT440	AOT500	AOT675	AOT870	AOT936
Concrete	24/6/2010	0.315	0.294	0.228	0.180	0.164
Concrete	24/6/2010	0.311	0.288	0.223	0.184	0.168
Concrete	24/6/2010	0.309	0.287	0.222	0.172	0.156
Concrete	10/7/2010	0.379	0.339	0.287	0.294	0.268
Concrete	10/7/2010	0.412	0.320	0.261	0.220	0.283
Concrete	10/7/2010	0.366	0.322	0.257	0.218	0.241
Concrete	27/8/2010	0.415	0.341	0.244	0.280	0.219
Concrete	27/8/2010	0.358	0.320	0.293	0.297	0.234
Concrete	27/8/2010	0.421	0.374	0.248	0.334	0.277
Concrete	28/9/2010	0.214	0.196	0.124	0.159	0.144
Concrete	28/9/2010	0.226	0.200	0.133	0.158	0.144
Concrete	28/9/2010	0.224	0.199	0.131	0.164	0.150
Concrete	10/11/2010	0.214	0.206	0.151	0.122	0.111
Concrete	10/11/2010	0.221	0.212	0.160	0.126	0.115
Concrete	10/11/2010	0.226	0.217	0.167	0.131	0.119
Concrete	9/12/2010	0.261	0.231	0.142	0.094	0.086
Concrete	9/12/2010	0.255	0.226	0.148	0.094	0.085
Concrete	9/12/2010	0.256	0.228	0.152	0.097	0.088
Concrete	2/05/2011	0.335	0.329	0.325	0.284	0.249
Concrete	2/05/2011	0.342	0.338	0.340	0.296	0.260
Concrete	2/05/2011	0.350	0.349	0.357	0.310	0.273
Black Sand	13/4/2010	0.281	0.252	0.189	0.131	0.120
Black Sand	13/4/2010	0.286	0.254	0.184	0.129	0.117
Black Sand	13/4/2010	0.290	0.257	0.181	0.126	0.115
Black Sand	29/4/2010	0.479	0.414	0.255	0.229	0.272
Black Sand	29/4/2010	0.427	0.393	0.327	0.292	0.230
Black Sand	29/4/2010	0.413	0.404	0.389	0.372	0.302
Black Sand	31/5/2010	0.301	0.387	0.287	0.329	0.299
Black Sand	31/5/2010	0.283	0.360	0.261	0.305	0.277
Black Sand	31/5/2010	0.267	0.269	0.190	0.229	0.209
Black Sand	31/5/2010	0.263	0.280	0.194	0.234	0.213
Black Sand	31/5/2010	0.261	0.300	0.207	0.250	0.228
Black Sand	31/5/2010	0.275	0.294	0.210	0.243	0.221
Black Sand	28/9/2010	0.253	0.233	0.167	0.231	0.210
Black Sand	28/9/2010	0.259	0.235	0.170	0.225	0.205
Black Sand	10/11/2010	0.303	0.285	0.216	0.169	0.154
Black Sand	10/11/2010	0.308	0.290	0.222	0.173	0.158
Black Sand	10/11/2010	0.314	0.296	0.230	0.178	0.162
Black Sand	9/12/2010	0.275	0.244	0.156	0.099	0.090
Black Sand	9/12/2010	0.273	0.243	0.161	0.101	0.092
Black Sand	9/12/2010	0.269	0.240	0.163	0.103	0.094
Black Sand	9/12/2010	0.265	0.238	0.167	0.107	0.097
Black Sand	2/05/2011	0.303	0.253	0.235	0.224	0.195
Black Sand	20/5/2011	0.303	0.253	0.233	0.224	0.195
Black Sand	2/05/2011	0.306	0.248	0.224	0.205	0.196

TARGET	DATE	AOT440	AOT500	AOT675	AOT870	AOT936
Compacted sand	13/4/2010	0.290	0.282	0.255	0.190	0.173
Compacted sand	13/4/2010	0.284	0.273	0.234	0.172	0.157
Compacted sand	13/4/2010	0.283	0.260	0.202	0.145	0.132
Compacted sand	29/4/2010	0.406	0.391	0.377	0.319	0.281
Compacted sand	29/4/2010	0.420	0.407	0.379	0.319	0.272
Compacted sand	31/5/2010	0.272	0.321	0.223	0.261	0.237
Compacted sand	31/5/2010	0.270	0.310	0.214	0.252	0.229
Compacted sand	31/5/2010	0.268	0.300	0.204	0.243	0.221
Compacted sand	16/6/2010	0.302	0.344	0.313	0.240	0.210
Compacted sand	16/6/2010	0.310	0.314	0.217	0.241	0.210
Compacted sand	16/6/2010	0.305	0.321	0.319	0.246	0.215
Compacted sand	24/6/2010	0.338	0.299	0.255	0.218	0.198
Compacted sand	24/6/2010	0.330	0.290	0.255	0.219	0.199
Compacted sand	24/6/2010	0.340	0.302	0.263	0.217	0.198
Compacted sand	10/7/2010	0.401	0.341	0.211	0.217	0.197
Compacted sand	10/7/2010	0.297	0.271	0.217	0.165	0.141
Compacted sand	27/8/2010	0.404	0.347	0.248	0.321	0.265
Compacted sand	27/8/2010	0.420	0.357	0.267	0.315	0.260
Compacted sand	27/8/2010	0.382	0.333	0.223	0.295	0.241
Compacted sand	28/9/2010	0.298	0.272	0.198	0.252	0.229
Compacted sand	28/9/2010	0.294	0.263	0.185	0.219	0.199
Compacted sand	28/9/2010	0.282	0.252	0.173	0.207	0.188
Compacted sand	10/11/2010	0.237	0.228	0.180	0.139	0.127
Compacted sand	10/11/2010	0.240	0.232	0.186	0.143	0.130
Compacted sand	10/11/2010	0.244	0.237	0.193	0.149	0.135
Compacted sand	9/12/2010	0.277	0.246	0.159	0.102	0.093
Compacted sand	9/12/2010	0.291	0.260	0.174	0.113	0.103
Compacted	9/12/2010	0.287	0.259	0.171	0.107	0.098

TARGET	DATE	AOT440	AOT500	AOT675	AOT870	AOT936
sand						
Compacted sand	2/05/2011	0.330	0.283	0.201	0.282	0.211
Compacted sand	2/05/2011	0.328	0.321	0.301	0.287	0.207
Compacted sand	2/05/2011	.307	0.299	0.277	0.269	0.182

Appendix 2 Table 1 AOT values from Microtops Sun photometer

Cimel Aeronet AOT values

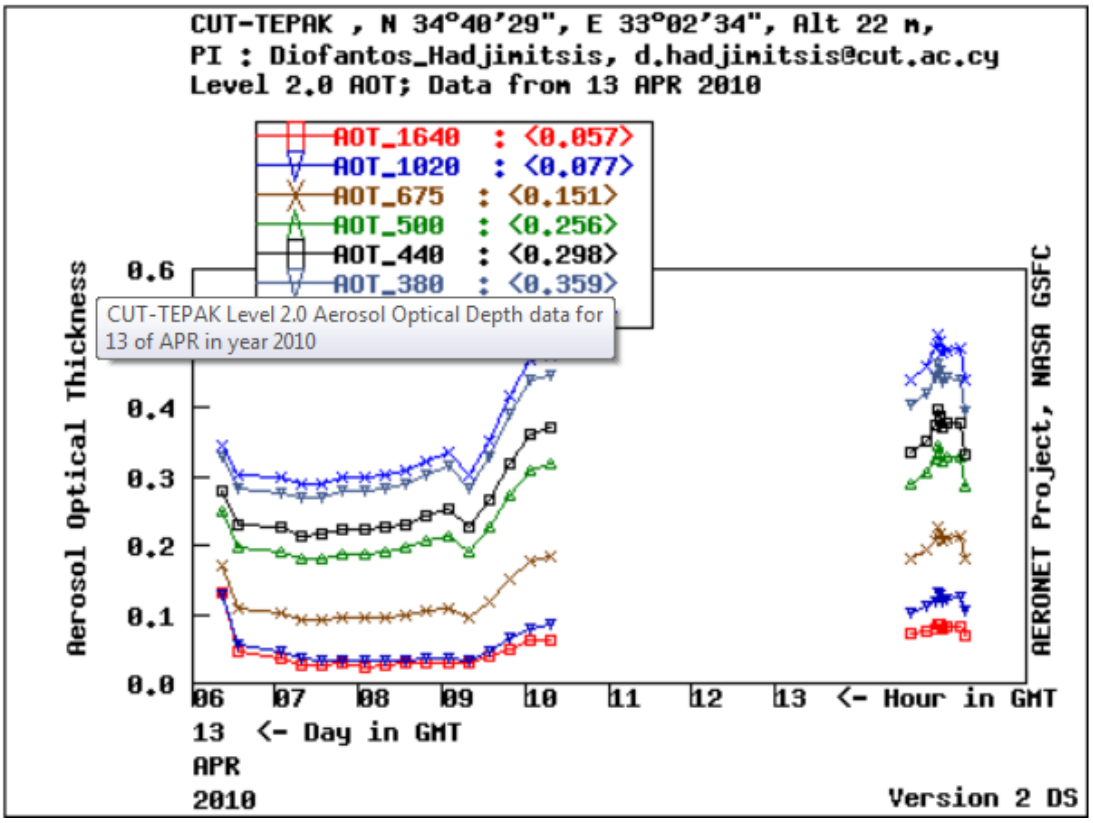

Appendix 2 Figure 1 AERONET values from 13/4/2010

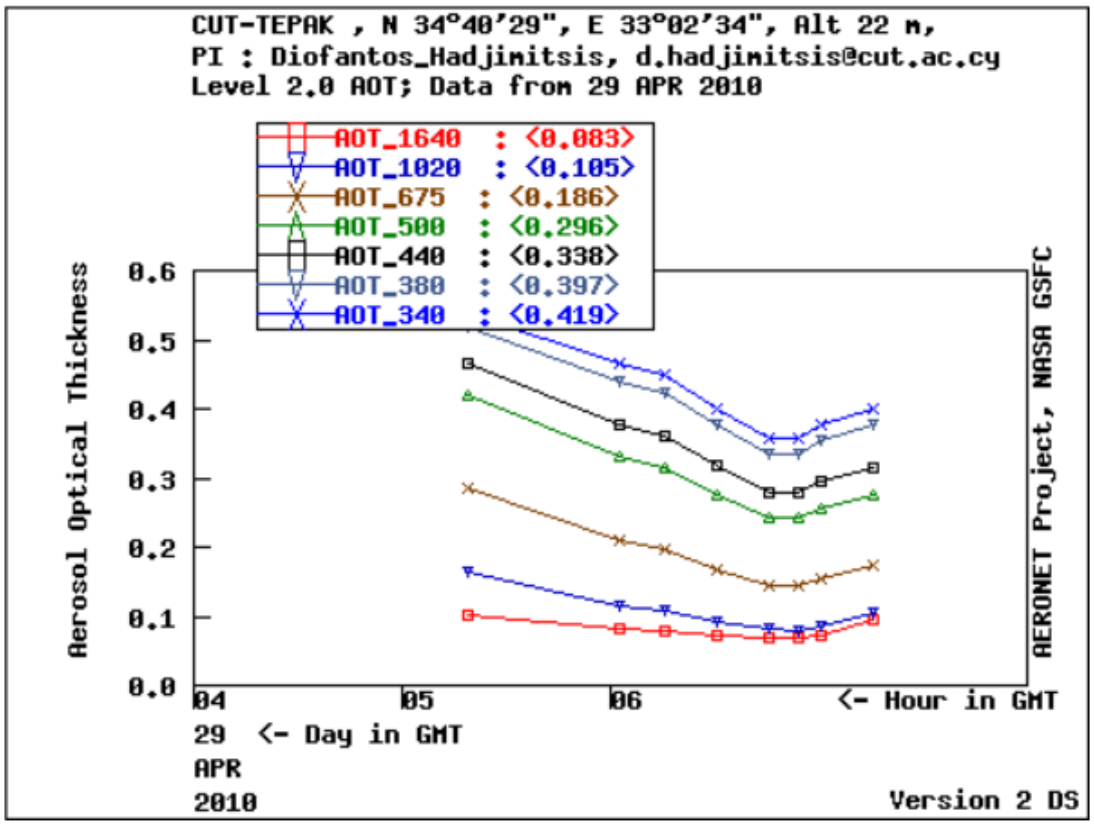

Appendix 2 Figure 2 AERONET values from 29/4/2010

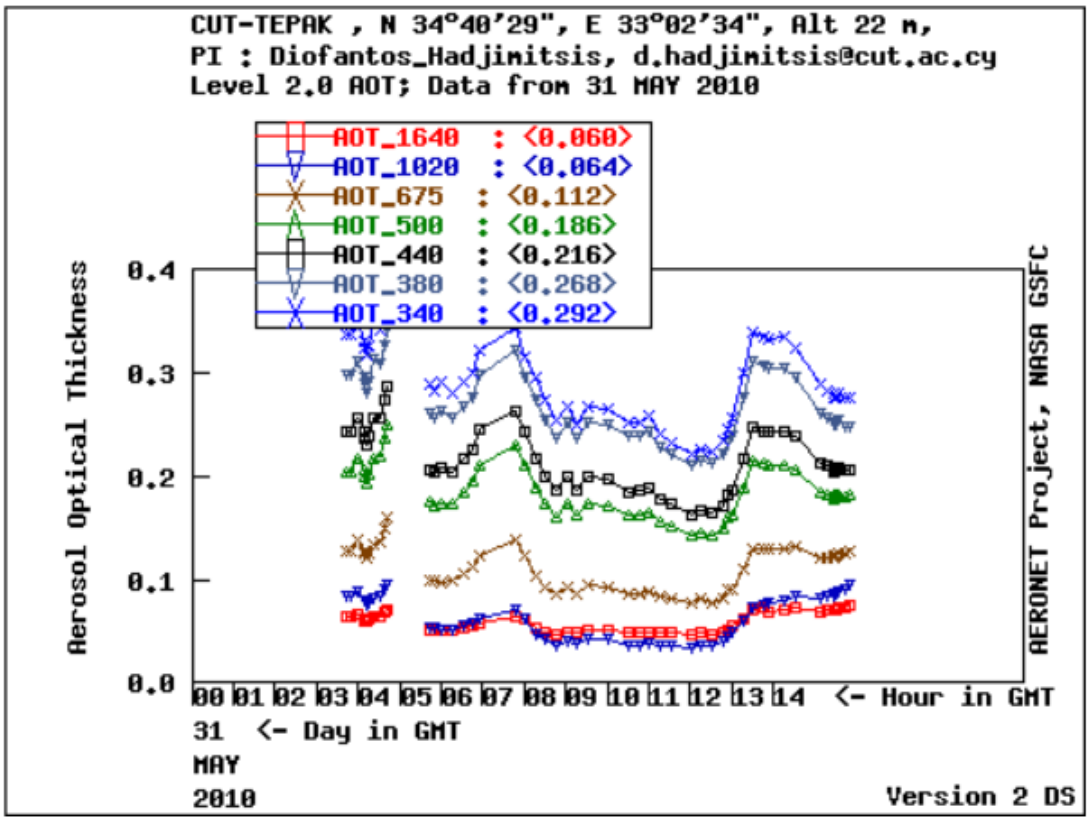

Appendix 2 Figure 3 AERONET values from 31/5/2010

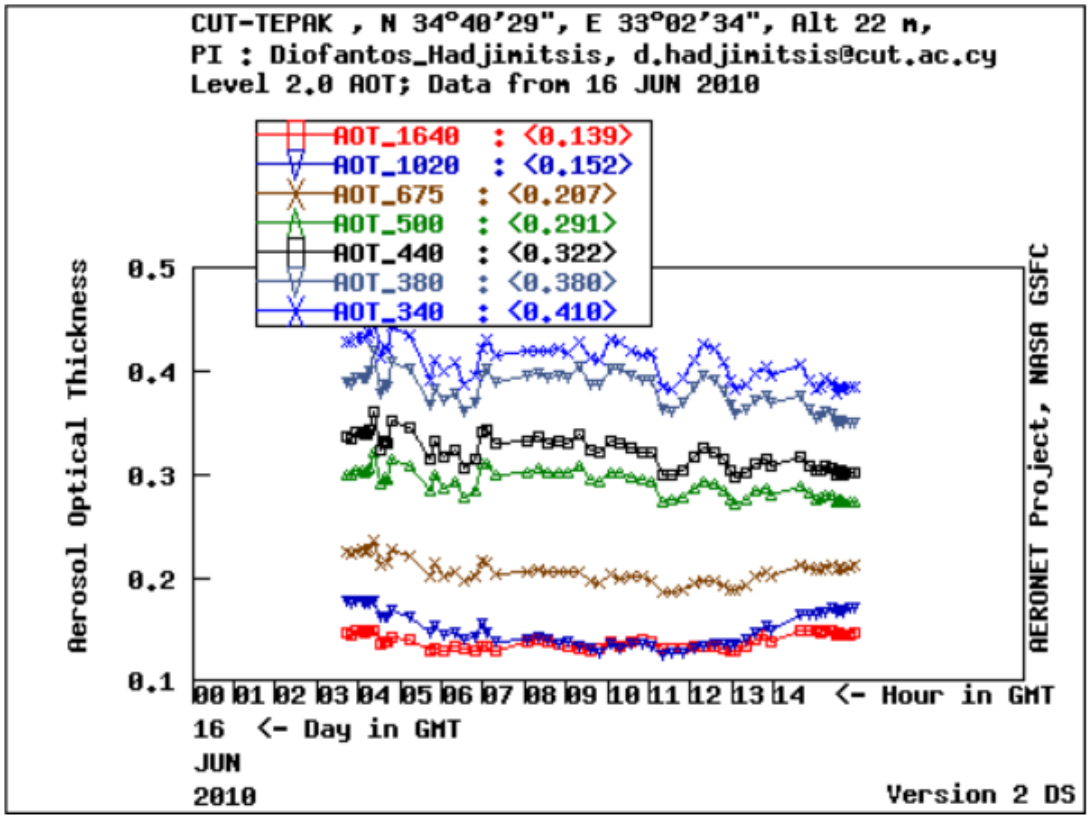

Appendix 2 Figure 4 AERONET values from 16/6/2010

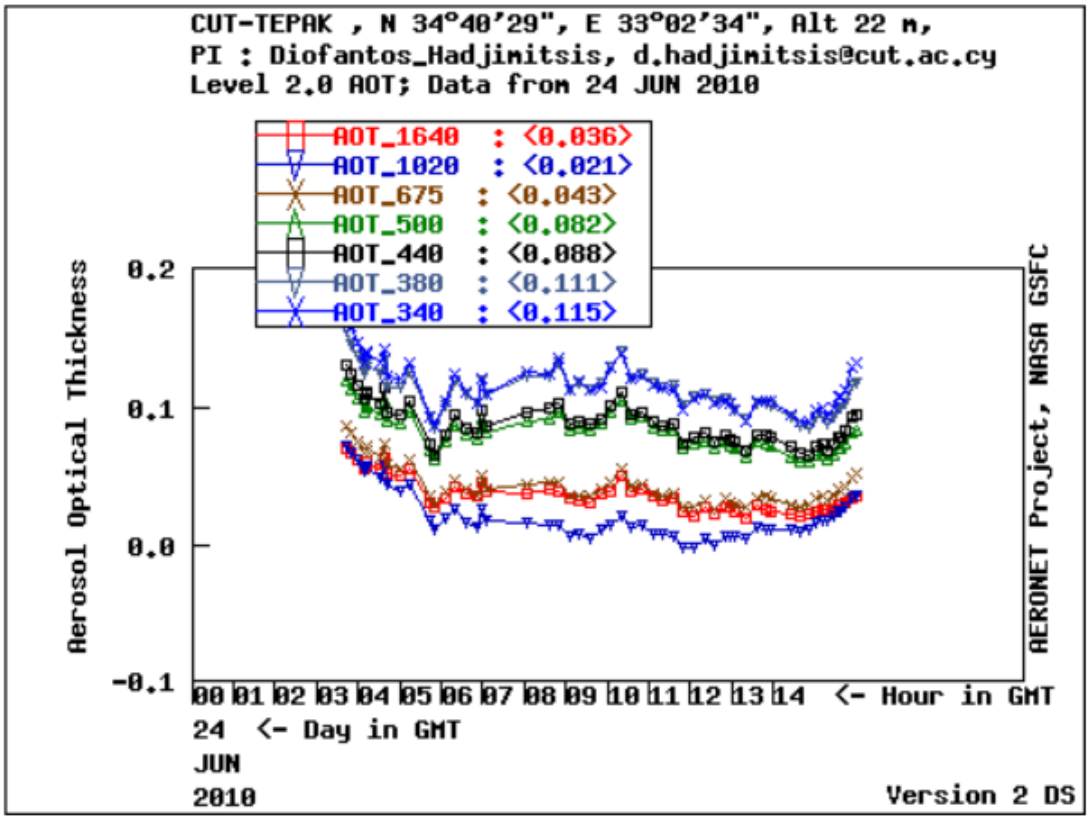

Appendix 2 Figure 5 AERONET values from 24/6/2010

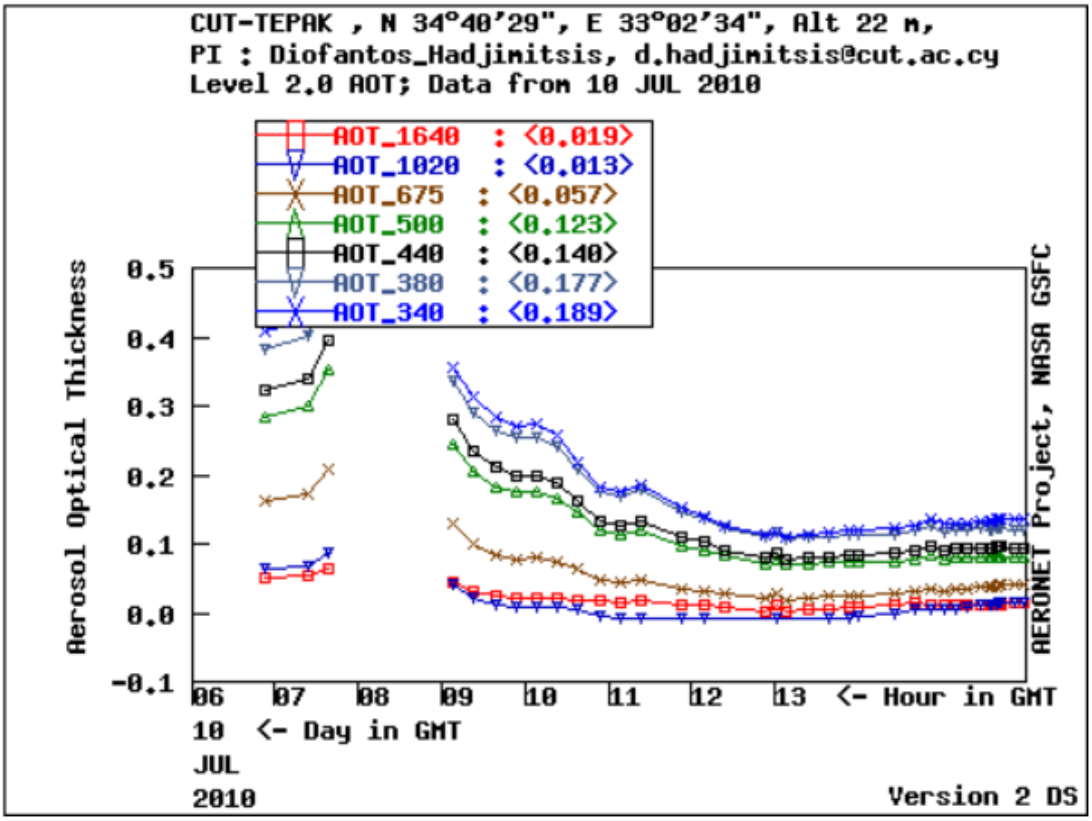

Appendix 2 Figure 6 AERONET values from 10/7/2010

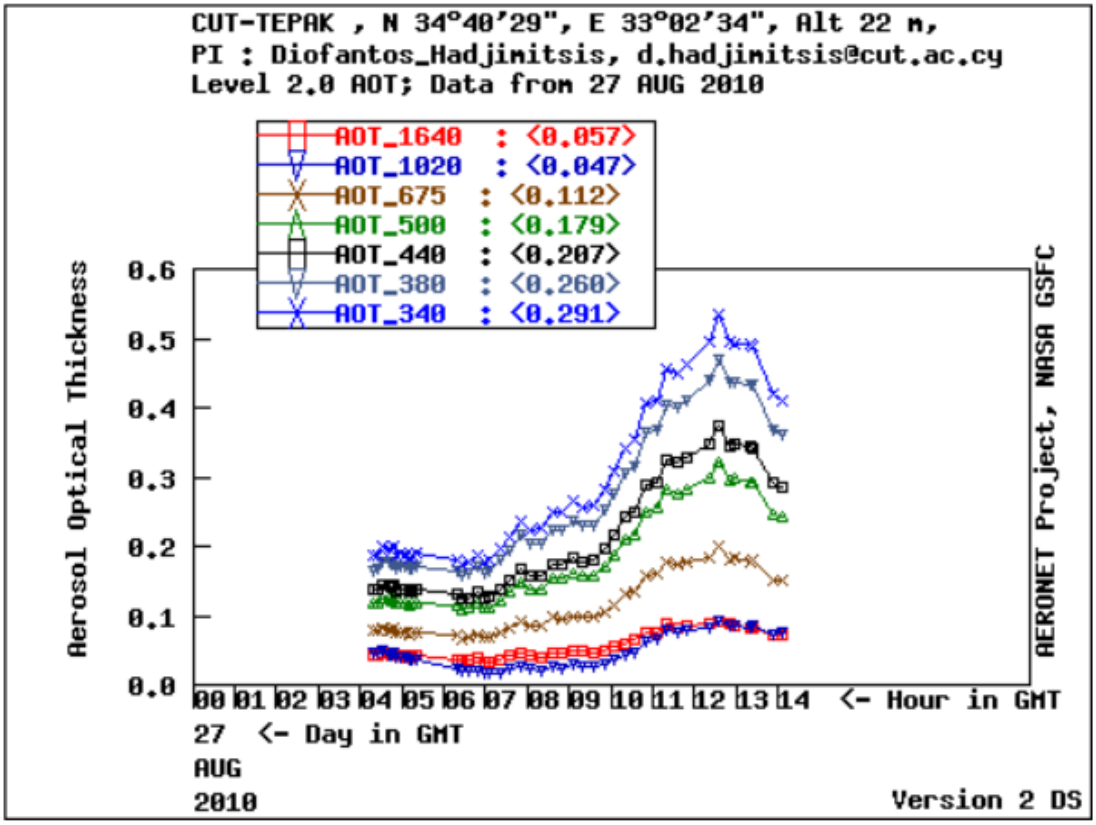

Appendix 2 Figure 7 AERONET values from 27/8/2010

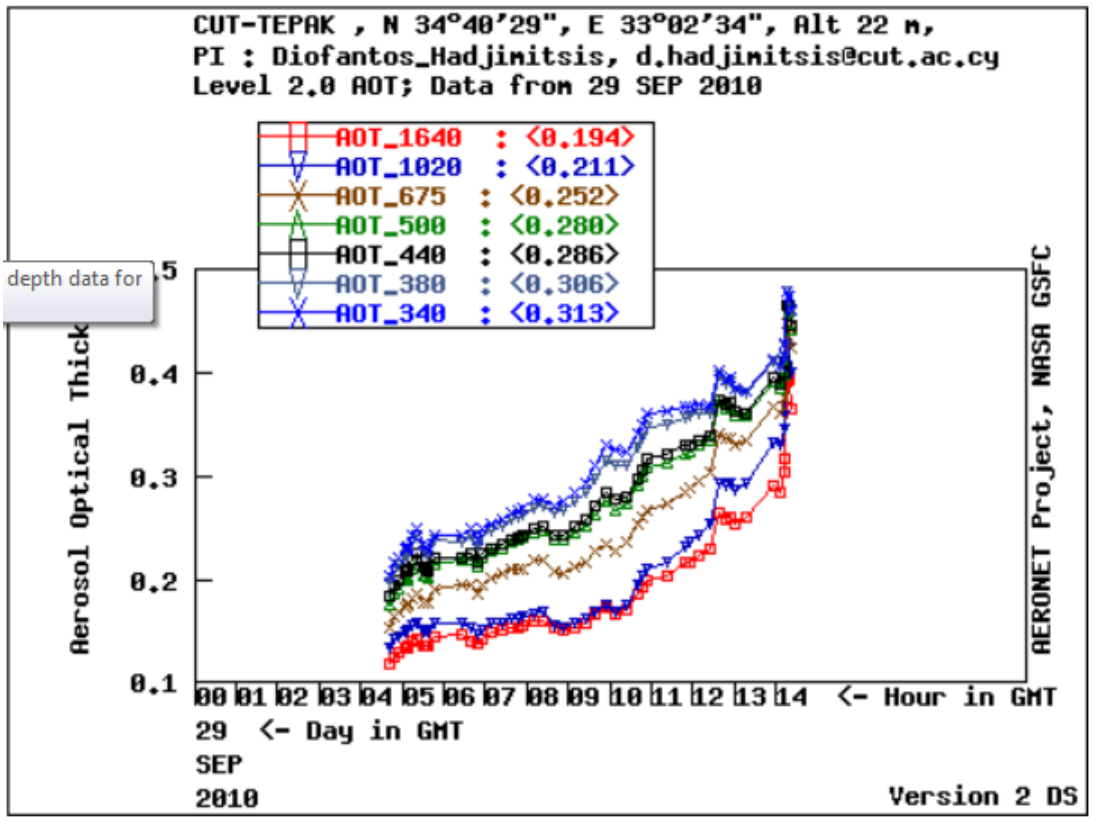

Appendix 2 Figure 8 AERONET values from 28/9/2010

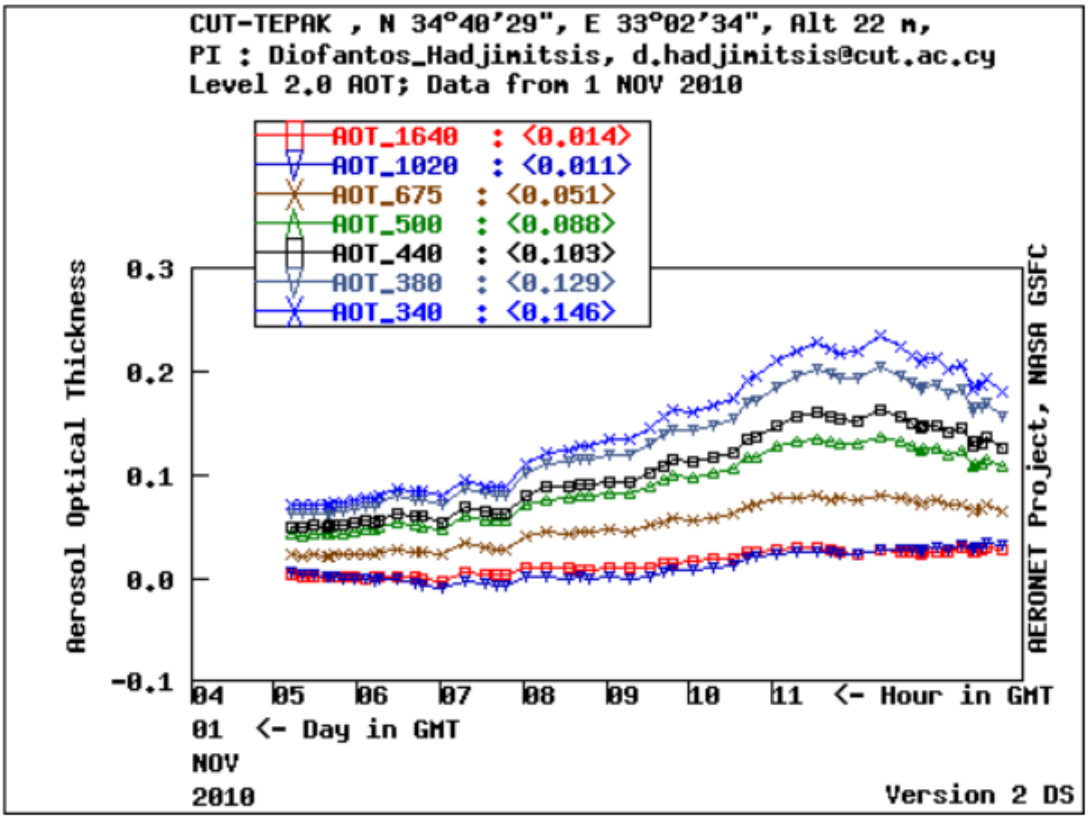

Appendix 2 Figure 9 AERONET values from 7/11/2010

Single Scattering Albedo

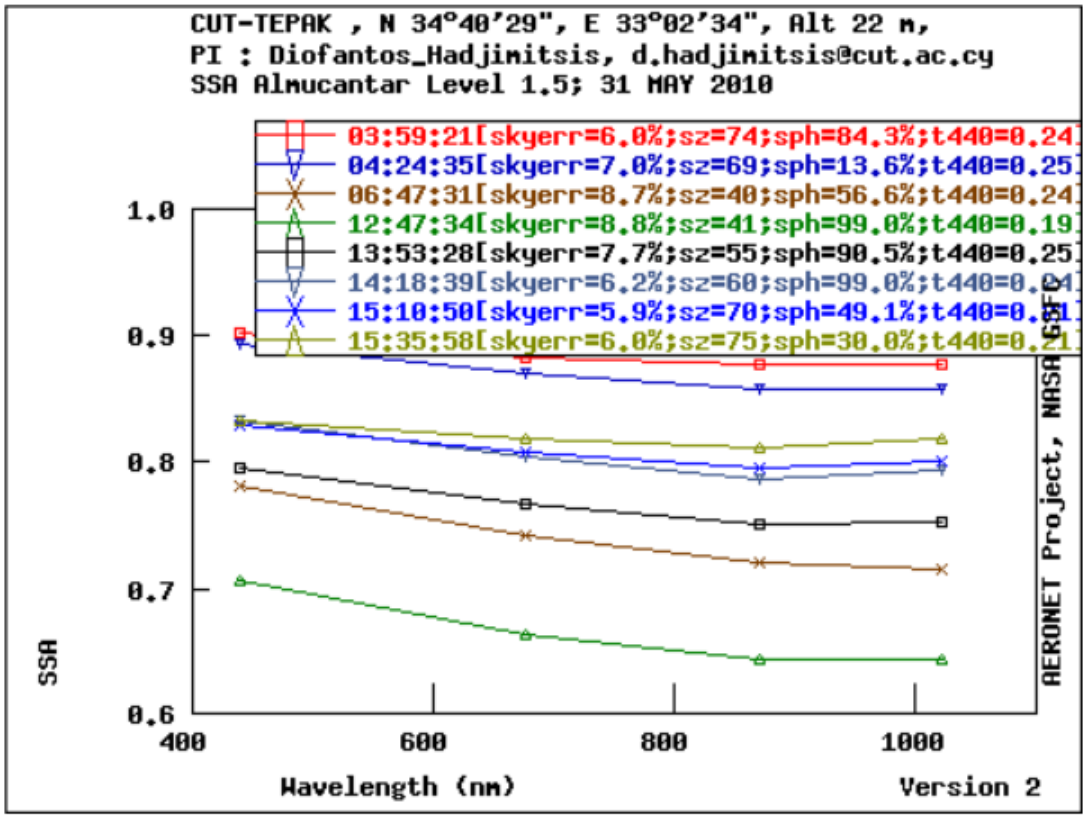

Appendix 2 Figure 10 Single Scattering Albedo for 31/5/2010 (AERONET)

Phase function, Limassol, by month

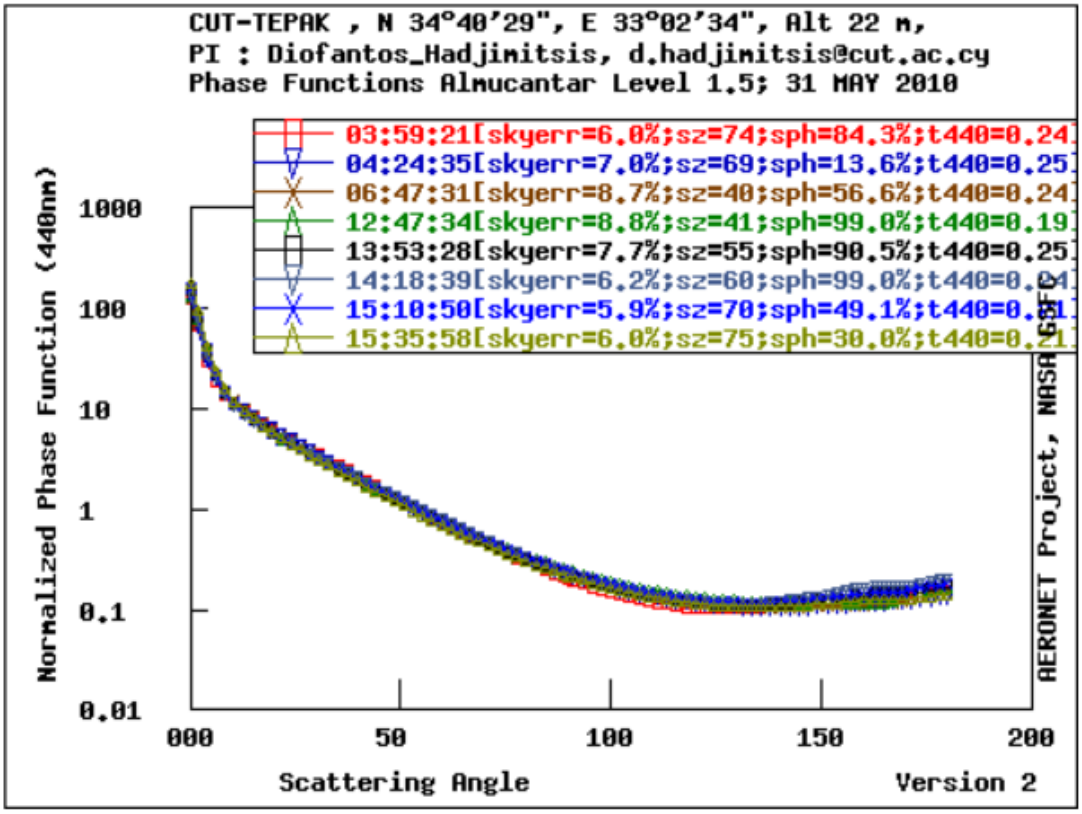

Appendix 2 Figure 11 Phase function for 31/5/2010 (AERONET)

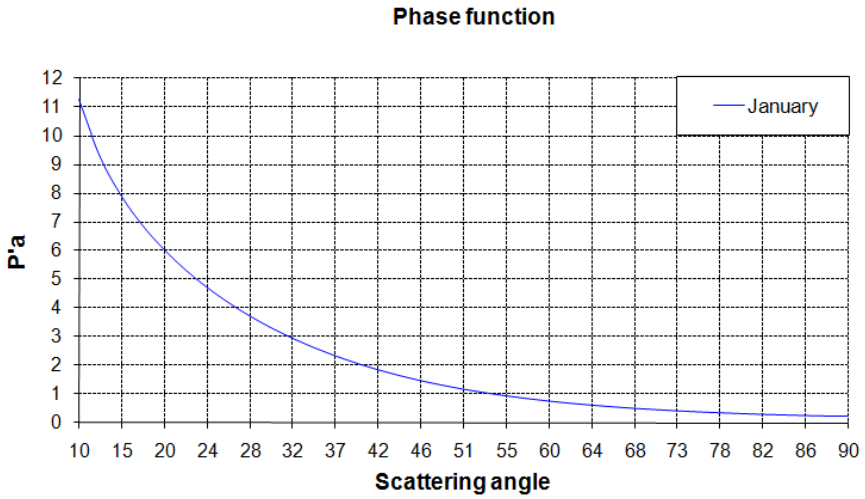

Appendix 2 Figure 12 Phase function graph, January

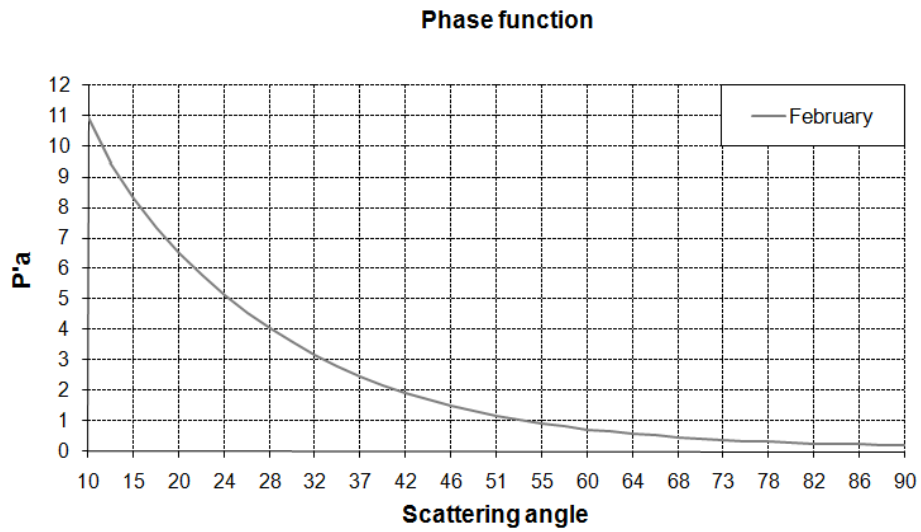

Appendix 2 Figure 13 Phase function graph, February

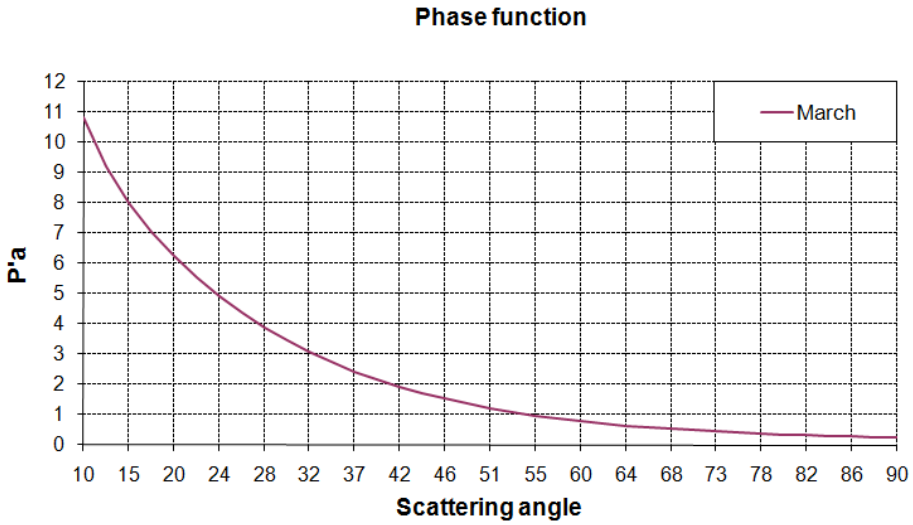

Appendix 2 Figure 14 Phase function graph, March

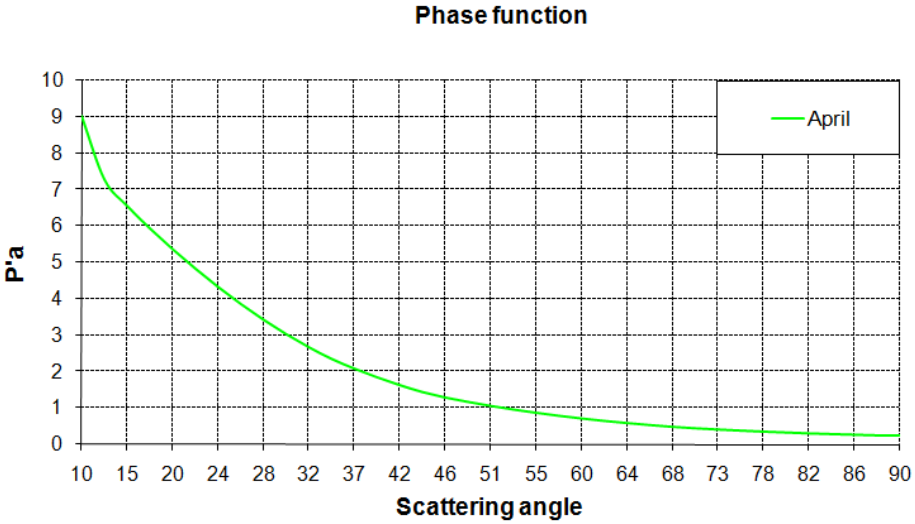

Appendix 2 Figure 15 Phase function graph, April

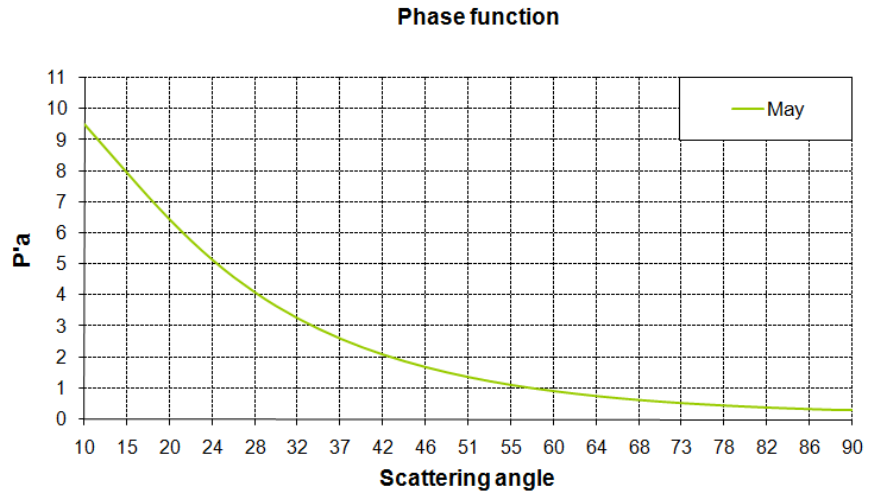

Appendix 2 Figure 16 Phase function graph, May

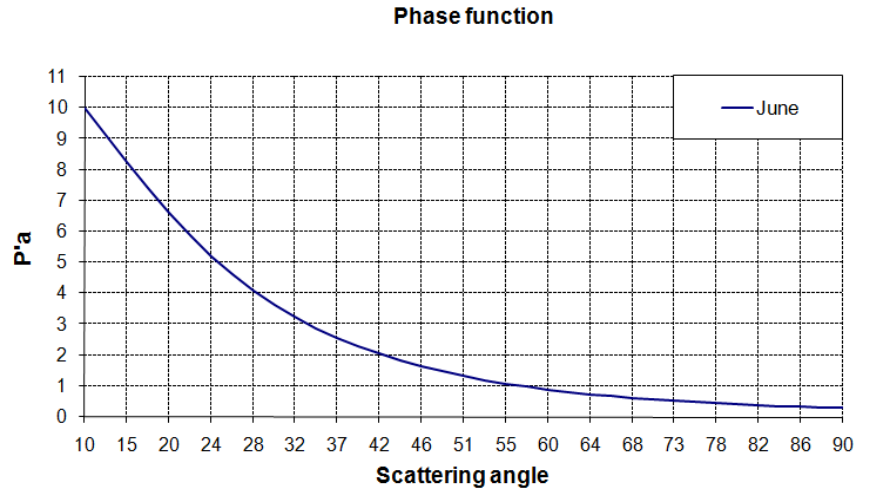

Appendix 2 Figure 17 Phase function graph, June

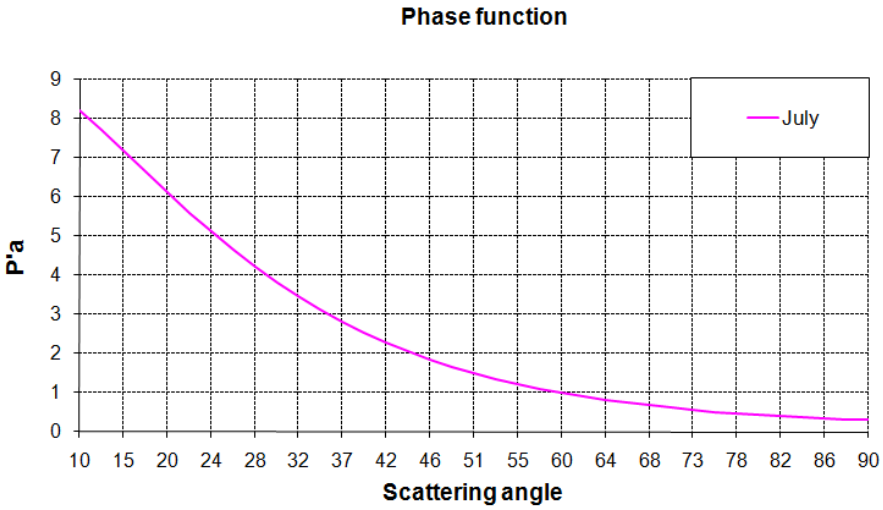

Appendix 2 Figure 18 Phase function graph, July

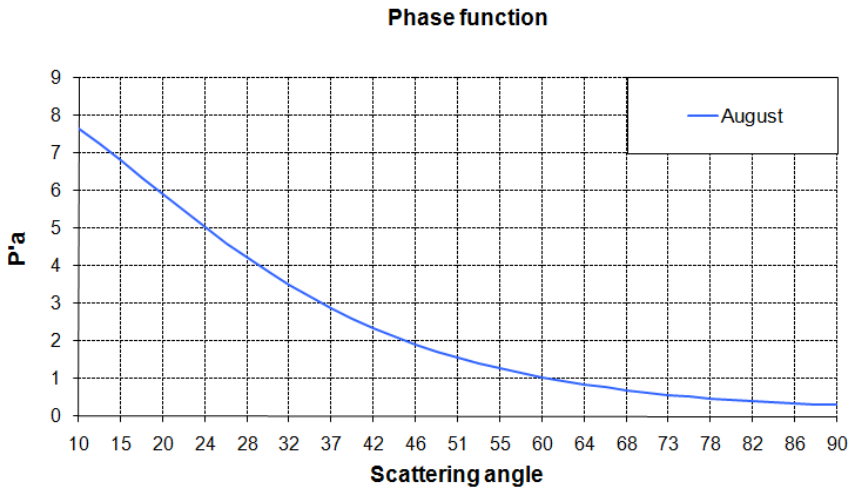

Appendix 2 Figure 19 Phase function graph, August

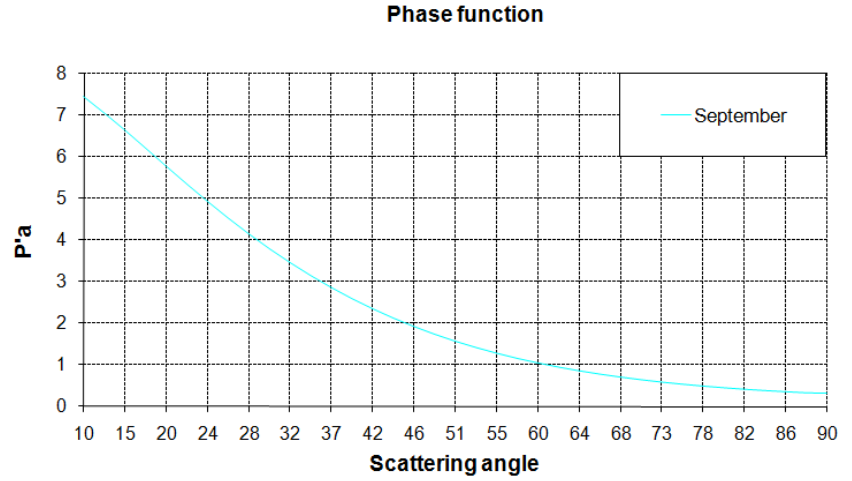

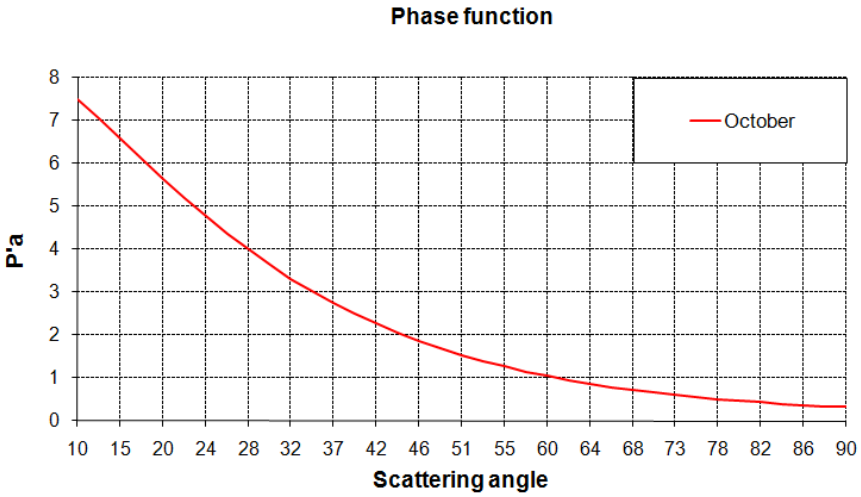

Appendix 2 Figure 20 Phase function graph, September

Appendix 2 Figure 21 Phase function graph, October

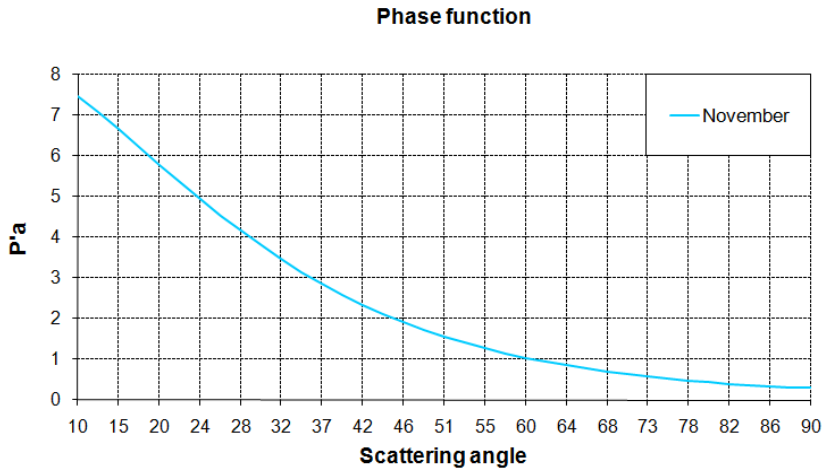

Appendix 2 Figure 22 Phase function graph, November

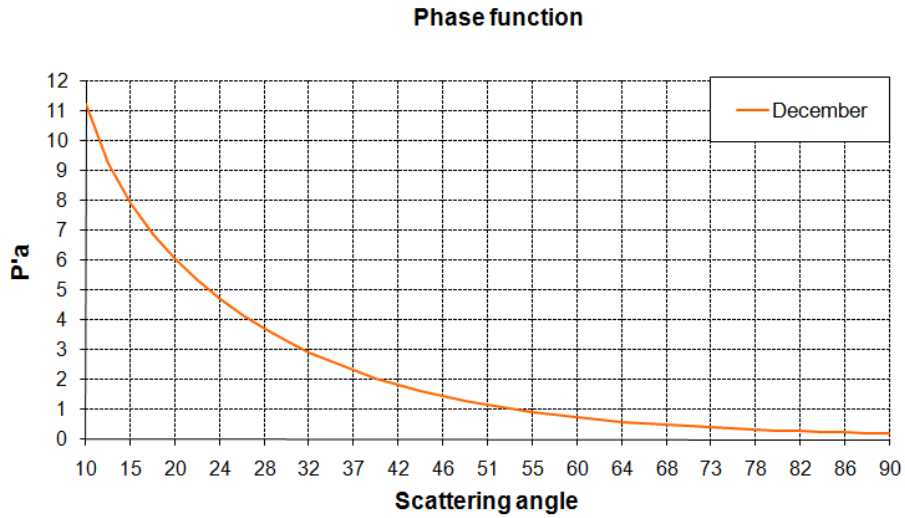

Appendix 2 Figure 23 Phase function graph, December

Appendix 3

- Earth-Date correction table
- Log sheet for Microtops Sun-photometer field campaign

Earth-Date correction table

Earth-Sun distance (d) in astronomical units for Day of the Year (DOY)											
DOY	**d**	**DOY**	**d**	**DOY**	**d**	**DOY**	**d**	**DOY**	**d**	**DOY**	**d**
1	0.98331	**61**	0.99108	**121**	1.00756	**181**	1.01665	**241**	1.00992	**301**	0.99359
2	0.98330	**62**	0.99133	**122**	1.00781	**182**	1.01667	**242**	1.00969	**302**	0.99332
3	0.98330	**63**	0.99158	**123**	1.00806	**183**	1.01668	**243**	1.00946	**303**	0.99306
4	0.98330	**64**	0.99183	**124**	1.00831	**184**	1.01670	**244**	1.00922	**304**	0.99279
5	0.98330	**65**	0.99208	**125**	1.00856	**185**	1.01670	**245**	1.00898	**305**	0.99253
6	0.98332	**66**	0.99234	**126**	1.00880	**186**	1.01670	**246**	1.00874	**306**	0.99228
7	0.98333	**67**	0.99260	**127**	1.00904	**187**	1.01670	**247**	1.00850	**307**	0.99202
8	0.98335	**68**	0.99286	**128**	1.00928	**188**	1.01669	**248**	1.00825	**308**	0.99177
9	0.98338	**69**	0.99312	**129**	1.00952	**189**	1.01668	**249**	1.00800	**309**	0.99152
10	0.98341	**70**	0.99339	**130**	1.00975	**190**	1.01666	**250**	1.00775	**310**	0.99127
11	0.98345	**71**	0.99365	**131**	1.00998	**191**	1.01664	**251**	1.00750	**311**	0.99102
12	0.98349	**72**	0.99392	**132**	1.01020	**192**	1.01661	**252**	1.00724	**312**	0.99078
13	0.98354	**73**	0.99419	**133**	1.01043	**193**	1.01658	**253**	1.00698	**313**	0.99054
14	0.98359	**74**	0.99446	**134**	1.01065	**194**	1.01655	**254**	1.00672	**314**	0.99030
15	0.98365	**75**	0.99474	**135**	1.01087	**195**	1.01650	**255**	1.00646	**315**	0.99007
16	0.98371	**76**	0.99501	**136**	1.01108	**196**	1.01646	**256**	1.00620	**316**	0.98983
17	0.98378	**77**	0.99529	**137**	1.01129	**197**	1.01641	**257**	1.00593	**317**	0.98961
18	0.98385	**78**	0.99556	**138**	1.01150	**198**	1.01635	**258**	1.00566	**318**	0.98938
19	0.98393	**79**	0.99584	**139**	1.01170	**199**	1.01629	**259**	1.00539	**319**	0.98916
20	0.98401	**80**	0.99612	**140**	1.01191	**200**	1.01623	**260**	1.00512	**320**	0.98894
21	0.98410	**81**	0.99640	**141**	1.01210	**201**	1.01616	**261**	1.00485	**321**	0.98872
22	0.98419	**82**	0.99669	**142**	1.01230	**202**	1.01609	**262**	1.00457	**322**	0.98851
23	0.98428	**83**	0.99697	**143**	1.01249	**203**	1.01601	**263**	1.00430	**323**	0.98830
24	0.98439	**84**	0.99725	**144**	1.01267	**204**	1.01592	**264**	1.00402	**324**	0.98809
25	0.98449	**85**	0.99754	**145**	1.01286	**205**	1.01584	**265**	1.00374	**325**	0.98789
26	0.98460	**86**	0.99782	**146**	1.01304	**206**	1.01575	**266**	1.00346	**326**	0.98769
27	0.98472	**87**	0.99811	**147**	1.01321	**207**	1.01565	**267**	1.00318	**327**	0.98750
28	0.98484	**88**	0.99840	**148**	1.01338	**208**	1.01555	**268**	1.00290	**328**	0.98731
29	0.98496	**89**	0.99868	**149**	1.01355	**209**	1.01544	**269**	1.00262	**329**	0.98712
30	0.98509	**90**	0.99897	**150**	1.01371	**210**	1.01533	**270**	1.00234	**330**	0.98694
31	0.98523	**91**	0.99926	**151**	1.01387	**211**	1.01522	**271**	1.00205	**331**	0.98676
32	0.98536	**92**	0.99954	**152**	1.01403	**212**	1.01510	**272**	1.00177	**332**	0.98658
33	0.98551	**93**	0.99983	**153**	1.01418	**213**	1.01497	**273**	1.00148	**333**	0.98641
34	0.98565	**94**	1.00012	**154**	1.01433	**214**	1.01485	**274**	1.00119	**334**	0.98624
35	0.98580	**95**	1.00041	**155**	1.01447	**215**	1.01471	**275**	1.00091	**335**	0.98608
36	0.98596	**96**	1.00069	**156**	1.01461	**216**	1.01458	**276**	1.00062	**336**	0.98592
37	0.98612	**97**	1.00098	**157**	1.01475	**217**	1.01444	**277**	1.00033	**337**	0.98577
38	0.98628	**98**	1.00127	**158**	1.01488	**218**	1.01429	**278**	1.00005	**338**	0.98562
39	0.98645	**99**	1.00155	**159**	1.01500	**219**	1.01414	**279**	0.99976	**339**	0.98547
40	0.98662	**100**	1.00184	**160**	1.01513	**220**	1.01399	**280**	0.99947	**340**	0.98533
41	0.98680	**101**	1.00212	**161**	1.01524	**221**	1.01383	**281**	0.99918	**341**	0.98519
42	0.98698	**102**	1.00240	**162**	1.01536	**222**	1.01367	**282**	0.99890	**342**	0.98506
43	0.98717	**103**	1.00269	**163**	1.01547	**223**	1.01351	**283**	0.99861	**343**	0.98493
44	0.98735	**104**	1.00297	**164**	1.01557	**224**	1.01334	**284**	0.99832	**344**	0.98481
45	0.98755	**105**	1.00325	**165**	1.01567	**225**	1.01317	**285**	0.99804	**345**	0.98469
46	0.98774	**106**	1.00353	**166**	1.01577	**226**	1.01299	**286**	0.99775	**346**	0.98457
47	0.98794	**107**	1.00381	**167**	1.01586	**227**	1.01281	**287**	0.99747	**347**	0.98446
48	0.98814	**108**	1.00409	**168**	1.01595	**228**	1.01263	**288**	0.99718	**348**	0.98436
49	0.98835	**109**	1.00437	**169**	1.01603	**229**	1.01244	**289**	0.99690	**349**	0.98426

50	0.98856	**110**	1.00464	**170**	1.01610	**230**	1.01225	**290**	0.99662	**350**	0.98416
51	0.98877	**111**	1.00492	**171**	1.01618	**231**	1.01205	**291**	0.99634	**351**	0.98407
52	0.98899	**112**	1.00519	**172**	1.01625	**232**	1.01186	**292**	0.99605	**352**	0.98399
53	0.98921	**113**	1.00546	**173**	1.01631	**233**	1.01165	**293**	0.99577	**353**	0.98391
54	0.98944	**114**	1.00573	**174**	1.01637	**234**	1.01145	**294**	0.99550	**354**	0.98383
55	0.98966	**115**	1.00600	**175**	1.01642	**235**	1.01124	**295**	0.99522	**355**	0.98376
56	0.98989	**116**	1.00626	**176**	1.01647	**236**	1.01103	**296**	0.99494	**356**	0.98370
57	0.99012	**117**	1.00653	**177**	1.01652	**237**	1.01081	**297**	0.99467	**357**	0.98363
58	0.99036	**118**	1.00679	**178**	1.01656	**238**	1.01060	**298**	0.99440	**358**	0.98358
59	0.99060	**119**	1.00705	**179**	1.01659	**239**	1.01037	**299**	0.99412	**359**	0.98353
60	0.99084	**120**	1.00731	**180**	1.01662	**240**	1.01015	**300**	0.99385	**360**	0.98348
										361	0.98344
										362	0.98340
										363	0.98337
										364	0.98335
										365	0.98333
										366	0.98331

GER 1500 & HR 1024

REMOTE SENSING LAB
CYPRUS UNIVERSITY OF TECHNOLOGY

SERIAL NO.		SHEET NO.	

SITE		REFERENCE PANEL	SPECTRALONE		
DATE		MODE	STAND ALONE	COMPUTER	DUAL BEAM
OPERATOR		OPTIC	STANDARD	4^0	
ILLUMINATION		OPTIC			

LOCATION	TIME	TYPE OF SURFACE	REF ID	TARG ID	TEMPRETURE		SUNPHOTOMETER SCAN ID	SKY
					SURFACE	AIR		

SKY CODES : [0] Clear sky; **[1] Haze;** [2] Clouds – sun not obscured; **[3] Clouds – sun obscured;** [4] Scattered Clouds; **[P] Photograph.**

Appendix 3 Table 2 Log sheet for Microtops Sun-photometer field campaign